E.ON Energy Research Center ERC | RWTH AACHEN UNIVERSITY

Model Predictive Control for Frequency Stability Enhancement of Converter-driven Power Systems

Tobias Heins
Institute for Automation of Complex Power Systems

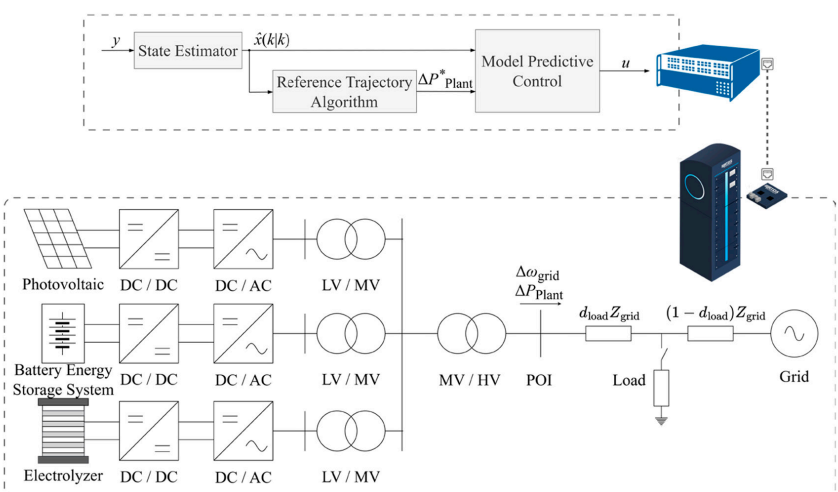

Model Predictive Control for Frequency Stability Enhancement of Converter-driven Power Systems

Von der Fakultät für Elektrotechnik und Informationstechnik
der Rheinisch-Westfälischen Technischen Hochschule Aachen
zur Erlangung des akademischen Grades eines Doktors
der Ingenieurwissenschaften genehmigte Dissertation

vorgelegt von

Tobias Heins, M. Sc.

aus
Oberhausen, Deutschland

Berichtende: Univ.-Prof. Antonello Monti, Ph. D.
Univ.-Prof. Dr. Veit Hagenmeyer

Tag der mündlichen Prüfung: 05. Mai 2026

Diese Dissertation ist auf den Internetseiten der Universitätsbibliothek online verfügbar.

Bibliographische Information der Deutschen Nationalbibliothek
Die Deutsche Nationalbibliothek verzeichnet diese Publikation in der Deutschen Nationalbibliografie; detaillierte bibliografische Daten sind im Internet über https://dnb.dnb.de abrufbar.

D 82 (Diss. RWTH Aachen University, 2026)

Herausgeber:
E.ON Energy Research Center

Institute for Automation of Complex Power Systems (ACS)
E.ON Energy Research Center
Mathieustraße 10
52074 Aachen

E.ON Energy Research Center I 154. Ausgabe der Serie
ACS I Automation of Complex Power Systems

Copyright Tobias Heins
Alle Rechte, auch das des auszugsweisen Nachdrucks, der auszugsweisen oder vollständigen Wiedergabe, der Speicherung in Datenverarbeitungsanlagen und der Übersetzung, vorbehalten.

Printed in Germany

ISBN: 978-3-948234-68-3
1. Auflage 2026

Verlag:
E.ON Energy Research Center, RWTH Aachen University
Mathieustraße 10
52074 Aachen
Internet: www.eonerc.rwth-aachen.de
E-Mail: post_erc@eonerc.rwth-aachen.de

Herstellung :
Druckservice Zillekens
Rainweg 19
52224 Stolberg
Mail: info@druckservice-zillekens.de

Kurzfassung

Motivation, Ziel und Aufgabenstellung der Arbeit

Der globale Wandel von fossilen Kraftwerken hin zu erneuerbaren Energiequellen (Renewable Energy Sources - RES), der durch leistungselektronische Umrichter ermöglicht wird, reduziert die Trägheit des elektrischen Netzes erheblich, wodurch weniger Zeit für automatisierte Maßnahmen bei plötzlichen Leistungsungleichgewichten bleibt und letztlich die Frequenzstabilität des Stromnetzes gefährdet wird. Da Umrichter keine inhärente Energiespeicherung bieten, sind schnelle Regelungsmaßnahmen erforderlich, um die betrieblichen Grenzen des Umrichters und der zugrunde liegenden RES einzuhalten, wodurch ihr Potenzial zur Frequenzstützung eingeschränkt wird. Darüber hinaus lassen sich die Umrichter in netzbildende (Grid-Forming - GFM) und netzfolgende (Grid-Following - GFL) Typen einteilen, die sich in ihren dynamischen Eigenschaften deutlich unterscheiden. Durch eine koordinierte Regelung können die individuellen Nachteile einzelner RES-Typen überwunden und ihre unterschiedlichen betrieblichen Grenzen und dynamischen Eigenschaften für eine effektive Frequenzregelung genutzt werden. Die Fähigkeit klassischer Regelungsstrategien, mit solchen Einschränkungen umzugehen, ist stark begrenzt. Darüber hinaus kann mit diesen Strategien die Koordination mehrerer heterogener RES nur durch eine Trennung der Zeitskalen und aufwendige Parametereinstellungen erreicht werden.

In diesem Zusammenhang erweist sich die modellprädiktive Regelung (Model Predictive Control - MPC) als fortschrittlicher Regelungsansatz, der unter betrieblichen Grenzen und schnellen Dynamiken optimale Regelungsmaßnahmen bietet. Die starke Kopplung der Leistungs- und Frequenzdynamik einzelner Umrichter mit dem Rest des Stromnetzes in Verbindung mit begrenzten verfügbaren Messungen im Zeitbereich der Umrichterregelung macht die Anwendung von MPC für eine schnelle Frequenzregelung mit erneuerbaren Energiequellen zu einer Herausforderung. Darüber hinaus beeinträchtigen Kommunikationssysteme die Regelungsleistung durch Zeitverzögerungen und Verluste bei Mess- und Regelsignalen. Zu diesem Zweck haben sich verteilte Regelungsalgorithmen als resilientere Regelungsimplementierung bewährt. Ziel dieser Dissertation ist die Entwicklung und Demonstration von MPC-Strategien für die Frequenz- und Leistungsregelung mehrerer RES, um die Frequenzstabilität von elektrischen Netzen zu verbessern, die von umrichtergekoppelten erneuerbaren Energiequellen dominiert werden.

Wesentliche wissenschaftliche Beiträge der Arbeit

Die Dissertation leistet einen Beitrag zur prädiktiven Frequenzregelung in den Bereichen der Modellierung von Frequenz- und Leistungsdynamik, der Auslegung zentraler und verteilter MPC-Systeme für umrichterbasierte erneuerbare Energiequellen und der Integration von Kommunikationssystemen in das Regelsystem.

Zunächst wird unter Verwendung des Konzepts des Frequenzteilers ein neues regelungsorientiertes Modell zur Prädiktion von Frequenz und Leistung hergeleitet. Das Modell formuliert Störungen der Last des Stromnetzes als Prozessrauschen, wodurch die Notwendigkeit entfällt, die Höhe der Störungen zu schätzen. Im Vergleich zu etablierten Modellen, die auf dem Leistungsaustausch über Übertragungsleitungen basieren, erfordert das vorgestellte Prädiktionsmodell keine zusätzlichen Störungszustände für die prädiktive Regelung und ist für jede Netzwerktopologie vollständig beobachtbar.

Zweitens werden MPC-Strategien für netzgekoppelte Umrichtersysteme, die als hybride erneuerbare Kraftwerke betrieben werden, und für inselbetriebene, vollständig umrichtergesteuerte Netze, oft als Microgrids bezeichnet, entwickelt. Bei netzgekoppelten Systemen steuert die MPC die Leistung der Anlage am Netzanschlusspunkt so, dass sie einer Referenztrajektorie folgt und dem System virtuelle Trägheit und eine schnelle Frequenzantwort verleiht. Im Inselbetrieb fungiert die MPC als schneller Sekundärregler, der das System stabilisiert und Störungen kompensiert. Die Regelungsstrategien sind für GFM- und GFL-Umrichter-basierte RES mit unterschiedlichen dynamischen Betriebseigenschaften ausgelegt, darunter Photovoltaik-Anlagen, Batteriespeichersysteme und Wasserstoffelektrolyseure.

Drittens wird die Leistungsfähigkeit der entwickelten MPC-Strategien in Simulationen und Hardware-in-the-Loop-Experimenten (HiL) validiert und anhand klassischer Regelungsstrategien bewertet. Die erhöhte Robustheit der MPC unter Verwendung des vorgestellten Prädiktionsmodells gegenüber dem etablierten Modell wird gezeigt. Eine globale Sensitivitätsanalyse (Global sensitivity analysis - GSA) identifiziert die wichtigsten Systemparameter, die die Robustheit beeinflussen, und quantifiziert deren Auswirkungen. Die GSA zeigt außerdem die unterschiedlichen Auswirkungen struktureller Unsicherheiten aus HiL-Experimenten auf die Regelung von netzgekoppelten Umrichtersystemen im Vergleich zu inselbetriebenen, vollständig durch Umrichter gesteuerten Netzen.

Viertens führt die Anwendung der Frequenzteilerformel im vorgestellten Prädiktionsmodell zu einer globalen Kopplung der Dynamik einzelner Umrichter. Es werden zwei Strategien entwickelt, um die dynamische Kopplung zu reduzieren und partitionierte Teilmodelle des globalen Prädiktionsmodells abzuleiten. Auf der Grundlage dieser beiden Strategien werden verteilte modellprädiktive Regler entwickelt und mit der zentralisierten Implementierung verglichen.

Fünftens werden Strategien entwickelt, um Kommunikationsverzögerungen und Signalverluste in der MPC zu berücksichtigen. Die Strategien werden durch Co-Simulation von inselbetriebenen Netzen und verschiedenen Kommunikationssystemen, einschließlich drahtgebundener und drahtloser Kommunikation, getestet. Die Überlegenheit der MPC bei schneller Frequenzregelung im Vergleich zu einem Smith-Predictor-basierten PI-Regler unter variierenden Verzögerungen aufgrund von Datenverkehr und Signalverlusten wird nachgewiesen.

Abstract

Motivation, Goal and Task of the Dissertation

The global shift from fossil-fuel-based power plants to Renewable Energy Sources (RES), enabled by power electronic converters, significantly reduces system inertia, thereby leaving less time for automated responses to sudden power imbalances and ultimately threatening the frequency stability of the power system. The lack of inherent energy storage in converters requires fast control actions to satisfy the operational constraints of the converter and the underlying RES, limiting their potential to provide frequency support. Furthermore, converters can be classified into Grid-Forming (GFM) and Grid-Following (GFL) types, which introduce distinctly different dynamic characteristics. Through coordinated control, the individual limitations of single RES types can be overcome, and their different operational constraints and dynamic characteristics can be leveraged to achieve effective frequency control. The ability of classical control strategies to handle constraints is severely limited. In addition, with these strategies, the coordination of multiple heterogeneous RES can be achieved only through time-scale separation and sophisticated parameter tuning. In this context, Model Predictive Control (MPC) emerges as an advanced control algorithm that can provide optimal control actions under constraints and in the presence of fast dynamics. The strong coupling between the power and frequency dynamics of individual converters and the rest of the power system, combined with limited available measurements on the time scale of closed-loop converter control, makes the application of MPC for fast frequency control with converter-interfaced RES challenging. Furthermore, communication systems impact control performance through delays and losses in measurement and control signals. To this end, distributed control algorithms have been proven to provide a more resilient control implementation. This dissertation aims to develop and demonstrate MPC strategies for frequency and power control of multiple RES to enhance the frequency stability of power systems dominated by converter-interfaced resources.

Major Scientific Contributions

The dissertation contributes to predictive frequency control in the areas of modelling frequency and power dynamics, the design of centralized and distributed MPC systems for converter-based RES, and the integration of communication systems into the control system.

First, a new control-oriented model for predicting frequency and power is derived using the Frequency Divider concept. The model formulates disturbances of the power system load as process noise, thereby avoiding the need to estimate the magnitude of the disturbances. Compared to established models based on Tie line power exchange, the proposed prediction model does not require additional disturbance states for closed-loop predictive control and is fully observable for any system topology.

Second, MPC strategies are designed for grid-connected converter systems operating as hybrid renewable power plants and for islanded fully converter-driven power systems, often called microgrids. For grid-connected systems, the MPC controls the plant power output at the grid connection point to follow a reference trajectory and provide virtual inertia and fast frequency response to the system. In islanded operation, the MPC acts as a fast secondary controller that stabilizes the system and rejects disturbances. The control strategies accommodate GFM and GFL converter-based resources with different dynamic operating characteristics, including Photovoltaic Generation, Battery Energy Storage Systems, and Hydrogen Electrolyzers.

Third, the performance of the developed MPC strategies is validated and evaluated against classical control strategies in simulation and Hardware-in-the-Loop (HiL) experiments. The increased robustness of MPC using the proposed prediction model versus the established model is demonstrated. Global sensitivity analysis (GSA) identifies the most important system parameters affecting the robustness and quantifies their impact. The GSA further reveals the different impact of structural uncertainty from HiL experiments on the control of grid-connected converter systems versus islanded fully converter-driven power systems.

Fourth, the application of the Frequency Divider formula in the proposed prediction model introduces global coupling of the dynamics of individual converters. Two strategies to reduce dynamic coupling and derive partitioned submodels of the global prediction model are developed. Distributed Model Predictive Controllers based on the two strategies are developed and compared with the centralized implementation.

Fifth, strategies to make MPC aware of communication delays and signal losses are developed and tested through co-simulation of islanded converter-driven power systems and different communication systems, including wired and wireless communication. The superior performance of MPC in fast frequency control compared to a Smith Predictor-based PI controller under varying delay from communication traffic and signal losses is demonstrated.

Table of Contents

1 Introduction **1**

1.1 Motivation 1
1.2 Contributions and Outline 3
1.3 Publications 5

2 Fundamentals **7**

2.1 Model Predictive Control 7
2.1.1 State Estimation, Disturbances and Offset-Free Tracking 11
2.1.2 Feasibility and Stability Considerations 12
2.1.3 Performance, Robustness and Sensitivity 13
2.2 Frequency Stability in Converter-driven Power Systems 17
2.2.1 Modeling of Power Converters 22
2.2.2 Grid-Following Control 24
2.2.3 Grid-Forming Control 27
2.3 Model Predictive Control for Power System Frequency Control 30
2.3.1 Hierarchical Control Framework 30
2.3.2 Review of Predictive Frequency Control Strategies and Research Questions 31

3 Control-Oriented Modelling **39**

3.1 Requirements for Prediction Models 39
3.2 Representation of Voltage Sources and Grid Dynamics 40
3.2.1 Tie line Model 42
3.2.2 Frequency Divider Model 44
3.2.3 Comparison of Modelling Approaches 48
3.3 Component Models 49
3.3.1 Grid-Forming Converter 49
3.3.2 Grid-Following Converter 51
3.3.3 Synchronous Generator and Turbine-Governor 53
3.4 Model Validation 54

4 Model Predictive Control Design **61**

4.1 Grid-connected Converter Systems 61
4.1.1 Scenario Description 61
4.1.2 Control System Design 63
4.1.3 Reference Trajectory Algorithm 67

4.1.4 Nominal Stability ... 69
4.2 Islanded Converter-driven Power Systems ... 70
4.2.1 Scenario Description ... 70
4.2.2 Control System Design ... 71
4.2.3 Nominal Stability ... 74
4.3 Communication Delay and Loss ... 74
4.3.1 Measurement delay and signal loss ... 75
4.3.2 Actuator delay and signal loss ... 77
4.3.3 Overview of the networked control system ... 78

5 Evaluation **81**

5.1 Grid-connected Converter Systems ... 81
5.1.1 Controller Benchmark and Performance Indices ... 81
5.1.2 Simulation of the Model Predictive Control under Nominal Conditions ... 83
5.1.3 Hardware-in-the-Loop Validation ... 89
5.1.4 Robustness and Sensitivity Analysis ... 92
5.2 Islanded Converter-driven Power Systems ... 97
5.2.1 Controller Benchmark and Performance Indices ... 97
5.2.2 Simulation of the Model Predictive Control under Nominal Conditions ... 99
5.2.3 Hardware-in-the-Loop Validation ... 104
5.2.4 Robustness and Sensitivity Analysis ... 107
5.3 Impact of Communication Systems ... 112
5.3.1 Scenario Description and System Models ... 112
5.3.2 Numerical studies of delay- and loss-aware model predictive control ... 115

6 Approaches for Distributed Predictive Frequency Control **121**

6.1 Modifications of the prediction model ... 121
6.1.1 Distributed Frequency Divider ... 122
6.1.2 Frequency Divider Trimming ... 124
6.2 Design of the Distributed Model Predictive Control ... 131
6.2.1 Distributed control based on Distributed Frequency Divider ... 131
6.2.2 Distributed control based on Frequency Divider Trimming ... 135
6.3 Simulations Results and Discussion ... 139
6.3.1 System description ... 139
6.3.2 Numerical studies of the Distributed Model Predictive Control Strategies ... 142
6.3.3 Summary and Discussion ... 149

7 Conclusion **151**

7.1 Conclusion ... 151

7.2 Outlook 153

A Additional Results of the Grid-connected Converter System **155**

B Additional Results of the Islanded Converter-driven Power System **163**

C Additional Results of the Co-simulation with Communication Systems **171**

Publications **175**

Curriculum Vitae **177**

Glossary **179**

List of Figures **181**

List of Tables **191**

Bibliography **193**

1 Introduction

1.1 Motivation

Power systems globally are shifting from fossil-fuel-based power plants to Renewable Energy Sources (RES) in the effort to decarbonise the energy sector. This trend reduces the kinetic energy storage provided by the synchronously rotating masses of Synchronous Generators (SGs) to the power system. This energy storage instantaneously responds to power imbalances through the electromechanical coupling of the SGs, delaying changes in power system frequency, and is hence called inertia. The decrease of system inertia reduces the time for automatic responses to sudden power imbalances, threatening the frequency stability of the power system.

The increasing penetration of RES, including generation, such as Wind and Solar Photovoltaic (PV), storage, such as battery systems, and flexible loads, like Hydrogen Electrolyzers (ELs), requires their participation in power system frequency control. RES are interfaced to the power system via power electronic converters, which are fast-acting and fully controllable devices. In the literature, different approaches for providing frequency control with converters have been developed [1], [2]. However, converters have no inherent energy storage. Hence, the converter's power response must conform to the operational limitations imposed by the connected RES.

Frequency control in the literature is based on classical linear control approaches, which cannot directly address operational limitations, such as minimum and maximum power or ramping constraints. These types of limitations, however, are widely present in the control of RES. For example, wind and PV generation are commonly operated at their maximum power points; Battery Energy Storage Systems (BESSs) have, besides their rated power restriction, limited available energy; and ELs must limit their power ramp for downstream chemical processes. In classical control, operational limitations are satisfied through the use of saturation and anti-windup schemes, which are unknown to the controller itself. These schemes further require sophisticated parameter tuning to achieve good control performance under constraints.

Frequency control of power systems is, in general, hierarchically organised. The primary control layer is implemented on a unit or plant level and supports the power system in a decentralized manner. The primary level does not explicitly control the overall power system. Instead, a specific power response to grid frequency deviations is provided. The secondary layer focuses on system-level

control. Its task is to coordinate the decentralized plants and recover the power system to a new steady-state after a disturbance. Participation in primary and secondary frequency control requires operating reserve during normal operation and compliance with specified control responses during disturbance incidents. It is therefore procured as a system or ancillary service, and the plant owner is paid for this service by the system operator. The different characteristics of RES, as briefly discussed above, prevent them from reliably providing frequency control without restrictions. Furthermore, the converters can be classified into Grid-Forming (GFM) and Grid-Following (GFL) types, introducing distinctly different dynamic characteristics. However, combining the heterogeneous RES and leveraging their complementary characteristics enables overcoming these limitations, such as limited availability and constrained dynamic response [3]. That said, coordinated control is required to facilitate the joint system response.

Model Predictive Control (MPC) is an advanced control algorithm based on online optimisation, allowing the controller to satisfy constraints on system inputs and outputs and to determine optimal actuation while accounting for fast dynamics. The explicit use of models enables intuitive parameterisation and the ability to capture the impact of unknown disturbances. MPC inherently supports Multiple-Input Multiple-Output (MIMO) control, allowing the coordination of independent units while capturing their interactions [4]. Exploring these advantages of MPC and making them suitable for frequency control with converter-based RES are the key focus of the thesis.

Converter-based RES are connected to bulk power systems (i.e., the grid) but are also a key enabling resource for smaller independent power systems operated as islands. In this thesis, MPC is applied to islanded converter-driven power systems, supervising the system behaviour as a secondary controller, and to grid-connected converter systems operated as hybrid renewable power plant, delivering a primary control response. While the control of a single renewable resource focuses on optimising the operation of an individual component, this thesis addresses the integration of multiple components into a plant or system. The objective is to harmonise their dynamic frequency control responses in order to achieve optimal overall system performance.

In this context, the number of RES can become very large, making centralized control of all resources computationally challenging, while introducing security risks and a single point of failure. To this end, distributed control algorithms have been proven to provide a more resilient control implementation. The implementation of Distributed Model Predictive Control (DMPC) introduces significant complexity and new communication requirements. In this regard, the formulation of the control problem and the choice of the algorithm dictate different requirements on the control and communication architecture, as well as on the necessary measurements from the system [5]. In addition, communication systems introduce delay and loss of control and measurement signals, which can critically affect

closed-loop control performance. The model-based approach of MPC incorporates the effects of communication systems into the prediction model and considers them during optimisation.

In real-world applications, the impact of model-plant mismatch between the internal prediction model used by the MPC and the real plant dynamics is critical to assess. Therefore, the robustness of MPC in a real-time Hardware-in-the-Loop (HiL) experimental setup is systematically investigated and compared with nominal simulations of the prediction model.

1.2 Contributions and Outline

The work presented in this thesis contributes to predictive frequency control in the areas of modelling frequency and power dynamics, the design of centralized and distributed MPC systems for converter-based RES, and the integration of communication systems into the control system:

1. A new control-oriented model for the prediction of frequency and power is derived, using the Frequency Divider concept. The model formulates disturbances of the power system load as process noise, thereby avoiding the need to estimate the magnitude of the disturbances. Compared to established models based on Tie line power exchange, the proposed prediction model does not require additional disturbance states for closed-loop predictive control and is fully observable for any system topology.
2. MPC strategies are designed for grid-connected converter systems operating as hybrid renewable power plants and for islanded fully converter-driven power systems, often called microgrids. For grid-connected systems, the MPC controls the plant power output at the grid connection point to follow a reference trajectory and provide virtual inertia and Fast Frequency Response (FFR) to the system. In islanded operation, the MPC acts as a fast secondary controller that stabilises the system and rejects disturbances. The control strategies accommodate GFM and GFL converter-based resources with different dynamic operating characteristics, including PV, BESS and ELs.
3. The performance of the developed MPC strategies is validated and evaluated against classical control strategies in simulation and HiL experiments. The increased robustness of MPC with the proposed prediction model compared to the established model is demonstrated. Global Sensitivity Analysis (GSA) identifies the most important system parameters affecting the robustness and quantifies their impact. The GSA further reveals the different impact of structural uncertainty from HiL experiments on the control of grid-connected converter systems versus islanded fully converter-driven power systems.
4. The application of the Frequency Divider formula in the proposed prediction model introduces global coupling of the dynamics of individual converters. Two strategies to reduce dynamic coupling and derive partitioned submodels of the

global prediction model are developed. DMPCs based on the two strategies are developed and compared with the centralized implementation.
5. Strategies to make MPC aware of communication delays and signal losses are developed and tested through co-simulation of islanded converter-driven power systems and different communication systems, including wired and wireless communication. The superior performance of MPC in fast frequency control compared to a Smith Predictor-based PI controller under varying delay from communication traffic and signal losses is demonstrated.

The thesis is structured in seven chapters.

Chapter 1: The main problem of the thesis, coordinated frequency control with converter-based RES, is introduced and motivated. The contributions and structure of the thesis are briefly presented.

Chapter 2: The chapter first introduces the mathematical foundations of MPC, the methodology for performance and robustness analysis, and GSA. Then, the challenges of frequency control in converter-driven power systems and the opportunities for MPC are discussed. To this end, the literature on the state of the art in grid-connected converter control and the applications of MPC in power system frequency control are reviewed. Finally, the main research objectives of the thesis are discussed and summarised.

Chapter 3: Chapter 3 introduces the prediction models for frequency control. A control-oriented model based on the Frequency Divider concept is derived. This model reformulates the states in terms of output power rather than the internal voltage angle to achieve full observability. It develops component models that capture the frequency and power dynamics of various resource types. The prediction models are validated in detailed simulations for different scenarios.

Chapter 4: In this chapter, the MPCs for grid-connected converter systems and for islanded converter-driven power systems are designed. The control system architecture is introduced, and the optimal control problems are formulated. The chapter discusses state estimation and presents a reference trajectory algorithm for the grid-connected application. Strategies for compensation of communication delay and signal loss are described.

Chapter 5: The developed MPCs are evaluated in Chapter 5. The performance for different scenarios and under various contingencies is validated in nominal simulations and HiL experiments. Model-plant mismatch is introduced through parametric uncertainty and as structural uncertainty in HiL experiments. The performance and robustness under uncertainty are systematically assessed and

compared against conventional control strategies. The chapter further determines the sensitivities, revealing the most influential system parameters and quantifying their impact on controller performance. The ability to compensate various communication system effects is demonstrated in a study cosimulating power systems, control and communication systems.

Chapter 6: Approaches for distributed predictive frequency control are presented in Chapter 6. Two strategies for modifying the prediction model and deriving partitioned submodels are developed and introduced. Based on these partitioned submodels, a control zone-based DMPC is first developed using the distributed Frequency Divider concept. The second approach leverages a trimming procedure of the Frequency Divider matrix and implements a fully distributed MPC architecture. The developed DMPCs are evaluated and compared with the centralized MPC implementation.

Chapter 7: The thesis concludes in Chapter 7 with a summary of the main results and directions for future research.

1.3 Publications

This thesis is based on content of the following peer-reviewed articles:

[J1] T. Heins, M. Josevski, S. K. Gurumurthy, and A. Monti, "Centralized Model Predictive Control for Transient Frequency Control in Islanded Inverter-Based Microgrids," *IEEE Transactions on Power Systems*, vol. 38, pp. 2641–2652, 2023.

[J2] M. Moritz, T. Heins, S. K. Gurumurthy, M. Josevski, I. Jahn, and A. Monti, "Distributed Model Predictive Frequency Control of Inverter-Based Power Systems," *IEEE Access*, vol. 12, pp. 53250–53265, 2024.

[J3] T. Heins, M. Ginocchi, and A. Monti, "Model Predictive Control for Fast Frequency Control in Hybrid Renewable Plants: Increasing Robustness through Enhanced Model Observability," *IEEE Open Journal of Industry Applications*, vol. 7, pp. 674-691, 2026.

[C1] T. Heins *et al.*, "Delay-aware Model Predictive Control for Fast Frequency Control," *2023 IEEE International Conference on Communications, Control, and Computing Technologies for Smart Grids (SmartGridComm)*, 2023.

[C2] T. Heins, P. Chanfreut, S. K. Gurumurthy, P. Srivastava, A. Monti, and A. M. Annaswamy, "Distributed Frequency Divider-based Model Predictive Control for Frequency Control of Multi-Area Power Systems," *2023 IEEE International Conference on Communications, Control, and Computing Technologies for Smart*

Grids (SmartGridComm), 2023.

[C3] T. Heins, T. Heynen, S. Simon, S. K. Gurumurthy, and A. Monti, "Com parison of aggregated and detailed large-scale hydrogen electrolyzer plant models for grid integration studies," *23rd Wind and Solar Integration Workshop*, 2024.

[C4] T. Heynen, T. Heins, M. Kuhn, W. Leterme, and A. Monti, "Systematic review on fast frequency ancillary services provided by large-scale hydrogen electrolyzer plants," *23rd Wind and Solar Integration Workshop*, 2024.

During my doctorate, the following papers and book chapters with my contribution have been published but are not part of this thesis:

[J4] T. Heynen, M. Deitert, T. Heins, M. Kuhn, A. Monti, and W. Leterme, "Design of the Electrical Interface of Hydrogen Electrolyzers Limiting the Power Ramp-Rate While Providing Instantaneous Reserves," *IEEE Transactions on Sustainable Energy*, vol. 17, no. 3, pp. 2487-2500, 2026.

[J5] S. K. Gurumurthy, T. Heins, P. A. Ganeshamurthy, F. Ponci, and A. Monti, "Load Bus Frequency Estimation in Converter-Driven Grids - A Dynamic Phasor Approach," *IEEE Transactions on Power Systems*, vol. 39, pp. 5338–5351, 2024.

[J6] T. Tran *et al.*, "Enhancing Performance of Andronov-Hopf Oscillator Based Grid-Forming Converters in Microgrids With Non-Invasive Online Impedance Estimation," *IEEE Transactions on Smart Grid*, vol. 14, pp. 4479–4493, 2023.

[J7] G. Mehlmann *et al.*, "The Kopernikus ENSURE Co-Demonstration Platform," *IEEE Open Journal of Power Electronics*, vol. 4, pp. 987–1002, 2023.

[J8] I. Sowa, T. Tran, T. Heins, D. Raisz, and A. Monti, "An Average Consensus Algorithm for Seamless Synchronization of Andronov-Hopf Oscillator Based Multi-Bus Microgrids," *IEEE Access*, vol. 9, pp. 90441– 90454, 2021.

[C5] T. Heins, T. Tran, D. Raisz, and A. Monti, "Power Control of Andronov-Hopf Oscillator Based Distributed Generation in Grid-Connected Microgrids," *Advances in Engineering Research and Application: Proceedings of the International Conference on Engineering Research and Applications*, ICERA 2020, 2020.

[B1] S. D'Arco, A. Monti, T. Heins, and J. Suul, "Control of converter interfaced generation," in *Advances in Power System Modelling, Control and Stability Analysis*, pp. 389–416.

2 Fundamentals

The chapter introduces the mathematical basics of MPC. The challenges of frequency control in converter-driven power systems and the opportunities for MPC are discussed, and the main research objectives of the thesis are summarized.

2.1 Model Predictive Control

Model Predictive Control is an advanced control method that has found high acceptance in the industry to, e.g., control and supervise chemical processes or coordinate the different actuators in combined cycle power plants, due to its capability of MIMO control and being easy to understand. The closed-loop control and receding horizon approach allow the controller to react to new information, such as updated measurement data, and perform both corrective and predictive actions. MPC can be highly customized through the choice of different models and the formulation of the optimization problem. It is further fine-tuned by different parameters, like the prediction and control horizon and the relative weights of its optimization objectives, which have a direct and straightforward to understand effect on the overall control behavior. These characteristics make MPC applicable in a wide range scenarios. This section introduces the fundamental principles and mathematical basics of MPC.

The MPC strategy is illustrated in Figure 2.1. Assume a discrete-time setting, where the current time step is denoted as k. The controller calculates an input trajectory $u(\cdot\,|k)$ over the control horizon H_u that optimizes the output $y(\cdot\,|k)$ to track the reference trajectory $r(\cdot\,|k)$ over a prediction horizon H_p. The free response of the system, $y_\mathrm{free}(\cdot\,|k)$, is the output trajectory if the last input $u(k-1)$ is held constant, i.e., if there would be no further control action by the MPC. The notation $(\cdot\,|k)$ refers to the predicted trajectory of a variable based on the knowledge in time step k. The actual value in future time steps will probably be different, e.g., $y(k+1|k+1) \neq y(k+1|k)$. While the variables in Figure 2.1 are displayed as one-dimensional, they are, in general, vectors and all concepts described in this section extend to multivariable settings with vectors of higher dimensions. After solving the optimal control problem, the first input $u(k) = u(k|k)$ is applied to the system. In the next iteration of the controller, the procedure is repeated, and the horizon is shifted one time step forward. Therefore, this is also called a receding horizon strategy. In applications that require high-frequency actuation or where the plant's sampling rate exceeds the controller's update frequency, a multi-rate approach may be adopted. In such

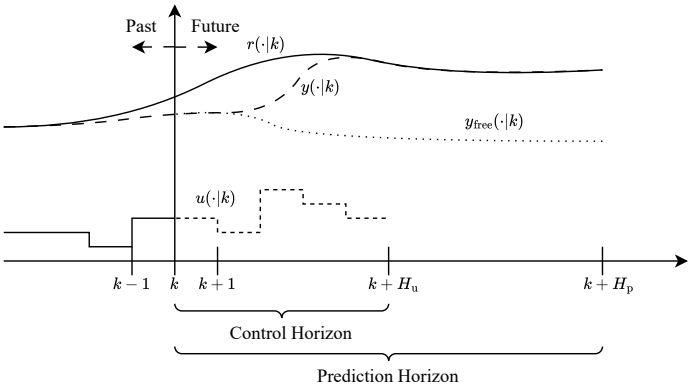

Figure 2.1: Model Predictive Control Strategy.

cases, instead of applying only the initial input, the controller implements the optimized trajectory $u(\cdot\,|k)$ over the entire interval until the next MPC execution.

The predictions are based on a model of the system, of which different formulations are possible. The most notable representations are state-space models, transfer functions or regression models. It has been shown, that step or impulse response models are particular cases of state-space models and that state-space based MPC can treat a wider range of problems than transfer function-based formulations [6]. Therefore, and because state-space is the most convenient representation for multivariable problems, a linear model in discrete state-space form is assumed in this thesis:

$$\begin{aligned} x(k+1) &= A_{\text{k}}x(k) + B_{\text{k}}u(k)\,, \\ y(k) &= C_{\text{k}}x(k)\,. \end{aligned} \tag{2.1}$$

For predictive control, the model does not include a feed-forward path ($D_{\text{k}} = 0$). The process of measurement, optimization and applying $u(k)$ to the actuators introduces some computational delay. Therefore the model must be strictly proper [7]. The model (2.1) can predict the trajectory of the states in matrix-vector form as [7]:

$$\begin{bmatrix} x(k+1|k) \\ \vdots \\ x(k+H_\mathrm{u}|k) \\ x(k+H_\mathrm{u}+1|k) \\ \vdots \\ x\big(k+H_\mathrm{p}|k\big) \end{bmatrix} = \underbrace{\begin{bmatrix} A_\mathrm{k} \\ \vdots \\ A_\mathrm{k}^{H_\mathrm{u}} \\ A_\mathrm{k}^{H_\mathrm{u}+1} \\ \vdots \\ A_\mathrm{k}^{H_\mathrm{p}} \end{bmatrix} x(k) + \begin{bmatrix} B_\mathrm{k} \\ \vdots \\ \sum_{i=0}^{H_\mathrm{u}-1} A_\mathrm{k}^i B_\mathrm{k} \\ \sum_{i=0}^{H_\mathrm{u}} A_\mathrm{k}^i B_\mathrm{k} \\ \vdots \\ \sum_{i=0}^{H_\mathrm{p}-1} A_\mathrm{k}^i B_\mathrm{k} \end{bmatrix} u(k-1) +}_{\text{free response } x_\mathrm{free}(\cdot|k)}$$

$$\underbrace{\underbrace{\begin{bmatrix} B_\mathrm{k} & \cdots & 0 \\ A_\mathrm{k}B_\mathrm{k}+B_\mathrm{k} & \cdots & 0 \\ \vdots & \ddots & \vdots \\ \sum_{i=0}^{H_\mathrm{u}-1} A_\mathrm{k}^i B_\mathrm{k} & \cdots & B_\mathrm{k} \\ \sum_{i=0}^{H_\mathrm{u}} A_\mathrm{k}^i B_\mathrm{k} & \cdots & A_\mathrm{k}B_\mathrm{k}+B_\mathrm{k} \\ \vdots & \vdots & \vdots \\ \sum_{i=0}^{H_\mathrm{p}-1} A_\mathrm{k}^i B_\mathrm{k} & \cdots & \sum_{i=0}^{H_\mathrm{p}-H_\mathrm{u}} A_\mathrm{k}^i B_\mathrm{k} \end{bmatrix}}_{\Omega} \underbrace{\begin{bmatrix} \Delta u(k|k) \\ \vdots \\ \Delta u(k+H_\mathrm{u}-1|k) \end{bmatrix}}_{\Delta u(\cdot|k)}}_{\text{forced reponse } x_\mathrm{force}(\cdot|k)} \tag{2.2}$$

The system output over the prediction horizon is then:

$$\underbrace{\begin{bmatrix} y(k+1|k) \\ \vdots \\ y\big(k+H_\mathrm{p}|k\big) \end{bmatrix}}_{y(\cdot|k)} = \underbrace{\begin{bmatrix} C_\mathrm{k} & 0 & \cdots & 0 \\ 0 & C_\mathrm{k} & \cdots & 0 \\ \vdots & \vdots & \ddots & \vdots \\ 0 & 0 & \cdots & C_\mathrm{k} \end{bmatrix}}_{\boldsymbol{C}} \begin{bmatrix} x(k+1|k) \\ \vdots \\ x\big(k+H_\mathrm{p}|k\big) \end{bmatrix} \tag{2.3}$$

The prediction is formulated to express the control input in terms of the change in each time step, defined as:

$$\Delta u(k|k) = u(k|k) - u(k-1) \tag{2.4}$$

The free response of the output (Figure 2.1) is $y_\mathrm{free}(\cdot\,|k) = \boldsymbol{C} \cdot x_\mathrm{free}(\cdot\,|k)$. Note that in (2.2), A_k^i is computed for possibly large values of i. This has important implications on the choice of the prediction model, as some elements of A_k^i may take on extremely large or extremely small values, possibly compromising numerical accuracy of computers and thereby causing wrong results [7]. To guarantee accurate results and a well-conditioned optimization problem, the model (2.1) is normalized in this thesis using the per-unit system.

Figure 2.2 shows the basic control diagram of a control loop with MPC. Based on the predictions (2.2), (2.3), the open-loop tracking error over the prediction horizon is calculated as:

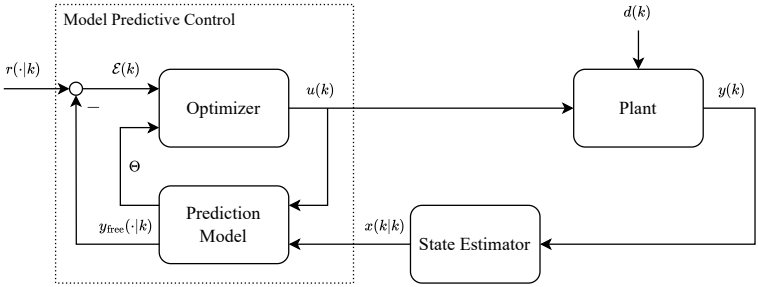

Figure 2.2: Control Loop with Model Predictive Control.

$$\mathcal{E}(k) = r(\cdot\,|k) - y_{\text{free}}(\cdot\,|k) \tag{2.5}$$

The impact of input changes $\Delta u(\cdot\,|k)$ on the output $y(\cdot\,|k)$ are expressed by $\Theta = \boldsymbol{C} \cdot \Omega$. Both $\mathcal{E}(k)$ and Θ are inputs for the optimizer, which must solve the optimal control problem, where the objective function is generally defined as [7]:

$$\min_{\Delta u(\cdot|k)} \sum_{i=1}^{H_\text{p}} \|y(k+i|k) - r(k+i|k)\|_Q^2 + \sum_{i=0}^{H_\text{u}-1} \|\Delta u(k+i|k)\|_R^2 \tag{2.6}$$

The objective function in (2.6) is minimized with respect to the sequence of future control increments $\Delta u(\cdot\,|k)$ over the control horizon H_u. The formulation employs the weighted squared Euclidean norm, defined for a generic vector z and a weighting matrix W as: $\|z\|_W^2 = z^\text{T} W z$. In this context, $Q \in \mathbb{R}^{n_\text{y} \times n_\text{y}}$ and $R \in \mathbb{R}^{n_\text{u} \times n_\text{u}}$ are the weighting matrices for the tracking error and the control effort where n_y and n_u are the number outputs and inputs, respectively. To ensure a well-posed optimization problem, these matrices are chosen to be positive semi-definite ($Q, R \succeq 0$), though R is often chosen to be positive definite ($R \succ 0$) to guarantee a unique solution. The most straight-forward choice of Q and R are diagonal matrices with only positive weights, which is assumed in this thesis. Mathematically, Q penalizes the deviation of the predicted outputs $y(k+i|k)$ from the reference trajectory $r(k+i|k)$ incentivizing aggressive control actions. R penalizes the magnitude of the control moves to provide a damped controller behavior.

To solve the optimization problem, all variables in (2.6) need to be expressed in terms of $\Delta u(\cdot\,|k)$. To this end (2.6) is first rewritten as:

$$\min_{\Delta u(\cdot|k)} \|y(\cdot\,|k) - r(\cdot\,|k)\|_Q^2 + \|\Delta u(\cdot\,|k)\|_R^2 \tag{2.7}$$

The output $y(\cdot\,|k)$ is calculated by combining (2.2) and (2.3) in terms of the free response and the future control input:

$$y(\cdot\,|k) = y_{\text{free}}(\cdot\,|k) + \Theta\Delta u(\cdot\,|k) \tag{2.8}$$

Substituting (2.8) and (2.5) into (2.7) gives [7]:

$$\min_{\Delta u(\cdot|k)} \|\Theta\Delta u(\cdot\,|k) - \mathcal{E}(k)\|_Q^2 + \|\Delta u(\cdot\,|k)\|_R^2 \tag{2.9}$$

Thereby, it becomes obvious how the prediction model enters into the optimization problem.

A main advantage of MPC is that it can include constraints into the optimization and solve them online. These constraints are formulated as linear inequalities and typically limit the absolute value of an input or output variable to a maximum or minimum, or the rate of change of a variable. Like the objective function, the constraints must be expressed in terms of $\Delta u(\cdot\,|k)$, which is achieved by virtue of (2.8) for output variables. Details about the formulation of constraints can be found in [7] and [8].

The resulting optimization problem is a standard Quadratic Programming (QP) problem, which has the convexity property. Convex problems have unique global minima and are guaranteed to be solved, therefore they are extremely desirable for online algorithms [7]. QP solvers are readily available, and the most established approaches are based on active-set or interior-point methods. Both methods have individual advantages and disadvantages in the context of predictive control, for a comparison see, e.g., [9] and [10].

2.1.1 State Estimation, Disturbances and Offset-Free Tracking

In practical applications, direct measurement of the full state vector, used in the prediction in (2.2), is often prohibitively expensive or technically unfeasible. Consequently, a state estimator must be employed to reconstruct the system states from available measurements, as illustrated in Figure 2.2. A formal distinction is typically drawn between an observer and an estimator. The former generally refers to deterministic state reconstruction (e.g., the Luenberger observer), whereas the latter is designed for stochastic systems. This work utilizes a Kalman filter (KF) to account for the stochastic nature of plant noise and measurement errors. The terminology additionally varies by field. In power systems, state estimation conventionally refers to a static scheme, often utilizing redundant measurements and Weighted Least Squares to estimate the current operating point [11]. In contrast, when a KF is applied to capture the time-varying trajectory of the system, it is categorized as dynamic state estimation [12]. While various observer and filtering techniques are compatible with MPC, the term ‘state estimator’ will be used throughout the remainder of this thesis to refer to the implemented KF-based dynamic estimation.

The state estimator can quantify the impact of disturbances. Assuming a constant disturbance, the state vector is augmented with $d(k+1) = d(k)$. This formulation is sufficient to ensure offset-free tracking in the presence of step-wise disturbances and model-plant mismatch [8], which are the main disturbances in power system frequency control.

$$\begin{aligned} \begin{bmatrix} x(k+1) \\ d(k+1) \end{bmatrix} &= \begin{bmatrix} A_\mathrm{k} & B_\mathrm{d,k} \\ 0 & I \end{bmatrix} \begin{bmatrix} x(k) \\ d(k) \end{bmatrix} + \begin{bmatrix} B_\mathrm{k} \\ 0 \end{bmatrix} u(k) \\ y(k) &= \begin{bmatrix} C_\mathrm{k} & C_\mathrm{d,k} \end{bmatrix} \begin{bmatrix} x(k) \\ d(k) \end{bmatrix} \end{aligned} \tag{2.10}$$

The choice of $B_\mathrm{d,k}$ and $C_\mathrm{d,k}$ models the disturbances $d(k)$ as either input or output disturbances. Input disturbances are measured or unmeasured, uncontrolled inputs that have a known (modelled) impact on the system dynamics. In the output variables on the other hand, unmodelled disturbances and model-plant mismatch can be captured. If the static gain matrix of the plant (calculated as $G(1) = C_\mathrm{k}(I - A_\mathrm{k})^{-1}B_\mathrm{k}$ for $x(k+1) = x(k)$) is not known exactly, the output of the plant differs from the prediction, thereby causing a steady-state offset in the controlled outputs [8]. It was shown in [13] that a number of integrated disturbances equal to the number of measurements is sufficient to guarantee offset-free performance. The integrated disturbances can be added to different combinations of variables while still being effective. However, the choice of the variables affected by the disturbances can result in strong variations of the transient [13]. More elaborate disturbance models can be used if the dynamics of the disturbance are identified. In any case, detectability of the augmented system model (2.10) must be ensured and the resulting unconstrained controller must be nominally stable [13].

2.1.2 Feasibility and Stability Considerations

The constrained optimal control problem can become infeasible if the constraints can not be satisfied, e.g., due to large disturbances or model-plant mismatch. In this case, QP solvers produce no output, which is unacceptable for a controller. Fallback strategies have to be implemented to either apply the last valid output, e.g., $u(k-1)$, or the next entry of the last feasible output trajectory, e.g., $u(k|k-1)$ [7]. It is important to avoid infeasible problems. This is generally achieved by softening constraints through slack variables. Slack variables allow violation of constraints, but are heavily penalized in the cost function to incentivize small to no violation. They are typically used on output constraints, as these are causing the infeasibility problem, e.g., if an output can not be maintained within its limits. Input constraints represent physical limitations of the actuators, which can not be violated by the controller. They do not cause

infeasibility of the control problem and are typically hard constraints. Other strategies than soft constraints exist to ensure feasibility, such as the relaxation of constraints following a priority list until feasibility is recovered. In this thesis, output constraints are generally softened through slack variables to ensure feasibility.

If no constraint is active, (2.6) can be solved explicitly and a linear control law is obtained:

$$\Delta u(\cdot\,|k) = K_{\mathrm{MPC}}\mathcal{E}(k) \tag{2.11}$$

Thus the closed-loop system is linear for the unconstrained case and nominal stability can be verified if the eigenvalues of the closed-loop matrix $A_{\mathrm{cl}} = (A_{\mathrm{k}} - B_{\mathrm{k}}K_{\mathrm{MPC}})$ lie within the unit circle.

While nominal stability is easily ensured, MPC becomes nonlinear if constraints are included in the optimal control problem, and alternative stability criteria must be considered. It has been theoretically proven that MPC is stable for infinite horizons in this case [8]. Obviously, MPC with an infinite horizon can not be implemented in a real system. For a finite horizon MPC, stability is typically established using Lyapunov stability theory. This is often achieved by introducing a terminal cost P and a terminal constraint set $\mathbb{X}_f$, which together ensure that the cost function acts as a valid Lyapunov function that decreases at every time step.

A problem arising with stability guarantees of MPC is that they require strong assumptions. Stability under constraints assumes that the prediction model is exact, i.e., that there is perfect knowledge of the plant, and there are no disturbances. It also assumes that the optimization problem has a solution and the global optimum is found in every time step. However, perfect plant knowledge is impossible in practice. Moreover, frequency control events are naturally caused by disturbances. Instead of theoretical stability guarantees, robustness to model-plant mismatch in the form of uncertainty and the performance in rejecting disturbances are more relevant in the practical development of MPC for frequency control applications and therefore investigated in this thesis.

2.1.3 Performance, Robustness and Sensitivity

To quantify the performance of a controller, performance indices must be chosen that represents the desired behavior of the closed-loop control system. The following performance indices are commonly used in control systems:

$$\begin{aligned}
&\text{Integral Absolute Error:} && IAE = \int_0^T |e(t)|\ dt \\
&\text{Integral Squared Error:} && ISE = \int_0^T e^2(t)dt \\
&\text{Integral Time Absolute Error:} && ITAE = \int_0^T t|e(t)|\ dt \\
&\text{Integral Time Squared Error:} && ITSE = \int_0^T te^2(t)dt
\end{aligned} \tag{2.12}$$

The error $e(t)$ is the difference between an output variable and its, possibly time-varying, reference. The Integral Absolute Error (IAE) quantifies the time-domain error by the integral of the error's absolute value. The Integral Squared Error (ISE) additionally squares the error to penalize larger errors more than small deviations. Many control applications focus on the settling time and steady-state error as performance criteria. To this end, the Integral Time Absolute Error (ITAE) and Integral Time Squared Error (ITSE) introduce a time variable, which penalizes later error values more strongly, and early errors, which normally occur for step responses, have a lesser weight in the overall index value.

In frequency control of power systems, the Rate of Change of Frequency (RoCoF) and maximum frequency deviation (nadir or zenith) are typically used to compare different scenarios. To determine the RoCoF a measurement interval has to be determined, e.g., the RoCoF over the first 250 ms after an event. In purely converter-driven systems, fast frequency control actions can however influence the frequency trajectory already in the initial measurement window. Additionally, to evaluate the MPC performance, tracking of power outputs is also of interest. As a unified and variable independent (frequency or power) index, the ISE is therefore chosen as the primary performance index in this thesis. In low-inertia systems, the initial seconds following a disturbance are critical. Control actions must occur fast to contain frequency events and stabilize the system until slower balancing reserves are dispatched. The ISE therefore represents the desired controller behavior, i.e., it penalizes large deviations and the early transient performance stronger than the other indices in (2.12).

The performance index is further used to evaluate the robustness of the developed controllers. In a robustness analysis, the performance of a controller that is designed for a nominal model without uncertainty is assessed when subjected to different forms of uncertainty [14]. Model uncertainty can be categorized into parametric and structural uncertainty [14], [15], [16]. Parametric uncertainty is present in a system, where the dynamics are known and modelled, however the parameters can not be determined exactly, e.g., due to insufficient information or measurements, aging of components or a variability in response behavior.

Structural uncertainty arises from dynamics that are not part of the model, because they are expected to have a minor impact and are neglected, or that are not modelled because they are unknown, e.g., the dynamic of a disturbance. The steady-state effect of model uncertainty can be compensated in MPC by disturbance models on the tracked outputs [7], [13], however the transient performance is still affected. The objective of the controller is to preserve stability and performance in spite of model uncertainty.

If the impact and uncertainty range of the model inaccuracy is known, robust MPC methods can be designed to guarantee the satisfaction of system constraint and performance metrics [8]. While robust MPC frameworks can theoretically guarantee constraint satisfaction under uncertainty, their efficacy depends on the availability of precisely defined and bounded uncertainty sets. In frequency control, characterizing these sets is particularly challenging, as parametric uncertainty ranges vary depending on system conditions, changes of the grid topology and connected components. Furthermore, robust MPC formulations often introduce significant computational overhead and lead to overly conservative control actions, which may be counterproductive in fast-acting frequency control applications. Given that nominal MPC is known to possess a degree of inherent robustness to model-plant mismatch, this thesis investigates the limits of this natural resilience. Rather than implementing a formal robust MPC law, the research focuses on a comprehensive robustness evaluation of nominal MPC algorithms when subjected to realistic parametric and structural uncertainties.

The individual impact of different sources of uncertainty on the controller performance can be identified through sensitivity analysis. Quantifying the relative importance of different uncertainty sources by their sensitivity is important to understand the weaknesses of a control strategy, and prioritize development and testing for relevant scenarios. To this end, a suitable sensitivity analysis method must be employed.

Method for Sensitivity Analysis

In literature, sensitivity analysis of MPC is most commonly carried out using local sensitivity analysis methods. Local approaches, such as sweeping one parameter at a time or computing sensitivity measures via partial derivatives, are only valid for small perturbations around nominal conditions. As a result, they provide only a partial, and sometimes even misleading, assessment of control performance under uncertainty. Furthermore, local sensitivity analysis is valid only under the assumption of system linearity, whereas constrained MPC is nonlinear. In addition, the effects of structural uncertainty cannot be captured with a local sensitivity analysis. Therefore, Global Sensitivity Analysis is conducted in this thesis. It has a broader range of applicability and enables a full accounting of

all uncertain inputs, allowing the overall MPC sensitivity pattern to be captured more accurately. By varying all inputs simultaneously, GSA is also less prone to bias than local sensitivity analysis methods.

Different GSA methods are available in literature, including the Morris method, correlation, and regression analysis [17]. In this thesis, variance-based sensitivity analysis is employed. Variance-based GSA has a high generality, and its results are valid over the entire input space. It is capable of identifying interaction effects between different inputs, including discrete inputs (e.g., from a discrete set of scenarios or models), and is therefore the primary method used in this work. The mathematical basics of variance-based GSA are introduced in the remainder of this section.

Consider the closed-loop control system in the form of a generic model $y = \mathrm{f}(\mathbf{u})$, where y is the performance indicator (e.g., the ISE) and $\mathbf{u}$ is the vector of the d uncertain factors $\{u_i\}_{i\in\{1,\dots,d\}}$, such as an uncertain parameter or the choice of a model. Variance-based GSA apportions the variability of the performance indicator to the selected uncertain factors. The decomposition of the variance $\mathrm{Var}(y)$ is based on the normalized equation of the performance indicator y [17]:

$$1 = \sum_i S_i + \sum_i \sum_{i<j} S_{ij} + \dots + S_{1\dots d}, \tag{2.13}$$

where S_i is the first order Sobol' Sensitivity Index (SI), quantifying the individual effect of the factor u_i on $\mathrm{Var}(y)$. The second order Sobol' SI S_{ij} quantifies the interaction effect of the factors u_i and u_j on $\mathrm{Var}(y)$, and so on, up to the d-th order Sobol' index $S_{1\dots d}$. The first order Sobol' SI is defined as:

$$S_i = \frac{\mathrm{Var}_{u_i}\left(\mathbb{E}_{\mathbf{u}_{\sim i}}[y|u_i]\right)}{\mathrm{Var}(y)}, \tag{2.14}$$

and the second order Sobol' SI as:

$$S_{ij} = \frac{\mathrm{Var}_{u_i,u_j}\left(\mathbb{E}_{\mathbf{u}_{\sim ij}}\left[y|u_i,u_j\right]\right)}{\mathrm{Var}(y)} - S_i - S_j. \tag{2.15}$$

Here, $\mathbb{E}$ indicates the expected value, and the subscripts of $\mathbb{E}$ and Var define the inputs over which the operators are taken. $\mathbf{u}_{\sim i}$ and $\mathbf{u}_{\sim ij}$ indicate the removal of the factor u_i and the factors pair $\left\{u_i, u_j\right\}$ from $\mathbf{u}$, respectively. Similar definitions hold for higher-order Sobol' SIs [17].

In addition to the Sobol' SIs, the total effect SI of the factor u_i is defined as:

$$T_i = S_i + \sum_{j=1,j\neq i}^{d} S_{ij} + \dots + S_{1\dots d} = \frac{\mathbb{E}_{\mathbf{u}_{\sim i}}\left(\mathrm{Var}_{u_i}(y|\mathbf{u}_{\sim i})\right)}{\mathrm{Var}(y)} \tag{2.16}$$

which quantifies the amount of $\mathrm{Var}(y)$ due to all contributions of u_i, including its interactive effects with other factors of $\mathbf{u}_{\sim i}$. For example, if $d = 3$,

$T_2 = S_2 + S_{12} + S_{23} + S_{123}$. For evaluation of the MPCs developed in this thesis, both the direct effect of uncertain inputs on the control performance, quantified by the Sobol SIs, and the total effect SIs will be assessed.

2.2 Frequency Stability in Converter-driven Power Systems

The integration of renewable energies into the power system influences frequency dynamics on a fundamental level. The frequency dynamics of AC power systems have historically been dominated by Synchronous Generators. SGs rotate synchronously with the power system frequency, introducing an electromechanical coupling between a mechanical input power and the electrical output power. The rotating mass of the generator (and turbine) serves as a kinetic energy storage, allowing a temporary imbalance between input and output power, and is commonly referred to as inertia. A power imbalance, which is caused by a change in load or generation in the power system, slows or accelerates the rotating speed of the SGs and thereby the power system frequency.

Renewable Energy Sources commonly do not operate with mechanical power. Instead they produce or consume DC power, like PVs, BESSs and ELs, or, in the case of Wind energy, use an intermediate DC circuit to decouple mechanical from power system dynamics for an optimized operation. They use an AC/DC power converter to connect to the AC power system. These converters are power electronic switching devices that have no physical energy storage. The interaction of the power system on the AC side, and a RES on the DC side, is therefore fully depending on the algorithms applied to control the converter.

The power balance in an AC power system can be expressed as [18]:

$$M_{\text{sys}}\dot{\omega}(t) = P_{\text{mech}}(t) + P_{\text{con}}(t) - P_{\text{load}}(t) - P_{\text{loss}}(t), \tag{2.17}$$

where M_{sys} is the total system inertia, P_{mech} and P_{con} are the mechanical input power of SGs and the power supply of converter-based generation, and P_{load} and P_{loss} are the power consumed by loads and transmission losses, respectively. The equation in (2.17) is commonly referred to as the system swing equation. It expresses the coupling of change in frequency $\dot{\omega}$ and power imbalances through the system inertia M_{sys}. Larger values of M_{sys} result in slower frequency dynamics, leaving time for control and automation systems to react to the power imbalance and apply countermeasures. The shift from fossil fuels to renewable energy results in a shift from SG-based generation to converter-based generation in power systems. Therefore, system inertia is reducing significantly. As $M_{\text{sys}} \searrow 0$, the power balance equation approaches:

$$0 = P_{\text{con}}(t) - P_{\text{load}}(t) - P_{\text{loss}}(t). \tag{2.18}$$

A power system that is fully supplied by converter-based generation therefore has no inherent coupling between frequency and power, and could be operated at an arbitrary frequency. However, power balance must be ensured to avoid

a system collapse. The fundamental frequency propagates throughout an entire synchronous AC system and can be used as a global variable to implement power balancing control systems, avoiding the need for a communication infrastructure to stabilize disturbance events. This unique feature, the fact that there will still always be some synchronous generation in the foreseeable future (e.g., from hydro power), and the lack of viable alternatives in todays power system, are the reasons control of power system frequency remains the primary mechanism to ensure power balance.

Frequency control is divided into a primary and a secondary control layer. The primary control is implemented in a decentralized manner, where participating units measure the local frequency and provide reserve power through a proportional control. The aim of primary control is to stabilize frequency transients and limit the frequency nadir/zenith. The secondary control layer restores the frequency to its nominal operating range, as proportional controllers always have a steady-state offset in the controlled variable. If the primary control can not limit the frequency within a specified band, load shedding relays disconnect load centers to help restore the power balance. Load shedding is a backup system to avoid the collapse of the overall power system, therefore it can only be used during an emergency state. To avoid this loss of service to the customers, limitation of the frequency nadir through control is important. The decline of system inertia reduces the time for primary control to limit frequency deviations. Additionally, load shedding relays have been reported to not operate correctly during high RoCoF events, as the algorithms fail to detect the underfrequency in time. This has led to a black system in South Australia in 2016, where low system inertia caused very high RoCoF values [19].

Figure 2.3 illustrates the primary control in classical SG dominated systems at the example of a power system supplied by three SGs equipped with turbine governors responding to a load disturbance at $t = 3$ seconds. Figure 2.3a shows the frequencies of the generators, which globally synchronize during the transient. The electrical power output $P_i \in \{1, 2, 3\}$ of the generators immediately responds to the load disturbance, whereas the mechanical input power $P_{\text{mech},i}$ from the primary controlled turbines has a delayed response (Figure 2.3b). The power balance of a single SG is described by:

$$P_i = P_{\text{mech},i} + P_{\text{inertia},i}. \tag{2.19}$$

Therefore, the difference between electrical and mechanical powers is supplied by the kinetic energy storage as an inertia response $P_{\text{inertia},i}$, shown in Figure 2.3c. This is example illustrates the role of inertia as an energy buffer between load disturbances and the primary frequency control response.

Power electronic converters do not normally have a significant energy storage.

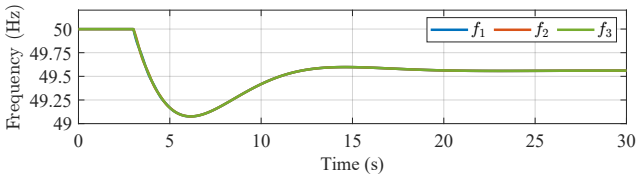

(a) Frequencies.

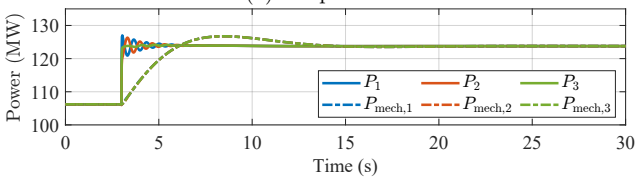

(b) Electrical and mechanical power.

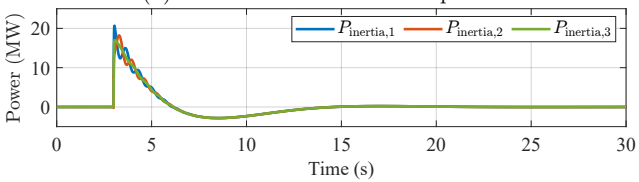

(c) Inertia response.

Figure 2.3: Synchronous generators dynamic response after a load disturbance.

However, their control response is significantly faster, than the turbine governor of SGs. If equipped with a sufficiently large energy storage on the DC side, or connected to a fast responding RES, power converters can replicate the inertial and primary control characteristics of SGs [20] in the Grid-Forming control mode [1].

In Figure 2.4, a system supplied by three GFM converters, implementing a Virtual Synchronous Machine (VSM) strategy, is subject to a load disturbance. The VSMs are tuned to have the same inertia and proportional primary control as the SGs in Figure 2.3. Figure 2.4a shows that an equal initial RoCoF at $t = 3$ seconds and equal steady-state frequency are achieved. Similarly, the electrical power output of the converters in Figure 2.4b is comparable to the electrical power of the SGs. However, a few important differences are pointed out. The absence of a physical inertia and of a slow mechanical control response reduces the frequency transient significantly (Figure 2.4a), as the VSM-controlled converter integrates both inertia and primary control response. For frequency control with

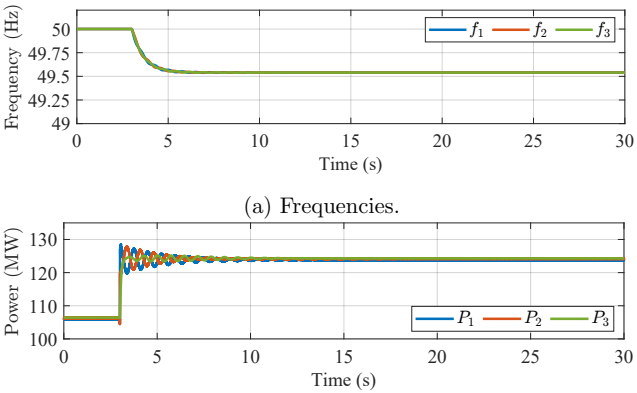

(a) Frequencies.

(b) Electrical power.

Figure 2.4: Grid-forming converters dynamic response after a load disturbance.

SGs, the mechanical power $P_{\text{mech},i}$ is the controlled variable that responds to frequency deviations, while the contribution from inertia ($P_{\text{inertia},i}$) provides a buffer to the electrical output. Here, the physical inertia instantaneously responds to the load disturbance. In contrast, for converters the electrical power P_i, which is supplied by the DC-side RES, is the controlled variable, resulting from the integration of inertia and primary control. Furthermore, the electrical power is subject to dynamic interactions with other generators, which can be seen in the oscillations of P_i in Figure 2.3b and Figure 2.4b, whereas the physical inertia effectively decouples the mechanical power $P_{\text{mech},i}$ from generator interactions. This renders a significant challenge for predictive frequency control with GFM converters, since the electrical power output is controlled and constrained, but its dynamic is coupled with the other components in the system.

In large interconnected power systems, frequency control is an ancillary service that is procured by the system operators and provided by plant owners based on a market mechanism. While markets for primary control on the time-scale of the turbine governor response (Figure 2.3b) are well established, inertial power reserve from kinetic energy storage has not been remunerated. The shift to converter-based RES and the resulting challenges of low-inertia systems have let to the development of new market-based ancillary services to close the gap in frequency control response. They can be fundamentally divided into two categories.

The first category are markets for momentary or instantaneous reserve that provides power as a frequency derivative response. This reserve is mathematically equivalent to an inertia response, which can be provided physically (e.g., from synchronous condensers or flywheels) or virtually emulated by converters, hence it is often called virtual inertia. It is described by:

$$P_{\mathrm{VI},i} = -T_{\mathrm{A},i} \cdot \frac{\mathrm{d}\omega_{\mathrm{grid}}}{\mathrm{d}t}, \tag{2.20}$$

where i denotes a unit (converter or synchronous condenser), $P_{\mathrm{VI},i}$ is the virtual inertia power response, $T_{\mathrm{A},i}$ the inertia constant, and ω_{grid} the grid frequency. This type of market is first established in Germany in 2026 [21] with the aim to increase the effective system inertia M_{sys}.

The second category are Fast Frequency Response services. These services aim to reduce the need for inertia as an energy storage by leveraging the fast controllability of converter-based RES. A fast primary control response allows the power system to operate at a lower system inertia. This type of market has been introduced, e.g., in Australia [22], the United Kingdom [23], or Finland [24]. The FFR has different specifications in each country, including different activation and hold-up times, thresholds for activation and size of the response. One variant implements a fast proportional response, which can be described by:

$$P_{\mathrm{FFR}} = -\frac{1}{R_{\mathrm{p}}} \cdot \Delta\omega_{\mathrm{grid}}, \tag{2.21}$$

where P_{FFR} is the power response, R_{p} the proportional gain and $\Delta\omega_{\mathrm{grid}}$ the deviation from the nominal grid frequency. A different variant is the activation of a fixed power reserve when the grid frequency reaches a certain threshold as a step response. For example, if the frequency drops below 49.5 Hz a plant increases its power output by 100 MW within 0.5 seconds for 30 seconds.

The widespread availability of RES at comparatively small power and voltage levels has given rise to independent power systems that operate as an island. They are often referred to as microgrids, and offer electrification for remote communities, but are also a promising approach for a modular and resilient power system through enhanced energy management. These islanded converter-driven power systems are characterized by a very high share of RES and therefore small to zero inertia. They host only a limited number of participants, which means that an outage of a generator or load constitutes a large share of the total system power. This makes frequency control a major challenge in islanded systems [25]. Ensuring frequency stability under these conditions requires coordination of a small number of resources, including aspects such as active power limitations, power sharing and differing dynamic responses. Instabilities typically occur in the form of large power and frequency swings due to poor control coordination

[25]. Islanded power systems are often operated with a centralized control system that provides secondary control and coordinated energy management. However, the centralized controller poses a single point of failure for the whole system. Therefore, distributed control strategies have been developed that make the islanded system more resilient.

Market based ancillary services and decentralized control are an effective way to coordinate multiple stakeholders in large power systems. In small islanded systems with only a few participants and fast dynamics, the responsibility for system stability and control is typically more centralized, or shared through distributed control schemes. Both types of systems have the same fundamental challenge of frequency control in converter-driven power systems, which are faster frequency dynamics due to low inertia and a shift of the controlled variable from the mechanical power of turbines to the electrical power of converters. Converter-based RES have a a high controllability, but have resource specific dynamic characteristics and are subject to tight operational constraints due to the lack of inherent energy storage. Model Predictive Control can realize their full potential, by leveraging the complementary characteristics of heterogeneous RES through optimal MIMO control including constraints. The development of model-based predictive controllers, however, requires a shift in modeling to capture the impact of load disturbances on the converters power output and their dynamic interactions, e.g., oscillations between units. Modeling approaches for frequency control in literature are reviewed and discussed in Chapter 3. Next, the representation of power converters and the dynamic characteristics of different control strategies are presented.

2.2.1 Modeling of Power Converters

Renewable Energy Sources commonly require an AC/DC power converter to connect to the public AC power system [26]. These converters are power electronic switching devices that must be controlled. Since their interaction with the power system and the RES fully depends on the applied control algorithms, modeling of both the hardware and the software, i.e. the control system, is required to describe their dynamics. Power converter dynamics cover a broad timescale, ranging from microseconds at the switching level to multiple seconds for power control. There are varying levels of detail at which power converters can be modeled, depending on the type of study [27]. Hereby, it is important to distinguish between converters of Grid-Following and Grid-Forming type. The differences and specific modeling of GFL and GFM converters are discussed later in this section.

Recommendations for the required model depth for different grid integration studies are given in [27]. It is suggested that for frequency studies, only a high-level representation is needed and that most of the inner dynamics can be neglected or simplified. The work in [27] is however limited to GFL converters.

GFM converters are specifically studied in [28]. Reduced order models from third order up to a full order model with 13 states are presented and compared. The study concludes that the application boundary of the reduced order models depends on the parametrization of the controller, filter and lines, since higher bandwidth control loops can interact with slow system modes from outer control loops [28]. Model reduction considering interactions of GFL and GFM converters has been further studied in [29]. It is shown that reduced models can give wrong results about stability of slow dynamics, which, in general, have a higher impact and wider propagation in the power system than fast dynamics. The timescale separation in power converters can be insufficient to fully neglect the impact of the fast inner control loops [29]. In [30], in addition to model accuracy, the impact of model depths on computational performance is investigated. The results show that the depth of the controller model does not add to the computational load in a simulation. Computational complexity is, however, affected by the choice of the hardware model of the converter, specifically, changing from an averaged circuit representation to a switching model strongly reduces performance, as it affects the representation of the electrical network model [30]. The discussion in [30] concludes that for GFM converters a higher level of detail should be used than for GFL converters. It was also shown that a higher depth of the controller model comes at no computational cost. Based on the results in [28], [29] and [30], in this thesis, averaged converter models including all inner control loops (full order) are used in detailed simulations in the Electromagnetic Transient (EMT) domain and to validate the performance of the developed MPC algorithms.

For grid-connected RES, Voltages Source Converters (VSCs) are the most commonly applied converter technology [26], [31]. VSCs can have different topologies. Most important for RES applications are the two-level and three-level topology. In contrast, Modular Multilevel Converters (MMCs) are heavily used in High Voltage Direct Current (HVDC) transmission systems. Regardless of the topology, VSCs implement a controlled voltage source behavior, where the desired AC voltage is determined by the controller and realized by the converter hardware. The investigation of different converter topologies is outside the scope of this thesis. Therefore, the two-level topology is adopted as a general VSC representation, which is shown in Figure 2.5.

The switching frequency of a VSC is typically in the range of kHz, therefore on the timescale of microseconds. Simulation of switched converter models is limited by computational capacity and only necessary for fault studies [30]. For control system design, the switching events are averaged over one cycle to get an equivalent representation useable in the Laplace or state-space domain [31]. An averaged VSC model is illustrated in Figure 2.6, which is the representation that is used in the remainder of the thesis. The DC current i_{dc} is supplied by the RES. For a generic RES, a simple first order current source model can be adopted.

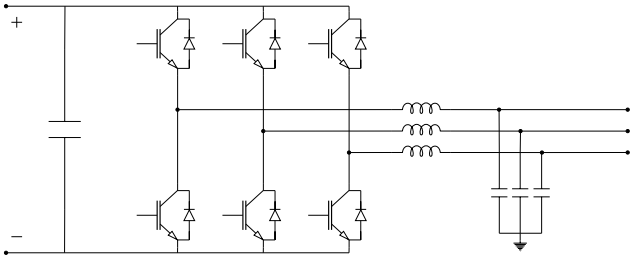

Figure 2.5: Two-level Voltage Source Converter.

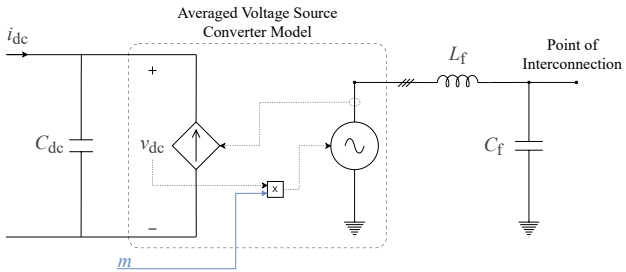

Figure 2.6: Averaged Voltage Source Converter.

In specific RES models, i_{dc} is the output of a DC/DC converter, connecting a detailed model, e.g., of a PV system.

As indicated earlier in this chapter, grid-connected converters are distinguished into Grid-Following and Grid-Forming type. The key difference between these two control philosophies is how the converter synchronizes to the grid. Grid synchronization is required to calculate the phase angle of the voltage that is realized by the VSC. Although GFL and GFM converters have fundamentally different characteristics, efforts are made to formulate their similarities. In [32], a duality theory is proposed and dual equations are derived that reveal insights into their dynamic interactions and complementary stability properties.

2.2.2 Grid-Following Control

In GFL control, the phase angle of the grid voltage is estimated by measuring the voltage at the converters Point of Interconnection (POI) and applying an estimation technique like a Phase-locked loop (PLL). At a fundamental level, the

objective of a GFL converter is to synchronize to the grid voltage and control the current injected into the grid at the POI. It is therefore often represented as an equivalent current source from the power system perspective. This type of control allows precise tracking of active and reactive power set-points through an outer loop by controlling the current set-points for the inner loops. GFL control has been developed and optimized for applications that are sensitive to power changes, like Wind and PV generation, that typically operate using a Maximum Power Point Tracking (MPPT) algorithm to maximize renewable energy production.

This type of synchronization has, however, important implications. The use of a PLL requires the presence of a grid voltage, which additionally has to be sufficiently stiff. Another component of the grid therefore has to establish a voltage, to which the GFL can synchronize to. In this context, stiff voltage means that a change of the injected current by the GFL controller can not affect the voltage at the POI too strongly, to avoid forming an unstable feedback loop between synchronization and current control. A non-stiff voltage is also called a weak grid condition. Several cases of weak grid instabilities with PLLs have been observed in real-world applications and some examples are reported in [33]. The presence of a grid voltage additionally implies that GFL converters are unable to supply and maintain an islanded converter-driven system without any other voltage forming component.

An overview of the Grid-Following control system is shown in Figure 2.7. The VSC controls the DC and AC voltages at its terminals through two outer control loops that provide references for the inner current control, which in turn determines the modulation index m for the hardware stage. Active power control is implemented by the RES, which supplies the DC current i_{dc}, typically through a DC/DC converter.

The three-phase AC voltages and currents of the converter and its filter (Figure 2.6) are transformed using a rotating reference frame to obtain steady-state signals without a fundamental frequency, which are usable for PI-based control. This frame-transformation is commonly applied for VSC control and known as Park transformation [31]. The transformation is implemented as:

$$\begin{bmatrix} u_d \\ u_q \end{bmatrix} = \frac{2}{3} \begin{bmatrix} \sin(\omega t) & \sin\left(\omega t - \frac{2\pi}{3}\right) & \sin\left(\omega t + \frac{2\pi}{3}\right) \\ \cos(\omega t) & \cos\left(\omega t - \frac{2\pi}{3}\right) & \cos\left(\omega t + \frac{2\pi}{3}\right) \end{bmatrix} \begin{bmatrix} u_a \\ u_b \\ u_c \end{bmatrix} \tag{2.22}$$

where $\theta = \omega t$ is the instantaneous internal phase angle of the converter and u is a voltage or current signal. For the GFL controller, the angle θ is obtained using a synchronous reference frame PLL, which also provides a measurement of the grid frequency. All control loops shown in Figure 2.7 are implemented using common PI control structures with feed-forward of the d- and q-components to achieve decoupled control, as derived in [31]. The PI controllers are equipped

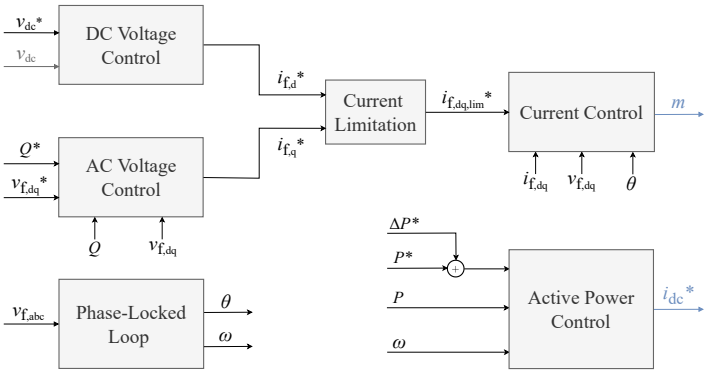

Figure 2.7: Grid-following converter control system.

with saturation of the output variables and anti-windup mechanisms. The AC voltage control further implements a voltage versus reactive power droop logic for decentralized voltage control.

Tuning

The PI controllers in this thesis are tuned using Matlab `pidtune` to ensure a fast and robust control response. The bandwidth of the inner control loops is chosen to be at least one order of magnitude faster than the outer loop for effective decoupling. Table 2.1 presents the Bandwidth, Phase Margin and the equivalent transfer function used to tune each control function. The bandwidth varies depending on the implemented RES model, e.g., PV or EL, and the switching frequency of the VSC, which is typically between 2 kHz and 5 kHz for high power applications. The transfer functions represent the dynamics of the output LC filter and the DC capacitor.

The PI gains, as well as any measurement signals in the GFL control system (Figure 2.7), are normalized by converting to the per unit system.

Function	Bandwidth [Hz]	Phase Margin [°]	Transfer function
Current Control	200 - 500	90	$\frac{1}{L_\mathrm{f}s+R_\mathrm{f}}$
DC Voltage Control	5 - 20	60	$-\frac{1}{C_\mathrm{dc}s}$
AC Voltage Control	10 - 20	60	$\frac{1}{C_\mathrm{f}s}$
Active Power Control	1 - 5	60	$\frac{1}{C_\mathrm{dc}s}$

Table 2.1: Tuning parameters of the PI controllers in GFL mode.

2.2.3 Grid-Forming Control

The limitations of GFL control, especially the inability to supply islanded systems, has motivated the development of GFM converter control. GFM converters control the voltage, frequency and phase angle at the POI. From the grids perspective, they can be represented as an equivalent voltage source behind an impedance. If there is only one voltage forming component like a GFM in a system, the frequency can be set to a fixed value. However, if more than one component forms the voltage, synchronization is required [34]. It is noted here that SGs are also voltage forming components. A GFM converter synchronizes with the grid through a power-based synchronization technique. The simplest representation of this synchronization is the droop technique, where deviations of the converter power output proportionally control the converter frequency used to calculate the VSCs voltage phase angle. Since the phase angle differences between different system nodes is related to the power flow, multiple converters synchronize through this technique as coupled oscillators [35]. The power-based synchronization requires the availability of a power reserve and therefore a sufficiently fast accessible energy source on the DC-side of the converter. When implemented in real systems, GFM converters are therefore often coupled with some form of energy storage to guarantee stable synchronization.

Figure 2.8 shows an overview of the GFM control system, emulating the behavior of an equivalent voltage source behind an impedance at the POI. To this end, the voltage magnitude and phase angle are determined by the outer control loops, while the inner loops control the current and voltage over the inductor and capacitor of the LC-filter (Figure 2.6). The inner current and voltage loops are implemented using common PI control structures with feed-forward decoupling of the dq-components [31]. The voltage reference control and the active power and synchronization control determine the dynamics of the equivalent voltage source, while the virtual impedance function emulates a series impedance to

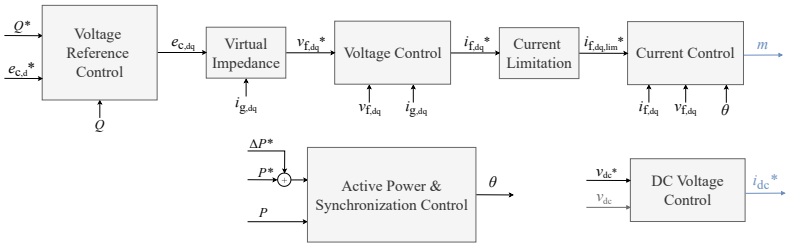

Figure 2.8: Grid-forming converter control system.

increase stability [32] and/or limit the current during faults [36]. An overview of the different variants of the control functions displayed in Figure 2.8 can be found in [1]. The voltage reference control implements a voltage versus reactive power droop logic for decentralized voltage control coordination.

Different types of GFM control exist in literature. Initially, the focus of GFM research was on the parallel operation of inverters to supply islanded microgrids [34]. In this context, droop controllers, inspired by the steady-state governor droop of SGs, were developed. The idea of mimicking SG behavior with power converters was then extended by developing the VSM [20] and Synchronverter [37] concepts, and applying them in grid-connected converter systems. Furthermore, the observation that the GFM synchronization mechanism is that of coupled oscillators [35] lead to the development of a new class of GFM controllers, namely Virtual Oscillator Control (VOC) [38]. While all GFMs have different formulations, it has been revealed that they exhibit comparable and under some conditions even equivalent small-signal characteristics [39], [40]. A detailed performance benchmark of the most widely spread GFM implementations is given in [41]. The immense potential of GFM converters to support the stability of interconnected power systems has been widely recognized and current efforts of GFM development focus on the grid integration, standardization, certification as well as the development of market models to incentivize large-scale implementation of this technology [42]. The GFM strategies used in this thesis are VSM and a decoupled VSM strategy, which are presented in more detail in Chapter 3.

Virtual Impedance

The virtual impedance emulates a series impedance between the internal voltage source $e_{\mathrm{c,dq}}$ of the GFM converter and the reference voltage $v^*_{\mathrm{f,dq}}$ at the POI. It implements the following equation:

Function	Bandwidth [Hz]	Phase Margin [°]	Transfer function
Current Control	500	90	$\frac{1}{L_\mathrm{f}s+R_\mathrm{f}}$
Voltage Control	50	60	$\frac{1}{C_\mathrm{f}s}+R_\mathrm{d}$
DC Voltage Control	100	60	$\frac{1}{C_\mathrm{dc}s}$

Table 2.2: Tuning parameters of the PI controllers in GFM mode.

$$\begin{aligned} v^*_{\mathrm{f,d}} &= e_{\mathrm{c,d}} - R_\mathrm{v} i_{\mathrm{g,d}} + X_\mathrm{v} i_{\mathrm{g,q}}, \\ v^*_{\mathrm{f,q}} &= e_{\mathrm{c,q}} - X_\mathrm{v} i_{\mathrm{g,d}} - R_\mathrm{v} i_{\mathrm{g,q}}, \end{aligned} \tag{2.23}$$

where $i_{\mathrm{g,dq}}$ is the current injected into the grid (Figure 2.6), and X_v and R_v are the virtual reactance and virtual resistance respectively. Virtual impedances are used for stabilization of small-signal effects as static impedances, or for overcurrent limitation, e.g., during faults, as transient impedances [43]. In this thesis, a static virtual impedance as in (2.23) is used.

Tuning

The PI controllers of the GFM are tuned using Matlab `pidtune` to ensure a fast and robust control response. The bandwidth of the inner control loops is chosen to be at least one order of magnitude faster than the outer loop for effective decoupling. Table 2.2 presents the Bandwidth, Phase Margin and the equivalent transfer function used to tune each control function, assuming a VSC switching frequency of 5 kHz.

The transfer functions for the current and voltage controller tuning represent the dynamics of the AC output filter inductance and capacitor respectively. The filter capacitor includes a series damping resistance R_d. The transfer function of the DC voltage dynamics describes the dynamic behavior of the DC link. The PI gains, as well as any measurement signals in the GFM control system (Figure 2.8), are normalized by converting to the per unit system.

2.3 Model Predictive Control for Power System Frequency Control

This thesis explores the application of MPC and proposes new formulations to enhance frequency stability in modern power systems through fast and coordinated control of power electronic converters. To this end, this section first provides an overview of the broader context of MPC in converter-driven power systems. Applications of MPC for frequency control in literature are reviewed, and the resulting gaps and research objectives of this thesis are discussed.

2.3.1 Hierarchical Control Framework

Power system control is conventionally divided into three hierarchical levels - primary, secondary and tertiary control. MPC can be applied on all of these hierarchical levels.

The primary control level is concerned with the control of individual devices, i.e., the converter in this work. This layer covers a broad range of control functions in a cascaded manner. The inner hardware-oriented functions include the control of currents and voltages and the minimization of harmonic distortion, among other objectives, to achieve high efficiency and reliability of the device. The outer system-oriented primary control objectives are the stabilization of voltage frequency and magnitude, providing fault current or inertia control to ensure stability of the power system. Both of these groups of control functions are part of the primary control system of a power converter, however there is a clear distinction between functions with relevance for the device or the system. For this reason, and to enhance interoperability, researchers have recently proposed to differentiate and divide the primary control into an upper open-source layer, and a lower closed-source layer [44], [45]. MPC can integrate multiple of the cascaded control loops and thereby simplify the control system, and also increase the overall bandwidth of the primary level [46]. The inner hardware-oriented control with MPC is outside the scope of this thesis, as it does not directly contribute to frequency control. An overview of this application is given in, e.g., [47] and [48]. Primary control with the outer system-oriented control contributes to frequency stability. An important characteristic of primary control is that it is implemented in a decentralized manner and does not require communication with other units or plants. This becomes especially crucial in interconnected power systems, where plant owners and system operators are different stakeholders.

Adverse interactions of decentralized primary controllers is commonly avoided by using a droop logic. The proportional control is able to stabilize system disturbances, however this type of control always has a steady-state offset. The secondary control layer completes this system level control task, by providing an integral action and recovering voltage and frequency into the nominal range [49]. In interconnected power systems secondary control acts very slowly (activated ≥ 30 seconds after a disturbance) to separate from inertial and primary control mechanism of SGs. Islanded converter-driven power systems on the other hand

have faster dynamics and the secondary control has a higher bandwidth to ensure stability [25]. In this context, MPC has the potential to increase frequency stability by providing a faster regulation and robust transients [50]. To this end, coordination of multiple converters is required, which can be implemented with varying degrees of communication, typically divided into centralized and distributed control schemes [51].

The tertiary layer is conventionally centered around steady-state optimization of a power systems operating point. This layer includes Optimal Power Flow (OPF) calculations that provide set-points and grid reconfiguration measures to avoid line congestion. In islanded converter-driven systems, energy management systems, such as [52], are used to ensure the continuous supply of energy considering uncertain forecasts and limited storage capacity. These algorithms also optimize the power exchange of microgrids with the main grid and provide an interface to the power market. The application of MPC for the energy management of microgrids is extensively discussed in [53]. The steady-state optimization of the power system operating point has no direct effect on the frequency stability and is therefore not in the scope of this work.

2.3.2 Review of Predictive Frequency Control Strategies and Research Questions

In the following, open research areas of MPC in power system frequency control are highlighted and the resulting research questions for this thesis are formulated.

MPC in synchronous generator-based power systems

In synchronous generator-based power systems, MPC has been applied for secondary frequency control. In [54], an interconnected power system is modelled with a lumped inertia model per control zone. The MPC constrains the Tie line power flow, as well as generator power limits and power rates. In [55], time-delays and time-varying parameters of a similar model are additionally accounted for in a Linear matrix inequality (LMI) approach to increase the controller robustness. To avoid a single point of failure, different DMPC approaches are developed in [56]. By taking the SG's primary control action into account, [54], [55] and [56] showed that MPC achieves better cooperation between secondary and primary control, providing a faster and more economic response than traditional PI-based approaches.

The dynamics of SG-based power systems are significantly slower than in converter-driven low-inertia systems. Therefore, computationally intensive approaches such as the LMI-based control [55] or a complex DMPC scheme [56] might become infeasible. The drawback of complexity was recognized in [55], and a non-predictive controller with lower computational effort has been designed, which, however, showed a significant decrease in performance.

MPC in converter-driven power systems

The application of MPC to enhance frequency control in converter-driven systems has been extensively researched at both primary and secondary control levels. Two distinct methodological approaches have emerged in the literature. The first category utilizes MPC to provide virtual inertia or FFR to the power system, effectively replicating traditional dynamics [57], [58], [59]. A more extensive body of research leverages the inherent optimization capabilities of MPC to dynamically adjust converter power output, directly constraining the RoCoF and absolute frequency deviations [60], [61], [62], [63], [64], [65], [66], [67], [68]. These studies demonstrate that MPC significantly improves frequency stability by providing rapid control actions while explicitly respecting physical resource constraints. While these methods excel in islanded systems, such as microgrids, due to the ability to reject disturbances quickly through fast secondary control [67] they may conflict with the regulatory frameworks of large-scale interconnected power systems. In the latter, market structures and grid code compliance necessitate standardized, predictable response behaviors rather than fully autonomous optimization. While standardized responses are expected by the system operator, plant owners have, however, freedom on how to provide this response from within the plant, providing new potential applications for MPC.

Some of the existing research relies on highly idealized resource representation that do not capture the complexity of converter-based RES. In [57], [58], converter dynamics are fully neglected and an ideal and undelayed power injection from MPC commands is assumed. The predominant trend in the literature is to consider generic GFM units with ideal DC sources [51], [59], [60], [62], [63], [69], [70], [71]. While some studies have advanced this by incorporating the internal state of energy storage systems behind the GFM interface [61], [64], [65], [66], the potential and diversity of other RES types, such PV and wind generation or flexible loads like ELs, are often overlooked. Although recent efforts have moved toward multi-resource coordination [72], they often fail to integrate the specific converter and RES dynamics, specifically the distinction between GFM and GFL control. This is a critical shortcoming, as the inherent strength of MPC lies in its MIMO coordination capabilities. This potential has not yet been rigorously studied for heterogeneous RES and mixed GFM and GFL systems, which are expected to predominate in the near future. As previously shown in [54], it is essential that primary control actions are explicitly accounted for within the prediction model to leverage the advantages of MPC.

While the theory on MPC suggests that MIMO systems and multi-objective problems are well-covered by the framework [4], empirical evidence in frequency control remains incomplete. Most studies utilize constraints to manage variables, but sophisticated multi-objective control, such as the simultaneous tracking of

multiple set-points, e.g., for frequency and State of Charge (SoC) in [64], [65] or DC voltages in [73], are rarely implemented. This lack of integrated study makes it difficult to determine how MPC actually compares to simpler linear control methods. Specifically, the limitations of traditional PI-based schemes in handling constrained coordination in MIMO frequency control remain unaddressed, as the theoretical advantages of MPC have only been demonstrated for isolated aspects rather than as a holistic solution.

The identified discrepancies between the theoretical capabilities of MPC and its current application in power systems raise the following research questions:

- How effectively can MPC provide primary or fast secondary frequency control while simultaneously fulfilling additional control objectives (e.g., tracking maximum power points or energy storage levels) across multiple heterogeneous converter-based RES?
- To what extend does an MPC-based coordination scheme prove advantageous over traditional decentralized or PI-based controllers?

Section 5.1 and Section 5.2 are dedicated to evaluating MPC in the context of these questions.

Modelling

The performance of MPC fundamentally depends on the accuracy of its internal prediction model. In frequency control applications, this model is typically linear, though the level of detail varies significantly across the literature (e.g., between [58] and [61]). A common practice in current studies is the use of an ideal plant model for simulation that is identical to the prediction model [57], [62], [67]. However, in real-world implementations, the prediction model must necessarily be a simplified representation of the complex underlying dynamics. In the following, considerations for prediction models are highlighted, while the specific impact of detailed plant modeling is discussed later in the context of MPC robustness and sensitivity.

A critical implication for prediction models, as established in Section 2.2, is that the primary control variable in converter-driven systems has shifted. In traditional power systems, the mechanical power input of turbines is controlled to stabilize frequency events, which is decoupled from grid dynamics by the kinetic energy stored as rotational inertia (Figure 2.3). In converter-driven systems, however, the electrical power output of converters must be controlled and constrained, which is directly exposed to grid dynamics, including rapid load disturbances and oscillatory converter interactions (Figure 2.4). Despite this, a large number of studies continue to neglect these critical dynamics by assuming a single frequency or completely decoupled models [51], [59], [68], [70], [71], [74].

A critical barrier to implementing dynamic system models for MPC is the availability and observability of system states. Some frameworks rely on wide-area monitoring systems for measurement data, however, the latency and accuracy of such systems represents a significant vulnerability on the fast timescales required for converter control [60], [61]. Other studies assume idealized full-state measurements and neglect the necessity of a state estimator entirely [70], [72]. Furthermore, the treatment of disturbances is often oversimplified, with some works assuming disturbances can be directly measured [64], [67]. Successful real-world implementation requires a prediction model that captures converter, system, and disturbance dynamics while remaining observable without requiring extensive additional infrastructure. A discussion of these implementation trade-offs is currently missing in the available literature.

The distinction between GFM and GFL converter modeling is vital in this context, yet existing studies typically consider only a single resource type [51], [71]. When GFM units are employed, they are frequently represented by unrealistic models, such as power sources driven by system frequency ($P(f)$-type models), that fail to account for their true internal dynamics [64], [72]. A unified representation that accounts for the interaction between both GFM and GFL dynamics within a single MPC framework is notably absent.

These identified gaps lead to the following research questions:

- Which model structures effectively capture relevant converter and system dynamics while remaining practically implementable as an observable MPC prediction model?
- How can the weaknesses and idealized assumptions of previous models be overcome or avoided in realistic grid scenarios?

To address these questions, the requirements for MPC prediction models and common modelling approaches are reviewed more extensively in Chapter 3.

Robustness and sensitivity

Quantifying the robustness of MPC to uncertainty is a critical assessment for its deployment in power systems. In this context uncertainty can be generally categorized in two forms: parametric uncertainty arising from inaccurate system information, and structural uncertainty resulting from unmodelled dynamics. In current literature, parametric uncertainty is typically analyzed by sweeping a single parameter to observe its effect on controller performance [59], [60], [67], [71], [72], [75]. While this approach is mathematically valid for purely linear systems, MPC is inherently a nonlinear controller due to its handling of constraints. Consequently, localized parameter sweeps provide an incomplete and potentially misleading picture of the controller's true stability margins and performance.

The second major limitation in existing studies is the reliance on an ideal plant model, where the simulated plant is identical to the controller's internal prediction model [57], [62], [64], [67], [76]. While this allows for rapid prototyping and simplified testing, it is fundamentally unable to account for structural uncertainty. As MPC is widely adopted in other disciplines like process control, it has been well-established that assessing the model-plant mismatch is essential for successful industrial implementation [77]. In the power systems domain, the increasing penetration of RES has increased the need for detailed EMT simulations and HiL level testing to de-risk control, protection and automation deployment [78], [79]. Despite the importance of high-fidelity testing, only a small number of studies implements MPC on detailed system models featuring phasor or EMT dynamics [60], [61], [63]. Developing and verifying EMT models is a resource-intensive and computationally heavy task. In contrast, nominal simulations, where prediction equals plant model, allow for a high volume of parameter variations to be tested quickly. However, a significant gap remains as no current study explicitly compares the accuracy of results from nominal simulations against EMT or HiL benchmarks. Consequently, the relative impact of parametric versus structural uncertainty remains unquantified. This comparative insight would enable the synergistic use of both modelling environments, i.e., nominal models for broad parameter sweeps and EMT for structural verification, to gain a holistic view of controller robustness [27], [30].

To this end, a global robustness and sensitivity analysis is necessary to move beyond the limitations of current studies and address the following research questions:

- How does MPC perform under uncertainty and model-plant mismatch compared to classical strategies in power system frequency control?
- Which types of uncertainty, parametric or structural, and which specific system parameters have the strongest effect on MPC performance?

The robustness and sensitivity analyses in Section 5.1 and Section 5.2 provide the basis for answering these research questions..

Communication systems and time delay

The application of MPC on the system level necessitates the use of communication infrastructure to exchange measurement signals and control commands between individual units. However, the unavoidable presence of communication delays can severely deteriorate performance and, in extreme cases, destabilize closed-loop operation [80], [81]. Communication networks further introduce stochastic behavior such as time-varying delays, packet loss or the intermittent unavailability of specific control units. These issues are particularly notable in

converter-driven power systems, since they exhibit much faster dynamics and are therefore inherently more sensitive to timing discrepancies. Despite the criticality of these effects, the current literature often neglects the impact of the communication systems [61]. Studies that incorporate them typically rely on oversimplified static delay models [59], [60], [67], [71], [72], [74]. While MPC possesses a degree of robustness to minor latencies, significant delays require active compensation through strategies such as state-space augmentation [75], [82]. The effectiveness of such delay-aware control has already been demonstrated in applications like wide-area damping control [83], [84], [85], yet a rigorous assessment in the context of frequency control is missing.

Specifically, there is a lack of research evaluating MPC against detailed communication models that feature stochastic, time-varying delays and packet loss between individual units. Furthermore, since the impact of delay is intrinsically related to the ratio between the delay and controller sampling time, it is likely that communication systems affect small-scale microgrids and large-scale transmission systems differently. This scale-dependent sensitivity has not been studied for MPC in power system frequency control, leading to the following research questions:

- What control strategies effectively compensate for the adverse effects of communication networks within MPC-based fast frequency control?
- How does the controller perform under realistic, stochastic communication conditions for different system scales, including islanded microgrids and large-scale transmission networks?

The questions posed are addressed through co-simulation of communication and power systems in Section 5.3.

Distributed predictive frequency control

For large-scale control systems, distributed architectures offer significant advantages over centralized frameworks, including enhanced scalability, modularity, and resilience by eliminating single points of failure. Furthermore, these architectures facilitate "plug-and-play" gradual deployment and increase the data privacy of individual participants. Different Distributed Model Predictive Control approaches for power system frequency control have been proposed in the literature [56], [69], [70], [71], [74], [76], [86]. Hereby, the specific formulation of the control problem and the choice of the distributed algorithm dictate different requirements for the control architecture, communication system, and necessary system measurements [5].

Most existing studies adopt a zone-based approach, where distributed control units manage specific sections of the power system while communicating solely

with neighboring units [56], [69], [74], [76], [86]. In this framework, each zone is typically represented by a lumped inertia model, where interactions of zones are modeled via Tie line power exchange [56], [76], [86]. While computationally efficient, this aggregated formulation fails to capture the frequency dynamics of individual units, most notably of GFM converters. Consequently, such schemes require an additional, lower-level control layer to manage GFM dynamics, however the challenge of disaggregating local zone commands to individual units remains largely unaddressed in these works.

Distributed control of individual converter-based RES has been studied in [70] and [71]. In this context it is important to consider the conditions of the distributed control scheme. Typically distributed control attempts to avoid global information exchange to preserve modularity, and increase privacy and resilience of the overall system. This necessitates model partitioning, where a global dynamic model is separated into local submodels that capture the local dynamics without relying on global measurements and parameter information. However, these partitioning strategies often introduce significant simplifications. The works in [70], [71] assume a complete decoupling of local dynamics. In [70], local converter dynamics are modelled in detail while neglecting the system dynamics by relying exclusively on terminal bus measurements. In [71], a similar approach is taken, and the coordination of the distributed control units is achieved only through the consensus of steady-state power flows, similar to [87]. A critical weakness in both approaches is the inability to predict or capture the transient interactive behavior between converters.

Alternatively, a distributed control scheme considering global information exchange could be designed, that still increases resilience of the overall system by avoiding a single point of failure. However, in this case, it must ultimately compete with centralized MPC secured through distributed redundancy, as centralized MPC achieves the optimal performance [56].

The limitations in current distributed strategies lead to the following research questions:

- How can a DMPC be designed to control individual GFM converters while capturing the coupling dynamics?
- What is the quantifiable performance loss when transitioning from a centralized controller to a distributed architecture?

Chapter 6 is dedicated to address these questions.

3 Control-Oriented Modelling

Model Predictive Control is based on the prediction of a systems future behavior from an initial state, and its response to control inputs and disturbances. In this chapter, requirements for prediction models are introduced. A new control-oriented model of power system frequency dynamics, using power instead of voltage angle as a state variable for voltage source components, is introduced. The proposed model eliminates the need to estimate the magnitude of load disturbances for the prediction, thereby it reduces the number of total state variables and increases observability. The prediction models are validated against detailed nonlinear time-domain simulations.

3.1 Requirements for Prediction Models

The prediction model is a central element of a Model Predictive Controller and its accuracy is very important, since the optimal control actions are computed based on the output predicted by the model. The prediction model enters the internal cost function of the optimal control problem as shown in (2.9). To ensure optimal performance of the control action, this results in the following requirements:

(1) The prediction model must represent the free response of the system from an initial state.
(2) The prediction model must represent the forced response of the system depending on control inputs and input disturbances.

These requirements are a consequence of the calculation of the state trajectory over the prediction horizon, stated in (2.2), and its integration in the MPC control as shown in Figure 2.2 and formulated in (2.9). The second requirement further extends from the formulation in (2.2) to include input disturbances of the augmented system model in (2.10) to ensure offset-free control under parametric uncertainty.

Full state measurement is typically not feasible for MPC applications, since it is often prohibitively expensive or technically impossible. Therefore, a state estimator is required to estimate unmeasured states as depicted in Figure 2.2, as well as to quantify step-wise disturbances, which are typically modelled as integrator states. The necessity of state estimation provides the third requirement:

(3) The augmented prediction model including disturbance states must be detectable.

Only for systems that are at least detectable, a stable state estimator can be calculated. Detectability is a weaker requirement than observability. Observability is given, if the observability matrix S_O has rank n_x, i.e., the number of states. It means that all states are visible in the output variables and can be estimated. The observability matrix is defined as:

$$S_\mathrm{O} = \begin{bmatrix} C_\mathrm{k} \\ C_\mathrm{k} A_\mathrm{k} \\ C_\mathrm{k} A_\mathrm{k}^2 \\ \vdots \\ C_\mathrm{k} A_\mathrm{k}^{n_\mathrm{x}-1} \end{bmatrix} \tag{3.1}$$

In contrast, detectability does not require full observability, but only that the unobservable states are stable. According to [8], the discrete time augmented system is detectable if the unaugmented system is detectable, i.e. the matrix $\begin{bmatrix} I-A_\mathrm{k} \\ C_\mathrm{k} \end{bmatrix}$ has rank n_x and the following condition is fulfilled:

$$\operatorname{rank} \begin{bmatrix} I - A_\mathrm{k} & -B_\mathrm{d} \\ C_\mathrm{k} & C_\mathrm{d} \end{bmatrix} = n_\mathrm{x} + n_\mathrm{d}, \tag{3.2}$$

where n_d is the number of disturbance states.

3.2 Representation of Voltage Sources and Grid Dynamics

Based on the requirements introduced above, different modelling approaches in literature can be reviewed regarding their suitability for Model Predictive Control of converter-based Renewable Energy Sources for frequency control.

The most simple representation of grid frequency dynamics is to model the system with a single swing equation, as described in (2.17). This model lumps the inertia of multiple generators together and focuses on the overall power balance, thereby defining the grid dynamics by a single frequency. Based on this frequency, different units respond with a $P(f)$-type function. This modelling approach is accurate to represent turbine governor response and GFL controlled RES, as they implement a $P(f)$ response to a measured frequency disturbance. It has been successfully used, e.g., in [65] for predictive electric vehicle charging control using GFL converters. GFM converters on the other hand implement a voltage source response with an independent swing equation behavior. Their contribution to frequency control is determined by their power synchronization control, as described in Section 2.2, and is therefore part of the overall system inertia constant M_sys. The power output of a GFM converter in this model could be extracted via an output equation, as shown in Figure 3.1, where a lumped

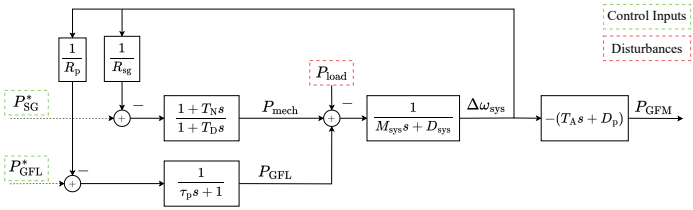

Figure 3.1: Lumped inertia model of a system with a Synchronous Generator, a Grid-Following and a Grid-Forming Converter.

inertia model for a SG, a GFL and a GFM converter is shown. In this figure, the SG turbine governor response P_{mech} is characterized by a lead and lag time constant T_{N} and T_{D}, as well as a droop coefficient R_{sg}. The GFL converter is modelled as a first-order element with time constant τ_{p} and a droop gain R_{p}. The output power of the GFM converter is determined by its inertia constant T_{A} and damping coefficient D_{p}. While this representation captures the free response of the GFM inertia contribution, the instantaneous response to load disturbances, as shown in Figure 2.4, is not fully captured, and there is no control input for a power set-point of the GFM converter. Furthermore, it is known that during transient events, the frequency is not equal at different system buses, and power and frequencies oscillate between different voltage source components (as it can be seen in the oscillations in Figure 2.4). Capturing these dynamics is however important to control the output power within the rated limitations and satisfy converter constraints. The lumped inertia model therefore does not fulfill requirement (2), and requirement (1) is only partly fulfilled for GFM converters.

Detailed representations of converters and SGs are used in models for small-signal stability studies, as described in, e.g., [49], [88] or [89]. Small-signal stability models aim to capture the interactions of multiple units by linearizing at a specified operating point and examining the models eigenvalues to detect and analyze angle or oscillatory instabilities. They typically neglect network dynamics or employ network reduction techniques [88]. Therefore, they do not include load disturbance inputs, or would require a detailed load model, undermining requirement (2). To accurately compute the system eigenvalues, inner control loops for converters, and higher order models for SGs in the Park (or dq-)domain are used, which requires to synchronize multiple reference frames for a multi-machine system. The estimation of these model states directly conflicts with requirement (3), since the inner control loop of the converter systems and the electromagnetic states of SGs are not available for a higher level controller. While suitable for offline simulation-based studies, where all system states are accessible, this representation is not feasible for online control of multiple units.

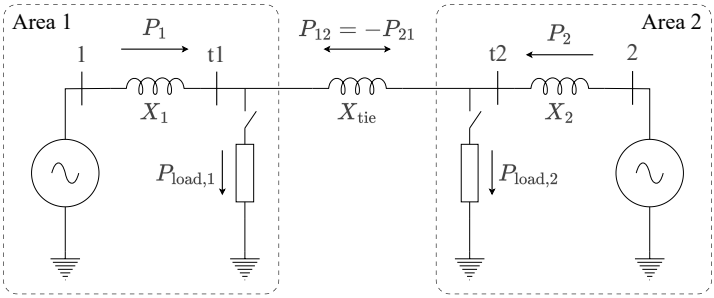

Figure 3.2: Power system model with two voltage sources.

For capturing the power and frequency dynamics, which are the variables of interest for frequency control, such a high level of modelling detail is, however, not necessary.

3.2.1 Tie line Model

The lumped inertia model (Figure 3.1) is extended by modelling the dynamic power flow over a Tie line to represent individual voltage source components with swing dynamics, i.e., SGs and GFM converters. This approach is commonly used in Automatic Generation Control (AGC) of large interconnected power systems, to control the power flow between different areas to their scheduled values [49]. A representation of two voltage sources with swing dynamics (or areas with lumped inertia) is shown in Figure 3.2, and the corresponding block diagram of the model in Figure 3.3. The model in Figure 3.2 and Figure 3.3 is generally applicable for SGs and GFM converters, where $P_{\text{in},i}$ is either the mechanical turbine power P_{mech} in case of an SG, or the power set-point P^* for a GFM converter. It is based on the small angle approximation $\sin(\delta) \approx \delta$, which is commonly used to linearize frequency control models [49], [88]. Assuming voltages are close to 1 pu and their angle difference is small, the Tie line parameter T_{Tie} is calculated as:

$$T_{\text{Tie}} = \frac{1}{X_{\text{T}}} = \frac{1}{X_1 + X_{\text{Tie}} + X_2}. \tag{3.3}$$

In Figure 3.3, the control inputs are the power injections, and the disturbance inputs are the load supplied by each voltage source respectively. The power output of each voltage source, as indicated in Figure 3.2, is:

$$P_i = P_{ij} + P_{\text{load},i}, \quad i \neq j, \quad i, j \in \{1, 2\} \tag{3.4}$$

This system can be written in state-space form as follows:

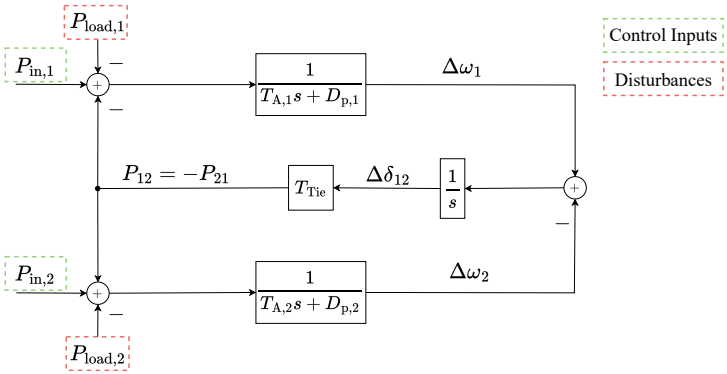

Figure 3.3: Block diagram of two voltage sources with swing dynamics and Tie line power flow.

$$\dot{x} = \underbrace{\begin{bmatrix} 0 & 1 & -1 \\ -\frac{T_{\text{Tie}}}{T_{\text{A},1}} & -\frac{D_{\text{p},1}}{T_{\text{A},1}} & 0 \\ \frac{T_{\text{Tie}}}{T_{\text{A},2}} & 0 & -\frac{D_{\text{p},2}}{T_{\text{A},2}} \end{bmatrix}}_{A} \underbrace{\begin{bmatrix} \Delta\delta_{12} \\ \Delta\omega_1 \\ \Delta\omega_2 \end{bmatrix}}_{x} + \underbrace{\begin{bmatrix} 0 & 0 \\ \frac{1}{T_{\text{A},1}} & 0 \\ 0 & \frac{1}{T_{\text{A},2}} \end{bmatrix}}_{B} \underbrace{\begin{bmatrix} P_{\text{in},1} \\ P_{\text{in},2} \end{bmatrix}}_{u}$$
$$+ \underbrace{\begin{bmatrix} 0 & 0 \\ -\frac{1}{T_{\text{A},1}} & 0 \\ 0 & -\frac{1}{T_{\text{A},2}} \end{bmatrix}}_{B_{\text{d}}} \underbrace{\begin{bmatrix} P_{\text{load},1} \\ P_{\text{load},2} \end{bmatrix}}_{d} \tag{3.5}$$
$$y = \begin{bmatrix} \Delta\omega_1 \\ \Delta P_1 \\ \Delta\omega_2 \\ \Delta P_2 \end{bmatrix} = \underbrace{\begin{bmatrix} 0 & 1 & 0 \\ T_{\text{Tie}} & 0 & 0 \\ 0 & 0 & 1 \\ -T_{\text{Tie}} & 0 & 0 \end{bmatrix}}_{C} \begin{bmatrix} \Delta\delta_{12} \\ \Delta\omega_1 \\ \Delta\omega_2 \end{bmatrix} + \underbrace{\begin{bmatrix} 0 & 0 \\ 1 & 0 \\ 0 & 0 \\ 0 & 1 \end{bmatrix}}_{C_{\text{d}}} \begin{bmatrix} P_{\text{load},1} \\ P_{\text{load},2} \end{bmatrix}$$

The measurable outputs are the frequency deviations $\Delta\omega_i$ and active power deviation of each source defined as:

$$\Delta P_i = P_i - P_{\text{in},i}, \quad i \in \{1, 2\}, \tag{3.6}$$

to ensure $D = 0$. By defining the disturbance vector d as additional states, the augmented system takes the form:

$$\begin{aligned}\begin{bmatrix}\dot{x}\\ \dot{d}\end{bmatrix} &= \begin{bmatrix}A & B_\mathrm{d}\\ 0 & 0\end{bmatrix}\begin{bmatrix}x\\ d\end{bmatrix} + \begin{bmatrix}B\\ 0\end{bmatrix}u,\\ y &= \begin{bmatrix}C & C_\mathrm{d}\end{bmatrix}\begin{bmatrix}x\\ d\end{bmatrix},\end{aligned} \tag{3.7}$$

which is the continuous-time equivalent of the augmented model in (2.10) for effective estimation and offset-free control of step-wise disturbances [8], [13], such as load changes in power systems.

The model (3.5), in the form of (3.7), is unobservable and undetectable. Observability is tested in continuous time, resulting in $\mathrm{rank}(S_\mathrm{O}) = 4 < 5 = n_\mathrm{x} + n_\mathrm{d}$. Detectability of MPC prediction models is only defined in discrete time. For the discretized system a rank of (3.2) equal to 4 is obtained. Therefore, the model is not implementable in an MPC in this form.

3.2.2 Frequency Divider Model

This thesis proposes a new modelling approach to represent the frequency and power dynamics for predictive control. The model reformulates the system states in terms of the output power of each voltage source component. The electrical output power is an important variable for converter systems that has to be controlled and constrained to satisfy hardware limitations. The new formulation, while accurately representing system dynamics (requirements (1) and (2)), must be detectable (requirement (3)), to be advantageous over the Tie line model.

In the Tie line model, the power output is divided into load power and power exchanged between voltage source components (3.4), resulting in states representing the angle differences and additional disturbance states to estimate loads. In contrast, this approach models the dynamics of the output power P_i directly as a state variable. Referring to Figure 3.2, the power flow over X_i, assuming a small angle and voltages $(V_i, V_{\mathrm{t}i})$ close to 1 pu, is described by:

$$P_i = \frac{V_i V_{\mathrm{t}i}}{X_i}\delta_{i,\mathrm{t}i} = \frac{1}{X_i}\delta_{i,\mathrm{t}i}, \quad i \in \{1, 2\}, \tag{3.8}$$

where $\delta_{i,\mathrm{t}i}$ is the voltage angle difference between the voltage source i and its terminal bus ti. The following expression is obtained by time differentiating (3.8):

$$\dot{P}_i = \frac{1}{X_i}\dot{\delta}_{i,\mathrm{t}i} = K_{\mathrm{c},i}\dot{\delta}_{i,\mathrm{t}i} = K_{\mathrm{c},i}\big(\Delta\omega_i - \Delta\omega_{\mathrm{t},i}\big). \tag{3.9}$$

The frequency $\Delta\omega_{\mathrm{t},i}$ is the frequency at the terminal bus ti. It can be calculated by using the Frequency Divider formula, which was derived in [90] and validated in a Hardware-in-the-Loop setup in [91]. The Frequency Divider is an analytical formulation to calculate the instantaneous frequency at any bus in an AC power system as a linear interpolation of frequency generators. Frequency generators include voltage source components in general, and can be extended to current

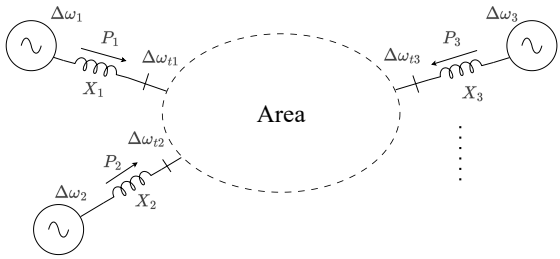

Figure 3.4: Conceptual representation of the proposed Frequency Divider-based prediction model.

source components, like GFLs. The inclusion of GFLs into the Frequency Divider framework is presented later in Section 3.3.2. A vector of generator frequencies is defined as:

$$\Delta\omega_{\mathrm{G}} = \begin{bmatrix} \Delta\omega_1 \\ \vdots \\ \Delta\omega_i \end{bmatrix}, i \in \{1...n_{\mathrm{G}}\}, \tag{3.10}$$

where n_{G} is the number of frequency generators. The Frequency Divider formula is then defined as:

$$\Delta\omega_{\mathrm{B}} = \underbrace{-B_{\mathrm{BB}}^{-1}\, B_{\mathrm{BG}}}_{F}\, \Delta\omega_{\mathrm{G}} = F\, \Delta\omega_{\mathrm{G}}, \tag{3.11}$$

where $\Delta\omega_{\mathrm{B}}$ is the vector of frequencies of passive buses (buses without a frequency generator). The Frequency Divider matrix F is calculated from the systems admittance matrix, by arranging the rows and columns according to frequency generator buses and passive buses:

$$I = Y \cdot V = \begin{bmatrix} Y_{\mathrm{GG}} & Y_{\mathrm{GB}} \\ Y_{\mathrm{BG}} & Y_{\mathrm{BB}} \end{bmatrix} \begin{bmatrix} V_{\mathrm{G}} \\ V_{\mathrm{B}} \end{bmatrix}. \tag{3.12}$$

Here, I and V are the systems current and voltage vector, and Y is the admittance matrix. In contrast to the traditional admittance matrix that is based on lines, transformers and physical buses, for the Frequency Divider calculation the matrix has to be extended with the generator impedance for SGs and the virtual impedance of a GFM converter, such that each component introduces an additional virtual bus as described in [90]. The submatrix $B_{\mathrm{BB}} = \mathrm{imag}(Y_{\mathrm{BB}})$ and $B_{\mathrm{BG}} = \mathrm{imag}(Y_{\mathrm{BG}})$, respectively. By extracting the row of F corresponding to the terminal bus ti of a voltage source component, and substituting into (3.9), the following relation is obtained:

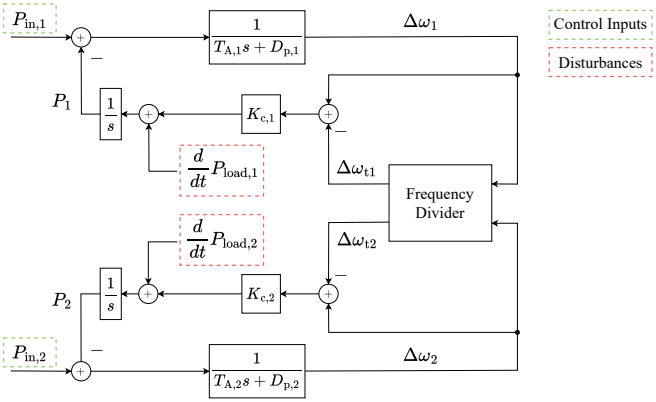

Figure 3.5: Frequency Divider model of two voltage sources with swing dynamics.

$$\dot{P}_i = K_{\text{c},i}\big(\Delta\omega_i - F_{\text{t},i}\ \Delta\omega_{\text{G}}\big). \tag{3.13}$$

The electrical output power is thereby reformulated as a dynamic function of generation frequencies instead of an algebraic function of the angle difference.

This formulation allows a modular extension of the model to any number of components by extending the vector $\Delta\omega_{\text{G}}$. A graphical representation of the proposed Frequency Divider model is shown in Figure 3.4. For each component, the local frequency and output power are modelled. This approach is applicable to any system topology, by calculating the Frequency Divider matrix F from the system admittance matrix.

Figure 3.5 shows a block diagram representation of the Frequency Divider model for the two voltage source system of Figure 3.2. The frequency dynamics, determined by the swing equations, are equal to the Tie line model. The power dynamics are expressed by (3.13). The model is written in state-space form, where the indices of F denote the respective matrix entries, as:

$$\dot{x} = \underbrace{\begin{bmatrix} -\frac{D_{\mathrm{p},1}}{T_{\mathrm{A},1}} & -\frac{1}{T_{\mathrm{A},1}} & 0 & 0 \\ K_{\mathrm{c},1}(1-F_{11}) & 0 & -K_{\mathrm{c},1}F_{12} & 0 \\ 0 & 0 & -\frac{D_{\mathrm{p},2}}{T_{\mathrm{A},2}} & -\frac{1}{T_{\mathrm{A},2}} \\ -K_{\mathrm{c},2}F_{21} & 0 & K_{\mathrm{c},2}(1-F_{22}) & 0 \end{bmatrix}}_{A} \underbrace{\begin{bmatrix} \Delta\omega_1 \\ P_1 \\ \Delta\omega_2 \\ P_2 \end{bmatrix}}_{x} + \underbrace{\begin{bmatrix} \frac{1}{T_{\mathrm{A},1}} & 0 \\ 0 & 0 \\ 0 & \frac{1}{T_{\mathrm{A},2}} \\ 0 & 0 \end{bmatrix}}_{B} \underbrace{\begin{bmatrix} P_{\mathrm{in},1} \\ P_{\mathrm{in},2} \end{bmatrix}}_{u}$$
$$+ \underbrace{\begin{bmatrix} 0 & 0 \\ 1 & 0 \\ 0 & 0 \\ 0 & 1 \end{bmatrix}}_{B_{\mathrm{d}}} \underbrace{\begin{bmatrix} \frac{d}{dt}P_{\mathrm{load},1} \\ \frac{d}{dt}P_{\mathrm{load},2} \end{bmatrix}}_{d} \tag{3.14}$$

$$y = \begin{bmatrix} \Delta\omega_1 \\ P_1 \\ \Delta\omega_2 \\ P_2 \end{bmatrix} = \underbrace{\begin{bmatrix} 1 & 0 & 0 & 0 \\ 0 & 1 & 0 & 0 \\ 0 & 0 & 1 & 0 \\ 0 & 0 & 0 & 1 \end{bmatrix}}_{C} \begin{bmatrix} \Delta\omega_1 \\ P_1 \\ \Delta\omega_2 \\ P_2 \end{bmatrix} + \underbrace{\begin{bmatrix} 0 & 0 \\ 0 & 0 \\ 0 & 0 \\ 0 & 0 \end{bmatrix}}_{C_{\mathrm{d}}} \begin{bmatrix} \frac{d}{dt}P_{\mathrm{load},1} \\ \frac{d}{dt}P_{\mathrm{load},2} \end{bmatrix}.$$

In contrast to the Tie line model, load disturbances enter the Frequency Divider model not by their absolute value, but instead as a time derivative. In other words, only a change of the load is disturbing the power. This type of disturbance is a state-less process noise, for which an estimator, such as a Kalman filter, can be designed for. It is not necessary (or helpful) to augment the system with additional disturbance states, as this disturbance is not step-wise.

The model in (3.14) is fully observable, with $\mathrm{rank}(S_{\mathrm{O}}) = 4 = n_{\mathrm{x}}$. In this formulation, full state measurement is obtained ($C = I$). However, even for a smaller number of measurements, the model maintains observability. In fact, even with a single measurement of any $\Delta\omega_i$ or P_i variable, the model is still fully observable, e.g., $C = [1\ 0\ 0\ 0]$. This is likely due to the higher degree of interactions of state variables, which is also indicated by a higher density of the A-matrix (here 0.5), compared to the augmented state matrix in (3.7), which has a density of 0.32. The relation between state interactions and observability has been investigated in [92] using a graphical approach, and the dual problem of controllability has been analyzed in [93] by the same authors. Their results show that sparse systems are harder to control (observe), and dense networks require less driver nodes (measurements) to obtain controllability (observability). More studies about the observability of systems based on interactions can be found in [94].

The modelling examples shown in this section represent a small system with only two sources. In this context, the scalability of the state matrix of the presented modelling approaches is interesting. Due to the absence of an absolute

Model approach	Component	Free response (1)	Forced response (2)	Detectable (3)
Lumped inertia	SG	+	+	+
	GFM	○	−	+
Small-signal stability	SG	+	○	−
	GFM	+	○	−
Tie line	SG	+	+	○
	GFM	+	+	○
Frequency Divider	SG	+	+	+
	GFM	+	+	+

Table 3.1: Evaluation of prediction model requirements for different modelling approaches of voltage source components.
Requirements are: + fulfilled, ○ partly fulfilled, − not fulfilled

voltage angle, one voltage source is typically chosen as a reference bus to which all angles are related. The size of the Tie line model therefore grows with

$$n_{\mathrm{x}} + n_{\mathrm{d}} = (2n - 1) + n = 3n - 1, \tag{3.15}$$

where n is the number of voltage source components. The Frequency Divider model on the other hand has $2n$ states, as no additional disturbance states are required. Hence, the state matrix of this model has a lower dimension than the Tie line model.

3.2.3 Comparison of Modelling Approaches

Table 3.1 summarizes the modelling approaches discussed in this section with respect to the prediction model requirements of Section 3.1. The lumped inertia model and models used in small-signal stability analysis are not suitable for application in MPC. The lumped inertia approach does not capture GFM converter dynamics as it is not detailed enough. Small-signal stability models on the other hand are of high order and require measurements that are infeasible for a plant or system-level controller. In consequence they are not implementable, because they are not detectable.

The Tie line model from literature and the Frequency Divider model proposed in this thesis capture the relevant system dynamics. The analysis of a simple two voltage source example indicates problems related to the detectability of the Tie line-based approach, caused by the need to augment the system with disturbance states. This model becomes implementable by introducing a simplification that is discussed in Chapter 4. MPCs with both models, using the same

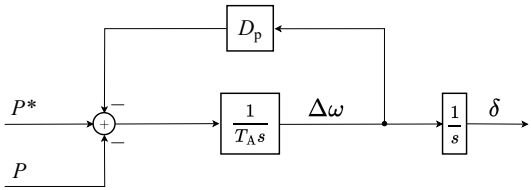

Figure 3.6: Block diagram of the Virtual Synchronous Machine strategy for Grid-Forming control.

system inputs and outputs, are developed. Their performance and robustness characteristics are evaluated and compared in Chapter 5.

3.3 Component Models

There are three main components that must be modeled for power system frequency control with distinctive dynamic characteristics. They can represent a larger set of different generation, load or storage technologies that use these common interfaces to connect to the grid. Grid-Forming and Grid-Following converters are power electronic interfaces that connect DC-based technologies. Synchronous Generators, on the other hand, transform mechanical to electrical power. Modelling of these components and their integration into the Tie line and Frequency Divider models is presented in the following.

3.3.1 Grid-Forming Converter

Grid-Forming converters implement a voltage source behavior using a power-based synchronization with the AC power system. The power synchronization control loop of this converter type determines its dynamic power and frequency response. Different implementations of GFM controllers have been proposed in literature (see [1] for an overview). The most popular variants are the Virtual Synchronous Machine and droop-based GFMs control. The equivalence of droop control and VSM has been shown in [39], therefore droop control is not explicitly shown and discussed here.

A VSM implements the swing equation of an SG, as shown in the block diagram in Figure 3.6. For the Tie line model, this results in the following dynamic equations:

$$\begin{aligned} \dot{\delta} &= \Delta\omega - \Delta\omega_\mathrm{ref}, \\ \Delta\dot{\omega} &= -\frac{D_\mathrm{p}}{T_\mathrm{A}}\Delta\omega - \frac{T_\mathrm{Tie}}{T_\mathrm{A}}\delta - \frac{1}{T_\mathrm{A}}P_\mathrm{load} + \frac{1}{T_\mathrm{A}}P^*, \end{aligned} \tag{3.16}$$

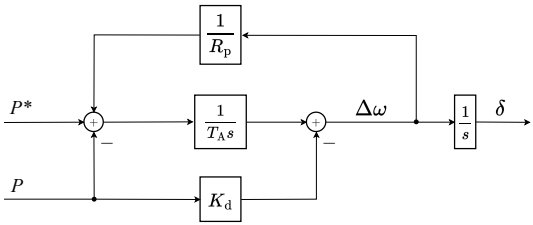

Figure 3.7: Block diagram of the Virtual Synchronous Machine strategy with decoupled parameters for Grid-Forming control [97].

where δ is the angle difference between the VSM controlled GFM converter and a reference source with frequency $\Delta\omega_{\text{ref}}$, as in (3.5). In the Frequency Divider modelling, the angle state is replaced by a power state, as introduced in Section 3.2.2:

$$\begin{aligned} \dot{P} &= K_{\text{c}}\Delta\omega - K_{\text{c}}\Delta\omega_{\text{t}}, \\ \Delta\dot{\omega} &= -\frac{D_{\text{p}}}{T_{\text{A}}}\Delta\omega - \frac{1}{T_{\text{A}}}P + \frac{1}{T_{\text{A}}}P^*. \end{aligned} \tag{3.17}$$

The formulation of the VSM in Figure 3.6 offers only two degrees of freedom to parameterize the model, namely T_{A} and D_{p}. Notably, D_{p} determines both the damping constant of the VSM, as well as the steady-state droop constant. However, a steady-state droop response is not always desired, and damping must be provided regardless, therefore it must be tuned separately. To increase the degrees of freedom for tuning and operation, alternative formulations of the VSM have been proposed. They commonly include a feed-forward path of the power or angle [95], or a derivative term on the feed-back path [96]. This alters the dynamic response of the GFM converter. One example of a decoupled VSM, based on [97], is shown in Figure 3.7, where damping is provided via a feed-forward gain K_{d} of the output power, and the steady-state droop is determined via an outer feed-back loop with gain R_{p}. The dynamic equations of this implementation for a Tie line model are:

$$\begin{aligned} \dot{\delta} &= \Delta\omega - \Delta\omega_{\text{ref}}, \\ \Delta\dot{\omega} &= \left(-\frac{1}{T_{\text{A}}R_{\text{p}}} - K_{\text{d}}T_{\text{Tie}}\right)\Delta\omega - \frac{T_{\text{Tie}}}{T_{\text{A}}}\delta - \frac{1}{T_{\text{A}}}P_{\text{load}} + \frac{1}{T_{\text{A}}}P^*. \end{aligned} \tag{3.18}$$

For the Frequency Divider model this is reformulated as:

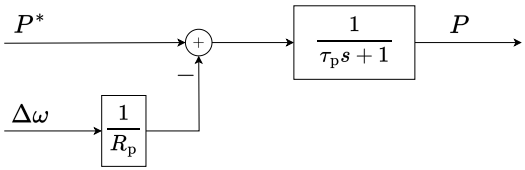

Figure 3.8: Block diagram of a GFL controlled converter with droop control.

$$\begin{aligned} \dot{P} &= K_\mathrm{c}\Delta\omega - K_\mathrm{c}\Delta\omega_\mathrm{t}, \\ \Delta\dot{\omega} &= \left(-\frac{1}{T_\mathrm{A}R_\mathrm{p}} - K_\mathrm{d}K_\mathrm{c}\right)\Delta\omega - \frac{1}{T_\mathrm{A}}P + K_\mathrm{d}K_\mathrm{c}\Delta\omega_\mathrm{t} + \frac{1}{T_\mathrm{A}}P^*. \end{aligned} \tag{3.19}$$

While there are many variants of GFM control in literature, this example highlights that the models in this thesis are not limited to a specific GFM variant, and extensions, such as feed-forward terms, can be integrated.

3.3.2 Grid-Following Converter

Grid-Following converters implement a current source behavior, by synchronizing with the power system through a PLL. In contrast to GFM converters, that dynamically exchange power based on swing dynamics, GFL converters are controlled to inject (or consume) a specific amount of power. The power response to a set-point change is therefore commonly modelled as a first-order system (e.g. in [72]). To participate in frequency control, the GFL power set-point is adjusted, typically with a droop logic. A block diagram of a GFL converter is shown in Figure 3.8.

GFLs are incorporated into Tie line models, by adding their power output to the input power of a voltage source component (SG or GFM converter). This is a practical approach if the voltage source component represents an area of the power system as a lumped inertia. For models representing individual components, however, an arbitrary voltage source component to which the output power is added, must be chosen. The dynamic equation of the GFL in this case is:

$$\dot{P} = -\frac{1}{\tau_\mathrm{p}}P - \frac{1}{R_\mathrm{p}\tau_\mathrm{p}}\Delta\omega + \frac{1}{\tau_\mathrm{p}}P^*, \tag{3.20}$$

where $\Delta\omega$ is the frequency of the assigned voltage source.

Because GFL converters are traditionally not considered to affect power system frequency directly, their contribution to frequency control has been modelled based only on the overall power balance. In recent years, research has revealed that GFL converters have a direct influence on the frequency through their power injections. This effect is investigated [98] and [99], where analytical

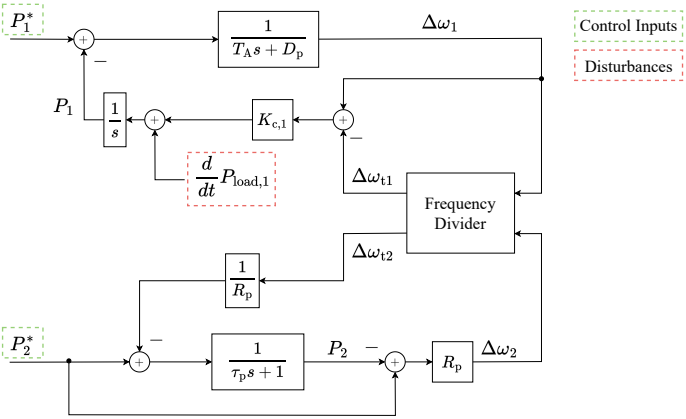

Figure 3.9: Frequency Divider model of a system with a GFM (index 1) and a GFL converter (index 2).

formulations are derived and validated, considering PLL and current injections effects. The idea is taken to the extreme in [100], where a stable simulation of a 100% GFL based power system is achieved.

In [101], conditions to include GFL converters into the Frequency Divider formula where derived. To this end, a virtual frequency, which augments the vector of generator frequencies $\Delta\omega_G$, is defined as:

$$\Delta\omega = -R_p(P - P^*) \quad \in \Delta\omega_G. \tag{3.21}$$

For calculation of the Frequency Divider matrix F, the admittance matrix (3.12) is extended with additional nodes for GFL converters that are connected to their coupling points via a virtual admittance calculated as:

$$B_{GFL} = \frac{1}{\omega_n R_p \tau_p}, \tag{3.22}$$

where $\omega_n = 2\pi f_n$, is the nominal system frequency, i.e. 50 or 60 Hz.

In [101], the GFL dynamic is then formulated by a frequency-based equation of the same form as (3.9). In MPC, however, the power output of the converter is the controlled variable. Therefore, instead of modelling the GFL dynamics in terms of the virtual frequency (3.21), the power state representation is retained, and the virtual frequency is used only as an interface to the Frequency Divider-based system dynamics. Thereby, the following dynamic state equation is obtained:

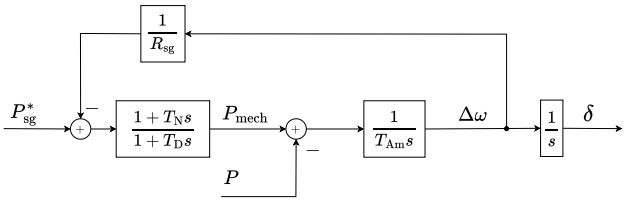

Figure 3.10: Block diagram of the SG model with turbine-governor.

$$\dot{P} = -\frac{1}{\tau_p} P - \frac{1}{R_p \tau_p} \Delta\omega_t + \frac{1}{\tau_p} P^*. \tag{3.23}$$

To illustrate how a GFL is incorporated into the Frequency Divider model, Figure 3.9 shows the model of a system consisting of a GFM and a GFL converter, based on (3.17), (3.21) and (3.23).

3.3.3 Synchronous Generator and Turbine-Governor

The mechanical power input of Synchronous Generators, provided by steam or hydro turbines, is controlled by a governor. Various types of turbine-governor models exist and are established in commercial software tools. Their implementation ranges from simple models, such as the TGOV1, to more detailed models that represent multiple turbine stages and controllers, like the IEEEG1 or TGOV5 models, presented in [102].

In this thesis, no specific turbine-governor is considered. For frequency control with converter-based RES, only the general dynamics of SGs and turbine-governors are of interest. The SG and turbine-governor model furthermore only needs to represent the aggregated dynamic of a large power system. Therefore, a simplified model is introduced that captures the significant characteristics of SG-based generation. Figure 3.10 shows a block diagram of the SG and turbine-governor model used in this thesis. It includes the mechanical inertia constant T_{Am} and the steady-state droop constant R_{sg}. The dynamic performance is determined by a lead-lag element, representing a fast response to frequency deviations from valve openings (parameter T_N), as well as the slower increase of mechanical power from the turbine, modelled by T_D, which is typically > 5 seconds.

The dynamic equations of the turbine-governor and SG in Figure 3.10 for a Tie line model are:

$$
\begin{aligned}
\dot{\delta} &= \Delta\omega - \Delta\omega_{\text{ref}}, \\
\Delta\dot{\omega} &= -\frac{T_{\text{Tie}}}{T_{\text{Am}}}\delta + \frac{1}{T_{\text{Am}}}P_{\text{mech}} - \frac{1}{T_{\text{Am}}}P_{\text{load}}, \\
\dot{P}_{\text{mech}} &= -\frac{1}{T_{\text{D}}}\left(1 + \frac{T_{\text{N}}}{T_{\text{Am}}R_{\text{sg}}}\right)P_{\text{mech}} + \frac{T_{\text{Tie}}T_{\text{N}}}{T_{\text{Am}}R_{\text{sg}}T_{\text{D}}}\delta \\
&\quad - \frac{1}{T_{\text{D}}R_{\text{sg}}}\Delta\omega + \frac{T_{\text{N}}}{T_{\text{Am}}R_{\text{sg}}T_{\text{D}}}P_{\text{load}} + \frac{1}{T_{\text{D}}}P^*_{\text{sg}}.
\end{aligned}
\tag{3.24}
$$

In the Frequency Divider model they are formulated as:

$$
\begin{aligned}
\dot{P} &= K_{\text{c}}\Delta\omega - K_{\text{c}}\Delta\omega_{\text{t}}, \\
\Delta\dot{\omega} &= -\frac{1}{T_{\text{Am}}}P + \frac{1}{T_{\text{Am}}}P_{\text{mech}}, \\
\dot{P}_{\text{mech}} &= -\frac{1}{T_{\text{D}}}\left(1 + \frac{T_{\text{N}}}{T_{\text{Am}}R_{\text{sg}}}\right)P_{\text{mech}} + \frac{T_{\text{N}}}{T_{\text{Am}}R_{\text{sg}}T_{\text{D}}}P - \frac{1}{T_{\text{D}}R_{\text{sg}}}\Delta\omega + \frac{1}{T_{\text{D}}}P^*_{\text{sg}}.
\end{aligned}
\tag{3.25}
$$

3.4 Model Validation

The control-oriented models derived in this chapter are validated against EMT simulations with detailed implementation including inner control loops in a dq-reference frame in Matlab Simulink. The models must represent the open-loop behavior of the system with respect to control and disturbance inputs. System constraints are enforced by the MPC in closed-loop operation and introduced in Chapter 4. Therefore any saturation or rate limiters are omitted for model validation.

A system including two GFM converters, employing the VSM (Figure 3.6) and decoupled VSM (Figure 3.7) control strategies, a GFL converter (Figure 3.8) and an SG with turbine-governor control (Figure 3.10) is simulated. The converters are rated at 10 MW = 1 pu, and the SG at 150 MW serving as a grid equivalent. The response of the Frequency Divider model (index "FD") and Tie line model (index "Tie") are compared to the EMT simulation results for different inputs.

First, the response of the system to step changes of the control inputs is shown. The power set-point P^* of the converters is increased by 0.5 pu at $t = 1\,\text{sec}$ for the VSM in Figure 3.11, the dVSM in Figure 3.12 and the GFL in Figure 3.13. Both models accurately capture the control response of the system. The second order response of the GFM converters is clearly visible, where an increase of the power reference first increases the converters frequency, and the output power follows as an integral of the frequency difference to the other GFM converter and

the SG. The GFL converter, on the other hand, has a first order response of the output power to a reference change.

A step disturbance of the load of 2 pu is simulated second. Figure 3.14 shows the converter and SG response to the load increase. It can be seen, that the GFM converters and the SG output power increases instantaneously to supply the load. The GFL and turbine-governor increase their output power more slowly as a result of the frequency transient and steady-state deviation.

In Figure 3.15, the impedance of the SG is increased and the same load step of 2 pu is applied. In this scenario, the load disturbance occurs electrically closer to the GFM converters, while all other parameters are unchanged. As a result, the instantaneous power response of the GFM converters increases by more than 100%, from $\Delta P = 0.16$ pu to $\Delta P = 0.38$ pu at $t = 1.05\,\text{sec}$. Although only a single load is increased, it is visible in the output power of all GFM converters and SGs, because they are part of the same coupled AC system. The location of the load step determines how much of the load is initially supplied by each component. In general, the location and magnitude of load disturbances is unknown for frequency control. This observation justifies to model load disturbances as separate inputs and to estimate the impact with individual disturbance states, as shown in (3.5).

In summary, the Frequency Divider model and the Tie line model both capture the power and frequency dynamics of the EMT model accurately, including the initial response to step inputs, transient phenomena like power or frequency oscillations, and steady-state values.

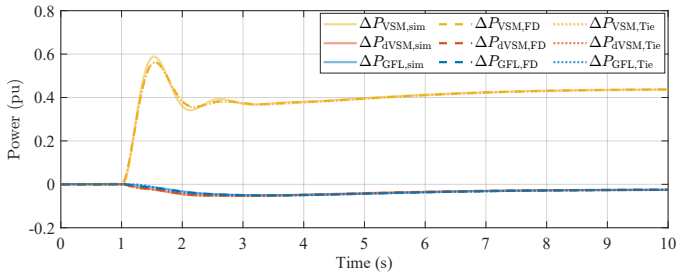

(a) Converter power.

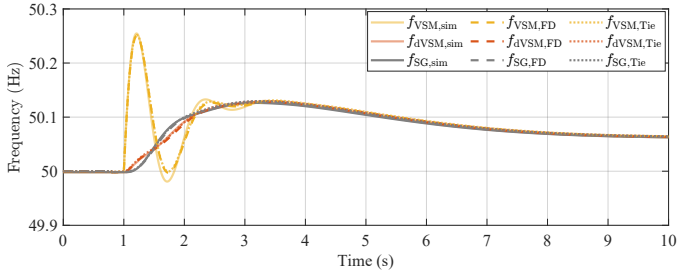

(b) Grid forming converter and synchronous generator frequency.

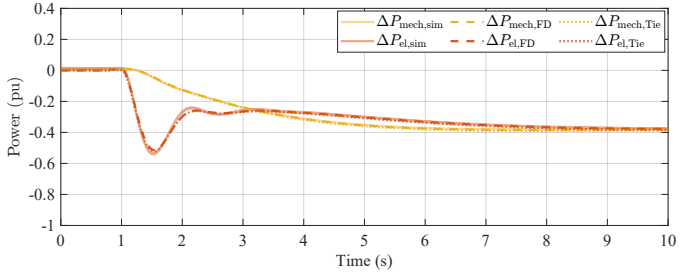

(c) Synchronous generator mechanical and electrical power.

Figure 3.11: Power set-point step of 0.5 pu on a VSM GFM converter. EMT simulation (“sim”), Frequency Divider model (“FD”), Tie line model (“Tie”)

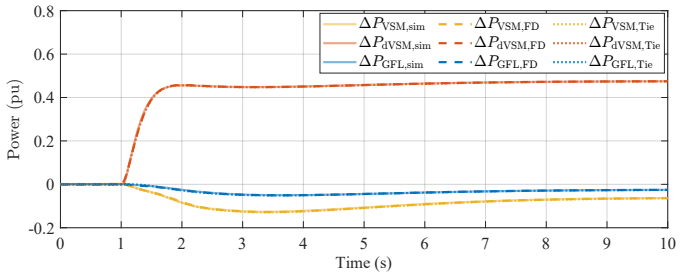

(a) Converter power.

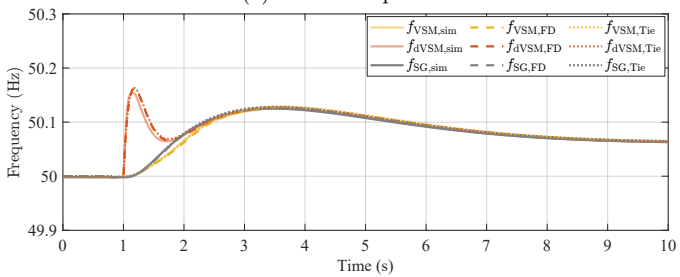

(b) Grid forming converter and synchronous generator frequency.

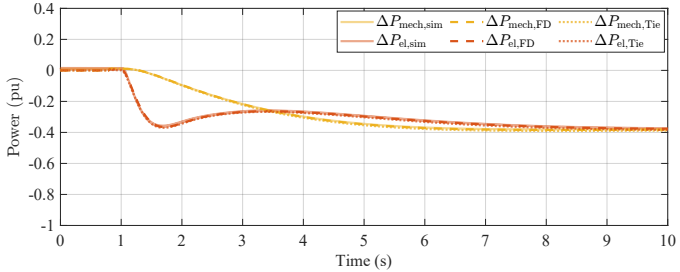

(c) Synchronous generator mechanical and electrical power.

Figure 3.12: Power set-point step of 0.5 pu on a decoupled VSM GFM converter. EMT simulation ("sim"), Frequency Divider model ("FD"), Tie line model ("Tie")

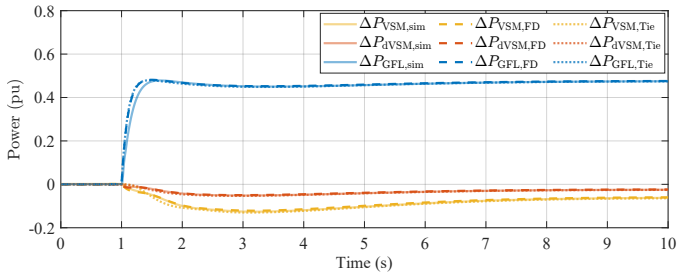

(a) Converter power.

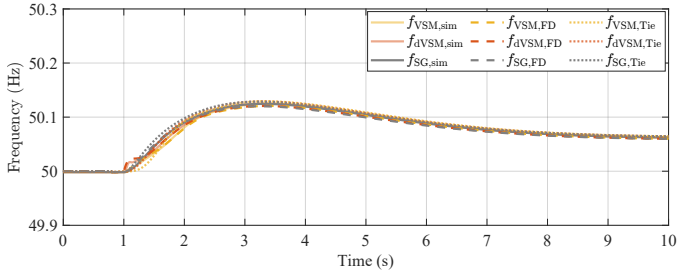

(b) Grid forming converter and synchronous generator frequency.

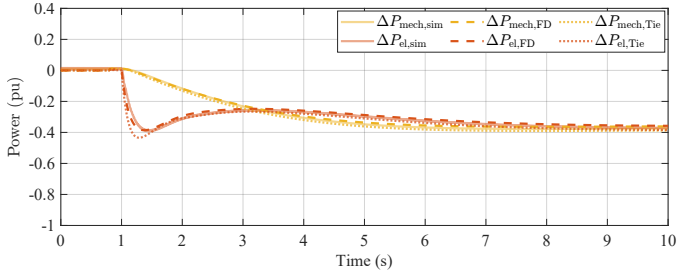

(c) Synchronous generator mechanical and electrical power.

Figure 3.13: Power set-point step of 0.5 pu on a GFL converter. EMT simulation (“sim”), Frequency Divider model (“FD”), Tie line model (“Tie”)

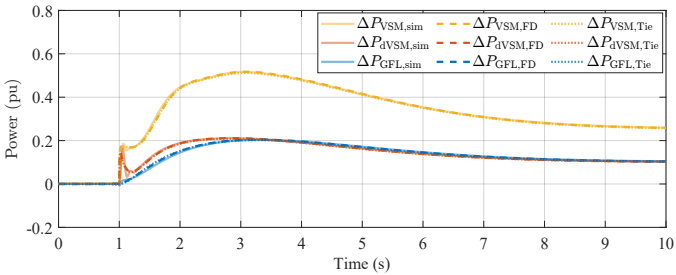

(a) Converter power.

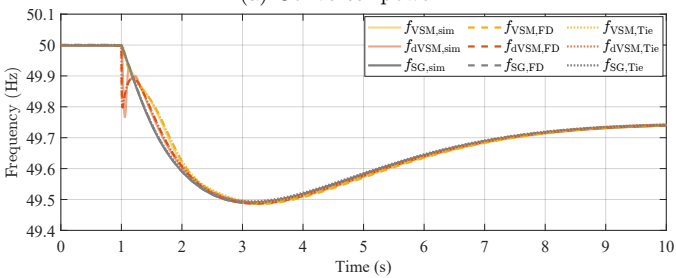

(b) Grid forming converter and synchronous generator frequency.

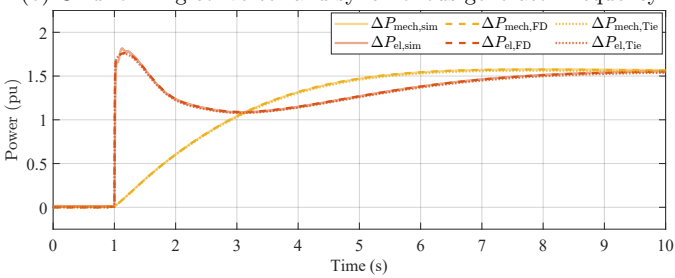

(c) Synchronous generator mechanical and electrical power.

Figure 3.14: Load step of 2 pu. EMT simulation (“sim”), Frequency Divider model (“FD”), Tie line model (“Tie”)

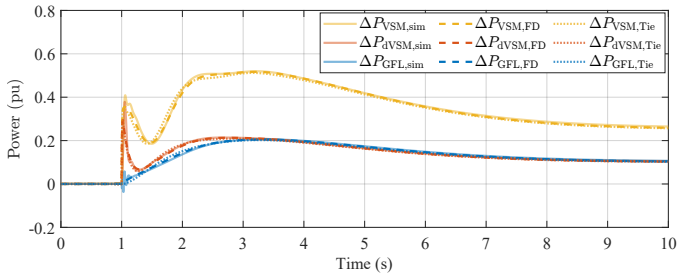

(a) Converter power.

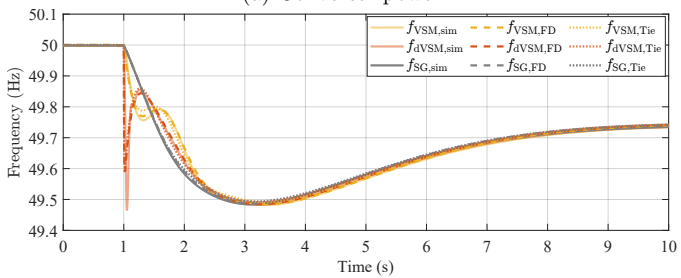

(b) Grid forming converter and synchronous generator frequency.

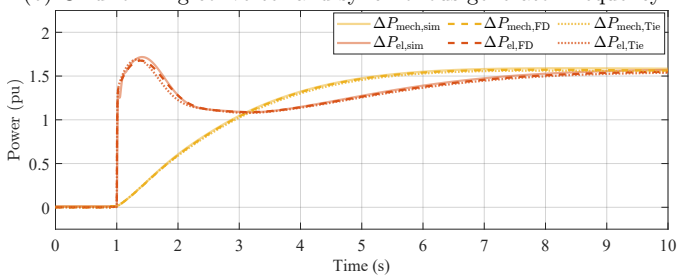

(c) Synchronous generator mechanical and electrical power.

Figure 3.15: Load step of 2 pu with increased SG impedance. EMT simulation (“sim”), Frequency Divider model (“FD”), Tie line model (“Tie”)

4 Model Predictive Control Design

This chapter presents the design of the Model Predictive Control strategies for grid-connected converter systems and for islanded converter-driven power systems. A strategy to make the control system aware of communication delay and loss of control and measurement signal packets is introduced.

4.1 Grid-connected Converter Systems

Converter-based Renewable Energy Sources can support frequency control in a larger power system. This section first presents a grid-connected converter system operating as a Hybrid Renewable Power Plant. An MPC plant controller is designed to provide primary frequency control on the plant level. Finally, the nominal stability of the designed control system is assessed.

4.1.1 Scenario Description

The most widely installed and grid-integrated RES are Photovoltaic and Wind power generation. They commonly operate at their maximum power point, which depends on the momentary insolation and wind speed levels. As a result, they are not freely dispatchable and can provide frequency support only by reducing their power output through curtailment. For effective frequency control and an optimized energy arbitrage, they are often combined with an energy storage, e.g., Battery Energy Storage Systems in [103], [104] or [105]. The additional storage can be placed on the same AC grid connection or, as in [106], on a common DC bus. The correct sizing of the required storage capacity is hereby critical to ensure economic operation of the plant [107]. Another approach for frequency control with RES is the use of flexible loads [108], [109]. In contrast to PV and Wind power, they are dispatchable and can be used for frequency control symmetrically. In [110], for example, MPC has been used to coordinate different loads and batteries of electric vehicles for secondary frequency control on the time scale of minutes.

While flexible loads are often small installations that only have a relevant system effect through aggregation, Hydrogen Electrolyzers are an emerging large load in power systems. ELs aims to economically produce hydrogen and, to this end, must flexibly follow electricity prices. Participation in ancillary service markets provides additional revenue streams for plant operators. With ELs, relatively few plants can have a strong effect on the power system frequency. Therefore, in [111], virtual inertia support from ELs is proposed. However, an

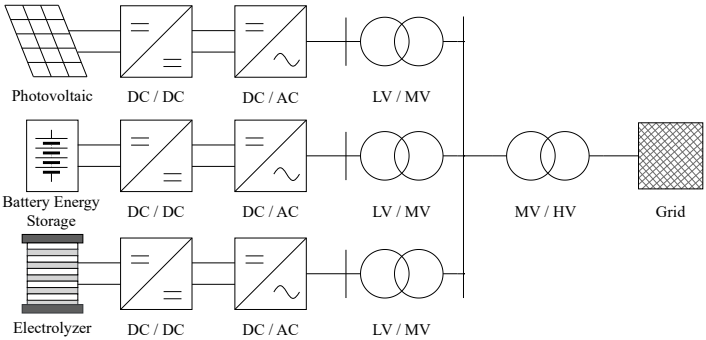

Figure 4.1: Hybrid Renewable Power Plant including a photovoltaic, battery energy storage and electrolyzer system.

electrolysis plant is a complex electrochemical process with additional balance of plant components that have slower actuation than power electronic converters. Stable operation on the plant level can therefore only be guaranteed when power ramp rates are limited to the capability of the supporting processes [112]. The capability of ELs to participate in frequency control is significantly enhanced with additional energy storage. For example, in [113], the dynamic control of ELs with BESS and PV is shown in a DC microgrid. The support of AC grids is also demonstrated in [114] with an EL and a supercapacitor. Most studies combine only two heterogeneous RES. A more complex setup is used, e.g., in [115], where a PV, Wind, BESS and a hydrogen storage system, consisting of an EL and a fuel cell, are controlled on the minute level to smooth the variable power output.

In this thesis, a Hybrid Renewable Power Plant (HRPP), as depicted in Figure 4.1, is considered as the grid-connected converter system. It includes a PV system to represent RES with variable power generation, operating at its maximum power point. An EL, as a freely dispatchable load with a limited power ramping rate, can provide steady-state adjustment of the plant output. Transient power balancing is achieved by a BESS, providing fast accessible energy storage. This HRPP thereby includes three resources with distinct operating characteristics. Furthermore, Grid-Following controlled converters for the PV and EL, and a Grid-Forming converter with VSM control for the BESS represent different converter dynamics.

4.1.2 Control System Design

Grid-connected converter systems can participate in ancillary service markets to support system frequency control. Ancillary services are defined products that system operators procure from plant operators to ensure system stability. The fulfillment of this service is a specified power response of the plant to a grid frequency deviation. Therefore, a plant controller is necessary that coordinates the different resources within the plant. This plant controller tracks the trajectory of the output power reference, defined by the provided ancillary service, and is to be realized with MPC. The ancillary service that the hybrid renewable plant provides in this work is a virtual inertia (2.20) and Fast Frequency Response (2.21), which are critical to ensure frequency stability in modern converter-based power systems.

Tracking of the power output reference is the primary objective of the MPC plant controller. Two additional control objectives are defined. The BESS of the plant provides the necessary energy storage to enable an accurate transient plant response. The energy storage is also used to economically optimize the steady-state operation of the plant. To this end, it is important to minimize the storage usage for frequency control and recover the storage level after an event. This is the second objective of the plant controller. Thirdly, the curtailment of renewable power generation from the PV system should be minimized to ensure the maximum energy yield of the overall plant. For a given total plant power output, these two objectives imply that the BESS has zero power output in steady-state and any additionally available power of the PV is used to produce hydrogen with the EL.

Classical plant control is based on a hierarchical organization of different objectives into separate time scales. This separation is not required with MPC, as all control objectives are part of the same optimal control problem. The ability and performance of the MPC in fulfilling the three control objectives simultaneously is evaluated in Chapter 5.

Figure 4.2 shows the control diagram of the MPC as a plant controller for the HRPP. The Model Predictive Control system consists of a state estimator, a reference trajectory algorithm, which is further described in Section 4.1.3, and the MPC controller. For this plant, the following control inputs and measured outputs are available:

$$u = [\Delta P^*_{\mathrm{PV}}, \Delta P^*_{\mathrm{BESS}}, \Delta P^*_{\mathrm{EL}}], \tag{4.1a}$$

$$y = [\Delta P_{\mathrm{PV}}, \Delta P_{\mathrm{BESS}}, \Delta \omega_{\mathrm{BESS}}, \Delta E_{\mathrm{BESS}}, \Delta P_{\mathrm{EL}}, \Delta P_{\mathrm{Plant}}, \Delta \omega_{\mathrm{Grid}}]. \tag{4.1b}$$

All variables are referred to their nominal steady-state values, indicated by Δ, to remove static offsets from the state-space prediction models. ΔE_{BESS} is the storage level, or SoC, of the BESS. It is calculated as:

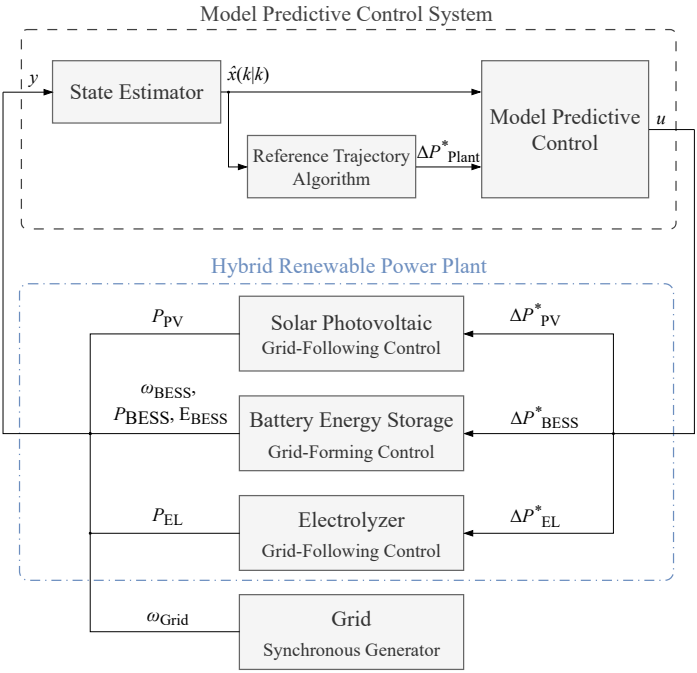

Figure 4.2: Model Predictive Control System for the Grid-connected Hybrid Renewable Power Plant.

$$\Delta \dot{E}_{\text{BESS}} = \frac{1}{E_{\text{cap}}} \Delta P_{\text{BESS}}, \tag{4.2}$$

where E_{cap} is the normalized capacity-to-power ratio measured in time. The plant power output is:

$$\Delta P_{\text{Plant}} = \Delta P_{\text{PV}} + \Delta P_{\text{BESS}} + \Delta P_{\text{EL}}, \tag{4.3}$$

and $\Delta\omega_{\text{Grid}}$ denotes a measurement of the grid frequency at the grid connection point of the plant. The states and disturbance inputs of the plant power and frequency dynamics using the Frequency Divider model are:

$$x = [\Delta P_{\text{PV}}, \Delta P_{\text{BESS}}, \Delta\omega_{\text{BESS}}, \Delta E_{\text{BESS}}, \Delta P_{\text{EL}}, \Delta P_{\text{Grid}}, \Delta\omega_{\text{Grid}}, \Delta P_{\text{mech}}], \tag{4.4a}$$

$$d = \left[\frac{\mathrm{d}}{\mathrm{d}\,t} P_{\text{load,BESS}}, \frac{\mathrm{d}}{\mathrm{d}\,t} P_{\text{load,Grid}}\right], \tag{4.4b}$$

where d corresponds to process noise as explained in Section 3.2.2. For the Tie line model, the following states are used:

$$x = [\Delta P_{\mathrm{PV}}, \Delta\delta_{\mathrm{BESS}}, \Delta\omega_{\mathrm{BESS}}, \Delta E_{\mathrm{BESS}}, \Delta P_{\mathrm{EL}}, \Delta\omega_{\mathrm{Grid}}, \Delta P_{\mathrm{mech}}]. \tag{4.5}$$

It was shown in Section 3.2 that this model becomes unobservable and undetectable if the disturbance inputs $\left[P_{\mathrm{load,BESS}}, P_{\mathrm{load,Grid}}\right]$ are estimated using independent integrator states. Observability can be recovered, if only one additional integrator state is used for all disturbance inputs. In this case, the disturbance input becomes:

$$\begin{bmatrix} P_{\mathrm{load,BESS}} \\ P_{\mathrm{load,Grid}} \end{bmatrix} = \underbrace{\begin{bmatrix} 0.5 \\ 0.5 \end{bmatrix}}_{B_{\mathrm{d}}} \underbrace{P_{\mathrm{load,sys}}}_{d}. \tag{4.6}$$

This simplification can be justified by the fact that even a single load disturbance has an effect on all voltage sources in the system. The numerical entries in B_{d} distribute the total system load disturbance among the voltage source components and should summate to one. This simplification implicitly assumes that the location of a load disturbance is known, since the share of the initial load increase is determined by the electrical distance, as it was shown in Section 3.4. In reality, the location (and magnitude) of a load disturbance, can not be known a priori. It is therefore expected that MPC using the Tie line prediction model is less robust and more sensitive to unknown load disturbances than MPC using the Frequency Divider model.

The external grid is modeled as an equivalent synchronous generator with turbine-governor control. From this grid model no detailed measurements are available, only the frequency at the grid connection point is measurable for the plant control system and assumed to reflect the internal frequency of the equivalent synchronous generator. The state-space model matrices for the Frequency Divider and Tie line prediction models are constructed from the equations given in Section 3.3, respectively.

Given the control objectives and prediction model, the MPC parameters can be chosen. The optimal control problem takes the form:

$$\min_{\Delta u(\cdot|k)} \sum_{n=1}^{H_{\mathrm{p}}} \|y(k+n|k) - r(k+n|k)\|_Q^2 + \sum_{n=0}^{H_{\mathrm{u}}-1} \|\Delta u(k+n|k)\|_R^2 \tag{4.7a}$$

$$\text{s.t.} \quad x(k+n|k) = A_{\mathrm{k}} x(k+n-1|k) + B_{\mathrm{k}} u(k+n-1|k), \tag{4.7b}$$

$$y(k+n-1|k) = C_{\mathrm{k}} x(k+n-1|k), \tag{4.7c}$$

$$\Delta P_{i,\min}^* \leq \Delta P_i^*(k+n|k) \leq \Delta P_{i,\max}^*, \tag{4.7d}$$

$$\Delta P_{i,\min} \leq \Delta P_i(k+n|k) \leq \Delta P_{i,\max}, \tag{4.7e}$$

Variable	Weight	Set point [pu]	Minimum [pu]	Maximum [pu]	Rate limit [pu/sec]
P_{PV}	0.1	1	0	1	-
P_{BESS}	0	0	-1	1	-
E_{BESS}	5	0.5	0	1	-
P_{EL}	0	-0.5	-1	-0.2	± 0.2
P_{Plant}	7	0.5	-	-	-

Table 4.1: Parameters of the optimal control problem for the grid-connected Hybrid Renewable Power Plant.

$$\Delta E_{i,\min} \leq \Delta E_i(k+n|k) \leq \Delta E_{i,\max}, \tag{4.7f}$$

$$dP_{i,\min} \leq dP_i(k+n|k) \leq dP_{i,\max}, \tag{4.7g}$$

$$n \in \{1, ..., H_{\mathrm{p}}\}, \quad i \in \{\mathrm{PV}, \mathrm{BESS}, \mathrm{EL}\},$$

where (4.7a) is the objective function introduced in (2.6), and (4.7b), (4.7c) is the discretized and augmented prediction model. The control inputs are hard constrained by (4.7d), whereas the output constraints (4.7e), (4.7f) and (4.7g) are softened by slack variables, which are not shown here. The notation $dP_i(k+n|k) = \Delta P_i(k+n|k) - \Delta P_i(k+n-1|k)$ describes rate constraints, and the subscript 'min' or 'max' indicate the maximum and minimum bound on the corresponding variable.

The choice of the prediction horizon, as a result of the MPC sample time T_{s} and prediction horizon steps H_{p}, calculated as $T_{\mathrm{s}} \cdot H_{\mathrm{p}}$, has an important impact on the closed-loop control performance. If the prediction horizon is too short, the shifted horizon at the next iteration includes a significant part of the systems transient. This affects the computation of the optimal control trajectory. Reaching a set-point should therefore occur within the prediction horizon. Hence, the horizon must be selected to ensure that $T_{\mathrm{s}} \cdot H_{\mathrm{p}}$ covers the open-loop transient of the system. In this case, the optimal trajectory in k+1 stays on the tail of the trajectory in k, which corresponds to the Bellman principle of optimality, and a similar performance to the infinite horizon controller can be achieved [7]. Based on the simulation results in Section 3.4, a $3s$ horizon covers the response to set point changes and the relevant disturbance dynamics. A sampling time of $T_{\mathrm{s}} = 100$ ms provides good control performance, resulting in $H_{\mathrm{p}} = 30$. The control horizon can be smaller and is chosen as $H_{\mathrm{u}} = 10$.

Table 4.1 summarizes the output weights and constraints of the optimization problem. For readability, all variables are expressed in their absolute term and the steady-state set point is given. The weights in Table 4.1 correspond to diagonal entries in the output weighting matrix Q in (4.7a), which is zero otherwise. They

are chosen according to the control objectives defined in the beginning of this section. Tracking of the plant power output has the highest weight, while the control of the energy storage level and PV output have a smaller weight. Since all values in the prediction models are in per unit and therefore normalized, the relative weight of each control objective can be given without any further scaling. The weighting matrix R of the rate of change of the control inputs in (4.7a) penalizes large control actions and ensures a damped controller response. A weight of 1 is given to all control inputs on the diagonal of R. The outputs $\Delta\omega_{\text{BESS}}$ and $\Delta\omega_{\text{Grid}}$ have a weight of 0 and no constraints, and are therefore not listed in the table. They are not controlled by the MPC, and are only used by the state estimator.

The minimum and maximum constraints in Table 4.1 represent the operational limitations of the plants RES. The PV system operates at its current maximum power point, which is chosen as 1 pu for simplicity. The constraints allow a reduction of the PV power output down to zero. The BESS can charge and discharge with full rated power, while its SoC must remain between 0% and 100%. The EL has a negative power output because it is a controllable load. ELs have a minimal operating point that must be maintained for stable operation, which is chosen here as -0.2 pu. Additionally, the EL has a power ramp limitation. While power ramping rates of 0.1 pu/sec are commercially available today [116], an increase of ramping capability up to 1 pu/sec is considered realistic in the future [117], [118]. The impact of different power ramping rates of the EL on the plant performance will be evaluated in Chapter 5. A standard value of 0.2 pu/sec is assumed in the design. The steady-state operating point for the BESS and EL are chosen to allow upwards and downwards control. In addition to the output constraints, the control inputs are constrained in (4.7d) to the same values as the output powers in Table 4.1, since converter control systems typically do not accept set points outside the rated power.

4.1.3 Reference Trajectory Algorithm

MPC can include future changes of the output references into the optimization problem through the calculation of the tracking error in (2.5). This feature enables the MPC to adjust control actions proactively, instead of reactively, improving transient performance, disturbance rejection and constraint satisfaction. It is a key advantage of MPC over classical feedback-based control strategies.

The primary control objective of the MPC plant controller is to control the output power of the HRPP and provide virtual inertia and FFR. The trajectory of these time-varying responses can be anticipated to determine a reference trajectory for the MPC. To this end, a reference model of the plant response that the MPC has to track is necessary. Figure 4.3 presents the reference trajectory model that is used to generate the plants power reference trajectory. It models an equivalent grid with a system inertia, a governor control and FFR feedback

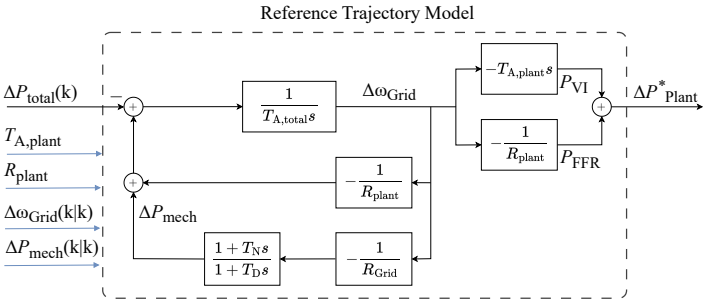

Figure 4.3: Model to generate the plant reference trajectory.

control. The plant response must be represented as an ideal virtual inertia and FFR response. Since the plants response has an impact on the grid frequency, a closed-loop model of the grid and plant is necessary to anticipate the trajectory accurately. The model is implemented in state-space form as:

$$\begin{bmatrix} \Delta\dot{\omega}_{\text{Grid}} \\ \Delta\dot{P}_{\text{mech}} \end{bmatrix} = \begin{bmatrix} -\frac{1}{R_{\text{plant}} T_{\text{A,total}}} & \frac{1}{T_{\text{A,total}}} \\ \frac{1}{T_{\text{D}} R_{\text{Grid}}} \left(\frac{T_{\text{N}}}{R_{\text{plant}} T_{\text{A,total}}} - 1 \right) & -\frac{1}{T_{\text{D}}} \left(1 + \frac{T_{\text{N}}}{R_{\text{Grid}} T_{\text{A,Grid}}} \right) \end{bmatrix} \begin{bmatrix} \Delta\omega_{\text{Grid}} \\ \Delta P_{\text{mech}} \end{bmatrix} + \begin{bmatrix} -\frac{1}{T_{\text{A,total}}} \\ \frac{T_{\text{N}}}{R_{\text{Grid}} T_{\text{A,total}} T_{\text{D}}} \end{bmatrix} \Delta P_{\text{total}}, \tag{4.8a}$$

$$\Delta P^{*}_{\text{Plant}} = \begin{bmatrix} \left(\frac{T_{\text{A,plant}}}{T_{\text{A,total}} R_{\text{plant}}} - \frac{1}{R_{\text{plant}}} \right) & -\frac{T_{\text{A,plant}}}{T_{\text{A,total}}} \end{bmatrix} \begin{bmatrix} \Delta\omega_{\text{Grid}} \\ \Delta P_{\text{mech}} \end{bmatrix} + \frac{T_{\text{A,plant}}}{T_{\text{A,total}}} \Delta P_{\text{total}} \tag{4.8b}$$

This model is a lumped inertia representation of the overall power system if the plant is controlled ideally. The total system inertia is: $T_{\text{A,total}} = T_{\text{A,Grid}} + T_{\text{A,plant}}$. The plant provides virtual inertia characterized by $T_{\text{A,plant}}$ (2.20) and FFR according to R_{plant} (2.21), which are input parameters to the model. The inertia and droop constants ($T_{\text{A,Grid}}$ and R_{Grid} respectively) of the grid model must be normalized to the same rated power as the plant. The initial states $\Delta\omega_{\text{Grid}}(k|k)$ and $\Delta P_{\text{mech}}(k|k)$ are obtained from the state estimator as shown in Figure 4.2. Input to the model is the current total power deviation in the system, calculated from the estimated states as $\Delta P_{\text{total}}(k) = \Delta P_{\text{Grid}}(k|k) + \sum_i \Delta P_{i,0}(k|k)$ for the Frequency Divider model, and $\Delta P_{\text{total}}(k) = P_{\text{load,sys}}(k|k)$ in the Tie line model.

In each iteration of the MPC, the model (4.8) is executed over the prediction horizon to generate a reference trajectory:

$$r(\cdot\,|k) = \Delta P^{*}_{\text{Plant}}(\cdot\,|k) = P_{\text{VI}}(\cdot\,|k) + P_{\text{FFR}}(\cdot\,|k) \tag{4.9}$$

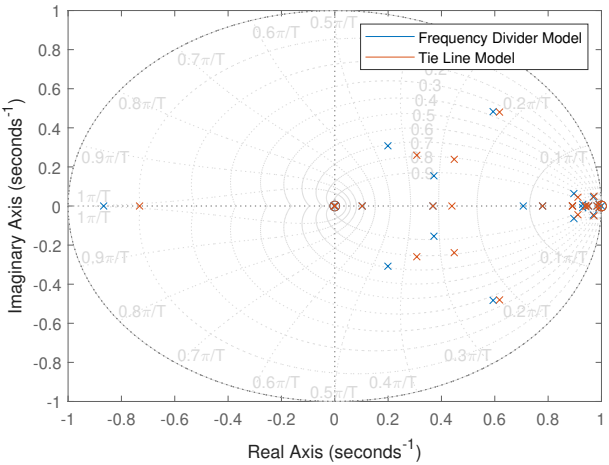

Figure 4.4: Pole-zero plot of the unconstrained MPC for the grid-connected converter system.

4.1.4 Nominal Stability

A first verification of the MPC design is to check the nominal stability. Nominal stability is assessed under the following assumptions:

1. The prediction model is exact.
2. No constraints are active.
3. There is a static reference.

When no constraints are active, the MPC can be transformed into its equivalent state-space representation. In this case, the closed-loop control system can be calculated as a linear discrete-time system, for which stability can be assessed via its poles. Figure 4.4, shows the pole-zero plot of the unconstrained control loop for the MPC using the Frequency Divider model and the Tie line model. Both MPCs are nominally stable, with all poles being on or inside the unit circle. The poles show slightly different damping characteristics, nonetheless the control loop is nominally stable.

Here, the prediction model exactly corresponds to the plant model used in the analysis. In the evaluation in Chapter 5, the impact of and robustness to model-plant mismatch will be assessed under constrained operation of the plant.

Also, the reference trajectory algorithm of Section 4.1.3 is not included in the calculation for Figure 4.4, and a static reference is assumed. During simulation, a time-varying reference will be given to the MPC.

4.2 Islanded Converter-driven Power Systems

The most extreme case of a renewable power system is a purely converter-driven system that includes no physical inertia from SGs. While large-scale interconnected power systems will most likely always include some form of physically rotating inertia, e.g., from hydropower, purely converter-driven systems are more common in smaller islanded systems, often called microgrids. These islanded converter-driven power systems require fast control actions and optimal resource usage to guarantee a stable operation. In this section, a supervisory MPC control system for islanded converter-driven power systems, acting as a fast secondary controller, is designed.

4.2.1 Scenario Description

As the primary converter-based RES, a GFL PV system, a GFM BESS and GFL EL are used to represent diverse RES types as introduced in Section 4.1.1. The scenario is extended by including an additional BESS 2 with an alternative GFM method, namely the decoupled VSM introduced in Section 3.3, and a second PV system to provide power generation.

The RES are placed in the CIGRE MV benchmark system in the European configuration, which is disconnected from the main power system. The CIGRE MV benchmark system was introduced in [119] to represent a European medium voltage system for studies of renewable energy integration. The topology of this system is shown in Figure 4.5. It includes 13 buses and the rated voltage is 20 kV. In contrast to the description in [119], bus 1 and 12 are combined into a single bus to close the radial feeders into a ring topology, and the bus numbering is adjusted accordingly. This modification is presented as a variant of the system in [119], where further system data is given.

BESS 1 and BESS 2 are connected to buses 3 and 1, whereas the PV systems are placed at buses 1 and 10, and the EL at bus 7, respectively. The topology of the system can be altered through three switches (S1, S2 and S3). In the nominal case, S1 and S2 are closed, forming a topology with two rings. S3 is always open, leaving a radial feeder. The loads are a combination of residential and commercial load with different power factors, as given in [119]. The original load at bus 1 represents the loading of additional feeders and is reduced, such that the total system load is 7.5 MW. The two PV system generate a total of 20 MW at 1 pu each. The EL consumes 5 MW, while BESS 2 is scheduled to charge with 7.5 MW. The EL and BESS 2 provide steady-state flexibility for the system, while BESS 1 is scheduled to maintain a fixed SoC level, and can only support during transient events.

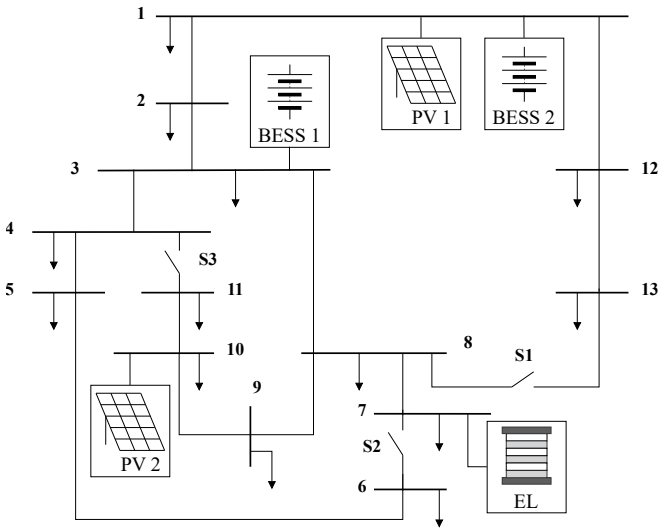

Figure 4.5: Topology of the CIGRE MV benchmark system in islanded mode with Renewable Energy Sources.

4.2.2 Control System Design

In an islanded converter-driven system, the MPC is responsible for system frequency stability and optimal allocation of power among the available units. It therefore operates as a fast secondary controller. The primary control objective is to keep the frequency stable. Hence, the MPC must reject disturbances from the static frequency reference. As in the grid-connected case, the secondary and tertiary control objectives are to maintain energy storage levels at reference and generate the maximum renewable power, i.e., minimize PV curtailment.

Figure 4.6 shows the control diagram of the islanded converter-driven power system. The system has the following control inputs and measured outputs:

$$u = [\Delta P^*_{\mathrm{PV1}}, \Delta P^*_{\mathrm{PV2}}, \Delta P^*_{\mathrm{BESS1}}, \Delta P^*_{\mathrm{BESS2}}, \Delta P^*_{\mathrm{EL}}], \tag{4.10a}$$

$$y = [\Delta P_{\mathrm{PV1}}, \Delta P_{\mathrm{PV2}}, \Delta P_{\mathrm{BESS1}}, \Delta \omega_{\mathrm{BESS1}}, \Delta E_{\mathrm{BESS1}}, \Delta P_{\mathrm{BESS2}}, \Delta \omega_{\mathrm{BESS2}}, \Delta E_{\mathrm{BESS2}}, \Delta P_{\mathrm{EL}}]. \tag{4.10b}$$

The states and disturbance inputs of the systems power and frequency dynamics in the Frequency Divider model are:

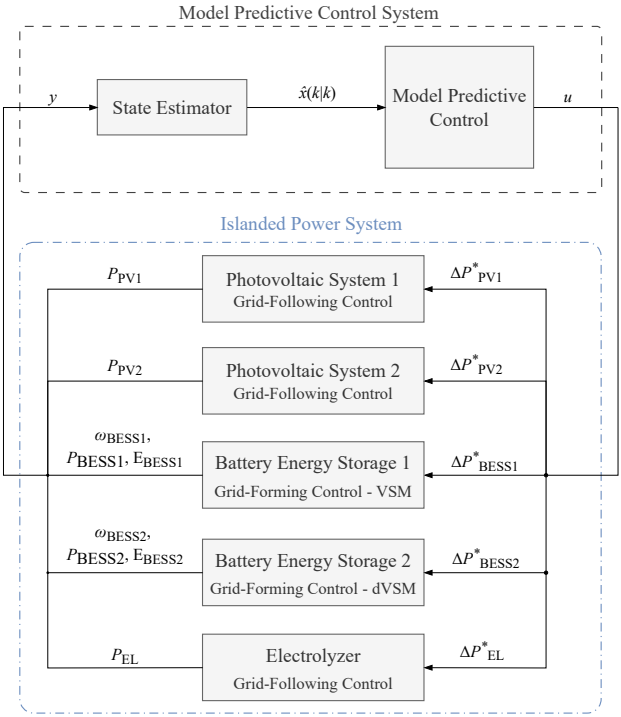

Figure 4.6: Model Predictive Control System for the islanded converter-driven power system.

$$x = [\ \Delta P_{\mathrm{PV1}}, \Delta P_{\mathrm{PV2}}, \Delta P_{\mathrm{BESS1}}, \Delta\omega_{\mathrm{BESS1}}, \Delta E_{\mathrm{BESS1}}, \Delta P_{\mathrm{BESS2}}, \Delta\omega_{\mathrm{BESS2}}, \Delta E_{\mathrm{BESS2}}, \Delta P_{\mathrm{EL}}], \tag{4.11a}$$

$$d = \left[\frac{\mathrm{d}}{\mathrm{d}\,t} P_{\mathrm{load,BESS1}}, \frac{\mathrm{d}}{\mathrm{d}\,t} P_{\mathrm{load,BESS2}}\right], \tag{4.11b}$$

where d represents process noise. For the Tie line model, the following states are used:

$$x = [\Delta P_{\mathrm{PV1}}, \Delta P_{\mathrm{PV2}}, \Delta\delta_{\mathrm{BESS1\text{-}2}}, \Delta\omega_{\mathrm{BESS1}}, \Delta E_{\mathrm{BESS1}}, \Delta\omega_{\mathrm{BESS2}}, \Delta E_{\mathrm{BESS2}}, \Delta P_{\mathrm{EL}}]. \tag{4.12}$$

Variable	Weight	Set point [pu]	Minimum [pu]	Maximum [pu]	Rate limit [pu/sec]
P_{PV1}, P_{PV2}	0.2	1	0	1	-
$\omega_{\text{BESS1}}, \omega_{\text{BESS2}}$	5	1	-	-	-
P_{BESS1}	0	0	-1	1	-
E_{BESS1}	3	0.5	0	1	-
P_{BESS2}	0.1	-0.75	-1	1	-
E_{BESS2}	0	0.5	0	1	-
P_{EL}	0.1	-0.5	-1	-0.2	± 0.2

Table 4.2: Parameters of the optimal control problem for the islanded converter-driven power system.

Similar to the grid-connected case, observability of this system is given only if a single disturbance state is used to estimate the load. The disturbance is therefore defined as:

$$\begin{bmatrix} P_{\text{load,BESS1}} \\ P_{\text{load,BESS2}} \end{bmatrix} = \underbrace{\begin{bmatrix} 0.5 \\ 0.5 \end{bmatrix}}_{B_{\text{d}}} \underbrace{P_{\text{load,sys}}}_{d}. \tag{4.13}$$

The optimal control problem takes the same form as (4.7). Table 4.2 summarizes the output variable weights and limitations. Because the primary objective of the MPC is to keep the system frequency stable, the GFM frequencies have the highest weight in the control problem. The energy storage levels of BESS 1 is to be controlled as the second priority to minimize energy storage deviations. The energy storage level has an additional terminal weight of 500 at the last step of the prediction horizon. The effect of the terminal weight is discussed in Chapter 5. Thirdly, the power output of the PV should be tracked at its maximum with a lower weight. The power output of EL and BESS 2 has the smallest weight, as it should be primarily used for steady-state adjustments. In contrast to the grid-connected case, the weight is non zero to incentivize the MPC to share the loading changes equally between these two RES. The set points are chosen according to the loading scenario described previously. Minimum and maximum constraints of the outputs are equal to the grid-connected case.

The open-loop dynamics of the islanded purely converter-driven system are significantly faster than the grid-connected system, and transients settle in < 1 second, due to the absence of physically rotating inertia. The prediction horizon could therefore be set shorter, however, since the EL is ramp limited between, a horizon that is too short prevents the MPC from effectively using the EL. For

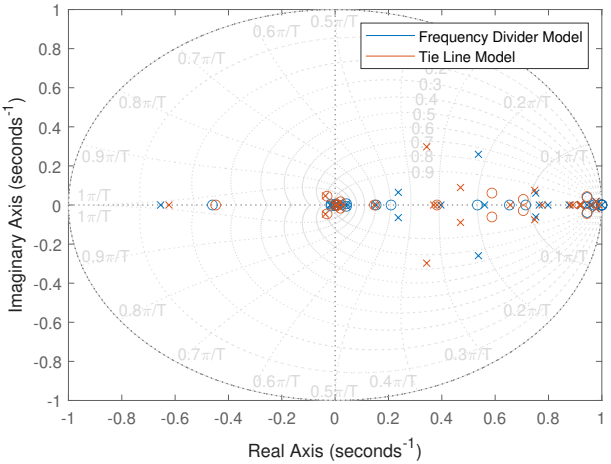

Figure 4.7: Pole-zero plot of the unconstrained MPC for the islanded converter-driven system.

this reason, the prediction horizon is chosen with the same length of 3 sec as in the grid-connected case, i.e., $T_s = 100$ ms and $H_p = 30$. The control horizon can be reduced to $H_c = 4$ without loss of performance due to the faster system dynamics.

4.2.3 Nominal Stability

Nominal stability of the MPC designed for the islanded converter-driven power system is assessed with the pole-zero plot in Figure 4.7. The MPC is nominally stable using the Frequency Divider model and the Tie line model with comparable eigenvalues. The plot assumes an exact representation of the system with the prediction model and that no constraints are active.

4.3 Communication Delay and Loss

Control of multiple converter-based RES requires communication systems to transmit measurement and control signals. The associated time delays and missing information from possible packet loss can critically affect the performance of the controller. The physical distance between the controller and the RES, as well as the available communication infrastructure determine the delay and loss probability, which can vary for different RES. For example, the communication

delay between the controller and RES 1 might be 50 ms, while the delay to RES 2 is 120 ms because of a longer communication distance and slower signal processing of RES 2. In this section, a strategy for a delay- and loss-aware MPC that minimizes these negative effects is presented. It is assumed that the delay is measurable through time-stamped packets and acknowledgements. In this context, delay and losses have a different effect on the measurement and actuator path of the control loop, and are accounted for separately. Delays from computation and signal processing are dealt with in a similar way, and can be added to the actuator delay.

4.3.1 Measurement delay and signal loss

For execution of the MPC, a full initial state vector is required. Each RES i sends its measurement $y_{i,k}$ with a fixed measurement interval at time k, where the transmission is subject to individually variable delay. As a result, the current measurements are not available at the execution time of the MPC. Thus, the current state must be estimated from previous measurements, and measurement values from RES with small delay have to be fused with measurements that have a larger delay. To this end, different Kalman filter-based approaches have been proposed in literature that carry out state estimation with random sensor delays and missing measurements or packet loss [120], [121]. The approach presented in [121], which combines a Kalman filter with a memory buffer storing the received measurement packets, is adopted and modified for the control scenario in this thesis. The Kalman filter with a buffer compensates for delayed and lost packets on the measurement path of the closed-loop networked control system.

Consider a buffer of $M \times N$ fields, where M is the number of RES and N is determined based on the maximum admissible delay $\tau_{\max}$ as:

$$N = \frac{\tau_{\max}}{T_{\mathrm{s}}^{\mathrm{K}}} \cdot r \in \mathbb{N}. \tag{4.14}$$

The sampling time of the Kalman filter is $T_{\mathrm{s}}^{\mathrm{K}}$, and r describes the ratio of measurement samples per Kalman filter execution. For example, if the Kalman filter is executed every 100 ms, and measurements are sent every 10 ms, $r = 10$. Measurements that are older than $t - \tau_{\max}$ are discarded from the estimation. Each buffer field consists of the measurement $y_{i,k}$ and an arrival variable $\upsilon_{i,k}$. which is defined as:

$$\upsilon_{i,k} = \begin{cases} 1 & \text{if } y_{i,k} \text{ arrived before or at time } t,\ t \geq k \\ 0 & \text{otherwise.} \end{cases} \tag{4.15}$$

Before a measurement $y_{i,k}$ has arrived, the buffer contains zero values. Through $\upsilon_{i,k}$, the Kalman filter distinguishes between real zeros and missing information. The buffer follows the moving horizon strategy of the MPC and stores values

Algorithm 4.1: Kalman filter with a buffer. The filter iterates through horizon N, performing prediction steps. Correction steps are only applied when measurements arrived (indicated by Υ_k).

Require: $\mathcal{Y}_k, \Upsilon_k, \mathcal{U}_k, \hat{x}_{r|k-1}, P_{r|k-1}, A_\mathrm{d}, B_\mathrm{d}, C_\mathrm{d}$

$\hat{x}_{0|k} \leftarrow \hat{x}_{r|k-1}$

$P_{0|k} \leftarrow P_{r|k-1}$

for $j = 1, 2, ..., N$ **do**

$\hat{x}^-_{j|k} = A_\mathrm{d}\hat{x}_{j-1|k} + B_\mathrm{d}\mathcal{U}_{j|k}$

$P^-_{j|k} = A_\mathrm{d}P_{j-1|k}A_\mathrm{d}^\mathrm{T} + Q_\mathrm{KF}$

$K_j = P^-_{j|k}C_\mathrm{d}^\mathrm{T}\left(C_\mathrm{d}P^-_{j|k}C_\mathrm{d}^\mathrm{T} + R_\mathrm{KF}\right)^{-1}$

$\hat{x}_{j|k} = \hat{x}^-_{j|k} + \Upsilon^\mathrm{T}_{j|k}K_j\left(\mathcal{Y}_{j|k} - C_\mathrm{d}\hat{x}^-_{j|k}\right)$

$P_{j|k} = \left(I - \Upsilon^\mathrm{T}_{j|k}K_jC_\mathrm{d}\right)P^-_{j|k}$

if $j = r$ **then**

$\hat{x}_{r|k} \leftarrow \hat{x}_{j|k}$

$P_{r|k} \leftarrow P_{j|k}$

end if

end for

return $\hat{x}_{N|k}$

from $t - \tau_\mathrm{max}$ to present time t. The correct ordering and entering in the buffer is ensured through time-stamping of the communication packets. To this end, accuracy in the range of 1 ms is sufficient, which can be achieved by GPS, among other sources [122]. The packet delay is $\tau_{i,k} = t_\mathrm{rx} - t_\mathrm{tx}$, where t_tx is the sending and t_rx the receiving time. The delay of each communication channel, i.e. to RES 1, RES 2, etc., is estimated as $\hat{\tau}_i$ by averaging the values of $\tau_{i,k}$ over the moving horizon N.

Besides the measurements, the Kalman filter requires the control inputs $u_{i,k}$ from the MPC, which must be stored and aligned with the measurements according to their arrival time. To this end, packets with control inputs $u_{i,k}$ have an identification number (*id*), and the RES return acknowledgments of the control signals with each measurement packet.

In each execution, the Kalman filter conducts multiple prediction and correction steps by iterating through the moving horizon N, as specified in Algorithm 4.1, and provides the estimated state $\hat{x}_{t,k}$ to the MPC. Matrices of appropriate size represent the buffered measurements ($\mathcal{Y}_k$), arrival variables (Υ_k), and control inputs ($\mathcal{U}_k$). P, Q_KF and R_KF denote the covariance matrices

of the Kalman filter. The arrival variables in Υ_k disable the correction step for measurements that have not arrived yet. For one iteration, only a subset of measurements could have arrived. Therefore, $\Upsilon_{j|k}$ consists of both ones and zeros to include all available measurement data in the estimation of the current state.

4.3.2 Actuator delay and signal loss

Compensation of delays and signal loss is carried out in two separate steps for the actuator path from the MPC to the RES. First, the prediction model of the MPC is augmented to make the prediction aware of the actuator delay. To this end, the actuator delay τ_a is defined as [82]:

$$\tau_\mathrm{a} = (\gamma - 1)T_\mathrm{s} + \tau_\mathrm{a}', \tag{4.16}$$

where γ is an integer denoting the multiple of the sampling time T_s. The fractional of the total actuator delay is τ_a'. Consider the discretized state-space system as:

$$x((k+1)T_\mathrm{s}) = \Phi(T_\mathrm{s})x(kT_\mathrm{s}) + \Gamma(T_\mathrm{s})u(kT_\mathrm{s}), \tag{4.17}$$

where $\Phi(t) = e^{At}$ and $\Gamma(t) = \int_0^\mathrm{T} e^{As} B \,\mathrm{d}\, s$. If the control signal $u(kT_\mathrm{s})$ is delayed by τ_a, the system becomes [82]:

$$\begin{aligned} x((k+1)T_\mathrm{s}) = \Phi(T_\mathrm{s})x(kT_\mathrm{s}) + \Phi(T_\mathrm{s} - \tau_\mathrm{a}')\Gamma(\tau_\mathrm{a}')u((k-\gamma)T_\mathrm{s}) \\ + \Gamma(T_\mathrm{s} - \tau_{\mathrm{a}'})u((k-\gamma+1)T_\mathrm{s}). \end{aligned} \tag{4.18}$$

The following state-space representation is obtained if $\tau_\mathrm{a} \leq T_\mathrm{s}$ and consequently $\gamma = 1$:

$$\begin{bmatrix} x(k+1) \\ u(k) \end{bmatrix} = \begin{bmatrix} \Phi(T_\mathrm{s}) & \Phi(T_\mathrm{s} - \tau_\mathrm{a}')\Gamma(\tau_\mathrm{a}') \\ 0 & 0 \end{bmatrix} \begin{bmatrix} x(k) \\ u(k-1) \end{bmatrix} + \begin{bmatrix} \Gamma(T_\mathrm{s} - \tau_\mathrm{a}') \\ I \end{bmatrix} u(k), \tag{4.19}$$

and for $\tau_\mathrm{a} > T_\mathrm{s}$, the system is formulated as:

$$\begin{bmatrix} x(k+1) \\ u(k-(\gamma-1)) \\ \vdots \\ u(k-1) \\ u(k) \end{bmatrix} = \begin{bmatrix} \Phi(T_\mathrm{s}) & \Phi(T_\mathrm{s}-\tau_\mathrm{a}')\Gamma(\tau_\mathrm{a}') & \Gamma(T_\mathrm{s}-\tau_\mathrm{a}') & \dots & 0 \\ 0 & 0 & I & \dots & 0 \\ \vdots & \vdots & \vdots & \ddots & \vdots \\ 0 & 0 & 0 & \dots & I \\ 0 & 0 & 0 & \dots & 0 \end{bmatrix} \begin{bmatrix} x(k) \\ u(k-\gamma) \\ \vdots \\ u(k-2) \\ u(k-1) \end{bmatrix} + \begin{bmatrix} 0 \\ 0 \\ \vdots \\ 0 \\ I \end{bmatrix} u(k), \tag{4.20}$$

In (4.19) and (4.20), T_s is omitted from the arguments of $x(\cdot)$ and $u(\cdot)$ for readability. Actuator delays can be incorporated into the prediction model during the discretization by applying the above definitions. The system state is augmented with the delayed control inputs and the system matrices expanded as shown. To this end, an estimate $\hat{\tau}_i$ of the actuator delay $\tau_{\mathrm{a},i}$ must be available, which is obtained from the Kalman filter buffer by averaging the delay of the received measurements over the moving horizon to provide a "best guess" of the next actuator delay. The discretization is carried out online during every MPC execution, hence making the controller adaptive to time-varying communication

Algorithm 4.2: Algorithm to compensate packet loss on the actuator path from the MPC to the RES.

Require: $u_{i,k}, u_{i,k-1}, id_k, id_{k-1}, t_{\text{next}}, t$
  if $id_k > id_{k-1}$ **then**
    $u_i \leftarrow u_{i,k}(1)$
    $t_{\text{next}} = t + T_{\text{s}}$
  else if $t \geq t_{\text{next}}$ **then**
    $it = \left\lfloor 1 + \left(t + \frac{t_{\text{next}}}{T_{\text{s}}} \right) \right\rfloor$
    $u_i \leftarrow u_{i,k-1}(it)$
    $u_{i,k} \leftarrow u_{i,k-1}$
    $id_k \leftarrow id_{k-1}$
  else if $t < t_{\text{next}}$ **then**
    $u_i \leftarrow u_{i,k}(i)$
  end if return u_i

delays. Individual delays for each control input u_i are modelled by selecting the respective rows and columns of $\Phi(t)$ and $\Gamma(t)$, and the expected computational delay is added to $\hat{\tau}_i$.

While the probabilistic loss of control signals can not be predicted for an individual packet, a unique feature of MPC can be leveraged in this context. MPC computes the control inputs over the whole control horizon $u_{i,k} = [u(k|k), ..., u(k + H_{\text{u}} - 1|k)]^{\text{T}}$, but commonly applies only the first value $u(k|k)$. Instead, the full trajectory $u_{i,k}$ is send to the RES in this strategy, and an actuator algorithm determines the applied control input. Upon arrival of a new packet, the control input is immediately applied. However, if no new input arrives at time $t + T_{\text{s}}$, the next control input of the last received control trajectory is used. This is iteratively repeated until the end of the control horizon H_{u}, where the last value is held. The actuator logic is formulated in Algorithm 4.2. This technique is uniquely applicable with MPC, leveraging the predictive nature of the controller and the explicit optimization over a horizon. It allows the RES to follow an optimized control input trajectory if communication delay suddenly increases or packets are lost.

4.3.3 Overview of the networked control system

Figure 4.8 provides an overview of the delay- and loss-aware MPC strategy, and the resulting closed-loop networked control system. The delay-aware MPC sends

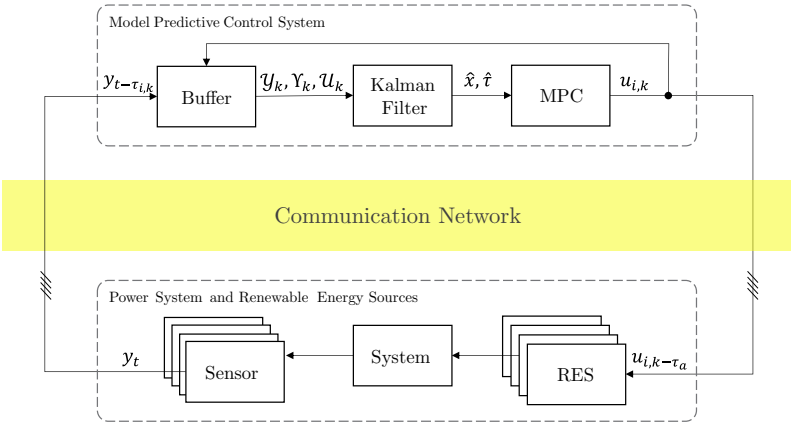

Figure 4.8: Closed-loop control system with the delay- and loss-aware Model Predictive Control Strategy.

the full optimized control trajectory $u_{i,k}$ to the RES through a communication network in time-stamped packets, subjecting the control signal to delay and packet loss. The RES receives the packets and employs Algorithm 4.2 to apply the control inputs, i.e. the power set-points. Measurements of the RES are send in time-stamped packets, including an acknowledgement of the previous received control input packet. The control system stores the measurements and control inputs in the moving horizon buffer in the correct order, identified via the time-stamps and acknowledgements. The Kalman filter employs Algorithm 4.1 to provide the state estimate $\hat{x}$ and an estimate of the delay of each communication channel $\hat{\tau}$ for augmentation of the prediction model, as shown in (4.20).

5 Evaluation

The developed MPCs are evaluated through time-domain simulations under nominal conditions, and under parametric and structural uncertainty in HiL experiments. The strategy that makes MPC aware of communication delays and signal loss is tested in a co-simulation of a network and a power system simulator. The MPCs are benchmarked against conventional control strategies.

5.1 Grid-connected Converter Systems

In this section, the performance and robustness of MPC using the Frequency Divider model and the Tie line model to control the Hybrid Renewable Power Plant, introduced in Section 4.1, are evaluated.

5.1.1 Controller Benchmark and Performance Indices

The HRPP provides a virtual inertia and FFR to the power system. In literature, plant-level frequency control coordination is based on the choice of local control parameters [123], [124], PI control [125], [126] or OPF algorithms [127], [128]. The OPF-based approaches mimic an MPC strategy by carrying out an optimization using a receding horizon approach. However, they apply a steady-state system model and have a high computational burden. As a result they are limited in bandwidth and approximate the desired output trajectory only in discrete steps (c.f. the results in [127]), therefore they are methodologically inferior to an MPC for dynamic plant control. As controller benchmark, a decentralized parametrization of the primary converter controllers (GFM and GFL converters) and a PI-based plant controller are implemented.

For the decentralized parametrization, the inertia coefficient of the BESS and the droop gains must be adjusted. The HRPP should provide virtual inertia with a time constant of $T_{\mathrm{A,plant}} = 25\,\mathrm{sec}$ and FFR with a droop constant of $R_{\mathrm{p,plant}} = 0.05$. Each RES in the HRPP in Figure 4.1 is rated at 10 MW = 1 pu and the plant has a total rating of 30 MW. The GFM BESS is the only unit that can provide virtual inertia inherently. Therefore the inertia constant is set to

$$T_{\mathrm{A,BESS}} = 3 \times 25\,\mathrm{sec} = 75\,\mathrm{sec}\,. \tag{5.1}$$

The energy storage level is only stable after a load disturbance if the BESS does not participate in the steady-state FFR. Therefore, the decoupled VSM method (Figure 3.7) is used as GFM strategy and the droop feedback path is disabled. The PV can only participate in FFR for overfrequency events, because of its

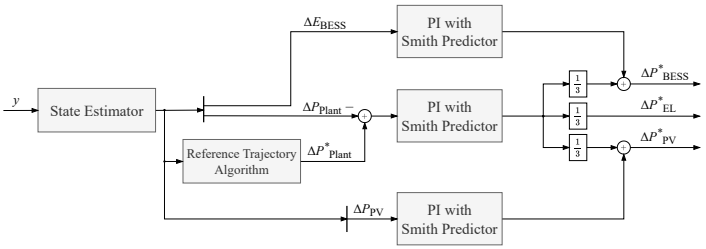

Figure 5.1: PI-based plant control system for the grid-connected Hybrid Renewable Power Plant.

maximum power point strategy. Therefore, FFR is provided only by the EL, which can adjust its power consumption symmetrically. The droop control of the PV is disabled and the EL is parameterized as:

$$R_{\mathrm{p,EL}} = \frac{0.05}{3} = 0.0167. \tag{5.2}$$

The second benchmark is a PI-based plant controller, shown in Figure 5.1. For a fair comparison of PI control versus MPC, the PI plant controller has the same state estimator and reference trajectory algorithm as the MPC with the Frequency Divider model. A single PI controller is used for the control of $\Delta P_{\mathrm{Plant}}$, and the control signal is distributed with even participation factors to the three equally rated RES. The plant transfer function is identified through an open-loop step response test. The controller is tuned using Matlab `pidtune`. A fast and robust control response under nominal conditions is obtained for a bandwidth of 0.25 Hz and a phase margin of 75°. The secondary control objectives can be achieved, by adding PI controllers for the individual RES units. One PI controller recovers the energy storage level, and an additional one tracks the PV output to its maximum. Coordination of the PI controllers must be achieved through time scale separation to avoid an oscillatory plant response from conflicting control behavior. The additional PI controllers are tuned based on the size of the energy storage and the PV response time with a bandwidth of 0.1 Hz and a phase margin of 60°. The computation and communication delay is compensated with a Smith Predictor extension for one time step.

To quantify the control performance, three performance indices are calculated:
1. Integral Squared Error:

$$ISE = \int_0^T e^2(t)\ \mathrm{d}\ t = \int_0^T \left(\Delta P_{\mathrm{Plant}}(t) - \Delta P^*_{\mathrm{Plant,ideal}}(t)\right)^2\ \mathrm{d}\ t \tag{5.3}$$

2. Maximum frequency deviation (Hz):

$$\Delta f_{\max} = \max(f_{\text{Grid}}(t)) - \min(f_{\text{Grid}}(t)) \tag{5.4}$$

3. Energy storage usage (MWs):

$$E_{\text{usage}} = \max(E_{\text{BESS}}(t)) - \min(E_{\text{BESS}}(t)) \tag{5.5}$$

The ISE, introduced in Section 2.1.3, of the plant power output is the primary controller performance index. The maximum frequency deviation (typically given as frequency nadir or zenith) is an important metric for the frequency stability of the connected power system. The energy storage usage describes the required energy capacity to perform the virtual inertia and FFR ancillary service. Reducing the energy storage usage results in more capacity that can be reserved for economic optimization of the overall plant operation, thereby reducing the investment cost to realize this ancillary service.

5.1.2 Simulation of the Model Predictive Control under Nominal Conditions

In the nominal simulation, the plant model is equal to the prediction model of the MPC and all parameters are known to the controller. The nominal model parameters are listed in Table 5.4 in Section 5.1.4, along their uncertainty ranges. The droop and inertia parameters of the RES are considered to be fixed and known to a plant controller. Furthermore, the droop constant of the grid equivalent, which quantifies the steady-state primary reserve, is assumed to be known, since it is commonly procured via a public ancillary service market and has a fixed value. These parameters are:

$$\begin{aligned} &T_{\text{A,BESS}} = 10\,\text{sec}, \quad D_{\text{p,BESS}} = 50\ \text{pu}, \quad R_{\text{p,EL}} = 0.05\ \text{pu}, \\ &R_{\text{p,PV}} = 0.05\ \text{pu}, \quad R_{\text{grid}} = 0.05\ \text{pu}. \end{aligned} \tag{5.6}$$

The energy storage capacity available for virtual inertia and FFR provision is set to $60\frac{\text{MWs}}{\text{MW}}$. For simulation, the nominal system model is extended by the minimum and maximum saturation, and ramp rate limitations of the RES, that were given in Table 4.1. To this end, the nominal simulations are carried out in Matlab Simulink using transfer function-based components. One plant control time step, i.e. 100 ms, is considered as delay between the plant controller and the plant model to account for computational and communication delays.

Load Step Positive

The first scenario is a load step in the grid of 1 pu = 10 MW at t = 3 sec, at an electrical distance to the plant of 40% of the grid impedance, expressed as $d_{\text{load}} = 0.4$. Under nominal conditions, the location of the load step is known to the plant controllers and the disturbance input weights in the prediction model are chosen accordingly.

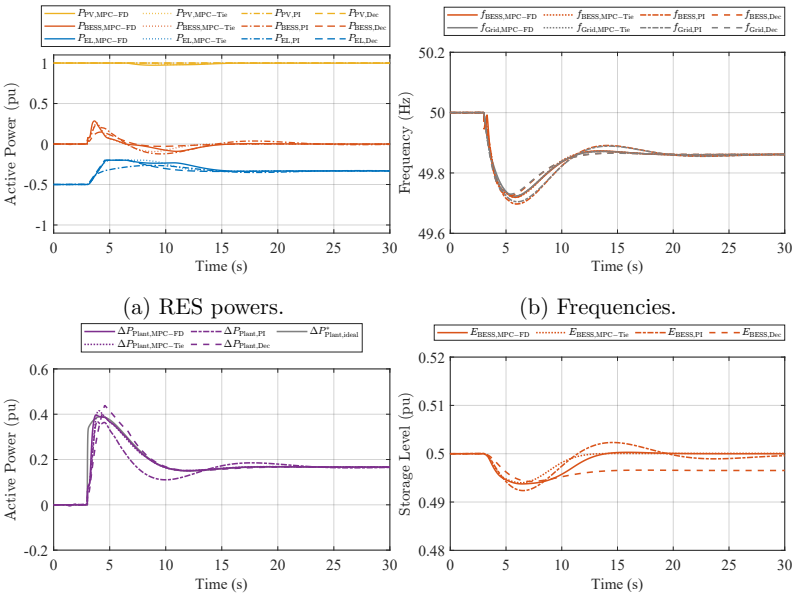

(a) RES powers. (b) Frequencies.

(c) Plant power. (d) Energy storage level.

Figure 5.2: Nominal simulation of the hybrid renewable power plant response to a load step of 1 pu with different plant control strategies.

Figure 5.2 presents the RES output powers, the frequency of the grid and GFM BESS, the change of the total plant power output along the ideal plant power reference and the energy storage level of the BESS, for the two MPC and the benchmark control strategies. The MPC strategies accurately track their plant power output reference and recover the energy storage level with a fast and damped system response. In the first seconds after the disturbance, the EL is controlled to reduce its power consumption and thereby increase the plant power output. The EL operates at the power ramp constraint, before reaching the maximum power limitation. The PV can not support the plant response, as it operates at the maximum power point.

The PI plant controller has a slower and less damped response of the plant output power and the energy storage level than the MPC strategies, which can be seen from the significant overshoots in these variables. The PI controller does not operate the EL at its constraints and has a longer settling time in all system variables. The decentralized strategy can not track the ideal plant reference

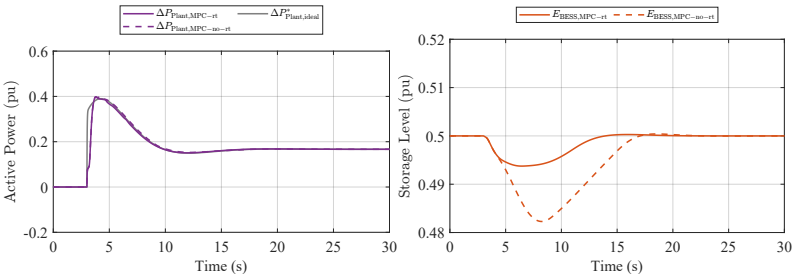

(a) Plant power. (b) Energy storage level.

Figure 5.3: Load step response of the hybrid renewable power plant for an MPC with the reference trajectory algorithm (rt) and a non-predictive reference (no-rt).

during the first seconds because of the power ramp constraint of the EL. After t = 8 sec the plant power output of the decentralized strategy corresponds to the MPC strategies. It is pointed out that the energy storage level stabilizes in steady-state, but does not return to its initial value. For the decentralized control strategy, the energy storage level is recovered only through secondary frequency control, which is not implemented here, recharging the storage during the frequency recovery to 50 Hz.

Effect of the Reference Trajectory Algorithm

Figure 5.3 compares the plant power output and energy storage level for the MPC with the reference trajectory algorithm (Section 4.1.3) to an MPC where the algorithm is disabled and the plant power reference is computed based on the momentary frequency measurement and kept constant over the prediction horizon (non-predictive reference). The plant power output slightly lags the reference in this case (Figure 5.3a). A larger effect can be seen in the energy storage level in Figure 5.3b, where a significantly larger storage capacity is used. With a reference trajectory, the MPC is able to control the RES predictively and make better control decisions resulting in a more accurate reference tracking while reducing resource usage compared to a non-predictive reference.

Load Step Negative

In the second scenario, for a −15 MW load step (Figure 5.4) the MPCs demonstrate accurate plant reference tracking, whereas the PI response is less damped and the decentralized strategy is unable to track the reference during the

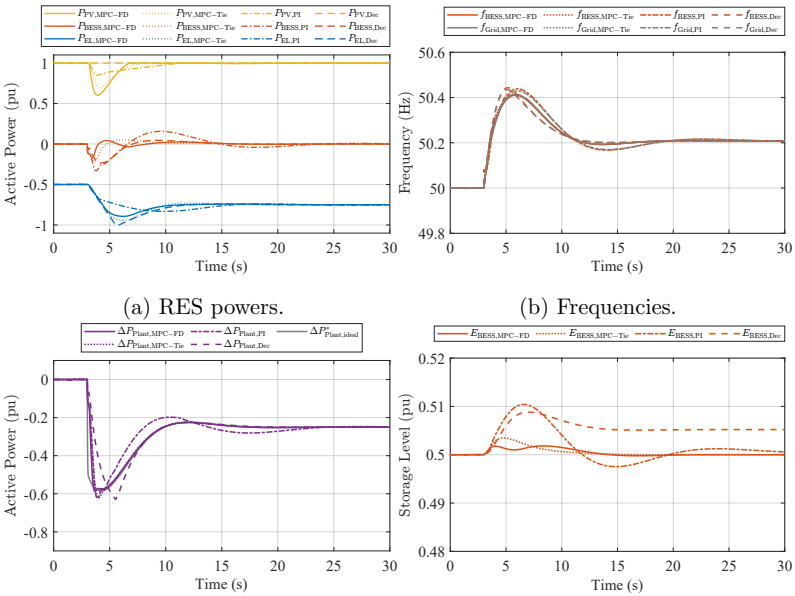

(a) RES powers. (b) Frequencies.

(c) Plant power. (d) Energy storage level.

Figure 5.4: Nominal simulation of the hybrid renewable power plant response to a load step of −1.5 pu with different plant control strategies.

initial transient. In contrast to the positive load step, the PV provides additional controllability in this scenario. The MPCs leverage this by significantly reducing the PV power during the transient (Figure 5.4a), while increasing the EL power consumption at the ramping constraint. As a result, the energy storage usage is significantly reduced compared to the benchmark control strategies (Figure 5.4d), which do not operate the EL at its constraints (PI control), or do not recover the energy storage level (decentralized).

PV Insolation Disturbance

In the next scenario a negative and positive step disturbance of the PV power generation, due to changing insolation levels is simulated. This disturbance occurs within the plant and its effect on the plant output must be rejected. Figure 5.5 presents the RES and the plant power response for a negative step change of -0.2 pu at $t = 3$ sec and a positive change of 0.1 pu at $t = 33$ sec of the PV power

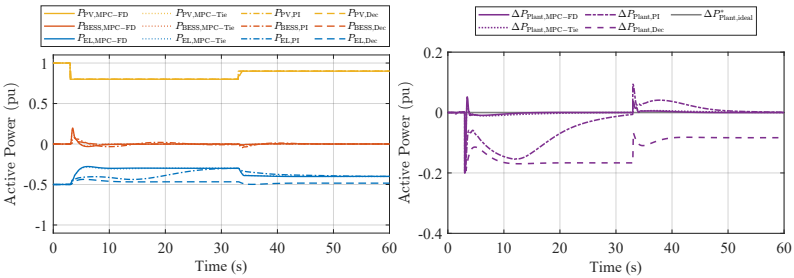

(a) RES powers. (b) Plant power.

Figure 5.5: Nominal simulation of the hybrid renewable power plant response to a step disturbance of the PV insolation of −0.2 pu and 0.1 pu with different plant control strategies.

generation. By comparing the MPPT voltage reference with the measured DC voltage, the PV provides a flag that allows dynamic updating of the maximum power constraint. The MPC strategies leverage the knowledge of the constraint to quickly stabilize the disturbance of the plant power with zero offset. Since the power deviation is fully compensated, no steady-state effect on the grid frequency is obtained. The decentralized control strategy, which has no communication between the RES, is unable to reject this disturbance. The BESS and EL of the plant respond to the frequency change from the reduced power generation, however a steady-state offset is obtained (Figure 5.5b). The PI controller tracks the plant reference following the frequency changes during the first seconds after the disturbance while the state estimator determines the disturbance magnitude through the output integrators. Since the disturbance is internal, the plant reference eventually returns to its pre-disturbance value, however, this estimation and recovery process is notably slow, as shown in Figure 5.5b.

Electrolyzer Trip

In the last scenario, the EL of the plant is tripped due to a protection event. This changes the structure of the control problem, as the EL becomes unavailable for plant control and stops influencing the dynamics. To handle this event, the prediction model of the MPC and state estimator must be updated online. It is assumed that the tripping of the EL can be detected within the MPC sampling time of 100 ms and is known to the plant control system before the next execution. A second state estimator that employs a prediction model without the EL is run

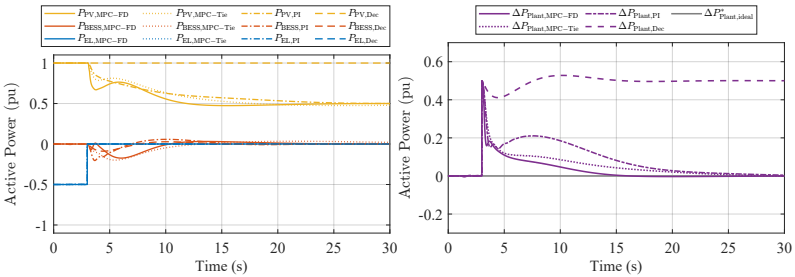

(a) RES powers. (b) Plant power.

Figure 5.6: Nominal simulation of the hybrid renewable power plant response to a protection trip of the Electrolyzer with different plant control strategies.

in parallel before the protection event to ensure a smooth transfer between the prediction models in the MPC.

Figure 5.6 illustrates the system response to the EL trip, where the loss of load is compensated by curtailing PV output. Similar to the PV disturbance, this event perturbs the system frequency during the initial transient, followed by a slow recovery of the plant power reference. The PI control system disables the PV control loop upon detecting the trip to match the MPC steady-state target. However, its reactive feedback nature prevents exact tracking of the reference trajectory making it significantly slower than MPC. The decentralized strategy fails to reject the disturbance entirely. The lack of coordination among RES results in persistent steady-state errors for both plant power and system frequency.

The performance indices presented in Table 5.1, Table 5.2, and Table 5.3 underline the MPC's effectiveness. Through its multi-objective and MIMO control architecture, the MPC plant controllers achieve superior reference tracking and significantly lower energy storage usage compared to both PI and decentralized benchmarks. Only in the EL trip scenario a higher energy capacity is required, where the BESS is used for fast compensation of the missing EL power consumption. This performance is driven by the MPC's ability to exploit the flexibility and coordinate the heterogeneous dynamics of the RES through prediction and dynamic constraints. While the PI controller offers a slight improvement over the decentralized method, its lack of unit coordination leads to higher energy capacity requirements and larger frequency deviations. In contrast, the MPC ensures offset-free disturbance rejection and faster recovery. Notably, the

enhanced observability provided by the Frequency Divider model yields tighter control and better resource management than the Tie line model.

Scenario	MPC-FD	MPC-Tie	PI	Dec.
Load Step Positive	1.8440	2.3253	5.8524	4.1216
Load Step Negative	3.4170	4.4649	8.4378	11.816
PV Insolation Change	0.9278	0.9219	28.17	98.71
Electrolyzer Trip	11.98	20.17	42.37	664.4

Table 5.1: Integral Squared Error (x100) of the grid-connected converter system with different control strategies under nominal conditions.

Scenario	MPC-FD	MPC-Tie	PI	Dec.
Load Step Positive	0.2764	0.2767	0.2958	0.2703
Load Step Negative	0.4147	0.4130	0.4294	0.4347
PV Insolation Change	0.0192	0.0191	0.0526	0.0528
Electrolyzer Trip	0.0815	0.0861	0.0840	0.1843

Table 5.2: Maximum frequency deviation (Hz) of the grid-connected converter system with different control strategies under nominal conditions.

Scenario	MPC-FD	MPC-Tie	PI	Dec.
Load Step Positive	3.920	3.650	5.971	3.449
Load Step Negative	1.220	2.093	7.723	5.284
PV Insolation Change	1.446	1.531	1.882	0.677
Electrolyzer Trip	6.510	9.510	3.717	2.388

Table 5.3: Energy storage usage (MWs) of the grid-connected converter system with different control strategies under nominal conditions.

5.1.3 Hardware-in-the-Loop Validation

The plant control strategies are experimentally validated in a laboratory Hardware-in-the-Loop environment. The HiL setup is shown in Figure 5.7 for an MPC plant controller. The HRPP and grid connection is modelled in the EMT domain in a NovaCor 1.0 real-time simulator from RTDS. Detailed PV panel, lithium-ion battery, and Proton Exchange Membrane (PEM) Electrolyzer stack models are used together with two-level VSC and buck/boost converter models to accurately represent the real behavior of the RES. The plant output power ΔP_{Plant} and grid frequency ω_{Grid} are measured at the high voltage grid connection of the plant. Therefore, any plant internal losses and the measurement dynamics of the PLL at the grid connection point are included. The other measurements are

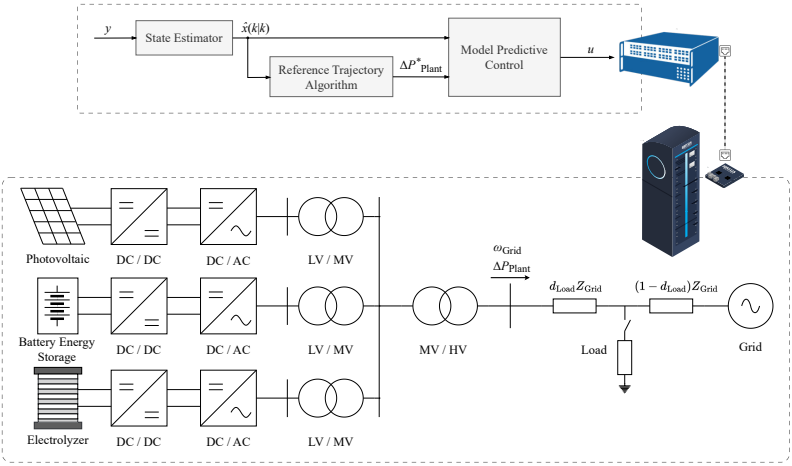

Figure 5.7: Hardware-in-the-Loop experimental setup for the Model Predictive Control Systems of the Hybrid Renewable Power Plant.

obtained from the RES primary control systems. Measurement values are sent to an Opal-RT OP5707XG, which serves as the rapid control prototyping platform. The OP5707XG executes the MPC and PI plant control systems. This laboratory setup constitutes a Control Hardware-in-the-Loop (CHiL) test system according to [78]. The EMT real-time simulation and the controller hardware communicate via a UDP connection. Measurement values are sent every 10 ms, and control commands after each plant controller execution with a sampling time of 100 ms. The EMT plant model is parameterized to the nominal values. The HiL setup allows to validate the plant controllers under a structural uncertainty. In contrast to the nominal model, the EMT model includes the detailed dynamics of a real power system and all relevant control loops of the converters, e.g., for AC and DC voltage control or converter modulation.

The nominal simulations scenarios are reproduced in the HiL setup to validate the plant controllers under realistic conditions. The performance indices for all scenarios are listed in Appendix A. The results for the positive load step are shown in the following to exemplarily highlight the difference between the nominal simulation and HiL experiment. Time-domain HiL results of the negative load step, PV disturbance and EL trip are shown in Appendix A. The performance indices and time-domain results demonstrate a close match between HiL experiments and nominal simulations, validating all control strategies under known system parameters.

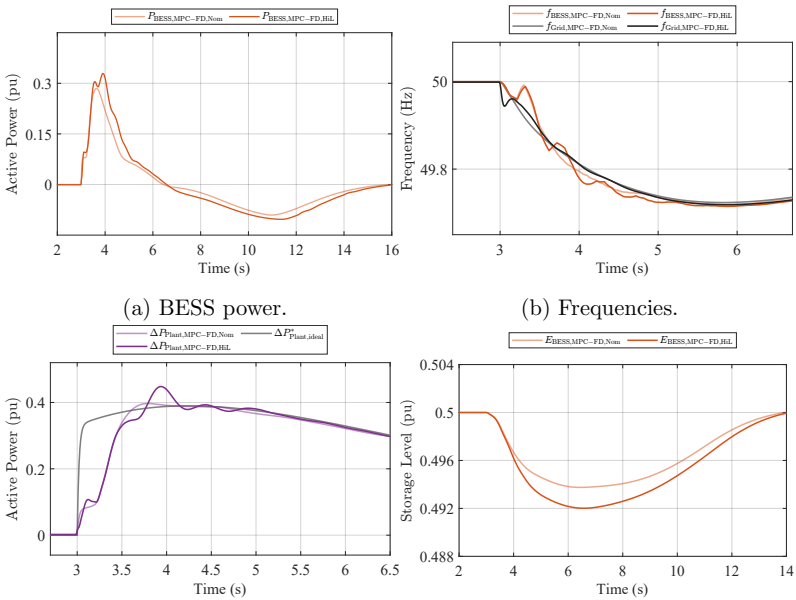

(a) BESS power. (b) Frequencies.

(c) Plant power. (d) Energy storage level.

Figure 5.8: Hardware-in-the-Loop validation of the hybrid renewable power plant response to a load step of 1 pu with MPC using the Frequency Divider model. Zoom in on the transient.

Positive Load Step

Figure 5.8 shows the transient performance of the MPC with the Frequency Divider model for the nominal simulation and the HiL experiment of a positive load step. As converter power, the BESS power is exemplarily highlighted in Figure 5.8a. Across all HiL experiments, this scenario and controller show the largest energy storage deviation, which is shown in Figure 5.8d. The plant power tracking of the MPC is more oscillatory in the HiL setting, however it remains well damped and achieves comparable results to the nominal simulation.

Parameter	Minimum	Maximum	Nominal	Type
$P_{\text{ramp,EL}}$ $[\frac{\text{pu}}{\text{sec}}]$	0.1	1	0.2	Scenario
d_{Load} [%]	0.05	0.75	0.4	Scenario
Z_{grid} [pu]	0.0133	0.3333	0.0667	Parametric uncertainty
$T_{\text{A,grid}}$ [sec]	5	12	10	Parametric uncertainty
T_{N} [sec]	0.2	2	1	Parametric uncertainty
T_{D} [sec]	2	10	6	Parametric uncertainty
$\tau_{\text{p,PV}}$ [sec]	0.05	0.2	0.1	Parametric uncertainty
$\tau_{\text{p,EL}}$ [sec]	0.05	0.2	0.1	Parametric uncertainty
T_{com} [sec]	50e-6	0.04	50e-6	Parametric uncertainty
Mode	Nominal or HiL			Structural uncertainty

Table 5.4: Inputs for robustness and global sensitivity analysis of the grid-connected Hybrid Renewable Power Plant. Nominal values and uncertainty characterization.

5.1.4 Robustness and Sensitivity Analysis

For a broad investigation of controller performance under model-plant mismatch, a robustness and sensitivity study is conducted. The analysis includes all parameters listed in Table 5.4, incorporating parametric uncertainty on all grid variables, with exception of the known steady-state reserve R_{grid}. The variable grid impedance Z_{grid} introduces uncertainty on the values of the Frequency Divider matrix and the Tie line parameter T_{Tie} in their respective prediction models. For example, a value of $Z_{\text{grid}} = 0.0133$ corresponds to $T_{\text{Tie}} = 2.3077$, and $Z_{\text{grid}} = 0.3333$ to $T_{\text{Tie}} = 1.6129$, considering the fixed transformer impedances and virtual impedance of the GFM converter. Additionally, the study accounts for varying GFL response times ($\tau_{\text{p},i}$), variable communication delays T_{com} up to 40 ms (in addition to the 100 ms HiL delay and a 50 μs simulator time step), and factors such as EL power ramp rates ($P_{\text{ramp,EL}}$) and electrical load distances (d_{Load}) that cover different scenarios. Structural uncertainty is captured by treating the operating mode, nominal simulation versus HiL, as a discrete uniform distribution. The input parameters from Table 5.4 are sampled via the scrambled low-discrepancy Sobol' sequences to achieve an optimal coverage of the parameters' space while limiting the computational cost of the study [17]. Each of the four control strategies is run for $N = 128$ combinations of the parameters' values in Table 5.4, resulting in 64 nominal simulations and 64 HiL experiments per controller. A positive load step of 1 pu and a negative load step of -1.5 pu are simulated for the N simulations/experiments.

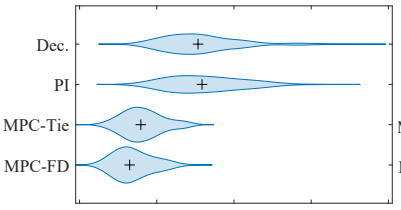

(a) Integral Squared Error.

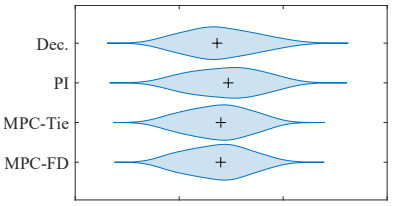

(b) Maximum Frequency Deviation.

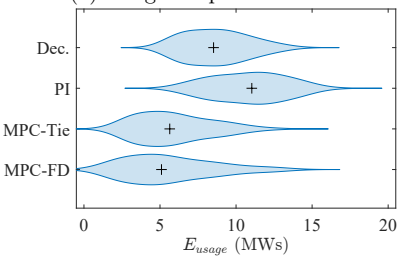

(c) Energy Storage Usage.

Figure 5.9: Distribution of the performance indicies in the robustness analysis for the Hybrid Renewable Power Plant for each plant control strategy.

The results of the robustness analysis are illustrated via the performance index distributions in Figure 5.9, with the median being indicated. While all nominal simulations remained stable, some HiL experiments encountered instabilities, such as synchronization failure or insufficient damping, likely caused by specific parameter combinations at the uncertainty extremes. These instabilities, whose detailed mechanisms are explored in [89] and [129], were excluded from the analysis. The total number of successful runs (nominal simulation and HiL) is 117 for the MPC with Frequency Divider model, 115 for the MPC with Tie line model, 122 for the PI controller, and 124 for the decentralized strategy, which is sufficiently large for a statistically valid variance-based analysis of each controller.

Figure 5.9a shows that the MPC control strategies are significantly more robust than the PI and the decentralized control strategy in providing virtual inertia and FFR with the HRPP. Table 5.5 lists the median and the lower and upper quartile (25th and 75th percentile) of each index and control strategy. The MPC using the Tie line model has a 48.3-50% increased performance over the conventional control strategies, with a median ISE of 7.937, compared to 15.86

Index	Control Strategy	Lower Quartile	Median	Upper Quartile
ISE (x100)	MPC-FD	5.109	6.485	8.555
	MPC-Tie	6.376	7.937	9.633
	PI	12.47	15.86	19.57
	Decentralized	12.34	15.35	18.05
Max. Frequency Deviation (Hz)	MPC-FD	0.5794	0.6997	0.7841
	MPC-Tie	0.577	0.7004	0.7865
	PI	0.5977	0.7361	0.8415
	Decentralized	0.582	0.6822	0.8225
Energy Storage Usage (MWs)	MPC-FD	3.404	5.097	7.53
	MPC-Tie	3.818	5.641	7.44
	PI	8.993	11.04	12.64
	Decentralized	6.968	8.522	10.05

Table 5.5: Performance Index Median, Lower and Upper Quartile of the robustness analysis for the Hybrid Renewable Power Plant.

for the PI controller and 15.35 with the decentralized strategy. By employing the proposed Frequency Divider prediction model, the MPC performance is further increased and the ISE is reduced by 18% from 7.937 to 6.485. The Frequency Divider model avoids the need to estimate the magnitude of the input disturbance by formulating the disturbance as process noise, while having full observability. This increases the robustness of the closed-loop control system under uncertainty. The maximum frequency deviation of the measured grid frequency is approximately equal for all 4 control strategies (Figure 5.9b and Table 5.5). The MPC plant controllers use significantly less energy storage capacity compared to the PI and the decentralized control strategy with medians of 5.10 MWs and 5.64 MWs versus 11.04 MWs and 8.52 MWs respectively.

The sensitivity of the robustness analysis results to each input parameter from Table 5.4 can be calculated via the variance-based sensitivity analysis introduced in Section 2.1.3, which quantifies the factors influencing the variability of the performance metrics. It is conducted separately for each performance index and control strategy.

For the ISE sensitivity indices, residuals in the range of 3-8% are obtained, confirming a good fit of the SIs to the real models. The Sobol sensitivity indices for the ISE are reported in Figure 5.10 and reveal distinct parameter influence across the control strategies. Both MPC controllers exhibit a similar sensitivity

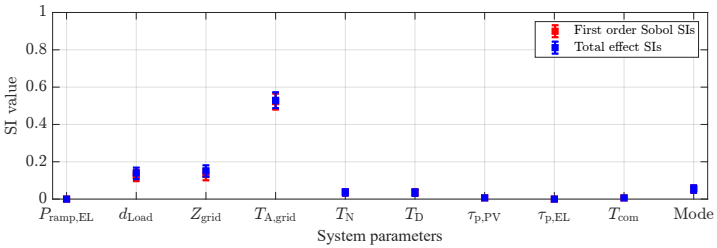

(a) MPC with Frequency Divider model.

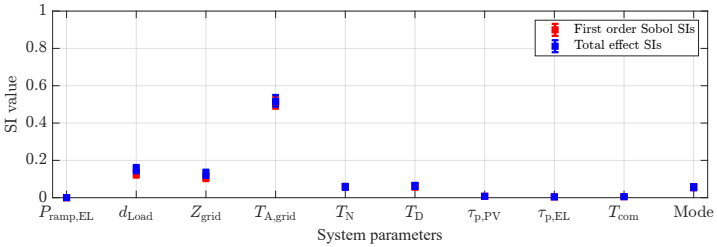

(b) MPC with Tie line model.

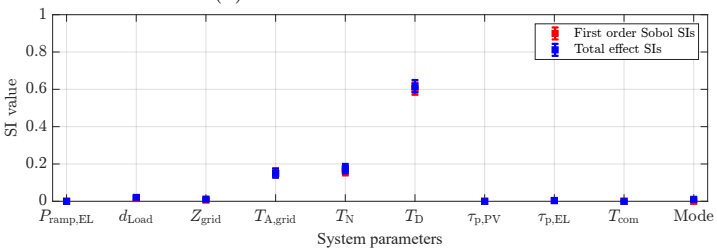

(c) PI controller.

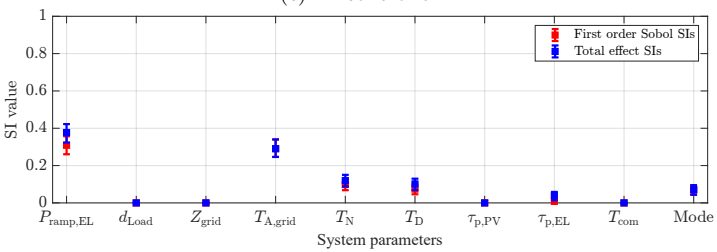

(d) Decentralized control.

Figure 5.10: Sensitivity analysis results for the ISE in terms of first order Sobol' and total effect SIs.

pattern dominated by the grid inertia $T_{\mathrm{A,grid}}$ (S_i of 0.50–0.53), followed by the grid impedance Z_{grid} and the disturbance location d_{Load}. This suggests that MPC robustness is most effectively ensured by employing online inertia estimation techniques such as [130], [131], supported by grid impedance measurement, e.g., [132], [133] or [134]. Notably, the negligible sensitivity to the operating mode ($S_i = 0.06$) confirms that the nominal model captures the essential dynamics required for these scenarios. In contrast, the PI controller is primarily influenced by the grid's primary control time constants, T_N and T_D, while the decentralized strategy is most sensitive to the EL's power ramp rate $P_{\mathrm{ramp,EL}}$ in addition to the grid inertia $T_{\mathrm{A,grid}}$, while Z_{grid} and d_{Load} have no influence for both strategies.

Regarding the maximum frequency deviation, sensitivity is uniformly dominated by the grid's primary control parameters, T_N (S_i of 0.61–0.74) and T_D (S_i of 0.25–0.32), across all strategies. This consistency indicates that all controllers perform sufficiently in providing virtual inertia and FFR from the HRPP, ensuring the system peak is determined by the slower SG-based resources rather than the specific plant control strategy. Detailed individual sensitivity results for each controller are provided in Appendix A.

While the energy storage usage of PI and decentralized controllers mirrors the sensitivity pattern of the frequency peak (see Appendix A), MPC demonstrates a more sophisticated resource usage. In addition to grid time constants, MPC is sensitive to $P_{\mathrm{ramp,EL}}$ ($S_i = 0.18$) and, for the Frequency Divider variant, the operating mode ($S_i = 0.08$). These sensitivities, paired with the reduced median of the energy usage shown in Figure 5.9c, highlight that MPC actively exploits EL flexibility to minimize energy storage demand even under uncertainty. In contrast, the classical strategies treat the energy storage as a reactive buffer whose usage is determined by the magnitude of the frequency excursion.

The GFL first-order response times $\tau_{\mathrm{p},i}$ and communication delay T_{com} have no impact on any performance index, which suggests that these values can be set flexibly within the studied variability range during controller design without affecting performance. Regarding the impact of structural uncertainty, it is important to note that only stable HiL experiments were included in the statistical evaluation. Since certain extreme parameter combinations resulted in instabilities in the EMT domain, HiL should be employed to verify the stability of a design early in the process. On the other hand, nominal simulations remain a reliable and comprehensive tool for assessing broader parameter influences, as they capture all essential information required for a detailed sensitivity analysis.

These results directly address the research questions regarding controller performance and the impact of uncertainty. Compared to classical strategies, MPC demonstrates superior robustness under model-plant mismatch, achieving a 48–50% median improvement in tracking accuracy and a 33–48% reduction in energy storage requirements by exploiting plant flexibility. In addition, the Fre-

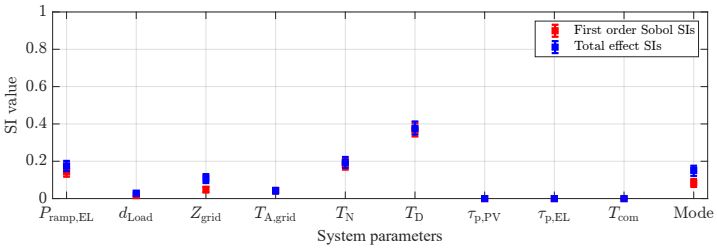

Figure 5.11: Sensitivity analysis results for the energy storage usage for the MPC with Frequency Divider model.

quency Divider model further reduced the tracking error by 18%, while reducing energy storage usage by 9%. Regarding the nature of uncertainty, the analysis reveals that parametric uncertainty, specifically concerning grid inertia, impedance, and EL ramp rates, has the strongest influence on MPC performance. While structural uncertainty associated with the transition to the EMT environment is measurable, its effect is minor compared to the parametric influence in stable scenarios.

5.2 Islanded Converter-driven Power Systems

In this section, the performance of the MPC secondary controllers designed in Section 4.2 to stabilize and reject disturbances in an islanded fully converter-driven power system is presented. The robustness and sensitivity to parametric and structural uncertainty is evaluated and compared against a conventional controller.

5.2.1 Controller Benchmark and Performance Indices

In secondary frequency control, PI is the predominant control strategy. Therefore, the MPCs are compared against a PI-based secondary controller. The structure of the PI controller is shown in Figure 5.12. The main objective is to control the average of the two GFM converter frequencies to its nominal value of 50 Hz, i.e. to drive the frequency deviation

$$\Delta f_{\text{ave}}(t) = \frac{\Delta f_{\text{BESS},1}(t) + \Delta f_{\text{BESS},2}(t)}{2} \tag{5.7}$$

to zero. To this end, all 5 converters receive power set-point changes from the secondary control with equal participation factors. The PI controller is tuned, by identifying the systems transfer function through an open-loop step response test. A negative step is applied to include the response of the PV systems. The

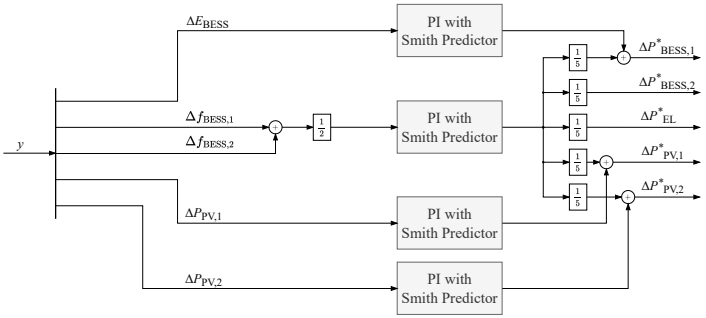

Figure 5.12: PI-based secondary control system for the islanded CIGRE MV distribution network.

controller is tuned using Matlab `pidtune`. A fast and robust control response under nominal conditions is obtained for a bandwidth of 0.5 Hz and a phase margin of 75°.

In addition to frequency control, the energy storage level of BESS 1, and the power output of the two PV systems are controlled to their reference values. The additional PI controllers must have a slower bandwidth to avoid adverse interactions with the main frequency controller. A bandwidth of 0.1 Hz with a phase margin of 60° for the equivalent transfer functions of the BESS and PV systems is sufficient to this end. All PI controller are equipped with a Smith Predictor extension to compensate for computational and communication delay.

The control performance is quantified with three performance indices.
1. Integral Squared Error:

$$ISE = \int_0^T e(t)^2 \text{ d } t = \int_0^T \Delta f_{\text{ave}}(t)^2 \text{ d } t \tag{5.8}$$

2. Maximum frequency deviation (Hz):

$$\Delta f_{\text{max}} = \max(\Delta f_{\text{ave}}(t)) - \min(\Delta f_{\text{ave}}(t)) \tag{5.9}$$

3. Energy storage usage (MWs):

$$E_{\text{usage}} = \max\big(E_{\text{BESS},1}(t)\big) - \min\big(E_{\text{BESS},1}(t)\big) \tag{5.10}$$

The ISE, introduced in Section 2.1.3, of the average frequency is the primary controller performance index, quantifying the frequency deviation for the whole transient. The maximum frequency deviation (typically formulated as frequency nadir or zenith) additionally quantifies the peak deviation, which can trigger

protection or load shedding relays. The energy storage usage describes the required energy capacity to stabilize the systems transient.

5.2.2 Simulation of the Model Predictive Control under Nominal Conditions

In the nominal simulation, the plant model corresponds to the prediction model of the MPC and all parameters are known to the controller. The nominal model parameters are listed in Table 5.9 in Section 5.2.4, along their uncertainty ranges. The following parameters concerning the virtual inertia and droop settings are considered to be fixed and known:

$$\begin{aligned} T_{\mathrm{A,BESS,1}} &= 10\,\mathrm{sec}, \quad D_{\mathrm{p,BESS,1}} \quad = 50 \text{ pu}, \\ T_{\mathrm{A,BESS,2}} &= 10\,\mathrm{sec}, \quad R_{\mathrm{p,BESS,2}} \; = 0.05 \text{ pu} \\ R_{\mathrm{p,EL}} &= 0.05 \text{ pu}, \quad R_{\mathrm{p,PV,1}} = 0.05 \text{ pu}, \\ R_{\mathrm{p,PV,2}} &= 0.05 \text{ pu}, \end{aligned} \tag{5.11}$$

The available energy storage capacity of BESS 1 for secondary control is $60\frac{\mathrm{MWs}}{\mathrm{MW}}$, therefore 600 MWs = 1 pu. For simulation, the nominal system model is extended by the minimum and maximum saturation, and ramp rate limitations of the RES, that were given in Table 4.2. To this end, the nominal simulations are carried out in Matlab Simulink using transfer function-based components. One plant control time step, i.e. 100 ms, is considered as delay between the secondary control system and the plant model to account for computational and communication delays.

Load Step

The first scenario is a load step of 6 MW at bus 2 of the CIGRE MV distribution system at $t = 3\,\mathrm{sec}$, and the removal of the same load at $t = 33\,\mathrm{sec}$. This correspond to a 30% increase of the total system load. The simulation results for the MPC using the Frequency Divider model, MPC using the Tie line model and the PI-based secondary control system are shown in Figure 5.13. The GFM-controlled BESS instantaneously respond to the load step at $t = 3\,\mathrm{sec}$ with an increased power output. The secondary control systems reject the disturbance on the frequency, and the EL and BESS 2 share the load in steady-state. The maximum frequency deviation is comparable for all control strategies (Figure 5.13b). The MPCs quickly stabilize the frequency at 50 Hz, whereas the PI controller only has a strong initial response with a slower settling time compared to the MPC strategies. The MPC using the Tie line model has a small overshoot on the average frequency. The PV systems operate at their maximum power point and can not support the frequency recovery for the positive load step. After the negative load step, the MPCs use the flexibility of the PVs briefly during the transient. BESS 1 supports the stability of the islanded converter-driven system with its

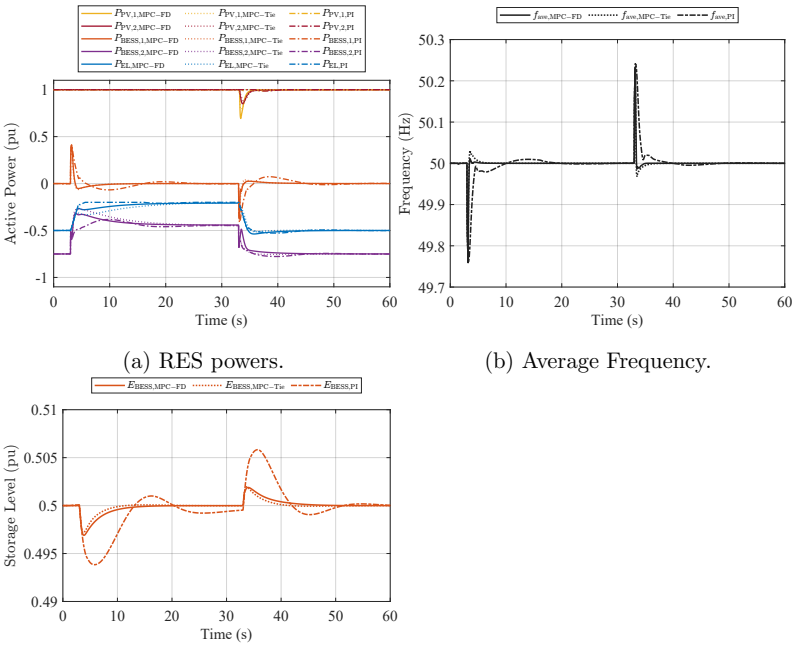

(a) RES powers.

(b) Average Frequency.

(c) Energy storage level.

Figure 5.13: Nominal simulation of a positive and negative load step in the islanded CIGRE MV distribution network with different control strategies.

Grid-forming converter, however the energy storage level shall be maintained at the reference $E^*_{\text{BESS}} = 0.5$ pu. Figure 5.13c shows the energy storage level. The MPC secondary controllers have a tighter energy storage control with a smaller peak usage, a faster recovery to steady-state and less oscillations than the PI controller. The performance indices for all scenarios and control strategies are listed in Table 5.6, Table 5.7 and Table 5.8, at the end of the section. The MPC strategies achieve similar results in all indices, while the PI controller has a larger ISE and requires more than twice of the energy capacity than the MPCs.

Effect of a terminal cost on energy storage usage

In this context the positive effect of the terminal cost on the energy storage level control of MPC is highlighted. Figure 5.14 compares the performance of

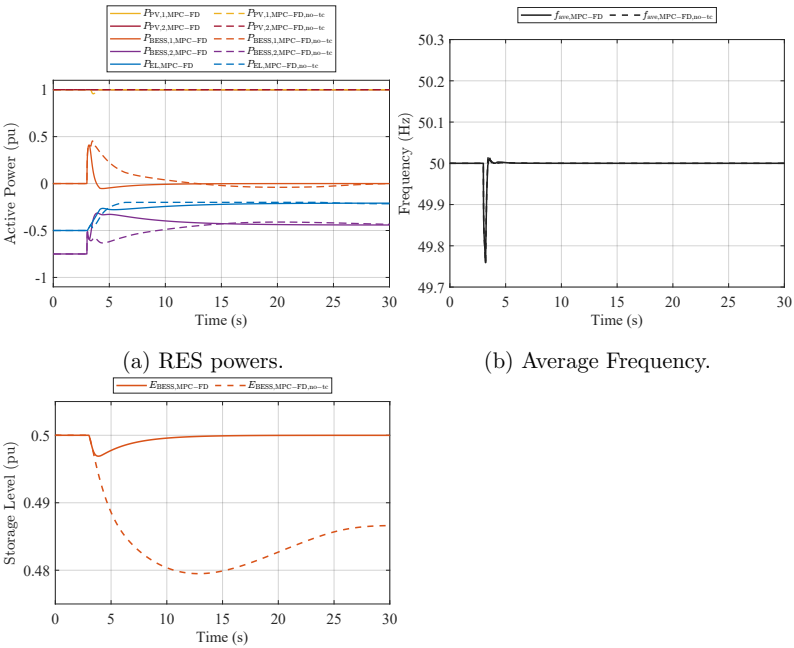

(a) RES powers.

(b) Average Frequency.

(c) Energy storage level.

Figure 5.14: Nominal simulation of a load step in the islanded CIGRE MV distribution network with and without terminal cost ("no-tc") on the storage level.

the MPC using the Frequency Divider model with and without terminal cost. Without the terminal cost, the energy storage level is not tracked at reference and a steady-state offset (Figure 5.14c) is obtained. This steady-state offset is not technically necessary, as the storage level is an integral of the power output of BESS 1, and the same power distribution in steady-state can be achieved, as demonstrated in Figure 5.14a. However, MPC can generally only guarantee offset free control in as many outputs as controllable inputs due to limited steady-state degrees of freedom. Here, deviations of the EL and BESS 2 power outputs from their respective reference are penalized in the cost function to coordinate the power sharing (Table 4.2), leading to 6 controlled outputs (7 if the frequencies are included separately), with only 5 controlled inputs. This causes the MPC to trade-off the offset on the energy storage level versus the power outputs over the prediction horizon. Through tuning of the cost function weights, the size of

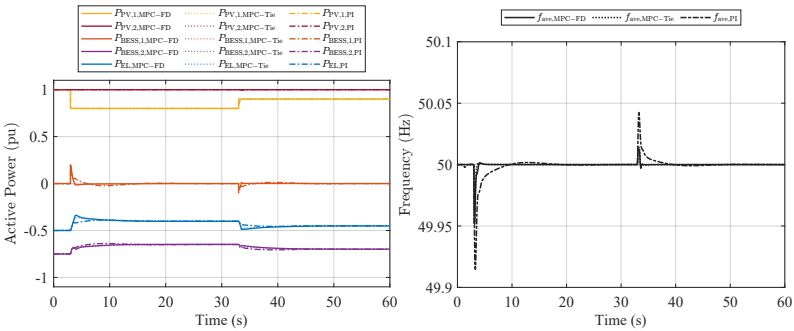

(a) RES powers. (b) Average Frequency.

Figure 5.15: Nominal simulation of a step disturbance of the PV 1 insolation of −0.2 pu and 0.1 pu in the islanded CIGRE MV distribution network with different control strategies.

the storage level offset can be reduced, however not entirely removed. With a large terminal cost on the energy storage level E_{BESS} at the end of prediction horizon, the conflict in the cost function can be resolved and the MPC tracks the storage level well damped and offset-free. This expands the traditional role of terminal weights from improving controller stability to enhancing the output tracking capability when controlling multiple RES.

PV Insolation Disturbance

A disturbance of the PV power output from insolation changes is simulated in Figure 5.15. The MPC secondary controllers reject the disturbance on the average frequency more effectively than the PI controller. The maximum frequency deviation is 61 mHz and 63 mHz with the MPCs versus 128 mHz with the PI controller (Table 5.7), and the ISEs are 0.0608 and 0.0629 compared to 0.1277 (Table 5.6). Similar to the load disturbance, the EL and BESS 2 share the power deviation in steady-state. The energy storage level has the same qualitative trajectory as for the load step and is therefore not shown. The PI controller uses 1.684 MWs, whereas the MPC using the Frequency Divider model uses 0.776 MWs and the MPC with the Tie line model 0.733 MWs of the energy storage (Table 5.8).

Electrolyzer Trip

Lastly, a protection trip of the EL is simulated, the results are shown in

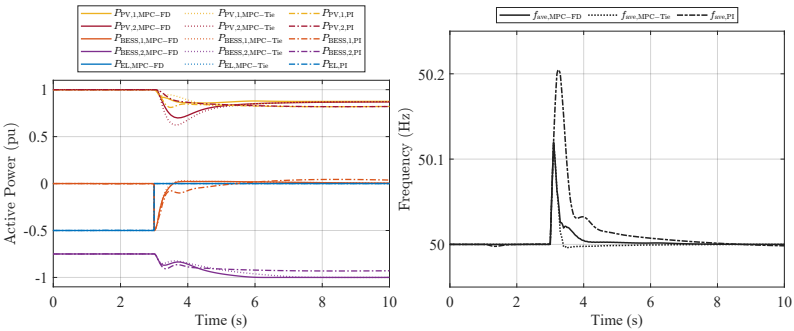

(a) RES powers. (b) Average Frequency.

Figure 5.16: Nominal simulation of a protection trip of the Electrolyzer in the islanded CIGRE MV distribution network with different control strategies.

Figure 5.16. Before the event, the EL consumes 5 MW of power. The trip of the EL changes the structure of control problem and cost function for the MPCs. Therefore, the prediction model is updated online in a mode switch of the MPC. To this end, a second state estimator based on the prediction model without EL is running in parallel to the original controller to ensure a smooth transition of the control modes. Similarly, the PI controller is also unable to fulfill its control objective without modification of the control system. To be able to drive the system into a steady-state after the loss of the EL, the PI controllers tracking the maximum power point of the PVs are turned off, allowing a steady-state curtailment. It can be seen in Figure 5.16a that all secondary controllers reduce the PV power output and increase the power consumption of BESS 2 after the trip. The MPCs drive BESS 2 to its minimum power of -1 pu, thereby ensuring the maximum energy yield of the islanded system. The PI controller does not operate the BESS at its constraint and settles at a suboptimal operating point. The average frequency is shown in Figure 5.16b for all controllers. The frequency peak is significantly larger for the PI controller at 50.207, compared to the MPCs. Additionally, an energy storage capacity of 2.334 MWs compared to 1.097 MWs and 1.067 MWs with the MPCs is used.

In summary, the MPC using the Frequency Divider and the MPC based on the Tie line model demonstrate comparable performance across all tested scenarios. Both MPCs achieve significantly better frequency tracking as quantified by the ISE (Table 5.6), while simultaneously reducing the required energy storage capacity by more than 50% compared to the PI controller (Table 5.8). Further-

more, the inclusion of a terminal cost in the MPC objective function substantially enhances energy storage tracking. This formulation enables offset-free control even in systems where the number of controlled outputs exceeds the available inputs. This characteristic can be strategically leveraged to fine-tune the steady-state power sharing among the RES.

Scenario	MPC-FD	MPC-Tie	PI
Load Step Positive & Negative	1.9785	1.9308	7.0098
PV Insolation Disturbance	0.0495	0.0529	0.3805
Electrolyzer Trip	0.1824	0.1624	1.3572

Table 5.6: Integral Squared Error (x100) of the islanded converter-driven power system with different control strategies under nominal conditions.

Scenario	MPC-FD	MPC-Tie	PI
Load Step Positive & Negative	0.4739	0.4711	0.4826
PV Insolation Disturbance	0.0608	0.0629	0.1277
Electrolyzer Trip	0.1193	0.1238	0.2068

Table 5.7: Maximum frequency deviation (Hz) of the islanded converter-driven power system with different control strategies under nominal conditions.

Scenario	MPC-FD	MPC-Tie	PI
Load Step Positive & Negative	2.9894	2.8786	7.1947
PV Insolation Disturbance	0.7760	0.7334	1.6835
Electrolyzer Trip	1.0971	1.0666	2.3336

Table 5.8: Energy storage usage (MWs) of the islanded converter-driven power system with different control strategies under nominal conditions.

5.2.3 Hardware-in-the-Loop Validation

The fast secondary control strategies are experimentally validated in a laboratory Hardware-in-the-Loop environment. The HiL setup for an MPC controller is shown in Figure 5.17. The islanded CIGRE MV distribution system and RES are modelled in the EMT domain in a RTDS NovaCor 1.0 real-time simulator. Detailed PV panel, lithium-ion battery, and PEM Electrolyzer stack models are used together with two-level VSC and buck/boost converter models to accurately represent the real behavior of the RES. The measurements, i.e. power P_i, frequency $f_{\mathrm{BESS},i}$ and energy storage level E_{BESS} are obtained from the RES primary control systems and sent to an Opal-RT OP5707XG, which serves as the rapid control prototyping platform. The OP5707XG executes the MPC and PI plant control systems, thereby implementing a CHiL test system [78]. The

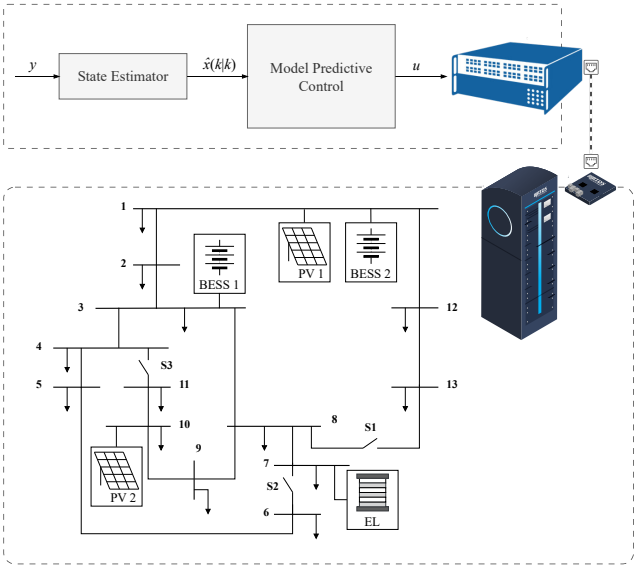

Figure 5.17: Hardware-in-the-Loop experimental setup for Model Predictive Control of the islanded CIGRE MV distribution system.

EMT real-time simulation and the controller hardware communicate via a UDP connection. Measurement values are sent every 10 ms, and control commands after each fast secondary control execution with a sampling time of 100 ms.

The EMT model of the RES and the CIGRE MV distribution system are parameterized to the nominal values for the validation. The topology of the CIGRE MV distribution system can be altered through three switches (S1, S2, and S3). S3 is considered to be always open. Under nominal conditions, S1 and S2 are closed. The HiL setup allows to validate the secondary controllers under a structural uncertainty. In contrast to the nominal model, the EMT model includes the detailed dynamics of a real power system and all relevant control loops of the converters, e.g., for AC and DC voltage control or converter modulation.

The scenarios of the nominal simulations are reproduced in the HiL setup. The performance indices for all scenarios, and their percentage change from the nominal simulation are listed in Appendix B. The results for the negative load step are shown in the following to exemplarily highlight the difference between the nominal simulation and HiL experiment. Time-domain HiL results of the PV

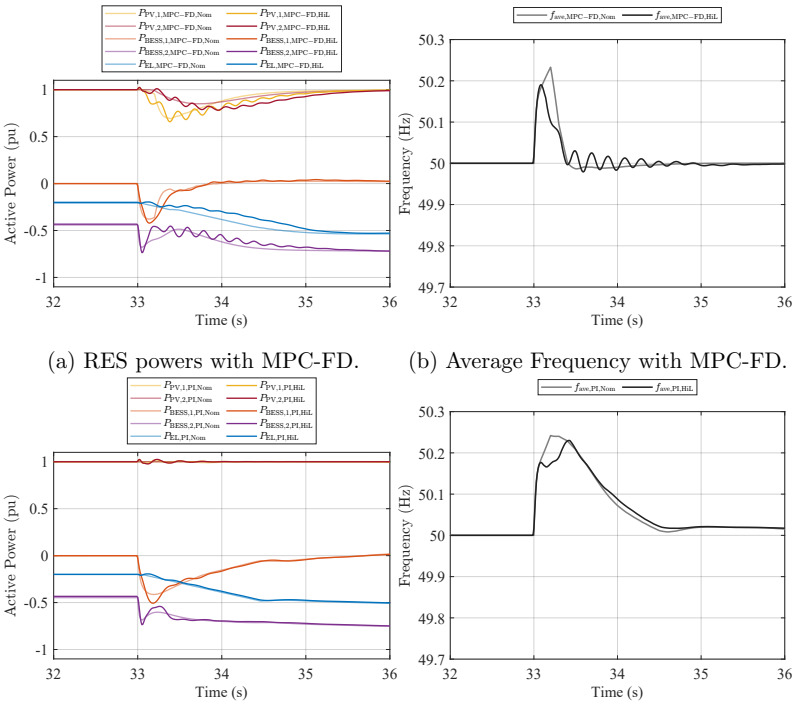

(a) RES powers with MPC-FD. (b) Average Frequency with MPC-FD.

(c) RES powers with PI. (d) Average Frequency with PI.

Figure 5.18: HiL experiment of a negative load step in the islanded CIGRE MV distribution network and comparison with the nominal simulation.

disturbance and EL trip are shown in Appendix B. The energy storage level has the same qualitative trajectory in all scenarios and is not shown.

Negative Load Step

The transient response to a negative 6 MW load step (Figure 5.18) shows that the MPC is less damped than the PI controller, notably in the power output of the PVs and BESS 2, and the average frequency. In comparison, the less aggressive PI behavior remains closer to the nominal case. The MPC is more sensitive to structural uncertainties from the EMT model due to the system's lack of inertia

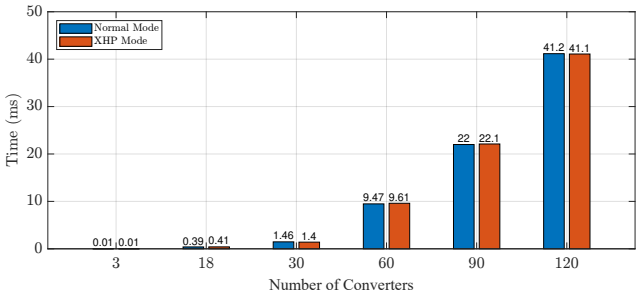

Figure 5.19: Maximum computation time of the MPC in an OP5707XG for different numbers of converters.

and fast dynamics. Nonetheless, both MPCs maintain stable, tight regulation and superior performance indices compared to the PI controller.

Computational performance for a large number of converters

To assess scalability, the computationally efficient linear MPC was tested on the OP5707XG platform by scaling the number converters using an infinite bus model with a 1:2 ratio of generic GFM to GFL converters. During a 0.3 pu load step, execution times remained in the microsecond range for up to 18 units and reached 41.2 ms for 120 units (Figure 5.19). This confirms real-time capability within the 100 ms sampling interval, despite the quadratic growth $O(n^2)$ driven by expanding system matrices in (2.2) and (linearly) increasing optimization variables. Because this computational demand limits centralized scaling, distributed strategies are developed in Chapter 6 to decouple the control problem size from the number of converters.

5.2.4 Robustness and Sensitivity Analysis

A robustness and sensitivity study is conducted to further assess the performance and quantify the impact of different types of uncertainty as model-plant mismatch on the control system. Table 5.9 lists the input parameters along their variability range, which are sampled via the scrambled low-discrepancy Sobol' sequences to achieve an optimal coverage of the parameters' space while limiting the computational cost of the study [17]. All parameters are sampled from a uniform distribution, indicated by their maximum and minimum values, whereas the load bus, switch positions and the operating mode are discrete uniform distributions. Each control strategy is run for $N = 128$ combinations of the parameters' values

Parameter	Minimum	Maximum	Nominal	Type
$P_{\text{ramp,EL}}$ $[\frac{\text{pu}}{\text{sec}}]$	0.1	1	0.2	Scenario
Load Bus	(1, 2, 3, 12)		2	Parametric uncertainty
Switch [S1,S2]	([0,0], [0,1], [1,0], [1,1])		[1,1]	Parametric uncertainty
$K_{\text{d,BESS,2}}$	0.01	0.03	0.0211	Parametric uncertainty
$\tau_{\text{p,PV,1}}$ [sec]	0.05	0.2	0.1	Parametric uncertainty
$\tau_{\text{p,PV,2}}$ [sec]	0.25	1.0	0.5	Parametric uncertainty
$\tau_{\text{p,EL}}$ [sec]	0.05	0.2	0.1	Parametric uncertainty
T_{com} [sec]	50e-6	0.04	50e-6	Parametric uncertainty
Mode	Nominal or HiL			Structural uncertainty

Table 5.9: Inputs for robustness and sensitivity analysis of the islanded CIGRE MV distribution system. Nominal values and uncertainty characterization.

in Table 5.9, resulting in 64 nominal simulations and 64 HiL experiments per controller of the previous load step scenario.

While the EL power ramp rate is considered known to represent specific unit variants, all other parameters were unknown to the controllers to simulate realistic model-plant mismatch. Structural uncertainty is represented by the choice of operating mode, nominal simulation against EMT dynamics in HiL. Parametric uncertainty is introduced through variations in the VSM damping gain ($K_{\text{d,BESS,2}}$), the first-order response times of GFL units ($\tau_{\text{p},i}$), and communication delays (T_{com}) of up to 40 ms. Furthermore, variations in the load bus location and the configuration of S1 and S2 alter the electrical distance between RES. These topological changes directly impact the instantaneous power sharing of GFM converters and introduce parametric shifts in the prediction models, such as variations in the Tie line parameter T_{tie} and the entries of the Frequency Divider matrix. For example, the smallest value of Tie line parameter is $T_{\text{tie}} = 0.7957$ and the highest $T_{\text{tie}} = 0.9345$ for these switch positions.

The results for the 128 runs of the robustness study are reported in Figure 5.20 for each performance index. The median and the lower and upper quartile (25th and 75 percentile) of each index and controller are further listed in Table 5.10. The results indicate that both MPC variants achieve nearly identical performance, with the Tie line model yielding a marginal 3.8% improvement in the median ISE. Most notably, both MPCs significantly outperform the PI controller, providing tighter frequency regulation while utilizing less than half the energy storage. While the maximum frequency deviation remained similar across all strategies, which is determined by the instantaneous converter response in this inertia-less

Index	Control Strategy	Lower Quartile	Median	Upper Quartile
ISE (x100)	MPC-FD	1.776	2.029	2.439
	MPC-Tie	1.676	1.951	2.323
	PI	5.449	5.770	6.446
Max. Frequency Deviation (Hz)	MPC-FD	0.4348	0.476	0.495
	MPC-Tie	0.4351	0.474	0.492
	PI	0.4480	0.488	0.506
Energy Storage Usage (MWs)	MPC-FD	2.85	3.14	3.48
	MPC-Tie	2.70	3.02	3.23
	PI	7.05	7.12	7.22

Table 5.10: Performance index Median, Lower and Upper Quartile of the robustness analysis of the CIGRE MV distribution network.

system, MPC proves far more efficient in managing the subsequent transient, quantified by the ISE and energy storage usage.

The sensitivity of the controllers to each of the input parameters in Table 5.9 is calculated as the first order Sobol and total effect SIs. The results for the ISE are presented in Figure 5.21. The sensitivity analysis reveals that MPC performance is primarily driven by structural uncertainty, showing a high sensitivity to EMT dynamics in the HiL environment ($S_i = 0.44$). In contrast, PI control is relatively insensitive to the operating mode ($S_i = 0.10$) but is heavily constrained by the EL ramp rate ($P_{\text{ramp,EL}}$), which dominates its sensitivity profile ($S_i = 0.67$). The communication delay (T_{com}) and local damping ($K_{\text{d,BESS,2}}$) have a minor to moderate effect on MPC performance. All other parameters, specifically the GFL response times and system topology, have a lesser impact than the load disturbance bus, which is naturally unknown. Therefore, they are irrelevant for assessing MPC performance.

Detailed sensitivity indices for the maximum frequency deviation and energy storage usage are provided in Appendix B. Regarding frequency deviation, the sensitivity patterns are nearly identical across all control strategies, being dominated by the operating mode with a moderate effect of the damping parameter ($K_{\text{d,BESS,2}}$). This confirms that the initial frequency peak is determined by the instantaneous converter response, particularly of the decoupled VSM which is captured more accurately in the HiL setting, rather than the specific secondary control logic. In terms of energy storage usage, the results underline the previous conclusion that MPC performance is more susceptible to structural uncertainty,

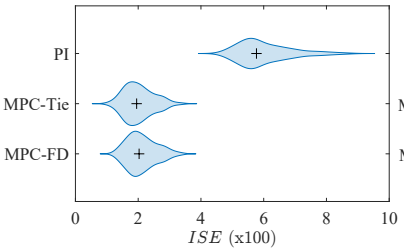

(a) Integral Squared Error.

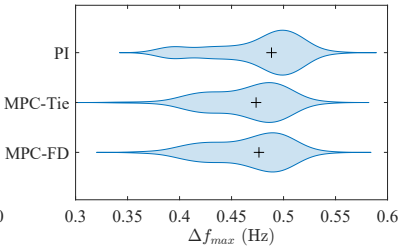

(b) Maximum Frequency Deviation.

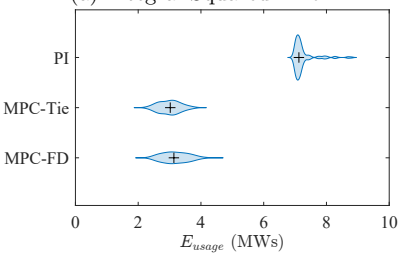

(c) Energy Storage Usage.

Figure 5.20: Results of the robustness analysis of the CIGRE MV distribution network in terms of the performance indices for each control strategy.

showing significantly higher sensitivity to EMT dynamics in the HiL environment (S_i up to 0.61) than the PI controller ($S_i = 0.11$). While the PI scheme suffers from complex parameter interactions and conflicting objectives between its frequency and storage-level control loops, the MPC leverages its multi-objective formulation to maintain a clear sensitivity profile with negligible dependence on GFL response times. However, the high sensitivity to the operating mode suggests that nominal simulations tend to yield overly optimistic results for the MPC's energy capacity requirements.

The high sensitivity of MPC to the EMT dynamics differs significantly to the results in Section 5.1.4. While GSA quantifies this impact, it can not explain the underlying cause. A possible explanation is the assumption of steady voltages close to 1 pu to formulate the power exchange in both prediction models (3.8). In the grid-connected scenario, the grid equivalent is a strong voltage source, limiting voltage deviations. In the islanded system, voltage is purely controlled by the converters and more volatile after sudden load changes, affecting the prediction accuracy of the MPC. Further investigation and a prove of the explanation

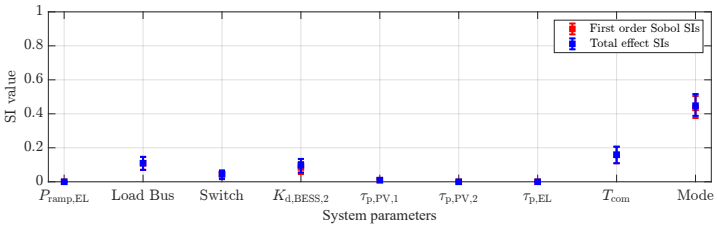

(a) MPC with Frequency Divider model.

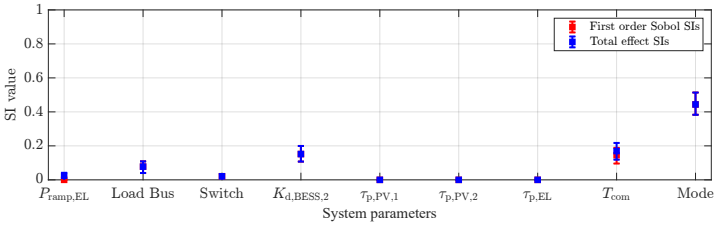

(b) MPC with Tie line model.

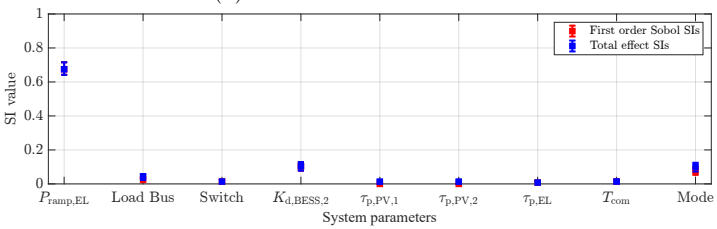

(c) PI controller.

Figure 5.21: Sensitivity analysis results for the ISE in terms of first order Sobol' and total effect SIs.

requires a methodological assessment beyond the scope of this thesis, e.g. through analytical EMT models, providing an avenue for future work.

In conclusion, the robustness and sensitivity study demonstrates that MPC achieves superior robustness and resource efficiency, providing better frequency tracking with significantly lower energy storage requirements than PI control. However, while PI performance is consistent across model fidelities, MPC is more susceptible to performance degradation when transitioning from nominal to high-fidelity EMT environments. This highlights that structural uncertainty (model-

plant mismatch regarding EMT dynamics) is the dominant factor influencing MPC performance in islanded purely converter-driven systems. Conversely, parametric uncertainty, specifically regarding actuator limits like power ramp rates, exerts the strongest influence on classical PI control. Other parametric variations in system topology and converter response times have a negligible impact on the overall performance of either controller.

5.3 Impact of Communication Systems

In this section, the impact of communication systems on the control performance is assessed. The MPC using the Frequency Divider model is extended by the delay- and loss-aware control strategy introduced in Section 4.3, and applied to power systems supplied by GFM converters. In the following, the study design is presented first, before showing the numerical simulation results.

5.3.1 Scenario Description and System Models

To evaluate the delay and loss-aware MPC strategy under realistic conditions, a co-simulation setup between Matlab Simulink and the network simulator ns-3 [135] is used. The co-simulation framework was developed in [136] and enables complex simulation scenarios to evaluate controllers with realistic communication delays and signal losses in combination with a detailed power system simulation. A detailed description of the interface between Matlab Simulink and ns-3 is given in [136]. The proposed delay- and loss-aware MPC strategy is applied to the fast secondary controller for purely converter-driven power systems. It is evaluated in co-simulations of a low-voltage microgrid and a high-voltage transmission system, thereby covering two systems of different scale, including fast and slow power and frequency dynamics, as well as different networking scenarios, i.e. with short and long physical communication distance.

Power system models

The microgrid is modelled using the WSCC 9-bus system topology, which is adapted to low voltage conditions with short line models, and the power and voltage ratings have been reduced respectively. For the high-voltage transmission system, the IEEE 39-bus system is used. In both systems, the SGs are exchanged for generic GFM converter-based RES. The power systems are implemented in the EMT domain using the Specialized Power Systems Library of Matlab Simulink [137]. The system specifications are listed Table 5.11.

The steady-state active power and voltage set-points are considered to be determined by a higher-level control instance. The delay- and loss-aware MPC is responsible for stabilizing and recovering the frequency after disturbance events, as in Section 5.2. For comparison, a PI controller enhanced with a Smith Predictor, as shown in Figure 5.12, is used. The tuning of the PI controller

	Microgrid	Transmission System
System voltage	400 V	345 kV
Number of RES	3	10
RES power rating	100 kW	100 MW

Table 5.11: Overview of the microgrid and transmission system.

relies on a first-order approximation derived from the open-loop step response of the primary-controlled RES. Meanwhile, the Smith Predictor integrates the identified plant transfer function to compensate for the delay. The predictor's delay transfer function, $G_d(z) = z^{-d}$, is designed to be adaptive. The discrete delay d is updated online by calculating the rounded average of the round-trip delay, which is extracted from the time-stamps embedded in the measurement packets.

Network topologies

Two distinct communication network configurations tailored to the scale of the power systems are used in this study. For microgrid applications, such as industrial complexes or local energy communities, the geographic scale is inherently limited. In this scenario, a star topology is implemented. The node hosting the secondary controller (Controller Node (CN)) and all relevant Electrical System Components (ESCs) (specifically RES and Phasor Measurement Units (PMUs)) are linked to dedicated edge routers. These edge components are connected to a central neighborhood router. The star topology is illustrated in Figure 5.22a.

In contrast, the 39-bus system utilizes a regional communication framework based on the Ion network from the Internet Topology Zoo [138]. This model represents a 125-node fiber-optic carrier network covering the region between Boston and New York. The CN is situated at a central node within this topology, while the remaining ESCs are distributed across the area to reflect the geographic positions of the generation nodes in the IEEE 39-bus system. It is conceptually illustrated in Figure 5.22b.

The communication networks are configured to ensure that packets transmitted by the CN and ESCs are subject to realistic bandwidth and delays. It is assumed that the network is not dedicated solely to secondary control, and instead, it is shared with other monitoring and control systems. Consequently, background traffic from SCADA systems, additional PMUs, and other control room applications leads to line congestion and the saturation of router queues. While the core nodes of the Ion network emulate the high throughput and low latency of a backbone system, the edge router links serve as bottlenecks by mimicking the bandwidth, delay, and queue characteristics typical of residential

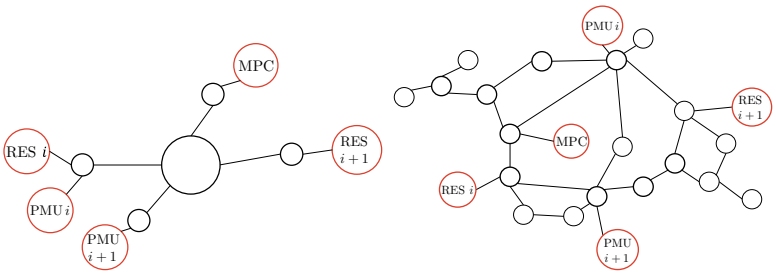

(a) Star topology. (b) Ion network - 125 nodes.

Figure 5.22: Conceptual representation of the communication network topologies.

connections in the United States. The connections between the CN/ESCs and the edge routers are modeled either as wired local Ethernet links with high bandwidth and low error rates, or as ns-3 802.11n WiFi links where losses and delays depend on the distance to the router. Small packets, ranging from three to four digits in bytes, are sent via UDP at each sampling interval. To simulate the resulting fluctuations in packet loss and delay, ns-3 OnOffApplications generate intermittent UDP background traffic to fill the router queues at the bottleneck links. These applications are restricted to wired connections, ensuring they influence queuing dynamics without directly affecting the physical layer of any potential WiFi connections used by the CN/ESCs.

Scenarios and variants

The evaluation of the proposed delay- and loss-aware MPC is conducted for three different network scenarios: fiber, DSL, and wireless. The fiber configuration serves as a near-ideal baseline, characterized by minimal delay and negligible packet dropouts. The DSL setup has a more restrictive bandwidth compared to fiber, which results in increased communication delays. In the wireless configuration, the connectivity for the ESCs, i.e., the RES and PMUs, is further challenged by significant and non-negligible packet loss rates.

To further stress-test the system, four variants are developed for each of these primary scenarios. In the fiber and DSL cases, these variants are defined by a progressive increase in the volume of background traffic. Conversely, the wireless variants do not incorporate background traffic. Instead, the packet loss rate is scaled by increasing the physical distance between the ESCs and the edge routers. An overview of the scenario configurations and the resulting expected average loss rates is provided in Table 5.12.

	Fiber & DSL	Wireless	
	Background traffic	Edge distance	[Exp. avg. loss rate]
A	No traffic	40 m	[6.7%]
B	Low traffic	60 m	[18.3%]
C	Moderate traffic	80 m	[35.3%]
D	Heavy traffic	100 m	[54.3%]

Table 5.12: Overview of the co-simulation scenarios and variants.

5.3.2 Numerical studies of delay- and loss-aware model predictive control

The effect of the communication system and background traffic on the delay characterization is illustrated by plotting the measured packet delay over time for the fiber in the transmission system case in Figure 5.23. The detailed packet delay for the DSL scenario is given in Appendix C. In variant A, the base communication delay is clearly visible. Because the base delay is smaller in the fiber scenario (around 25 ms, Figure 5.23a), compared to the DSL scenario (around 100 ms), the positioning of the RES has a larger impact on the individual channel delay, i.e. from the controller to RES 1, to RES 2 etc. The background traffic introduces significant variance on the packet delay. Some routers are not co-located with traffic applications, and therefore show the constant base delay, even in variants B to D, due to the strong core network. With moderate and heavy traffic, router queues start to fill up, whilst for heavy traffic, many queues become completely filled for an extended time. In the latter case, the packet delay exhibits an upper bound, since packets that arrive at a full queue are lost.

The co-simulation results show that communication delay can not be described through a simple distribution. Packet delay depends strongly on the position of the RES in the network and the presence of network traffic causing congestion and full queues of the network routers. The background traffic also causes correlation in the time-domain, which is visible by the saw tooth-like delay curves for the DSL scenario (Appendix C). Furthermore, the packet delay shows an upper bound, determined by the capacity of the communication network.

The performance of the delay- and loss-aware MPC and the Smith Predictor-based PI controller are evaluated through the average frequency of all GFM converters Δf_{ave}. In this study the IAE, instead of the previously used ISE is employed, since the communication system introduces significant dead times, resulting in unavoidable large frequency deviations during early transients that skew the informative value of this index. As a second index, the recovery time is calculated. This index is defined as the time to recover the frequency within a 0.01 Hz band around the nominal after a disturbance.

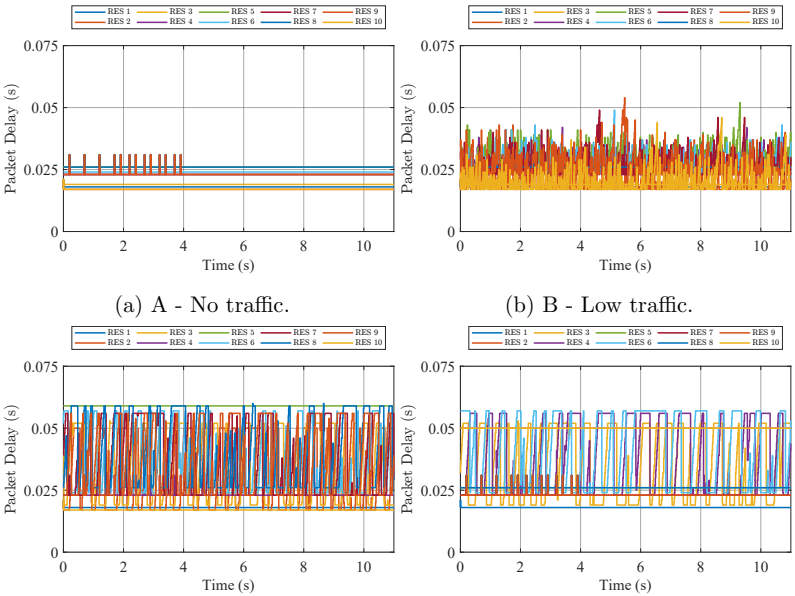

(a) A - No traffic.

(b) B - Low traffic.

(c) C - Moderate traffic.

(d) D - Heavy traffic.

Figure 5.23: Packet delay in the fiber scenario for different levels of network traffic.

The average system frequency of the microgrid across the fiber, DSL, and wireless scenarios is illustrated in Figure 5.24, where variants A and D are shown to represent the best and worst-case performance, respectively. Detailed results in terms of the IAE and frequency recovery times are reported in Table 5.13 and Table 5.14. In the fiber scenario, the proposed MPC demonstrates a performance advantage of approximately 30-45% over the PI controller for both criteria. However, as shown in Figure 5.24a, both control strategies respond effectively to load step changes. An interesting observation arises in variant C, which shows better performance than variant B despite having more background traffic. This occurred because the co-simulation framework co-located only traffic destinations, and no sources, with the RES, meaning that only the incoming control signals were impacted. This indicates that a loss of measurement data has a more detrimental effect on control performance than the loss of control signals themselves.

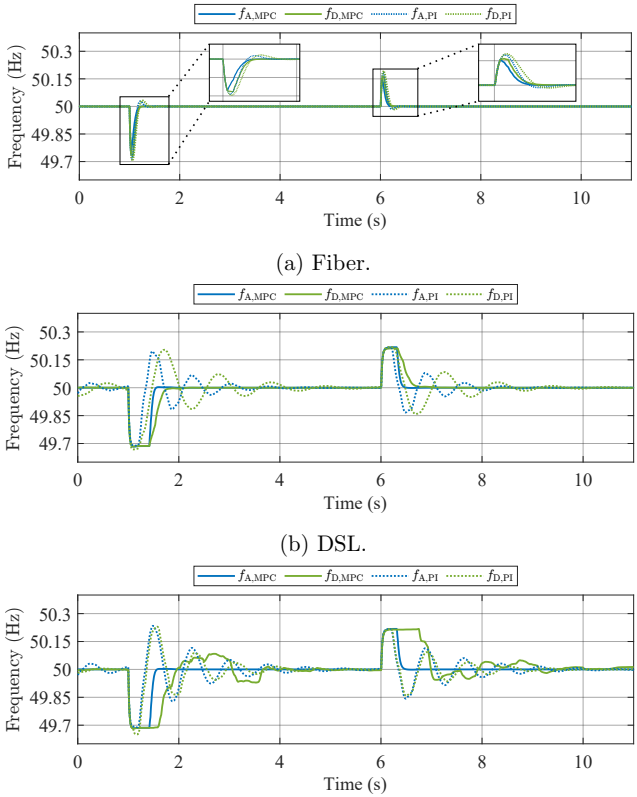

(a) Fiber.

(b) DSL.

(c) Wireless.

Figure 5.24: Average frequency for variants A and D of each scenario in the microgrid case.

A more distinct performance gap between the two controllers is evident in the DSL and wireless environments. The PI controller exhibits a clearly underdamped response. While it remains stable, it suffers from a significantly extended frequency recovery period. The delay-aware MPC provides a well-damped response that substantially outperforms the PI controller in the DSL A-D and wireless A-C scenarios. Specifically, the IAE is improved by 28-50%, and the recovery time is reduced by 60-86%. However, in the wireless D variant,

	Fiber		DSL		Wireless	
	MPC	PI	MPC	PI	MPC	PI
A	3.14	4.97	21.21	31.97	21.47	44.74
B	3.61	5.31	22.07	34.46	21.41	42.78
C	3.15	4.97	22.65	36.42	26.77	37.47
D	4.47	6.37	27.12	47.92	59.65	40.08

Table 5.13: IAE (x100) of the average frequency in the microgrid case.

	Fiber		DSL		Wireless	
	MPC	PI	MPC	PI	MPC	PI
A	0.165	0.279	0.480	2.302	0.487	3.574
B	0.179	0.286	0.497	2.537	0.564	3.358
C	0.166	0.279	0.740	2.631	0.960	2.827
D	0.194	0.342	0.716	3.267	3.899	3.005

Table 5.14: Recovery time [s] of the average frequency in the microgrid case.

which poses an extreme case with a 54.3% expected loss rate, the PI controller demonstrates better performance. It is worth noting that the PI controller's response is generally resilient to packet loss, with its performance in wireless scenarios remaining comparable to that in DSL scenarios. A loss rate of 54.3%, where only about half of the control signals reach the RES, represents a highly unusual and temporary condition for these types of applications. Nevertheless, even under these severe circumstances, the MPC is capable of stabilizing the system and reaching a steady-state, as seen in Figure 5.24c.

The time-domain results for the transmission system are illustrated in Figure 5.25 for the DSL scenario, while the IAE for all scenarios is reported in Table 5.15. The recovery time and time-domain results for the fiber and wireless scenario are given in Appendix C. Here, the delay-aware MPC achieves a reduction in IAE of approximately 20-26% relative to the PI controller, while recovery times are improved by less than 20%. Overall, both control strategies deliver comparable and effective time-domain performance in the transmission system case. A notable difference from the microgrid results is that the transmission system's control performance is largely unaffected by the various communication scenarios. This result can be explained by comparing the system dynamics and control bandwidth of the secondary control systems in both study cases. The microgrid

operates with a secondary controller sampling interval of 20 ms to accommodate its fast system dynamics, while the transmission system utilizes a 100 ms sampling period, reflecting the slower primary RES dynamics at high-voltage levels. Since converter switching frequencies in low-voltage microgrids are often an order of magnitude higher than in high-voltage systems, the transmission level naturally has a lower control bandwidth. Additionally, the longer transmission lines dampen the coupling dynamics between the GFM RES, making the control less vulnerable to delays. Furthermore, while the absolute communication delays, largely introduced at the edge routers, are marginally higher in the transmission case, they represent a smaller fraction of the overall controller sampling time. As a result, the increasing background traffic from variant A to D has no significant negative impact on the IAE or frequency recovery times.

In light of the research questions established in Section 2.3.2, several key conclusions can be drawn from these findings. The results demonstrate that the strategies detailed in Section 4.3 effectively enhance the capability of the MPC to mitigate communication system effects in fast frequency control applications. Specifically, the MPC maintains optimal performance even under high delay and packet loss rates of up to 35%, while remaining stable even at higher rates. Whilst communication systems introduce an unavoidable dead-time into the control loop, as shown in Figure 5.24, the MPC successfully establishes a first-order control response under these conditions. In contrast, the PI controller equipped with a Smith Predictor proves less robust, exhibiting underdamped behavior and pronounced oscillations when subjected to high delays. The comparison between a small-scale microgrid and a large-scale transmission system reveals that communication system effects are more pronounced in smaller systems due to their fast dynamics and higher sampling frequencies. In larger, slower-acting transmission systems, the performance gap between the MPC and traditional PI-based controllers narrows significantly. Consequently, the adoption of MPC in such large-scale contexts should be justified by other operational advantages, such as the enhanced coordination of constrained RES shown in Section 5.2 or the economic efficiencies highlighted in [54].

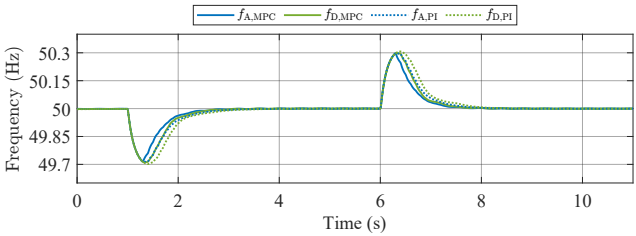

Figure 5.25: Average frequency for variants A and D in the DSL scenario in the transmission system case.

	Fiber		**DSL**		**Wireless**	
	MPC	PI	MPC	PI	MPC	PI
A	20.85	28.19	33.33	41.85	33.29	41.85
B	20.88	28.18	33.52	41.82	33.24	41.78
C	20.92	28.04	35.38	42.72	33.15	41.85
D	21.48	27.84	39.31	48.83	33.66	41.78

Table 5.15: IAE (x100) of the average frequency in the transmission system case.

6 Approaches for Distributed Predictive Frequency Control

In large-scale control problems it can be beneficial to *break* the global control problem into smaller subproblems, and solve for local inputs distributively with local control units. The overall system control is then accomplished through interactions and coordination of the local controllers [8]. In contrast to other distributed control methods, such as consensus-based approaches [139], Distributed Model Predictive Control offers the unique optimal and predictive nature of MPC, together with its capacity to effectively handle constraints. However, the latter comes with increased computational complexity and communication requirements. In this regard, the formulation of the problem and the choice of the algorithm dictate different requirements on the control and communication architecture, as well as, on the necessary measurements from the system [5].

In this chapter, two approaches for DMPC with GFM converters are developed to address the questions in Section 2.3.2. Compared to the literature, the DMPCs model the individual GFMs to avoid the need to disaggregate the control signal of a zone. Also, the dynamic interactions are included in the model, enabling fast control under constraints in a distributed manner.

To this end, the centralized prediction model based on the Frequency Divider is modified. The design of the DMPCs and the distributed optimization algorithms employed to solve the optimal control problems are presented. Finally, the two approaches are evaluated against the centralized implementation and their individual advantages are discussed.

6.1 Modifications of the prediction model

The formulation of a DMPC requires a prediction model that represents the dynamics of the local control unit without requiring global information of the system. The Frequency Divider prediction model (Figure 3.4) features global coupling of the frequency and power dynamics of the system components through the Frequency Divider formula (3.11), which is a fully dense matrix, independent of the system topology. In this section, two methods to reduce the coupling between components in the Frequency Divider model are developed. In the first approach, the power system is divided into control zones, where the dynamics of the local zone are modeled in detail, whereas the neighboring zones are represented by equivalent generators. The second approach manipulates the entries of

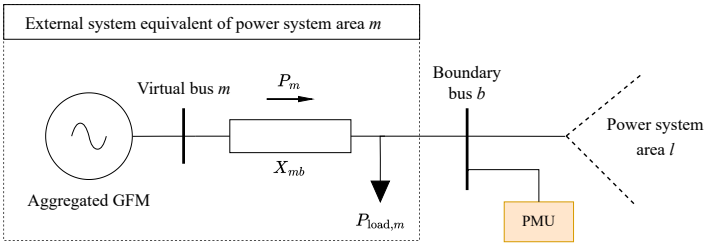

Figure 6.1: External system equivalent for the Distributed Frequency Divider represented by an aggregated generator, equivalent system impedance and the total area load.

the Frequency Divider matrix to reduce ("trim") the global coupling to a specified number of neighbors with the highest impact on the dynamics.

To this end, consider a power system supplied by $i \in \mathcal{N}_{\text{GFM}} = \{1, ..., n_{\text{GFM}}\}$ GFM-based RES, where ω_i is the internal GFM frequency. The vector of generator frequencies is therefore

$$\Delta\omega_{\text{G}} = \begin{bmatrix} \Delta\omega_1 \\ \vdots \\ \Delta\omega_{n_{\text{GFM}}} \end{bmatrix}, \tag{6.1}$$

where $\Delta\omega_i = \omega_i - \omega_{\text{n}}$ is the deviation from the nominal frequency ω_{n}. For simplicity, GFL-based RES and SGs are not explicitly modelled. The developed approaches can however be extended to these components and applied as shown in Chapter 3.

6.1.1 Distributed Frequency Divider

The distributed Frequency Divider framework introduced in [140] partitions the power system into discrete areas, utilizing boundary bus frequency measurements and Thevenin equivalent models for frequency estimation. The Distributed Frequency Divider approach [140] is adopted to decompose the centralized model (3.13) into partitioned submodels. The methodology is further extended by enhancing the Thevenin equivalent to capture external control dynamics, thereby facilitating its use as a predictive model within DMPC frameworks.

An area of the power system is denoted by $l \in \mathcal{N}_{\text{Areas}}$ and contains $n_{\text{GFM},l}$ GFM units. The set of neighboring areas for area l is defined as $m \in \mathcal{N}_{\text{Neigh},l} = \{\text{A1}, \text{A2}, ..., \text{An}_{m,l}\}$, with each neighbor containing $n_{\text{GFM},m}$ GFM units. As illustrated in Figure 6.1, the neighboring system is represented as an aggregated GFM located behind an equivalent system impedance X_{mb}, which accounts for

the total area load $P_{\text{load},m}$. The resulting state equations for the aggregated GFM are analogous to the VSM state equations defined in (3.17).

$$\dot{P}_m = K_{\text{c},mb}\Delta\omega_m - K_{\text{c},mb}\Delta\omega_{\text{b}}, \tag{6.2a}$$

$$\Delta\dot{\omega}_m = -\frac{D_{\text{p},m}}{T_{\text{A},m}}\Delta\omega_m - \frac{1}{T_{\text{A},m}}P + \frac{1}{T_{\text{A},m}}P^*. \tag{6.2b}$$

The frequency ω_b at boundary bus b is determined by applying the Frequency Divider matrix for power system area l, which is augmented with the frequency ω_m of the aggregated GFM.

Consequently, the partitioned submodel for power system area l is formulated as follows:

$$\dot{x}_l = A_l x + B_l u_l, \tag{6.3a}$$

$$y_l = C_l x_l, \tag{6.3b}$$

with the state, input and output vectors

$$x_l = \left[\Delta\omega_1, ..., \Delta\omega_{n_{\text{GFM},l}}, \Delta P_1, ..., \Delta P_{n_{\text{GFM},l}}, \Delta\omega_m, \Delta P_m\right]^{\text{T}}, \tag{6.4a}$$

$$u_l = \left[\Delta P_1^*, ..., \Delta P_{n_{\text{GFM},l}}^*, \Delta P_m^*\right]^{\text{T}}, \tag{6.4b}$$

$$y_l = \left[\Delta\omega_1, ..., \Delta\omega_{n_{\text{GFM},l}}, \Delta P_1, ..., \Delta P_{n_{\text{GFM},l}}, \Delta P_m, \Delta\omega_b\right]^{\text{T}} \tag{6.4c}$$

The matrices A_l and B_l are derived from the area l prediction model (as in Chapter 3) and are augmented with the states of the neighboring area's equivalent generator (6.2). The set-point ΔP_m^* represents the aggregated power requested by area l from neighboring area m. Consistent with the centralized implementation in Chapter 4, the measured outputs consist of the frequency $\Delta\omega_i$ and power ΔP_i of the internal GFMs units. Furthermore, the equivalent inertia $T_{\text{A},m}$, damping constant $D_{\text{p},m}$, and total generation measurement ΔP_m are shared by the control units. The external system frequency $\Delta\omega_m$ is subsequently determined from the boundary bus measurement $\Delta\omega_b$ using the Distributed Frequency Divider method described in [140].

The calculation of the augmented admittance and Distributed Frequency Divider matrices requires the Thevenin equivalent impedance. While an online recursive estimation method is proposed in [140] to account for converter impedance uncertainty, this work employs a wideband-frequency impedance measurement procedure for the parameterization of the external system equivalent, as detailed in Section 6.2.1.

Through the application of the Distributed Frequency Divider approach, the detailed frequency and power dynamics of individual components within a specific power system area are retained, while the influence of neighboring areas on local

dynamics is simultaneously captured. This method necessitates only the exchange of aggregated information from neighboring areas, which simplifies data communication and reduces both sensitivity and vulnerability to data inaccuracies.

6.1.2 Frequency Divider Trimming

In this section, a procedure is presented to remove entries in the Frequency Divider matrix F with the goal of eliminating coupling dynamics between individual components in the Frequency Divider prediction model. In particular, the procedure removes negligible entries while preserving the physical interpretability of the frequency values. It is further shown how the resulting model can be partitioned into partly coupled submodels. The submodels are later used to develop a fully distributed control scheme, where each GFM is equipped with a distributed control unit.

An entry $F_{(r,i)}$ within the Frequency Divider matrix quantifies the contribution of a specific generation frequency ω_i to an arbitrary bus frequency ω_r. Since the calculation is derived from the nodal admittance matrix, the value of $F_{(r,i)}$ is determined by the electrical distance between the corresponding buses. A higher impedance results in a lower numerical value for $F_{(r,i)}$. In large-scale systems, where the electrical distance between certain generator-bus pairs is substantial, $F_{(r,i)}$ becomes negligible. Under such conditions, the impact of distant generators on local node dynamics is minimal. By approximating these entries to zero, the local frequency is rendered dependent only on electrically proximal generators, thereby eliminating the state couplings introduced by (3.13).

This procedure, defined as *Frequency Divider Trimming*, consists of two stages. First, specific criteria are applied to set selected entries of F to zero, resulting in the matrix F^{elim}. Second, the rows of F^{elim} are scaled to produce the trimmed Frequency Divider matrix F^{trim}. Specifically, each row is scaled to ensure a row sum of 1 using the following formula:

$$F^{\text{trim}}_{(r,i)} = \frac{F^{\text{elim}}_{(r,i)}}{\sum_{r=1}^{(n_b - n_{\text{GFM}})} F^{\text{elim}}_{(r,i)}}, \quad r \in \mathbb{N}_{[1,(n_b - n_{\text{GFM}})]}, i \in \mathbb{N}_{[1,n_{\text{GFM}}]}. \tag{6.5}$$

The matrices F^{elim} and F^{trim} are defined as $(n_b - n_{\text{GFM}}) \times n_{\text{GFM}}$ dimensions, where n_b represents the total number of buses in the grid.

As established in (3.11), a specific bus frequency ω_r is calculated by the product of the corresponding Frequency Divider matrix row F_r and the generator frequency vector ω_{G}, representing a weighted average of all generation frequencies. Row scaling is therefore performed to ensure that each bus frequency estimated via F^{trim} maintains a cumulative weight of 1, thereby preserving the physical interpretability of the model post-trimming.

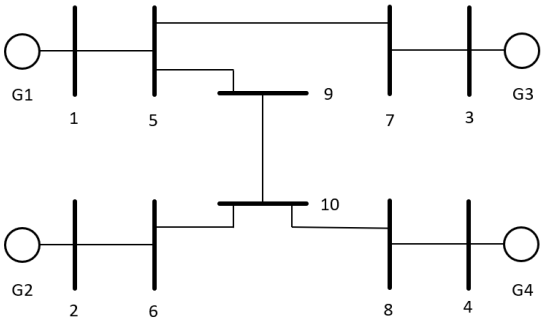

Figure 6.2: Single-line representation of a power system with four generators.
© 2024 IEEE. Reprinted, with permission, from [J2].

Frequency Divider Trimming facilitates the adjustment of dynamic coupling levels within the prediction model. The elimination of entries is governed by two distinct criteria, defined as follows:

1. Define an elimination threshold th.
2. Define a minimum number of neighbors $\mathcal{N}_{\min}$ to be retained.
3. Obtain F^{elim}: If the number of (non-zero) entries in a row F_r remains greater than $\mathcal{N}_{\min}$, set to zero entries $F_{(r,i)} \leq th$, starting with the smallest entry.

To illustrate the procedure, an exemplary power system is considered as shown in Figure 6.2, which comprises four generators and ten buses. Generators G_1 through G_4 are connected to buses 1 through 4, respectively. In this configuration, ω_{G} represents the generation frequencies ω_1 through ω_4. The frequencies of the remaining buses are determined by the Frequency Divider formula as follows:

$$\begin{bmatrix}\omega_5 & \omega_6 & \omega_7 & \omega_8 & \omega_9 & \omega_{10}\end{bmatrix}^{\text{T}} = F \begin{bmatrix}\omega_1 & \omega_2 & \omega_3 & \omega_4\end{bmatrix}^{\text{T}}. \tag{6.6}$$

Evaluating the Frequency Divider for ω_6, ω_7, and ω_9 yields

$$\omega_6 = 0.15\omega_1 + 0.75\omega_2 + 0.02\omega_3 + 0.08\omega_4 \tag{6.7a}$$
$$\omega_7 = 0.13\omega_1 + 0.03\omega_2 + 0.82\omega_3 + 0.02\omega_4 \tag{6.7b}$$
$$\omega_9 = 0.5\omega_1 + 0.22\omega_2 + 0.1\omega_3 + 0.18\omega_4. \tag{6.7c}$$

The values of the Frequency Divider entries correspond to the electrical distance between respective buses. For instance, the frequency ω_6 is primarily influenced by ω_2 due to the physical proximity of bus 6 and bus 2. In contrast, the contribution of ω_3 to ω_6 is minimal, reflecting the significant electrical distance

separating these nodes. Similar observations apply to the relationships involving ω_7 and ω_9.

For the Frequency Divider Trimming procedure, the parameters th=5% and $\mathcal{N}_{\min} = 2$ are selected. This trimming process results in the matrix F^{trim}. Evaluating the trimmed Frequency Divider for the previously noted frequencies yields:

$$\omega_6 \approx 0.153\omega_1 + 0.765\omega_2 + 0\omega_3 + 0.082\omega_4 \tag{6.8a}$$

$$\omega_7 \approx 0.133\omega_1 + 0.031\omega_2 + 0.837\omega_3 + 0\omega_4 \tag{6.8b}$$

$$\omega_9 = 0.5\omega_1 + 0.22\omega_2 + 0.1\omega_3 + 0.18\omega_4. \tag{6.8c}$$

These three frequencies demonstrate the practical application of the trimming criteria. For ω_6, the influence of ω_3 is neglected, thereby removing the coupling between these two frequencies, while the 5% threshold prevents the elimination of the contribution from ω_4. In the case of ω_7, although the influences of both ω_2 and ω_4 fall below the threshold, the constraint $\mathcal{N}_{\min} = 2$ ensures that only the smaller contribution from ω_4 is removed. Conversely, for ω_9, the trimming process does not eliminate any coupling because bus 9 maintains an intermediate electrical distance to all generators.

In summary, th and $\mathcal{N}_{\min}$ serve as tuning parameters for the systematic Frequency Divider Trimming, allowing for varying degrees of entry elimination in F. The threshold criterion ensures the removal of negligible frequency couplings, while the minimum neighbor criterion establishes a baseline for the connectivity persisting after the procedure. By substituting F with F^{trim}, a centralized prediction model is constructed with reduced state coupling between the various GFMs units.

Partitioning

Frequency Divider Trimming reduces interactions within the prediction model, ensuring that state coupling is no longer global. However, because each component maintains an individual set of coupled neighbors and these sets overlap, executing the model over the prediction horizon still results in globally coupled dynamics. Consequently, the MPC decision variables cannot be directly distributed in this state. To obtain a representation suitable for a DMPC scheme, the model must be partitioned following the trimming procedure.

Inspired by the methodology in [56], the individual partitioned prediction models are constructed as follows:

$$x^{(i)}(k+1) = A^{(i)}x^{(i)}(k) + B^{(i)}u^{(i)}(k) \tag{6.9a}$$

$$y^{(i)}(k) = C^{(i)}x^{(i)}(k). \tag{6.9b}$$

In this formulation, $x^{(i)}$ is a stacked vector containing the states $\{x_i, \{x_j\}_{j\in\mathcal{N}_{j,i}}\}$, where x_i represents the states of a specific component and x_j the states of

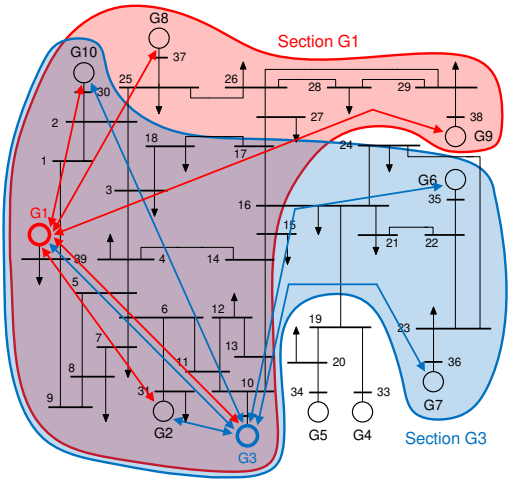

Figure 6.3: Construction of partitioned models for generators 1 and 3 in the IEEE 39-bus system.

its coupled neighbors. The set of neighbors $\mathcal{N}_{j,i}$ is determined by the coupling remaining after Frequency Divider Trimming. Specifically, these neighbors correspond to the generator frequencies required to evaluate (3.13) using F^{trim}. It is noted that Frequency Divider Trimming with a specified $\mathcal{N}_{\text{min}}$ ensures that $|\mathcal{N}_{j,i}| \geq \mathcal{N}_{\text{min}}$ for all GFMs i. Analogous to the state vector, the input vector $u^{(i)}$ is defined as $u^{(i)} = \{u_i, \{u_j\}_{j \in \mathcal{N}_{j,i}}\}$.

The partitioned prediction models represent localized sections of the power system. The trimming parameters *th* and $\mathcal{N}_{\text{min}}$ determine the extent of these sections and are tuned to ensure they overlap. This overlap facilitates partial coupling between the individual partitioned prediction models. Consequently, the submodels, and by extension the DMPC control units, share a subset of variables, particularly control inputs, with multiple but not all other partitioned models. This structure enables the distributed control system to converge toward a globally coordinated control action.

The partitioning approach is illustrated in Figure 6.3, which highlights the specific sections for generators 1 and 3 within the IEEE 39-bus system. In this configuration, the partitioned prediction models for both generator 1 and generator 3 each incorporate an individual set of five neighbors. Generators 1, 2, 3, and 10 constitute the overlapping portion of these sections and are included in the prediction models of both generator 1 and generator 3. On the contrary,

generators 8 and 9 are included exclusively in the model for generator 1, while only the model for generator 3 accounts for coupling with generators 6 and 7. Notably, neither of these two specific partitions considers the dynamics of generators 4 and 5. Consistent with the sections shown for generators 1 and 3, all other generators within the system are associated with individual grid sections, resulting in ten partially overlapping partitions.

The comprehensive procedure for deriving these partitioned prediction models is summarized in Algorithm 6.3.

Frequency Divider Trimming Sensitivity Analysis

A quantitative study is performed to evaluate the impact of Frequency Divider Trimming, specifically examining how the elimination threshold th and the minimum number of neighbors $\mathcal{N}_{\min}$ affect prediction model accuracy. The IEEE 39-bus system described in Section 5.3.1 serves as the test case. A total of 25 trimming configurations are investigated, with th ranging from 2.5% to 10% and $\mathcal{N}_{\min}$ ranging from 1 to 5. For each case, the proposed trimming procedure is applied and the resulting F^{trim} matrices are stored. The coupling graphs exhibit high connectivity for low th and high $\mathcal{N}_{\min}$ values, becoming increasingly sparse as the threshold rises and the neighbor requirement decreases. Consequently, trimming effectively removes numerous component couplings when th is high and $\mathcal{N}_{\min}$ is low.

To quantify the impact of these adjustments, a quasi-Monte Carlo simulation approach utilizing Halton sequences is conducted. These sequences facilitate the generation of randomized load steps at buses 12, 15, 16, 23, 24, and 27, with magnitudes bounded by $P_{\text{step,min}}$ and $P_{\text{step,max}}$. The cumulative worst-case load step equals 525 MW. The use of Halton sequences ensures uniform, unbiased coverage of the load step scenarios. Across 70 simulation runs, the normalized Root Mean Square Error (RMSE) of the frequency estimation for each F^{trim} matrix is determined by comparison with the PMU frequency at each GFM terminal bus. Additionally, the RMSE for the original, non-trimmed Frequency Divider is calculated. For clear visualization, the RMSE of each trimming case is scaled relative to the RMSE of the non-trimmed model.

$$\text{RMSE}_{\text{trim,scaled}} = \frac{\text{RMSE}_{F^{\text{trim}}}}{\text{RMSE}_{F}} \tag{6.11}$$

To evaluate the aggregate impact of the different trimming configurations, the scaled variable $\text{RMSE}_{\text{trim,scaled}}$, averaged across all GFM terminal buses, is analyzed. As illustrated in Figure 6.4, the scaled RMSE for any given $\mathcal{N}_{\min}$ approaches unity as the threshold th decreases. Conversely, for a fixed th, increasing $\mathcal{N}_{\min}$ similarly drives the scaled RMSE toward 1. Configurations yielding a scaled RMSE near 1 are characterized by a high degree of coupling, whereas those with

Algorithm 6.3: Construction of partitioned prediction models via Frequency Divider Trimming.

Input: Frequency Divider matrix F, elimination threshold th, minimum number of neighbors $\mathcal{N}_{\min}$

1) Extract all rows F_g corresponding to terminal buses from F to obtain the matrix F_{G}:

$$F_{\mathrm{G}} \coloneqq \begin{bmatrix} -F_{g_1} - \\ \vdots \\ -F_{g_{n_{\mathrm{GFM}}}} - \end{bmatrix} \tag{6.10}$$

2) Trim F_{G} using the following criteria:

a) Only entries $\leq th$ are trimmed

b) Each row has at least $\mathcal{N}_{\min} + 1$ entries that are $\neq 0$

c) All couplings after trimming must be bidirectional:

If an entry in row g and column i is non-zero after trimming, the entry in the row corresponding to the terminal bus of i and the column corresponding to the GFM of g is also non-zero.

for $i \in \mathcal{N}_i$ **do**

3) Use $F_{\mathrm{G}}^{\mathrm{trim}}$ to construct individual submatrices $F^{(i)}$ for each GFM:

a) Define the neighborhood of GFM $i, \overline{\mathcal{N}_{j,i}}$:

If $F_{\mathrm{G}(i,j)}^{\mathrm{trim}} \neq 0$, GFM j is in the neighborhood of GFM i. By definition, $i \in \overline{\mathcal{N}_{j,i}} = \left\{i, \mathcal{N}_{j,i}\right\}$.

b) Remove all rows of $F_{\mathrm{G}}^{\mathrm{trim}}$ which correspond to buses outside of $\overline{\mathcal{N}_{j,i}}$.

c) Remove all columns $j \notin \overline{\mathcal{N}_{j,i}}$.

d) To obtain $F^{(i)}$, scale all rows of the remaining matrix, such that each row has a row sum of 1.

4) Construct GFM i's partitioned prediction model (6.9) analog to the centralized prediction model using $F^{(i)}$.

end for

a higher RMSE utilize a simplified coupling scheme. Consequently, the selection of th and $\mathcal{N}_{\min}$ represents a definitive trade-off between estimation accuracy and the complexity of dynamic couplings.

To assess the precision of F^{trim} at individual GFM terminal buses, the scaled RMSE is evaluated for three specific trimming scenarios: Case 1 ($th = 10\%$, $\mathcal{N}_{\min} = 1$), which produces a disconnected coupling graph; Case 2 ($th = 5\%$,

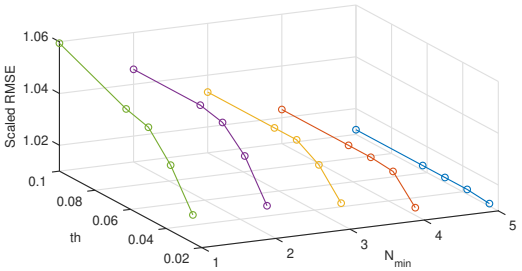

Figure 6.4: Scaled RMSE over all buses as threshold and minimum number of neighbors are varied in Frequency Divider Trimming.
© 2024 IEEE. Reprinted, with permission, from [J2].

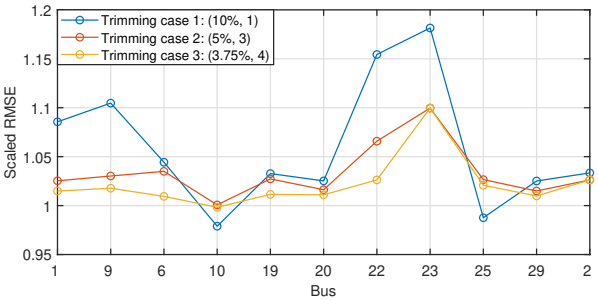

Figure 6.5: Scaled RMSE at all GFM terminal buses in the IEEE-39-bus system.
© 2024 IEEE. Reprinted, with permission, from [J2].

$\mathcal{N}_{\min} = 3$); and Case 3 ($th = 3.75\%$, $\mathcal{N}_{\min} = 4$), which maintains a complex coupling structure. The resulting scaled RMSE for each terminal bus across these cases is presented in Figure 6.5. The highest error is observed in case 1, while cases 2 and 3 exhibit comparable accuracy for most buses. These findings suggest that further reductions in the threshold or increases in the minimum neighbor requirement do not yield significant improvements in RMSE, yet they substantially increase the number of coupling links, thereby diminishing the practical utility of the model.

The impact of Frequency Divider Trimming is further examined through time-domain simulations. In these tests, frequency measurements obtained from a PMU and estimations from the original Frequency Divider are compared against the results from trimming cases 1 and 2. The simulation scenario incorporates a

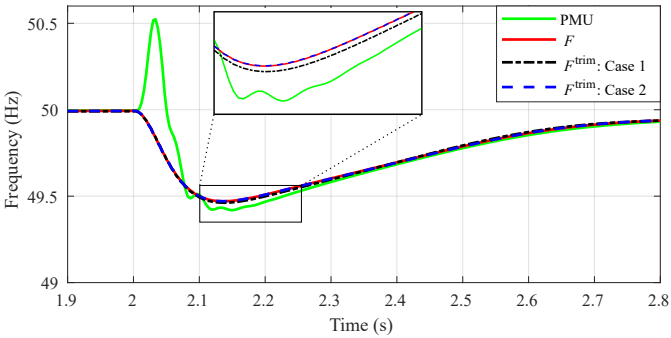

Figure 6.6: Comparison of frequency estimations at bus 10 in the IEEE 39-bus system after a load step.

load step at $t = 2\,\text{sec}$. As illustrated in Figure 6.6, the results for bus 10 indicate that both case 1 and case 2 align closely with the non-trimmed Frequency Divider F. However, the magnified view reveals that the frequency estimation for case 2 is closer to F than case 1. These observations are consistent across all GFM terminal buses.

6.2 Design of the Distributed Model Predictive Control

In this section, the design of the Distributed Model Predictive Control strategies is presented. Based on the partitioned prediction models, global optimal control problems of partitioned structure are formulated, which can be solved using distributed optimization algorithms.

6.2.1 Distributed control based on Distributed Frequency Divider

The distributed MPC framework, utilizing the Distributed Frequency Divider model (6.3), is formulated for each individual control zone within the power system. The DMPC employs dual decomposition [141] to dynamically optimize the set-points ΔP_i^* for all $i \in \mathcal{N}_{\text{GFM}}$. As detailed in [141], dual decomposition methods partition global optimization problems into smaller subproblems that are solved iteratively in parallel. This approach introduces dual variables, specifically Lagrange multipliers, to enforce constraint satisfaction and steer the iterative process toward a globally optimal solution.

A discrete-time framework is adopted, where k denotes the discrete-time index. Accordingly, $x_l(k)$, $u_l(k)$, and $y_l(k)$ represent the state, input, and output of power system area l at instant k, respectively. Within this context, the following objective function is defined for each area l:

$$\ell_l(k) = y_l^{\mathrm{T}}(k+1)\, Q_l\, y_l(k+1) + \Delta u_l^{\mathrm{T}}(k)\, R_l\, \Delta u_l(k). \tag{6.12}$$

The weighting matrices Q_l and R_l are defined as positive definite, while $\Delta u_l(k)$ represents the input increment between consecutive time steps, such that $\Delta u_l(k) = u_l(k) - u_l(k-1)$.

Coupling constraints are established to ensure that the power injected into a neighboring area m matches the power requested by the control unit of area l. Specifically, these constraints enforce that the sum of the set-points within the detailed system representation of control unit m equals the set-point of the area equivalent for m as modeled in control unit l. These coupling constraints are defined as follows:

$$\Delta P_m^*(k) = \sum_{r=1}^{n_{\mathrm{GFM},m}} \Delta P_r^*(k) \quad \forall m \in \mathcal{N}_{\mathrm{Neigh},l}. \tag{6.13}$$

It is noted that a symmetrical formulation for each control unit yields $2 \times n_{m,l}$ coupling constraints. For simplicity, the DMPC investigated in this thesis focuses on a two-area configuration, designated as areas A1 and A2, such that $n_{m,l} = 1$. Considering this, the control problem is structured to prioritize the satisfaction of the coupling constraints defined in (6.13) alongside performance optimization. Specifically, the global optimization problem to be solved at each time instant k is formulated as follows:

$$\min_{\mathbf{u}_{\mathrm{A1}},\mathbf{u}_{\mathrm{A2}}} \sum_{n=k}^{H_{\mathrm{p}}-1} \left(\ell_{\mathrm{A1}}(n|k) + \ell_{\mathrm{A2}}(n|k)\right) \tag{6.14a}$$

$$\text{s.t.} \quad x_l(n+1|k) = A_{l,\mathrm{k}} x(n|k) + B_{l,\mathrm{k}} u_l(n|k), \tag{6.14b}$$

$$y(n|k) = C_{l,\mathrm{k}} x_l(n|k), \tag{6.14c}$$

$$\Delta P_{i,\min}^* \le \Delta P_i^*(n|k) \le \Delta P_{i,\max}^*, \tag{6.14d}$$

$$\Delta P_{i,\min} \le \Delta P_i(n+1|k) \le \Delta P_{i,\max}, \tag{6.14e}$$

$$dP_{i,\min} \le dP_i(n+1|k) \le dP_{i,\max}, \tag{6.14f}$$

$$\Delta P_{\mathrm{A1}}^*(n|k) = \sum_{o=1}^{n_{\mathrm{GFM,A1}}} \Delta P_o^*(n|k), \tag{6.14g}$$

$$\Delta P_{\mathrm{A2}}^*(n|k) = \sum_{r=1}^{n_{\mathrm{GFM,A2}}} \Delta P_r^*(n|k). \tag{6.14h}$$

$$n \in \{k, ..., H_{\mathrm{p}} - 1\}, \quad l \in \mathcal{N}_{\mathrm{Areas}} = \{\mathrm{A1}, \mathrm{A2}\},$$

$$i \in \mathcal{N}_{\mathrm{GFM}} = \{1, ..., n_{\mathrm{GFM,A1}}\} \cup \{1, ..., n_{\mathrm{GFM,A2}}\}$$

The notation $(n|k)$ denotes the prediction of a variable for time n generated at instant k. The sequences of current and future control inputs to be optimized are

defined as $\mathbf{u}_{\mathrm{A1}}$ and $\mathbf{u}_{\mathrm{A2}}$, specifically $\left[u_l(k|k), u_l(k+1|k), ..., u_l\big(k+H_p-1|k\big)\right]^{\mathrm{T}}$ for $l \in \{\mathrm{A1}, \mathrm{A2}\}$.

The feasible sets determined by the local constraints of areas A1 and A2 in the optimization problem (6.14) are represented by $\mathcal{F}_{\mathrm{A1}}$ and $\mathcal{F}_{\mathrm{A2}}$, respectively. Furthermore, the coupling constraints (6.14g) and (6.14h) may be condensed into a single matrix equality involving the variables $\mathbf{u}_{\mathrm{A1}}$ and $\mathbf{u}_{\mathrm{A2}}$. The resulting reformulation is expressed as follows:

$$G_1\mathbf{u}_{\mathrm{A1}} + G_2\mathbf{u}_{\mathrm{A2}} = 0, \tag{6.15}$$

The matrices G_1 and G_2 are constructed such that (6.15) accounts for both (6.14g) and (6.14h). Based on this, the optimization problem (6.14) can be compactly reformulated as follows:

$$\min_{\mathbf{u}_{\mathrm{A1}}\in\mathcal{F}_{\mathrm{A1}}, \mathbf{u}_{\mathrm{A2}}\in\mathcal{F}_{\mathrm{A2}}} \; J_1(x_{\mathrm{A1}}(k), \mathbf{u}_{\mathrm{A1}}) + J_2(x_{\mathrm{A2}}(k), \mathbf{u}_{\mathrm{A2}}) \tag{6.16a}$$

$$\text{s.t.} \quad G_1\mathbf{u}_{\mathrm{A1}} + G_2\mathbf{u}_{\mathrm{A2}} = 0. \tag{6.16b}$$

The functions $J_1(\cdot)$ and $J_2(\cdot)$ are derived by substituting the model equations (6.14b) and (6.14c) into the objective function definition, as detailed in Chapter 2. The Lagrangian for the compact optimization problem (6.16) is defined as follows:

$$\begin{aligned}\mathcal{L}(\mathbf{u}_{\mathrm{A1}}, \mathbf{u}_{\mathrm{A2}}, \lambda) = \\ J_1(x_{\mathrm{A1}}(k), \mathbf{u}_{\mathrm{A1}}) + J_2(x_{\mathrm{A2}}(k), \mathbf{u}_{\mathrm{A2}}) + \lambda^\top(G_1\mathbf{u}_{\mathrm{A1}} + G_2\mathbf{u}_{\mathrm{A2}}) \\ = \underbrace{J_1(x_{\mathrm{A1}}(k), \mathbf{u}_{\mathrm{A1}}) + \lambda^\top G_1\mathbf{u}_{\mathrm{A1}}}_{\mathcal{L}_{\mathrm{A1}}(x_{\mathrm{A1}}(k), \mathbf{u}_{\mathrm{A1}}, \lambda)} + \underbrace{J_2(x_{\mathrm{A2}}(k), \mathbf{u}_{\mathrm{A2}}) + \lambda^\top G_2\mathbf{u}_{\mathrm{A2}}}_{\mathcal{L}_{\mathrm{A2}}(x_{\mathrm{A2}}(k), \mathbf{u}_{\mathrm{A2}}, \lambda)}\end{aligned} \tag{6.17}$$

The dual variable λ represents a vector of Lagrange multipliers. The dual decomposition algorithm utilized to solve (6.14) involves an iterative procedure in which the control units optimize their respective input sequences and exchange their results to update the multipliers. Using the superscript p to denote the iteration count, and starting from the initial multipliers λ^0, the control units perform the following steps at each time instant k:

$$\mathbf{u}_l^{*,p} = \mathrm{argmin}_{\mathbf{u}_l\in\mathcal{F}_l}\mathcal{L}_l(x_l(k), \mathbf{u}_l, \lambda^p), \quad l \in \{\mathrm{A1},\mathrm{A2}\}, \tag{6.18a}$$

$$\lambda^{p+1} = \lambda^p + \alpha(G_1\mathbf{u}_{\mathrm{A1}}^{*,p} + G_2\mathbf{u}_{\mathrm{A2}}^{*,p}), \tag{6.18b}$$

This iterative process continues until the algorithm converges to a solution. In (6.18b), the parameter $\alpha > 0$ serves as a tuning factor that regulates the update rate of the dual variables.

For the practical implementation, the sampling time of the DMPC is set to $T_s = 0.1$ s, while both the prediction and control horizons are defined as $H_p = H_c = 3$ to facilitate fast convergence. The specific parameters for the objective function are detailed in Table 6.1. The control strategy prioritizes tracking frequency variables to their nominal references, while ensuring converter power outputs remain within their rated constraints. The step size for the Lagrangian

Variable	Weight $\boldsymbol{Q}$ / $\boldsymbol{R}$	Set point [pu]	Minimum [pu]	Maximum [pu]
$\omega_{\mathrm{GFM},i}$	1000	1	-	-
$P_{\mathrm{GFM},i}$	0	0.6	0	1
$\Delta P^{*}_{\mathrm{GFM},i}$	0.1	0	-0.6	0.4

Table 6.1: Objective function parameters of the zone-based DMPC, using the Distributed Frequency Divider model.

multiplier update is set at $\alpha = 0.02$. It is critical to note that an excessively small α significantly increases the number of iterations required for convergence, whereas an overly large value may cause the individual optimization problems to diverge.

Estimation of network impedance

The parametrization of the external system equivalent for the Distributed Frequency Divider-based prediction model necessitates determining the equivalent impedance of the partitioned areas. This equivalent impedance allows for the independent computation of the Frequency Divider matrix for each area. To this end, different impedance estimation algorithms could be implemented, such as [134]. In this work, a Wideband-Frequency impedance (WFZ) measurement device connected at the boundary bus is used. The WFZ device is a three-phase converter equipped with a DC-link capacitor. It initially synchronizes with the power system and utilizes DC-link voltage control to maintain the capacitor's voltage level [142], [143]. Upon triggering an impedance measurement, the device injects small-signal wideband perturbation currents by modulating the steady-state duty cycle with a Pseudo-Random-Binary-Sequence (PRBS) of small amplitude for N_s samples. Under the assumption that the power system impedance remains steady during this interval, the impedance is computed as follows:

$$Z(j\omega) = \frac{V_{\mathrm{pert}}(j\omega) - V_{\mathrm{no,pert}}(j\omega)}{I_{\mathrm{pert}(j\omega)} - I_{\mathrm{no,pert}}(j\omega)} = \frac{\Delta V(j\omega)}{\Delta I(j\omega)} \tag{6.19}$$

In (6.19), $V_{\mathrm{pert}}(j\omega)$ and $I_{\mathrm{pert}}(j\omega)$ represent the fast Fourier transform (FFT) of the voltage and current during the perturbation phase, while $V_{\mathrm{no,pert}}(j\omega)$ and $I_{\mathrm{no,pert}}(j\omega)$ represent the FFT of the voltage and current during the observation phase. A more detailed characterization of the WFZ device is provided in [133].

In this specific application, calculating the impedance of the partitioned areas requires measuring the boundary bus voltage V_b alongside the currents exiting the

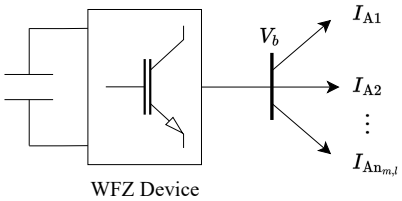

Figure 6.7: Wideband-frequency impedance estimation device setup.

partition node, namely I_{A1} and I_{A2}. This measurement configuration is illustrated in Figure 6.7. The non-parametric impedance for each area m is then computed as follows:

$$Z_m(j\omega) = \frac{\Delta V_b(j\omega)}{\Delta I_m(j\omega)} \tag{6.20}$$

For the specific requirements of the DMPC, the Frequency Divider calculation necessitates only the imaginary component of the impedance at 50 Hz. Consequently, the impedance value is extracted precisely at $\Im\big(Z_{m(j\omega_n)}\big)$. This simplification focuses the model on the inductive and capacitive characteristics of the network that dominate frequency dynamics, effectively ignoring resistive losses that have a secondary impact on frequency distribution.

6.2.2 Distributed control based on Frequency Divider Trimming

In this section, a fully distributed MPC scheme is constructed, where each GFM is governed by its own dedicated DMPC unit utilizing the partitioned prediction models derived in Section 6.1.2. The resulting optimal control problem adopts a partition-based structure, characterized by the overlapping of individual decision variables as described in [144]:

$$\min_{\{\mathcal{U}_i\}_{i\in\mathcal{N}_i}} \sum_{i=1}^{n_i} J_i\Big(\{\mathcal{U}_i, \{\mathcal{U}_j\}_{j\in\mathcal{N}_{j,i}}\}\Big) \tag{6.21a}$$

$$s.t. \quad \underbrace{\Big\{\mathcal{U}_i, \{\mathcal{U}_j\}_{j\in\mathcal{N}_{j,i}}\Big\}}_{\mathcal{U}^{(i)}} \in \mathcal{C}_i \quad \forall i \in \mathcal{N}_i. \tag{6.21b}$$

In this framework, the DMPC control unit for each GFM i optimizes a local cost function J_i relative to its local constraint set $\mathcal{C}_i$. Both the cost function and constraints are dependent on the local decision variables $\mathcal{U}_i$ as well as those of neighboring peers $\mathcal{U}_j$, which together constitute the partitioned decision vector $\mathcal{U}^{(i)}$. The global optimal solution vector $\mathcal{U}^*$ is comprised of the individual optimal components $\mathcal{U}_i^*$ [145].

The coupling of decision variables within the local problems in (6.21) mirrors the state coupling observed in the respective prediction models. Consequently, the selection of the Frequency Divider Trimming parameters, th and $\mathcal{N}_{\min}$, is critical, as it dictates the coupling structure of the partition-based optimal control problem. To ensure a globally coordinated control action, the resulting coupling structure must represent a connected graph. Because the specific values for th and $\mathcal{N}_{\min}$ depend on the unique nodal admittance matrix of the system, they must be tailored to the specific application. As a guideline, the trimming parameters should be selected according to the following criteria:

1. Choose th at least large enough, such that coupling in $F_{\mathrm{G}}^{\mathrm{trim}}$ is not global.
2. Choose $\mathcal{N}_{\min}$ large enough, such that the coupling graph defined by $F_{\mathrm{G}}^{\mathrm{trim}}$ is connected.

Optimization problems structured like (6.21) are typically solved using distributed dual decomposition or Alternating Direction Method of Multipliers (ADMM). Certain variants of these algorithms are specifically tailored to exploit partitioned architectures [145], such as the partition-based relaxed ADMM introduced in [146], which is adopted for this DMPC. A primary advantage of this approach is localized data access, where each control unit only interacts with decision variables relevant to its own subproblem. In contrast, a direct application of standard consensus methods often results in poor scalability and redundant information exchange [147]. Furthermore, these algorithms are truly distributed, relying on a peer-to-peer communication scheme. The partition-based relaxed ADMM offers robust convergence across a broad range of parameter settings and maintains convergence guarantees even under communication loss, a feature of significant practical importance for DMPC implementation. Additionally, ADMM schemes generally exhibit faster convergence rates compared to traditional dual decomposition methods [148].

A comprehensive pseudo-code description of the partition-based relaxed ADMM is available in [146]. To implement the algorithm, three key parameters must be defined: the maximum number of iterations $\nu_{\max}$, which serves as the stopping criterion, the penalty parameter ρ, analogous to classical ADMM, and the relaxation parameter α, which is used to update auxiliary variables during execution.

The proposed DMPC scheme comprises local control units at each GFM that collectively execute the partition-based relaxed ADMM algorithm. This process solves the global partitioned optimization problem by addressing local subproblems with overlapping decision variables. Because the algorithm relies on bidirectional communication, the communication network is aligned with the coupling graph of the trimmed Frequency Divider model, which is purposefully designed to remain connected. This design remains independent of the system's

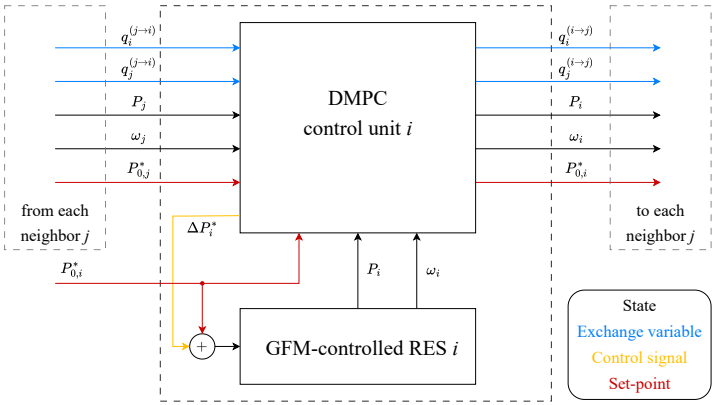

Figure 6.8: Frequency control configuration of each control unit int the fully distributed MPC scheme.

operating point, as it is derived solely from the network's admittance matrix. While online changes to grid topology do affect the admittance values, the coefficients of F_G^{trim} can be updated without altering the underlying sparsity structure. Modifying the sparsity itself would necessitate changes to the physical communication scheme, which is not currently intended for online execution and reserved for future research.

While keeping the structure of the distributed control problem constant, the optimal control problem has to be initialized in every execution with the current system information. As illustrated in Figure 6.8, the DMPC control unit i collects its own state information and set-points, as well as those of its neighbors. Once initialized, control unit i iteratively exchanges optimization variables with its neighbors until the algorithm converges, ensuring a coordinated control response across the partitioned network.

A detailed flowchart of the distributed MPC scheme is provided in Figure 6.9, illustrating the computational and communication sequences inherent to the partition-based relaxed ADMM. Within this framework, each DMPC unit i augments its local optimization problem using auxiliary variables $p_i^{(j,i)}$ and $p_j^{(j,i)}$. During the iterative process, unit i transmits exchange variables $q_i^{(i\to j)}$ and $q_j^{(i\to j)}$ to its neighbors while simultaneously collecting the corresponding variables $q_i^{(j\to i)}$ and $q_j^{(j\to i)}$ from them. These auxiliary variables are updated at the end of every iteration ν. Notably, any slack variables introduced for constraint softening remain strictly local and are excluded from neighbor-to-neighbor data exchange.

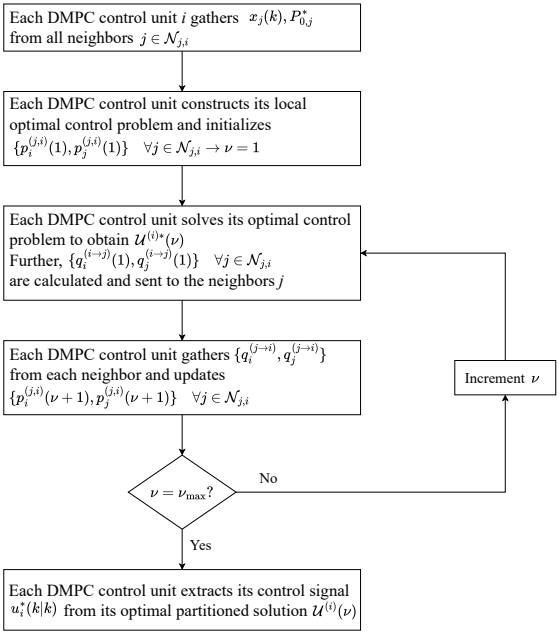

Figure 6.9: Flowchart of the DMPC scheme based on the partition-based relaxed ADMM.

Once the stopping criterion is met, each unit extracts and applies only the first local control input $u_i^*(k|k)$ from its optimal decision vector $\mathcal{U}^{(i)^*}$.

The algorithm is designed with inherent resilience to communication disruptions. In case of a short communication loss of a control unit i during the execution of the iterative distributed optimization process, control unit i does not communicate or receive any exchange variables with/from its neighbors for one or more iterations. Convergence is still guaranteed by updating only the auxiliary variables for which exchange data was successfully received. For more persistent communication failures spanning multiple MPC execution cycles, the control units rely on the last available state information from their neighbors to formulate their local problems. To enhance efficiency, a warm-start strategy is employed, where all units store their auxiliary variables, exchange variables, and solutions at the end of each execution to serve as initial values for the subsequent cycle. Observations indicate that this strategy significantly accelerates the algorithm's convergence rate.

Variable	Weight Q / R	Set point [pu]	Minimum [pu]	Maximum [pu]
$\omega_{\mathrm{GFM},i}$	1000	1	-	-
$P_{\mathrm{GFM},i}$	0	0.6	0	1
$\Delta P^{*}_{\mathrm{GFM},i}$	0.1	0	-0.6	0.4

Table 6.2: Objective function parameters of the fully distributed MPC based on Frequency Divider Trimming.

The parameters for the objective function are summarized in Table 6.2. In this study, frequency regulation serves as the primary control objective. Consequently, $\omega_{\mathrm{GFM},i}$ is assigned a high weighting value in Q. The input weight R is tuned to ensure a well-damped control response. The DMPC operates with a sampling time of $T_s = 100$ ms. Through an iterative tuning procedure, the prediction and control horizons are set to $H_p = H_u = 4$, to achieve an optimal balance between control performance and the speed of algorithm convergence. During the tuning phase, it is observed that while longer horizons enhance the overall performance in simulations, shorter horizons significantly reduce the number of iterations required for convergence. The specific ADMM parameters, ρ and α, are determined via a trial-and-error approach to maximize convergence speed within the given simulation environment. Subsequently, the maximum iteration count $\nu_{\max}$ is established at a value that ensures sufficient accuracy for the optimal solution. These parameters are defined as follows:

$$\nu_{\max} = 10, \quad \rho = 5 \cdot 10^{-8}, \quad \alpha = 0.8.$$

6.3 Simulations Results and Discussion

In this section, the control zone-based DMPC, using the distributed Frequency Divider for modeling, and the fully distributed MPC based on Frequency Divider Trimming are evaluated and their individual advantages and disadvantages are discussed.

6.3.1 System description

The proposed DMPC strategies are implemented on the IEEE 39-bus transmission system. In this setup, the 10 original synchronous generators are replaced by generic GFM-based RES, following the modeling approach detailed in Section 5.3.1. These RES units are interfaced with the grid through step-up transformers, mirroring the original generator connections. A higher-level control layer is assumed to determine the steady-state active power set-points, P_i^*, via

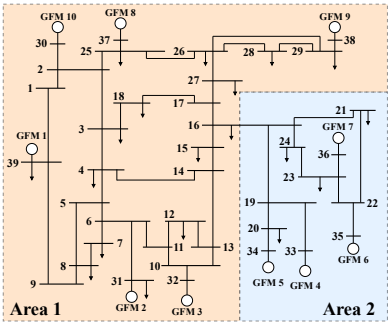

(a) IEEE 39-bus power system.

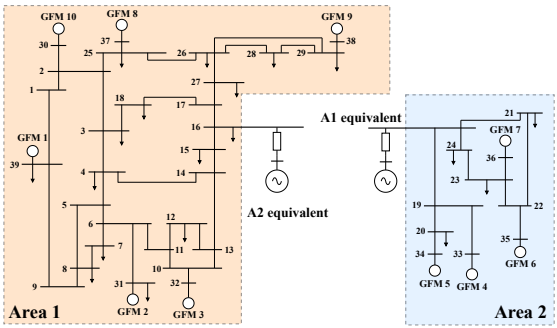

(b) Representation of the 39-bus system in the DMPC with distributed Frequency Divider.

Figure 6.10: Power system test case. a) Topology of the IEEE 39-bus power system. b) System representation with the Distributed Frequency Divider for each power system area.

an OPF algorithm. For the timescale of this zone-based frequency controller (spanning several seconds), Tie line power flow deviations are considered negligible and are expected to be restored by the OPF.

To facilitate distributed Frequency Divider-based modeling, the system is partitioned into two distinct areas, with bus 16 serving as the boundary. Area 1 encompasses RES 1–3 and 8–10, while Area 2 contains RES 4–7. Each RES maintains a direct communication link with the DMPC unit governing its respective zone. Both the WFZ device and a PMU are installed at the boundary

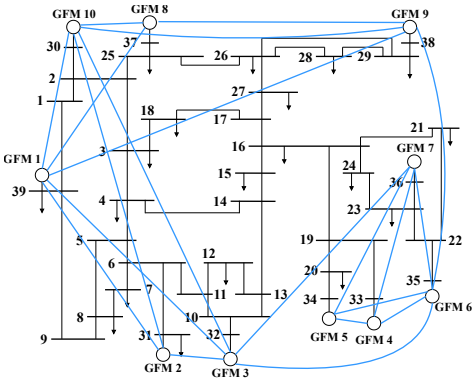

Figure 6.11: Communication/coupling graph of the fully distributed MPC scheme based on Frequency Divider Trimming in the IEEE 39-bus system.

bus 16. The PMU provides the real-time local frequency measurements required to initialize the distributed Frequency Divider calculations, consistent with the methodology in [140]. The system topology and its representation within the DMPC framework are illustrated in Figure 6.10.

For the fully distributed MPC scheme, the Frequency Divider Trimming parameters are set to $th = 5\%$ and $\mathcal{N}_{\min} = 3$, based on the sensitivity analysis performed in Section 6.1.2. This configuration maintains an accuracy within approximately 3% of the non-trimmed Frequency Divider model. The resulting partitioning, which dictates the communication topology for the fully distributed MPC, is shown in Figure 6.11. This sensitivity-based coupling graph further justifies the selection of the two control areas utilized in the zone-based DMPC in Figure 6.10b. Notably, even in the fully distributed architecture, only a few communication links persist between the two areas, indicating a weak inter-area coupling. Specifically, the cross-area connections consist of GFM 7 being coupled to GFM 3, and GFM 6 maintaining links with both GFM 3 and GFM 9.

The DMPCs are compared against the Centralized MPC (CMPC), which is an upper bound to the control performance as it models the full system, as shown in Figure 6.10a, in a single optimal control problem. Additionally, the controllers are compared against the central PI-based controller that represents traditional approaches for secondary frequency control. The PI controller is designed as described in Section 5.2. Numerical simulations are carried out in Matlab Simulink with the Specialized Power Systems library [137] to capture the EMT dynamics of the fully converter-driven power system.

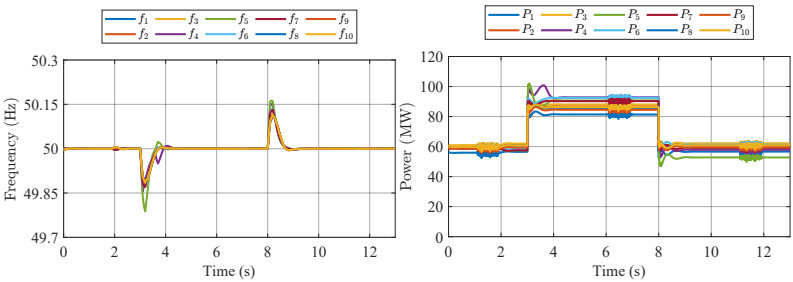

(a) Frequencies. (b) Powers.

Figure 6.12: Frequencies and powers of the GFMs for a load step in area 2 controlled by the zone-based DMPC.

6.3.2 Numerical studies of the Distributed Model Predictive Control Strategies

The nominal performance of the DMPCs is evaluated in three scenarios: (i) a load step in area 1, (ii) a load step in area 2, (iii) a load step in area 1 & area 2. The load steps are distributed across multiple loads in areas 1 or 2, while the total load step is 300 MW in all cases. The initial system load sums up to $P_{\text{load,total}} = 600$ MW. At $t = 5$ sec, the load is increased at several buses. The additional load is removed at $t = 10$ sec.

Performance of the DMPCs

Figure 6.12 presents the GFM frequencies and power outputs for the control zone-based DMPC, which models the system using the distributed Frequency Divider, in scenario (ii). The controller quickly stabilizes the frequency and recovers it to 50 Hz. After the first load step, the power output of GFM 5 reaches its constraint of 100 MW. The DMPC control unit of area 2 compensates for the natural response by increasing the power of GFM 4 during the transient, while recovering both GFM frequencies to 50 Hz. The GFMs in area 1 are not affected.

After each load step, the WFZ measurement device is triggered to measure the equivalent impedances of both areas. Before triggering the device, it is ensured that the system frequency is in steady state condition. The WFZ device requires a steady state observation phase before the disturbance injection phase. During the disturbance injection, the DMPC is turned off to avoid interactions between the controller and the measurement device. If a load step or frequency deviation occurs during the measurement period, then the measurement routine can be canceled and the DMPC is turned on again. During the injection phase, a disturbance of the active powers can be observed in Figure 6.12b. The disturbance

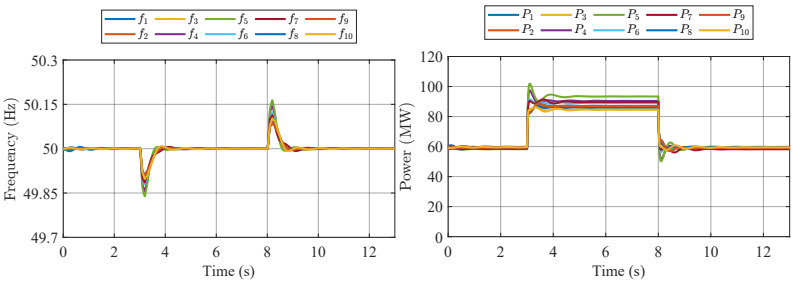

(a) Frequencies. (b) Powers.

Figure 6.13: Frequencies and powers of the GFMs for a load step in area 2 controlled by the the fully distributed MPC.

of the frequencies is negligible since the GFM controller acts as a low pass filter of the power measurement on the frequency, and thus removes the high-frequency content introduced by the PRBS perturbation. The frequency output of the GFM converters has no noise, ensuring the stability of the system during the measurement phase.

The imaginary part of the impedance at 50 Hz obtained during the above load step simulation scenario are $X_{\mathrm{A1},1} = 0.0697\,\Omega$, $X_{\mathrm{A1},2} = 0.0700\,\Omega$, and $X_{\mathrm{A1},3} = 0.0699\,\Omega$ at the three measurement intervals for Area 1 . For area 2, the measured impedances are $X_{\mathrm{A2},1} = -0.1063\,\Omega$, $X_{\mathrm{A2},2} = -0.1056\,\Omega$, and $X_{\mathrm{A2},3} = -0.1060\,\Omega$ respectively. Area 1 behaves inductive with respect to the boundary bus due to a positive impedance phase angle and area 2 behaves capacitive due to a negative impedance phase angle.

The performance of the fully distributed MPC, which is constructed from the trimmed Frequency Divider matrix, is assessed for the same step increase and subsequent decrease of the system load. Figure 6.13 shows the frequency and power outputs of the GFMs during the simulation. It is observed that the powers are quickly stabilized, and the frequency is recovered into a ± 0.01 Hz band around 50 Hz within 640 ms in both transients. In comparison to the zone-based DMPC, the controller distributes the power of GFM 5 more evenly, when reaching the maximum power constraint. Overall, the response of the fully distributed MPC is closer to the CMPC than with the zone-based DMPC.

Figure 6.14 shows the average of the GFM frequencies in scenario (iii), i.e. the load step in both areas, for all considered controllers. The control response of the DMPCs has a similar dynamic than the CMPC, but with a slower recovery

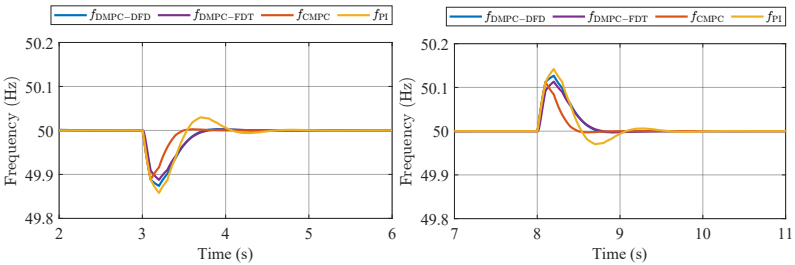

(a) Load step increase.

(b) Load step decrease.

Figure 6.14: Average GFM frequencies for a load step in area 1 and area 2 for the DMPC based on Distributed Frequency Divider (DMPC-DFD), DMPC based on Frequency Divider Trimming (DMPC-FDT), CMPC and PI controller.

time. The DMPCs are significantly more damped and faster than the centralized PI controller, which has an overshoot on the average frequency of approximately 0.03 Hz in both transients. The overshoot and recovery time pose a design trade-off during tuning of the PI controller. Here, a balance between both performance metrics was chosen. None of the MPC strategies have an overshoot in their control response.

To quantify the results, the ISE and the time to recover the average system frequency within a 0.01 Hz band around 50 Hz are calculated. The performance indices are given in Table 6.3 and Table 6.4 for all scenarios and controllers. The DMPCs show a comparable recovery time of 619-640 ms over all scenarios, which is also visible in the time domain in Figure 6.14. Thereby, they both outperform the centralized PI controller, which has a recovery time of approximately 960 ms. The CMPC, which poses an upper bound on the control performance of the distributed controllers, has an approximately 35% reduced recovery time compared to the DMPCs. The ISE quantifies the frequency deviation over the complete transient. Similarly, both DMPCs outperform the PI controller. In this index, the fully distributed MPC shows a performance gain over the zone-based DMPC of 21-25%. This is mainly a result of a smaller frequency nadir/zenith, as visible in Figure 6.14. The choice of bus 16 as the boundary bus results in two asymmetric areas, with area 1 hosting 50% more generation capacity than area 2, as well as most of the load. The location of the load step could significantly influence the area equivalent representation, which is used in the zone-based DMPC. However, the results in Table 6.3 and Table 6.4 show only a small dependence of the control performance on the load step location. The worse performance in scenario (ii) is explained by GFM 5 reaching its power limitation, which is reflected in the indices for all controllers.

Scenario	DMPC-DFD	DMPC-FDT	CMPC	PI
(i) Step A1	7.91	6.19	3.62	9.48
(ii) Step A2	8.32	6.21	3.64	9.65
(iii) Step A1 & A2	8.15	6.26	3.66	9.66

Table 6.3: Integral Squared Error ($\times$ 1000) of the average frequency.

Scenario	DMPC-DFD	DMPC-FDT	CMPC	PI
(i) Step A1	0.619	0.639	0.402	0.953
(ii) Step A2	0.635	0.638	0.410	0.969
(iii) Step A1 & A2	0.627	0.640	0.404	0.960

Table 6.4: Recovery time $[s]$ of the average frequency.

Overall, the transient performance of distributed and centralized MPCs remains comparable, while the distributed variants have a smaller control bandwidth, considering the same tuning. When comparing DMPC and CMPC, note that there is, in general, no guarantee that satisfying the constraints of the distributed optimal control problem implies that the constraints for the more accurate centralized control problem are satisfied. However, the principal difference between the models is the estimation of the frequency ω_t at the GFM's terminal bus. When approaching steady state, all GFM frequencies approach the nominal frequency, and the error introduced by the distributed Frequency Divider and the Frequency Divider Trimming with respect to the frequency amplitude vanishes, such that the constraints of the centralized control problem are met with negligible error.

Impact of limited iterations

For the distributed optimization algorithms, the MPC control units iteratively exchange information about their decision variables, i.e., the control inputs over the control horizon $\mathcal{U}^*(k)$, with other control units. The computational and communication burden of the control schemes critically scales with the number of required iterations until a feasible or acceptable solution is reached. Additionally, the algorithms can be terminated earlier to reduce vulnerability, or if real-time capability is lost.

Figure 6.15 shows the algorithm iterations of the zone-based DMPC for all scenarios. The zone-based DMPC takes up to 30 iterations during transients to converge. In steady-state, only 2 iterations are taken, whereas the algorithm is

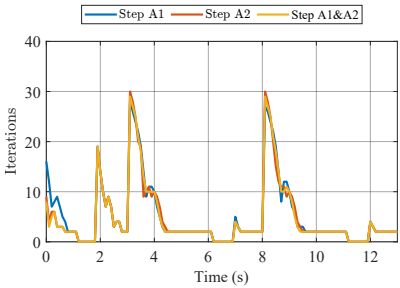

Figure 6.15: Number of iterations per execution of the zone-based DMPC for each scenario.

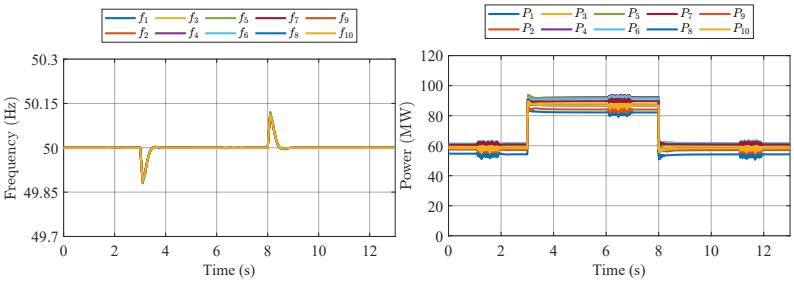

(a) Frequencies. (b) Powers.

Figure 6.16: Frequencies and powers of the GFMs controlled by the zone-based DMPC for scenario (iii), while each MPC execution call is terminated after one iteration.

turned off during the WFZ measurement intervals. The simulation of the three scenarios are repeated, where the algorithm is terminated after a maximum iteration number of 10, 5, 2 and 1. It is found that in the scenarios (i) and (iii), i.e. when no power constraint is active, the DMPC performance increases for a reduced number of iterations. When terminated after 1 iteration, the zone-based DMPC performs equivalent to the CMPC, with an ISE of 3.674 and a recovery time of 402 ms in scenario (iii). Scenario (i) gives equivalent results. Figure 6.16 presents the time-domain results of this case.

In scenario (ii), where a power constraint is active, the control performance, however, strongly declines for a limited number of iterations. Figure 6.17 shows

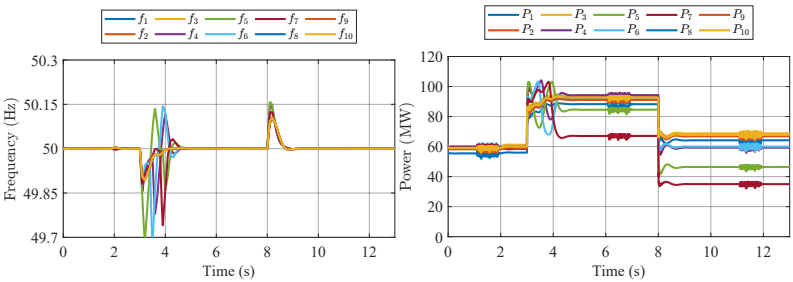

(a) Frequencies. (b) Powers.

Figure 6.17: Frequencies and powers of the GFMs controlled by the zone-based DMPC for scenario (ii), while each MPC execution call is terminated after 5 iterations.

the results for scenario (ii) when terminating the algorithm after 5 iterations. Strong oscillations between all GFMs in area 2 are visible, while the GFMs in area 1 are not affected. In this case, the system stabilizes after approximately 1 second. When terminated with less iterations, the oscillations become stronger and the system collapses.

In the fully distributed MPC, the number of algorithm iterations is a tuning variable, which is set to $\nu_{\max} = 10$ for the nominal case. The algorithm achieved convergence and a close to optimal solution in this time. Figure 6.18 presents the simulation results when the optimization is terminated after $\nu_{\max} = 1$ iteration, zoomed-in on the first load step for scenario (i). It can be seen that the control performance does not critically decline. In this case, GFM 1 shows oscillations in frequency and power against the rest of the GFMs, which were not observed previously. The oscillations are damped and a steady-state is reached with a slightly longer recovery time of 679 ms (compared to 639 ms). The other two scenarios show a similarly close performance.

Loss of communication

The DMPCs can be affected by temporary loss of communication. In the zone-based DMPC, communication loss can occur either within a zone between the control unit and the GFMs, or between the control units of different zones. In the first case, the communication loss is equivalent to the signal loss discussed in Section 5.3. In the second case, the DMPC control units do not receive an update of the decision variables, such that the Lagrangian multipliers in (6.18b) are not updated, and the algorithm can be terminated. A full loss of communication

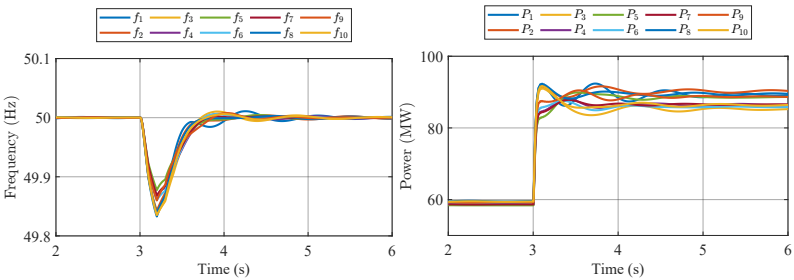

(a) Frequencies. (b) Powers.

Figure 6.18: Frequencies and powers of the GFMs controlled by the fully distributed MPC for scenario (i), while each MPC execution call is terminated after one iteration.

between the control units is therefore equivalent to the case, where the maximum number of iterations is set to 1, i.e., each control unit optimizes its local control problem once, without updating the Lagrangian multipliers. The impact of this case has been presented above.

For the fully distributed MPC, communication loss can occur between single control units, while the other control units maintain communication. In Figure 6.19 the communication with DMPC control unit 4 is lost from $t = 5.5\,\text{sec}$ until $t = 10.5\,\text{sec}$. A total loss of communication over the span of multiple sampling times means that DMPC control unit 4 is neither sending nor receiving any information to/from its neighbors. This results in missing updates of state variables, and algorithm exchange variables, as shown in Figure 6.8. The DMPC control units continue execution using the latest available information. In this scenario, the maximum number of iterations is again set to 10.

In steady-state, the loss of communication has no impact on the power system. Due to the warm start strategy, the optimization is initialized with the variables and solution from the previous time step. Thus, no deviation due to communication loss is observed. The communication is restored 2.5 sec after the load step at $t = 10.5\,\text{sec}$. It can be observed that the frequency recovers with a stable response. Due to the communication loss, the frequency at GFM 4 shows an increased zenith of 50.21 Hz and has a noticeable overshoot with damped oscillations. The active power sharing is more uneven compared to the previous cases, settling in two groups of GFMs, with a higher and a lower power output, as visible in Figure 6.19b. The power output of GFM 4 is subject to a larger overshoot. It is noted that the system remains stable also for a longer, simulta-

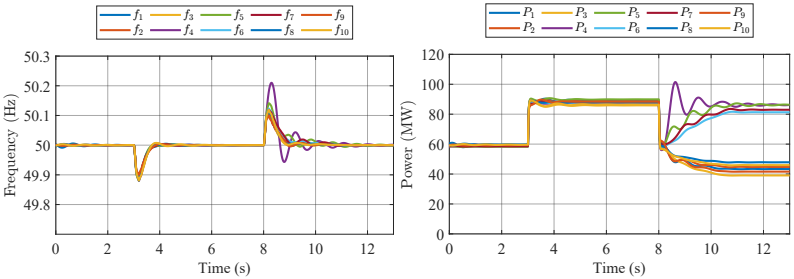

(a) Frequencies. (b) Powers.

Figure 6.19: Frequencies and powers of the GFMs controlled by the fully distributed MPC, during a communication loss of DMPC control unit 4 (5.5 sec - 10.5 sec).

neous communication loss of two DMPC control units until $t = 15$ sec, however, at the cost of larger transient responses in the frequency and active power.

6.3.3 Summary and Discussion

The zone-based DMPC using the distributed Frequency Divider concept offers a distributed control solution for multi-area control in power systems. It realizes the following conceptual advantages:

- Neighboring power system areas are represented as a lumped system equivalent while the local power system area is modeled in detail. The control action is optimized for individual units and the need to disaggregate the control signal for the area is avoided.
- The approach provides scalability, as the size of the optimization problem only scales with the number of participating units within the local power system area. The control problem does not increase in size for larger power systems (compared to an OPF that scales with more buses and lines) or an increased number of generation units in neighboring areas.
- It requires only lumped information about parameters and measurements of neighboring systems, thereby offering security and privacy of the algorithm.
- The control system is adaptive to changing system conditions through measurement of the external equivalent system impedance.

The DMPC based on Frequency Divider Trimming can leverage the benefits of fully distributed control and realizes the following advantages:

- It presents a scalable control system architecture that requires communication of each local controller with a set of neighbors. The set of neighbors and

the resulting degree of coupling is tunable through the Frequency Divider Trimming input parameters.
- The submodels do not scale with the size of the system. Only local dynamics are described in the prediction model explicitly and included based on sensitivity.
- The DMPC is applicable to any grid topology, particularly meshed grids, and does not rely on additional measurement infrastructure.
- The DMPC is highly robust to communication system effects, by employing an algorithm that is guaranteed to converge under communication losses.

With the DMPC approach based on Frequency Divider Trimming, the intermediate range between centralized and decentralized MPC can be covered without any modifications to the modeling through the tuning parameters of the trimming procedure.

The numerical simulations of the proposed DMPC schemes prove that a control performance comparable to the centralized MPC based on the same prediction model is achievable. The limitation of algorithm iterations highlights the differences of the two approaches. The results show that the fully distributed MPC is highly robust against a limited number of iterations, by providing close to unlimited iteration performance, even under constrained operation. Furthermore, the fully distributed MPC can handle a loss of communication of some control units. If too many control units lose communication simultaneously for an extended amount of time, fallback strategies should be implemented, such as reverting to a decentralized secondary control or turning the secondary control off and relying only on the primary control. The requirements on the computation and communication systems can be significantly reduced for an acceptable cost of performance with this algorithm. The zone-based DMPC is less robust to a limited number of iterations when constraints become active. In the unconstrained case, however, a performance close to the centralized MPC is obtained. The results suggest that for multi-area control, a decentralized approach might be optimal, where the control units of each area do not exchange information online, and constraints must be handled within the control zone, i.e., the set-point for the other zone would not be part of the optimization problem. In this case, the system representation becomes similar to the MPC for grid-connected converter systems from Section 4.1, where states of the external grid are estimated from POI measurements. The influence of the external controller could be modeled through disturbances. However, conflicting control behavior must be carefully investigated in this setting.

7 Conclusion

This thesis investigated the application of Model Predictive Control for improving frequency stability in modern power systems dominated by converter-based Renewable Energy Sources, characterised by low to zero inertia. The work addressed both grid-connected and islanded operating conditions, in particular primary and fast secondary frequency control of Grid-Following and Grid-Forming converters. By explicitly considering heterogeneous RES dynamics, communication constraints, and scalable distributed control architectures, the thesis contributes a comprehensive predictive control framework suited for modern converter-driven power systems.

7.1 Conclusion

From a control performance perspective, MPC consistently outperformed conventional PI and decentralized strategies by leveraging a multi-objective MIMO control architecture to manage heterogeneous RES dynamics effectively. Addressing the core research questions, the studies demonstrate that MPC is exceptionally capable of balancing fast frequency control with additional objectives, such as tracking energy storage levels and maximum power points, by proactively exploiting the flexibility of converter-based RES. This predictive coordination results in a significant improvement in tracking accuracy (ISE) and reduction in energy storage requirements compared to traditional control strategies. Ultimately, while reactive PI and decentralized controllers lack the necessary unit coordination to minimise resource usage, MPC's predictive nature and explicit handling of dynamic constraints lead to superior reference tracking, faster disturbance rejection, and increased damping. In addition, this thesis demonstrated that terminal cost terms in MPC can be exploited beyond their classical stabilising role. A terminal cost term was used to enable offset-free control of energy storage states while maintaining coordinated power sharing through appropriate cost penalisation. Notably, offset-free control was achieved even in a system with more controlled outputs than manipulated inputs, namely an islanded purely converter-driven power system.

A central contribution of this work is the development of a novel MPC prediction model based on the Frequency Divider formula. This model overcomes the observability limitations of the classical Tie line-based approach and proves advantageous particularly in grid-connected applications where external grid states are not directly measurable. The results demonstrate that the higher

observability of the Frequency Divider model leads to faster, more damped, and more robust frequency responses compared to the Tie line model, while achieving equivalent performance in islanded operation.

The robustness and global sensitivity analyses confirm that MPC achieves superior performance and resource efficiency under model-plant mismatch compared to classical strategies. However, the influence of uncertainty types depends heavily on the system configuration. In grid-connected scenarios, parametric uncertainty, specifically regarding grid inertia, impedance, and actuator ramp rates, dominates MPC performance, while structural mismatch from EMT dynamics remains secondary. In contrast, for islanded converter-driven systems, structural uncertainty becomes the primary driver of performance degradation. This increased sensitivity to the transition from nominal to EMT environments likely stems from the reduced voltage stiffness in islanded systems, which challenges the idealised voltage assumptions inherent in the MPC prediction models. These findings highlight that while nominal simulations are sufficient for assessing robustness and parametric variance in larger grids, early-stage HiL or EMT validation is essential for MPC deployment in weak converter-dominated systems to capture critical dynamic interactions.

The thesis further addressed computational and communication aspects that are critical for practical deployment. It was shown that the computational burden of centralized MPC scales quadratically with the number of converters, motivating the development of distributed solutions. Communication delays were found to significantly affect control performance in islanded, purely converter-driven systems, while grid-connected plant control showed no sensitivity. Importantly, co-simulation studies revealed that communication delays cannot be accurately represented by simple statistical models. Delays depend strongly on network topology, traffic congestion, and router queuing effects, and exhibit temporal correlation and bounded behaviour. Despite these challenges, delay-aware MPC strategies effectively compensate for the adverse effects of stochastic networks, maintaining a robust, first-order response even under high latency and packet loss rates of up to 35%. In contrast, a PI controller with Smith Predictor exhibits underdamped oscillations under similar conditions. The impact of these communication constraints is highly scale-dependent. In fast-acting islanded microgrids, the delay-aware MPC provides a critical stability margin that classical approaches cannot match. Conversely, in large-scale transmission networks, slower system dynamics and higher sampling times naturally buffer communication latency, narrowing the performance gap between strategies. Consequently, while delay resilience is a primary driver for MPC adoption in microgrids, its implementation in large-scale systems is principally justified by its superior coordination of constrained RES and economic efficiency rather than delay compensation alone.

Finally, the thesis proposed and evaluated Distributed Model Predictive Control strategies based on partitioned submodels of the Frequency Divider

formulation to achieve dynamic distributed control of individual GFM units. Numerical results confirm that DMPC can achieve frequency control performance comparable to centralized MPC, including constraints. By limiting the number of distributed optimisation iterations, a favourable trade-off between performance and resource usage was obtained; in particular, computational and communication requirements could be significantly reduced. Furthermore, the introduction of Frequency Divider Trimming enables systematic tuning between centralized and decentralized system representations. Sensitivity analyses showed that, with appropriate trimming criteria, transient frequency estimation errors remain below 3%, providing an effective and flexible means to scale MPC-based frequency control.

In summary, this thesis demonstrates that MPC, when combined with suitable prediction models, communication-aware design, and distributed architectures, is a powerful and robust control approach for enhancing frequency stability in future low-inertia power systems. The presented methods address key technical challenges associated with converter-dominated grids and provide a solid foundation for the practical deployment of advanced predictive control strategies in modern power systems.

7.2 Outlook

The results of this thesis open several promising directions for future research and practical implementation. While the proposed MPC and DMPC strategies already demonstrate strong performance under a wide range of operating conditions, further methodological extensions can enhance robustness, scalability, and functionality in increasingly complex converter-dominated power systems. A natural next step is the integration of robust MPC formulations. Robust MPC methods offer additional benefits by explicitly accounting for bounded uncertainties, unmodeled dynamics, and time-varying disturbances. In the context of converter-driven power systems, this includes parameter uncertainty in converter models, variability of renewable generation, and imperfect knowledge of inertia and damping contributions. Robust formulations could further improve closed-loop stability margins, reduce sensitivity to model–plant mismatch observed in EMT and HiL studies, and provide formal guarantees on constraint satisfaction under worst-case disturbances. This is particularly relevant for zero-inertia systems, where fast dynamics increase the impact of uncertainties on frequency control performance.

Beyond frequency control, the proposed modelling and control approaches can be extended to capture additional system dynamics. In particular, extending the prediction model to explicitly include voltage dynamics represents a significant opportunity. Recent developments, such as the Complex Frequency framework [149], provide a promising basis for jointly addressing frequency and voltage behaviour within a unified predictive control formulation. This would be

especially relevant for islanded converter-driven systems, where the impact of voltage variations on MPC-based frequency control must be further studied.

From an implementation perspective, real-time deployment of the proposed DMPC strategies represents a key research challenge. Although numerical simulations confirm that DMPC can achieve near-centralized performance with reduced computational effort, real-time execution requires careful consideration of solver selection, computational hardware, and synchronisation with communication networks. Extending the DMPC framework to multiple interconnected grid areas is of particular interest, as it would enable coordinated frequency control across transmission and distribution levels. The presented Frequency Divider-based modelling approach provides a suitable foundation for such multi-area extensions, but practical deployment will require further investigation into scalability, latency management, and hierarchical coordination.

An important and largely unexplored topic concerns the online adaptation of communication structures within the DMPC framework. In particular, dynamically adding or removing communication links based on operating conditions, network congestion, or failures could significantly improve resilience and efficiency. The trimming-based partitioning of the Frequency Divider model offers a promising mechanism to adapt the level of system coupling in real time. However, the impact of such online reconfiguration on convergence properties, stability, and performance of the DMPC algorithm remains an open research question.

The results of this thesis further suggest that decentralized or semi-decentralized multi-area control architectures may be beneficial for future power systems. Investigating the trade-offs between centralized, distributed, and decentralized MPC schemes in large-scale multi-area systems therefore constitutes an important avenue for future work.

Finally, the MPC-based approaches developed in this thesis could be applied to related support functions, most notably power oscillation damping. By incorporating electromechanical oscillatory modes into the prediction model and cost function, MPC could provide coordinated damping control across multiple converters and grid areas, potentially outperforming classical decentralized damping controllers. Such extensions would further strengthen the role of MPC as a versatile and unifying control framework for stability enhancement in future power systems.

Overall, the presented outlook highlights that MPC and DMPC offer substantial potential beyond the scope of this thesis, both in terms of theoretical development and practical deployment, and that continued research in these directions is well justified by the increasing complexity of converter-dominated power systems.

A Additional Results of the Grid-connected Converter System

The appendix shows the HiL validation results of the negative load step, PV insolation disturbance and the EL trip, as well as the performance indices for all scenarios with a comparison to the nominal simulation. Sensitivity indices for the maximum frequency deviation and the energy storage usage are listed.

Scenario	**MPC-FD**	**MPC-Tie**	**PI**	**Dec.**
Load Step Pos.	1.95 [+6.0%]	2.47 [+6.3%]	5.53 [−5.5%]	4.27 [+3.6%]
Load Step Neg.	4.01 [+17.4%]	5.01 [+12.2%]	8.77 [+3.9%]	12.0 [+1.6%]
PV Insolation	1.91 [+106%]	2.11 [+129%]	31.02 [+10%]	122.4 [+24%]
EL Trip	12.4 [+3.4%]	20.6 [+2.1%]	42.82 [+1.1%]	652.0 [−1.9%]

Table A.1: Integral Squared Error (x100) of the grid-connected converter system with different control strategies in a Hardware-in-the-Loop experiment.

Scenario	**MPC-FD**	**MPC-Tie**	**PI**	**Dec.**
Load Step Pos.	0.281 [+1.5%]	0.281 [+1.6%]	0.301 [+1.6%]	0.275 [+1.8%]
Load Step Neg.	0.417 [+0.6%]	0.416 [+0.7%]	0.433 [+0.8%]	0.438 [+0.6%]
PV Insolation	0.05 [+153%]	0.05 [+153%]	0.056 [+7.1%]	0.058 [+10%]
EL Trip	0.083 [+2.2%]	0.088 [+1.6%]	0.087 [+2.9%]	0.186 [+0.8%]

Table A.2: Maximum frequency deviation (Hz) of the grid-connected converter system with different control strategies in a Hardware-in-the-Loop experiment.

Scenario	**MPC-FD**	**MPC-Tie**	**PI**	**Dec.**
Load Step Pos.	5.00 [+27.6%]	4.04 [+10.8%]	5.88 [−1.5%]	3.51 [+1.8%]
Load Step Neg.	1.34 [+9.9%]	2.15 [+2.5%]	7.58 [−1.9%]	5.27 [−0.2%]
PV Insolation	3.62 [+150%]	3.20 [+109%]	2.01 [+6.7%]	0.74 [+9.6%]
EL Trip	6.37 [−2.2%]	9.35 [−1.6%]	3.63 [−2.3%]	2.40 [+0.4%]

Table A.3: Energy storage usage (MWs) of the grid-connected converter system with different control strategies in a Hardware-in-the-Loop experiment.

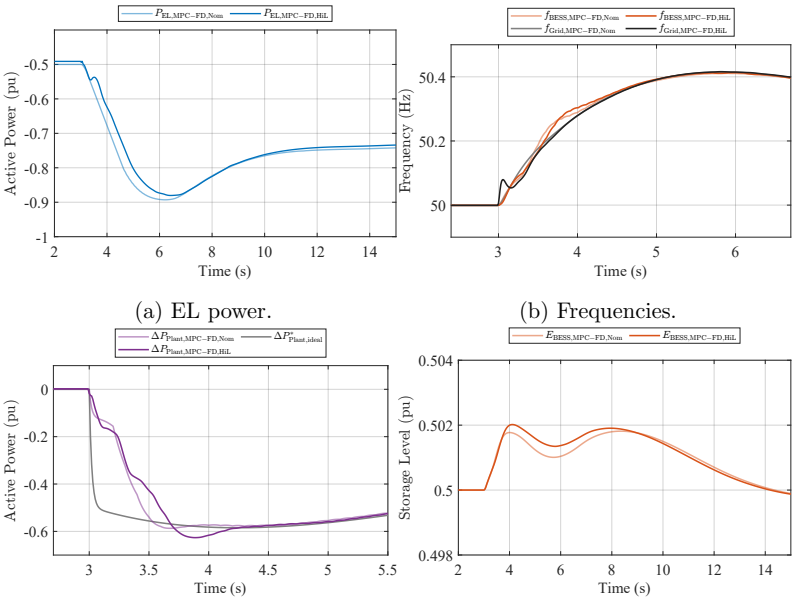

(a) EL power. (b) Frequencies.

(c) Plant power. (d) Energy storage level.

Figure A.1: Hardware-in-the-Loop validation of the hybrid renewable power plant response to a load step of −1.5 pu with MPC using the Frequency Divider model. Zoom in on the transient.

HiL Validation of the negative Load Step

For the negative load step, the plant response with the MPC using the Frequency Divider model is presented in Figure A.1 and the converter output power of the EL is highlighted exemplarily. The figure illustrates the close match of the nominal simulation and the HiL experiment. The maximum frequency deviation (Table A.2) and energy storage usage (Table A.3) are similar in both load step scenarios and mostly show small deviations across all controllers. The ISE of the MPC plant controllers differs up to 13.3%. This case is shown in Figure A.1c. It can be seen that the tracking of the reference trajectory is slightly slower than in the nominal simulation, however the qualitative trajectory is maintained in the HiL experiment.

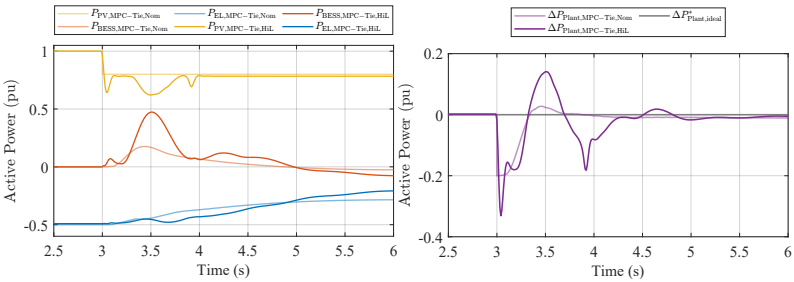

(a) RES power. (b) Plant power.

Figure A.2: Hardware-in-the-Loop validation of the hybrid renewable power plant response to a step change of the PV insolation of $-200\frac{\mathrm{W}}{\mathrm{m}^2}$ with MPC using the Tie line model. Zoom in on the transient.

HiL Validation of the PV Insolation Disturbance

A step reduction of the PV insolation level from $1000\frac{\mathrm{W}}{\mathrm{m}^2}$ to $800\frac{\mathrm{W}}{\mathrm{m}^2}$ on the insolation input of the RTDS PV array model is simulated in the HiL experiment. A strong decrease in the performance indices from the nominal simulation is obtained for both MPC control strategies (Table A.1 and Table A.3). Figure A.2 shows the RES powers and the plant output for the MPC with the Tie line model. In the HiL experiment, the PV power overshoots the steady-state deviation from the insolation disturbance by approximately 50%, which is also visible in the plant power output in Figure A.2b. The controller quickly increases the plant power, however, the MPC shows oscillations stemming from the reference trajectory algorithm in the HiL experiment. The oscillation is damped and the disturbance can be rejected, leading to a steady-state.

HiL Validation of the Electrolyzer Trip

A protection trip of a RES is simulated by blocking the VSC and DC/DC converters of the EL unit. The trip is assumed to be caused by an internal fault of the EL system, e.g., gas crossover of the membrane, necessitating a sudden shutdown. Figure A.3 shows the plant response with an MPC plant controller using the Tie line model. In the nominal simulation, the power supply is simply disconnected from the dynamic model. In the HiL experiment, converter blocking is simulated, which is a more accurate representation of this event. The inertial

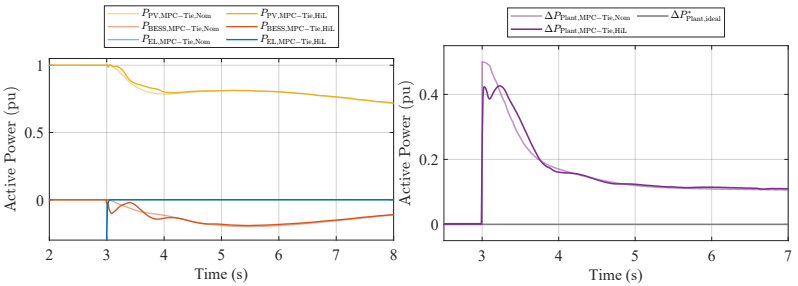

(a) RES powers. (b) Plant power.

Figure A.3: Hardware-in-the-Loop validation of the hybrid renewable power plant response to a protection trip of the Electrolyzer with MPC using the Tie line model. Zoom in on the transient.

response of the GFM BESS to the resulting phase jump reduces the peak of the plant power in the HiL experiment. Overall, the control performance is very close to the nominal simulation. Plant disturbances, like the tripping of the EL, can be explicitly accounted for by the plant controller through a change of prediction model structure or, in less extreme cases, such as change of PV power, through dynamic constraints. These disturbance are rejected very effectively by the MPC.

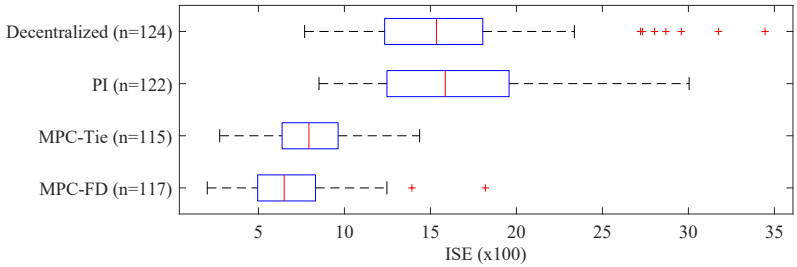

(a) ISE.

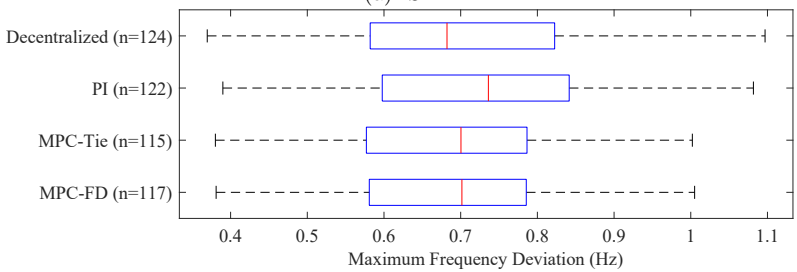

(b) Maximum Frequency Deviation.

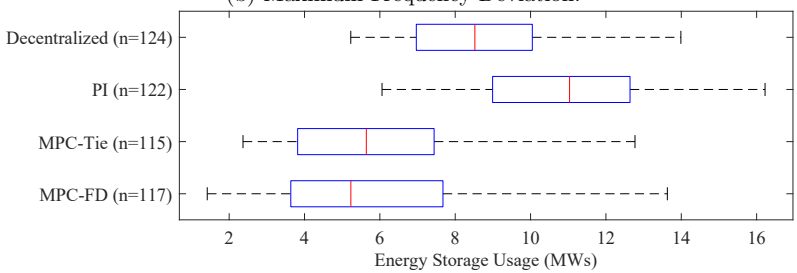

(c) Energy Storage Usage.

Figure A.4: Results of the robustness analysis for the Hybrid Renewable Power Plant in terms of the performance indices for each plant control strategy.

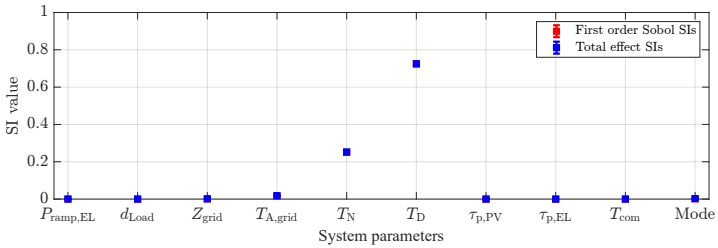

(a) MPC with Frequency Divider model.

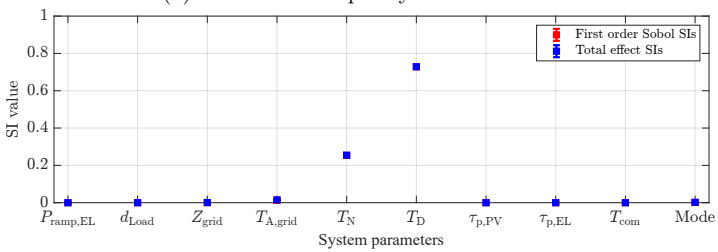

(b) MPC with Tie line model.

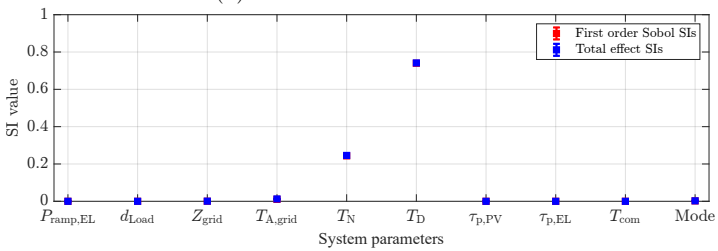

(c) PI controller.

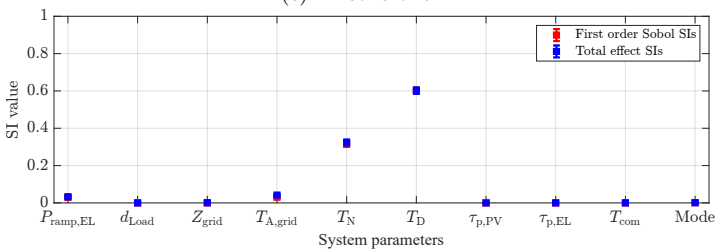

(d) Decentralized control.

Figure A.5: Sensitivity analysis results for the maximum frequency deviation (Hz) in terms of first order Sobol' and total effect SIs.

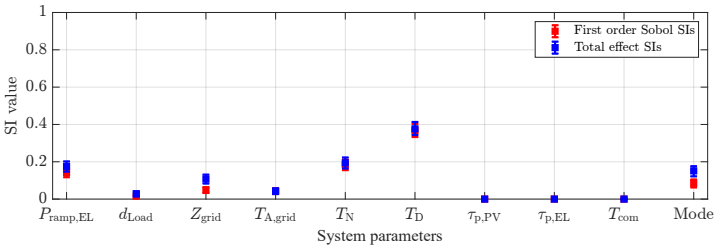

(a) MPC with Frequency Divider model.

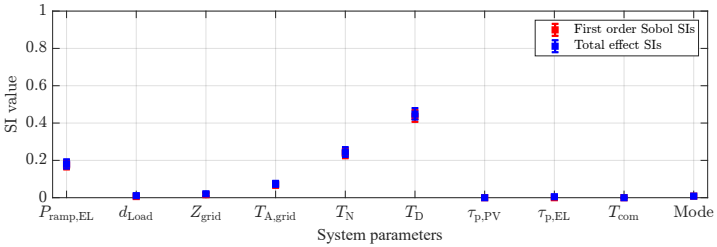

(b) MPC with Tie line model.

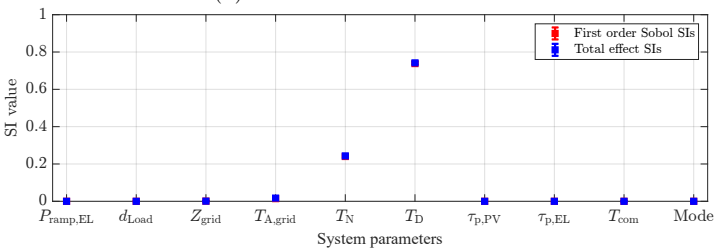

(c) PI controller.

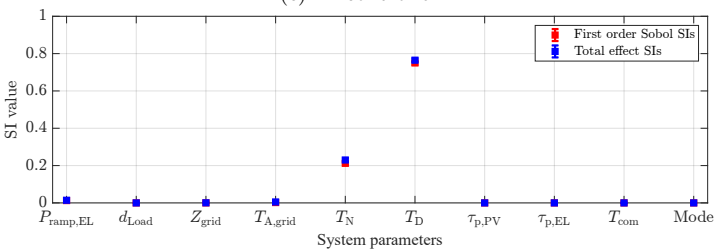

(d) Decentralized control.

Figure A.6: Sensitivity analysis results for the energy storage usage (MWs) in terms of first order Sobol' and total effect SIs.

B Additional Results of the Islanded Converter-driven Power System

The appendix shows the HiL validation results of the PV insolation disturbance and the EL trip, as well as the performance indices for all scenarios with a comparison to the nominal simulation. Sensitivity indices for the maximum frequency deviation and the energy storage usage are listed.

Scenario	**MPC-FD**	**MPC-Tie**	**PI**
Load Step Positive & Negative	1.40 [−29.4%]	1.48 [−23.4%]	6.44 [−8.1%]
PV Insolation Disturbance	0.18 [+263%]	0.18 [+242%]	0.39 [+2.0%]
Electrolyzer Trip	0.55 [+200%]	0.39 [+137%]	1.08 [−20.1%]

Table B.1: Integral Squared Error (x100) of the islanded converter-driven power system with different control strategies in a Hardware-in-the-Loop experiment.

Scenario	**MPC-FD**	**MPC-Tie**	**PI**
Load Step Positive & Negative	0.434 [−8.4%]	0.434 [−7.9%]	0.481 [−0.3%]
PV Insolation Disturbance	0.16 [+165%]	0.16 [+157%]	0.14 [+7.8%]
Electrolyzer Trip	0.17 [+47.4%]	0.16 [+34.3%]	0.19 [−8.5%]

Table B.2: Maximum frequency deviation (Hz) of the islanded converter-driven power system with different control strategies in a Hardware-in-the-Loop experiment.

Scenario	**MPC-FD**	**MPC-Tie**	**PI**
Load Step Positive & Negative	3.50 [+17.1%]	3.27 [+13.5%]	7.31 [+1.6%]
PV Insolation Disturbance	1.00 [+29.4%]	0.94 [+27.4%]	1.83 [+8.7%]
Electrolyzer Trip	1.28 [+16.7%]	1.40 [+31.0%]	2.24 [−3.9%]

Table B.3: Energy storage usage (MWs) of the islanded converter-driven power system with different control strategies in a Hardware-in-the-Loop experiment.

PV Insolation Disturbance

A disturbance of the PV generation is simulated in the HiL setup by reducing the

insolation level of PV 1 by $200\frac{\mathrm{W}}{\mathrm{m}^2}$. The average frequency for the MPC using the Frequency Divider model and the PI controller are shown in Figure B.1. Similar to the load step, the MPC has a stronger response, but shows a greater difference to the nominal simulation than the PI controller. This is also represented in large percentage deviations in the ISE and maximum frequency deviation in Table B.1 and Table B.2. The stronger peak of the frequency in the HiL setting is caused by the GFM control strategy of BESS 2, which is explained in the next scenario.

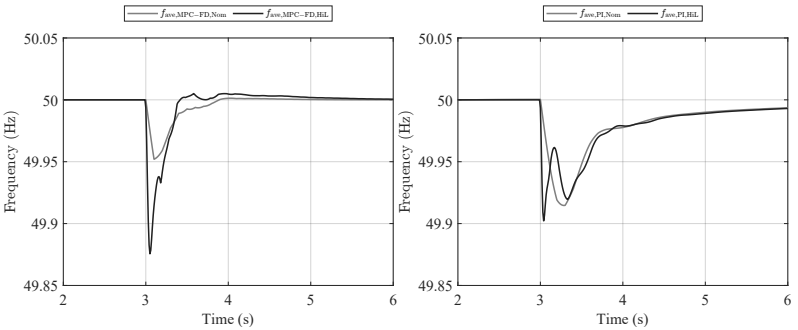

(a) Average Frequency with MPC-FD. (b) Average Frequency with PI.

Figure B.1: HiL experiment of a PV insolation disturbance of $-200\frac{\mathrm{W}}{\mathrm{m}^2}$ in the islanded CIGRE MV distribution network and comparison with the nominal simulation.

Electrolyzer Trip

A protection trip of a RES is simulated by blocking the VSC and DC/DC converters of the EL, thereby removing a large load and a controllable unit from the system. The trip is assumed to be caused by an internal fault of the EL system, e.g., gas crossover of the membrane, necessitating a sudden shutdown. Figure B.2 shows the system response with the MPC using the Tie line model.

In the nominal simulation of the Tie line model, the power output of a GFL converter must be assigned to a voltage source component, i.e. a GFM converter or an SG, as shown in Figure 3.1. Its power output is summed up in the power balance determining the frequency dynamics of that component. Therefore, after the protection trip, the full power imbalance of -0.5 pu is supplied by BESS 1 in the nominal simulation initially, which can be seen in Figure B.2a at $t = 3\,\mathrm{sec}$. In the HiL experiment, however, the GFM converters of both BESS instantaneously respond to the power imbalance. Since the EL has an approximately equal impedance to both GFMs, the power of BESS 1 and BESS 2 jumps by

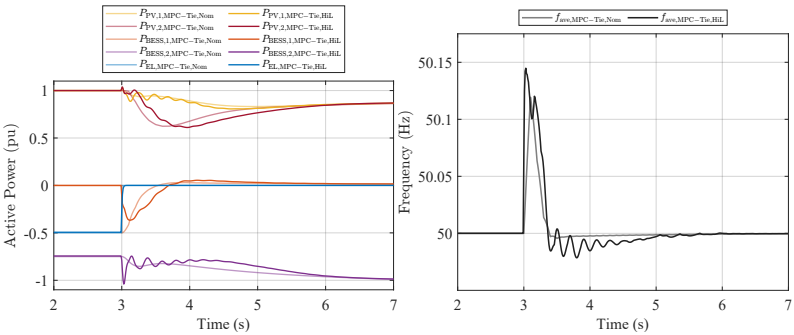

(a) RES powers with MPC-Tie. (b) Average Frequency with MPC-Tie.

Figure B.2: HiL experiment of a protection trip of the Electrolyzer in the islanded CIGRE MV distribution network and comparison with the nominal simulation.

approximately −0.25 pu in the HiL experiment. BESS 2 employs the decoupled VSM control strategy, which includes a feed-forward path of the power output to the frequency (Figure 3.7). This causes the larger initial frequency deviation in Figure B.2b. The same mechanism applies for the PV power output, which explains the stronger frequency jump in Figure B.1a and Figure B.1b.

The performance indices show a larger percentage deviation between the nominal simulation and the HiL experiments for the islanded converter-driven power system compared to the grid-connected converter system in Section 5.1.3, especially for the MPC controllers in the EL trip scenario. The time-domain representation of the HiL experiments validate that the controllers work correctly. The relative performance difference between the MPC and PI controllers in the nominal simulation is reflected in the results of the HiL experiments.

Robustness and Sensitivity Analysis

The sensitivity indices of the maximum frequency deviation are shown in Figure B.4. The maximum frequency deviation is most sensitive to the operating mode, nominal simulation or HiL experiment, followed by the damping parameter $K_{\mathrm{d,BESS,2}}$ for all control strategies. The equal sensitivity pattern and the strong overlap of the robustness results in Figure 5.20b confirm the observation that the frequency peak is not significantly influenced by the controller. Instead, it is determined by the instantaneous response of the converters.

Figure B.5 presents the sensitivities for the energy storage usage of each controller. The MPC using the Frequency Divider model has a strong sensitivity to the HiL experiment with a total SI of 0.61 for the operating mode, followed by $P_{\mathrm{ramp,EL}}$ with 0.18 and $K_{\mathrm{d,BESS,2}}$ with 0.09. The MPC using the Tie line model has a more even sensitivity profile. The operating mode has an SI of 0.36, while the SI of $P_{\mathrm{ramp,EL}}$ is 0.29 and 0.23 for $K_{\mathrm{d,BESS,2}}$. Strong interactions of the input parameters are visible with the PI controller. Sensitivity indices of the third order amount to 0.10 for an interaction of $P_{\mathrm{ramp,EL}}$, $\tau_{\mathrm{p,EL}}$ and T_{com}, and another third order SI of 0.13 indicates an interaction of $P_{\mathrm{ramp,EL}}$, the switch positions and $K_{\mathrm{d,BESS,2}}$. A second order SI shows an interaction between $\tau_{\mathrm{PV,1}}$ and τ_{EL} of 0.08. The HiL experiment has a relatively weaker effect for the PI controller, compared to the MPCs, of 0.11. The interactions on the energy storage usage indicate a conflicting controller behavior of the energy storage level control, which adjusts the power set-point of BESS 1, and the main PI frequency controller, that adjust the power set-points of all RES, notably of the EL and BESS 2 that share the power deviation in steady-state. The MPC secondary controllers, in contrast, perform a multi-objective control action, and have no interactions between the uncertain parameters, and very small to zero sensitivity to the response time of the GFL-based RES. The results of the sensitivity analysis and the HiL validation in Table B.3 show that the nominal simulation is too optimistic in the energy storage usage of the MPC.

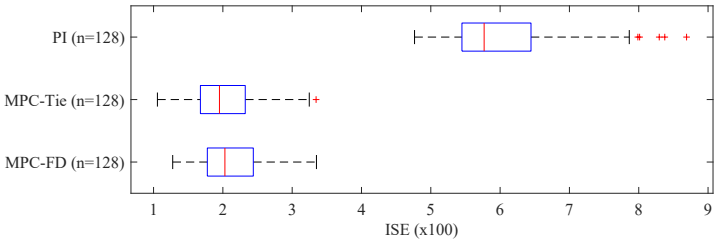

(a) ISE.

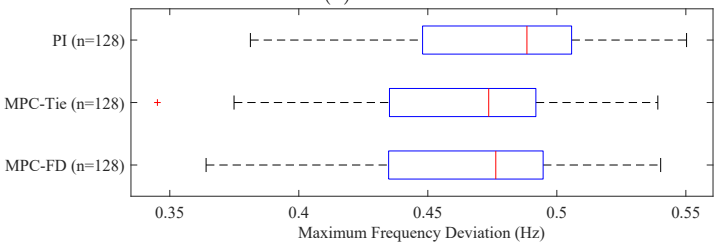

(b) Maximum Frequency Deviation.

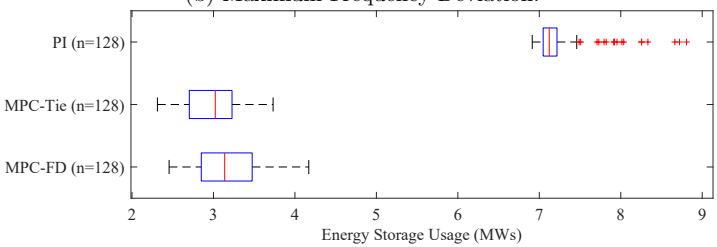

(c) Energy Storage Usage.

Figure B.3: Boxplots of the robustness analysis of the CIGRE MV distribution network in terms of the performance indices for each control strategy.

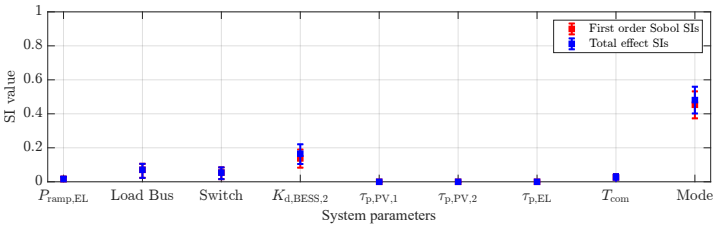

(a) MPC with Frequency Divider model.

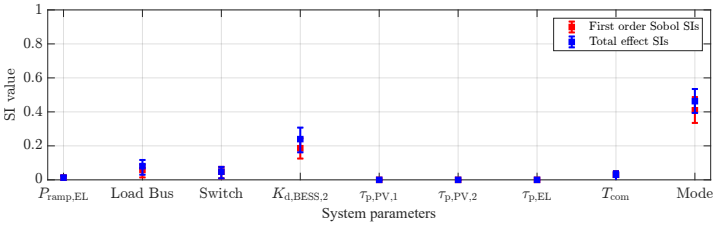

(b) MPC with Tie line model.

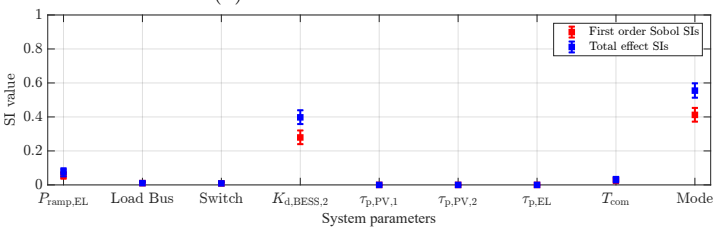

(c) PI controller.

Figure B.4: Sensitivity analysis results for the maximum frequency deviation (Hz) in terms of first order Sobol' and total effect SIs.

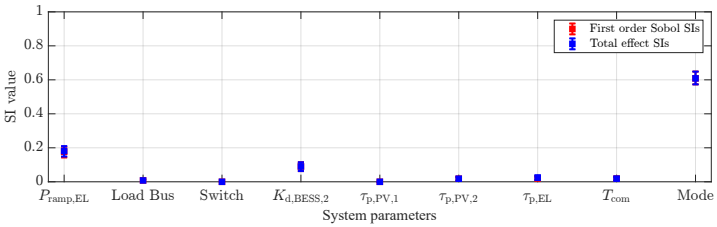

(a) MPC with Frequency Divider model.

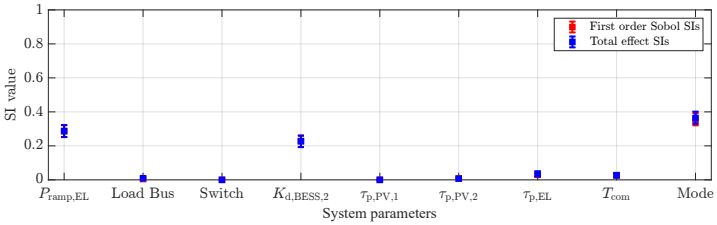

(b) MPC with Tie line model.

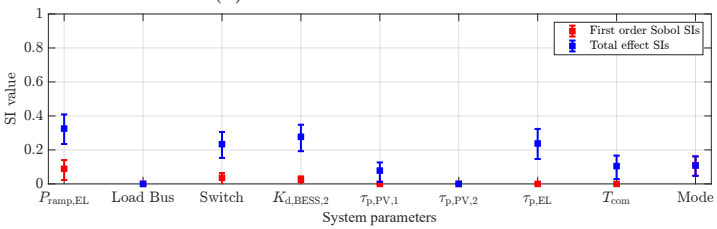

(c) PI controller.

Figure B.5: Sensitivity analysis results for the energy storage usage (MWs) in terms of first order Sobol' and total effect SIs.

C Additional Results of the Co-simulation with Communication Systems

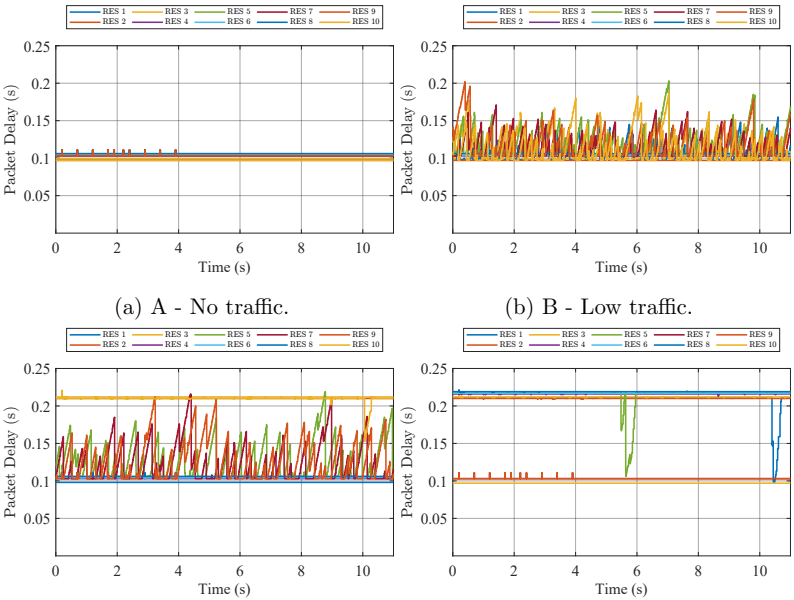

(a) A - No traffic.

(b) B - Low traffic.

(c) C - Moderate traffic.

(d) D - Heavy traffic.

Figure C.1: Packet delay in the DSL scenario for different levels of network traffic.

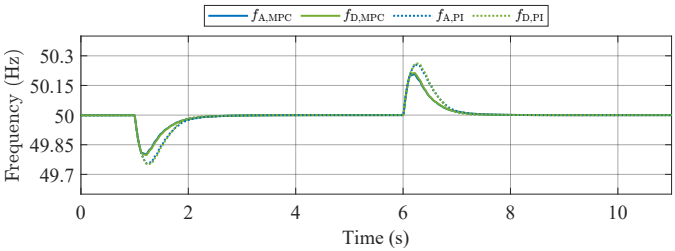

(a) Fiber.

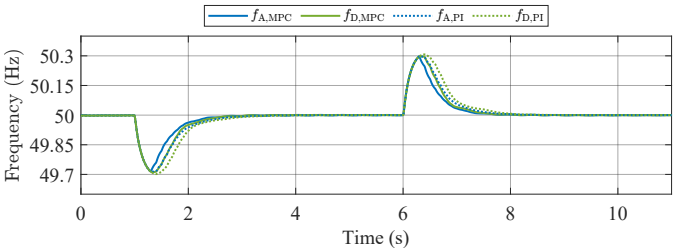

(b) DSL.

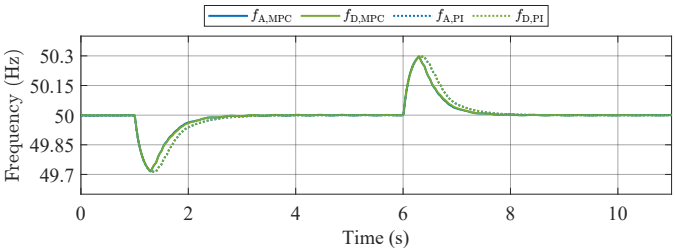

(c) Wireless.

Figure C.2: Average frequency for variants A and D in the transmission system case for all communication network scenarios.

	Fiber		**DSL**		**Wireless**	
	MPC	PI	MPC	PI	MPC	PI
A	1.220	1.245	1.485	1.745	1.485	1.750
B	1.220	1.235	1.500	1.725	1.490	1.750
C	1.225	1.170	1.515	1.510	1.490	1.750
D	1.240	1.105	1.560	1.940	1.490	1.745

Table C.1: Recovery time [s] of the average frequency in the transmission system case.

Publications

This thesis is based on content of the following peer-reviewed articles:

Journal Articles

[J1] T. Heins, M. Josevski, S. K. Gurumurthy, and A. Monti, "Centralized Model Predictive Control for Transient Frequency Control in Islanded Inverter-Based Microgrids," *IEEE Transactions on Power Systems*, vol. 38, pp. 2641–2652, 2023.

[J2] M. Moritz, T. Heins, S. K. Gurumurthy, M. Josevski, I. Jahn, and A. Monti, "Distributed Model Predictive Frequency Control of Inverter-Based Power Systems," *IEEE Access*, vol. 12, pp. 53250–53265, 2024.

[J3] T. Heins, M. Ginocchi, and A. Monti, "Model Predictive Control for Fast Frequency Control in Hybrid Renewable Plants: Increasing Robustness through Enhanced Model Observability," *IEEE Open Journal of Industry Applications*, vol. 7, pp. 674-691, 2026.

Conference Articles

[C1] T. Heins *et al.*, "Delay-aware Model Predictive Control for Fast Frequency Control," *2023 IEEE International Conference on Communications, Control, and Computing Technologies for Smart Grids (SmartGridComm)*, 2023.

[C2] T. Heins, P. Chanfreut, S. K. Gurumurthy, P. Srivastava, A. Monti, and A. M. Annaswamy, "Distributed Frequency Divider-based Model Predictive Control for Frequency Control of Multi-Area Power Systems," *2023 IEEE International Conference on Communications, Control, and Computing Technologies for Smart Grids (SmartGridComm)*, 2023.

[C3] T. Heins, T. Heynen, S. Simon, S. K. Gurumurthy, and A. Monti, "Com parison of aggregated and detailed large-scale hydrogen electrolyzer plant models for grid integration studies," *23rd Wind and Solar Integration Workshop*, 2024.

[C4] T. Heynen, T. Heins, M. Kuhn, W. Leterme, and A. Monti, "Systematic review on fast frequency ancillary services provided by large-scale hydrogen electrolyzer plants," *23rd Wind and Solar Integration Workshop*, 2024.

During my doctorate, the following papers and book chapters with my contribution have been published but are not part of this thesis:

Journal Articles

[J4] T. Heynen, M. Deitert, T. Heins, M. Kuhn, A. Monti, and W. Leterme, "Design of the Electrical Interface of Hydrogen Electrolyzers Limiting the Power Ramp-Rate While Providing Instantaneous Reserves," *IEEE Transactions on Sustainable Energy*, vol. 17, no. 3, pp. 2487-2500, 2026.

[J5] S. K. Gurumurthy, T. Heins, P. A. Ganeshamurthy, F. Ponci, and A. Monti, "Load Bus Frequency Estimation in Converter-Driven Grids - A Dynamic Phasor Approach," *IEEE Transactions on Power Systems*, vol. 39, pp. 5338–5351, 2024.

[J6] T. Tran *et al.*, "Enhancing Performance of Andronov-Hopf Oscillator Based Grid-Forming Converters in Microgrids With Non-Invasive Online Impedance Estimation," *IEEE Transactions on Smart Grid*, vol. 14, pp. 4479–4493, 2023.

[J7] G. Mehlmann *et al.*, "The Kopernikus ENSURE Co-Demonstration Platform," *IEEE Open Journal of Power Electronics*, vol. 4, pp. 987–1002, 2023.

[J8] I. Sowa, T. Tran, T. Heins, D. Raisz, and A. Monti, "An Average Consensus Algorithm for Seamless Synchronization of Andronov-Hopf Oscillator Based Multi-Bus Microgrids," *IEEE Access*, vol. 9, pp. 90441– 90454, 2021.

Conference Articles

[C5] T. Heins, T. Tran, D. Raisz, and A. Monti, "Power Control of Andronov-Hopf Oscillator Based Distributed Generation in Grid-Connected Microgrids," *Advances in Engineering Research and Application: Proceedings of the International Conference on Engineering Research and Applications*, ICERA 2020, 2020.

Book Chapters

[B1] S. D'Arco, A. Monti, T. Heins, and J. Suul, "Control of converter interfaced generation," in *Advances in Power System Modelling, Control and Stability Analysis*, pp. 389–416.

Curriculum Vitae

05.05.2026	Doctoral Examination for Dr.-Ing.
2020-2026	Research Associate and Doctoral Candidate Institute for Automation of Complex Power Systems RWTH Aachen University, Germany
2017-2020	Master of Science in Business Administration and Engineering: Electrical Power Engineering RWTH Aachen University, Germany
2019-2020	ERASMUS Semester at Chalmers University of Technology, Gothenburg, Sweden
2014-2017	Bachelor of Science in Business Administration and Engineering: Electrical Energy Technology RWTH Aachen University, Germany
2006-2014	High School Diploma (Abitur) Elsa-Brändström-Gymnasium, Oberhausen, Germany

Glossary

ADMM	Alternating Direction Method of Multipliers
AGC	Automatic Generation Control
BESS	Battery Energy Storage System
CHiL	Control Hardware-in-the-Loop
CMPC	Centralized MPC
CN	Controller Node
DMPC	Distributed Model Predictive Control
EL	Electrolyzer
EMT	Electromagnetic Transient
ESC	Electrical System Component
FFR	Fast Frequency Response
FFT	fast Fourier transform
GFL	Grid-Following
GFM	Grid-Forming
GSA	Global Sensitivity Analysis
HRPP	Hybrid Renewable Power Plant
HVDC	High Voltage Direct Current
HiL	Hardware-in-the-Loop
IAE	Integral Absolute Error
ISE	Integral Squared Error
ITAE	Integral Time Absolute Error
ITSE	Integral Time Squared Error
KF	Kalman filter
LMI	Linear matrix inequality
MIMO	Multiple-Input Multiple-Output
MMC	Modular Multilevel Converter

MPC	Model Predictive Control
MPPT	Maximum Power Point Tracking
OPF	Optimal Power Flow
PEM	Proton Exchange Membrane
PLL	Phase-locked loop
PMU	Phasor Measurement Unit
POI	Point of Interconnection
PRBS	Pseudo-Random-Binary-Sequence
PV	Photovoltaic
QP	Quadratic Programming
RES	Renewable Energy Source
RMSE	Root Mean Square Error
RoCoF	Rate of Change of Frequency
SG	Synchronous Generator
SI	Sensitivity Index
SoC	State of Charge
VOC	Virtual Oscillator Control
VSC	Voltage Source Converter
VSM	Virtual Synchronous Machine
WFZ	Wideband-Frequency impedance

List of Figures

Figure 2.1 Model Predictive Control Strategy. 8
Figure 2.2 Control Loop with Model Predictive Control. 9
Figure 2.3 Synchronous generators dynamic response after a load disturbance. 18
Figure 2.3a Frequencies. 19
Figure 2.3b Electrical and mechanical power. 19
Figure 2.3c Inertia response. 19
Figure 2.4 Grid-forming converters dynamic response after a load disturbance. 19
Figure 2.4a Frequencies. 20
Figure 2.4b Electrical power. 20
Figure 2.5 Two-level Voltage Source Converter. 23
Figure 2.6 Averaged Voltage Source Converter. 24
Figure 2.7 Grid-following converter control system. 25
Figure 2.8 Grid-forming converter control system. 28
Figure 3.1 Lumped inertia model of a system with a Synchronous Generator, a Grid-Following and a Grid-Forming Converter. . . 41
Figure 3.2 Power system model with two voltage sources. 42
Figure 3.3 Block diagram of two voltage sources with swing dynamics and Tie line power flow. 42
Figure 3.4 Conceptual representation of the proposed Frequency Divider-based prediction model. 44
Figure 3.5 Frequency Divider model of two voltage sources with swing dynamics. 46
Figure 3.6 Block diagram of the Virtual Synchronous Machine strategy for Grid-Forming control. 49
Figure 3.7 Block diagram of the Virtual Synchronous Machine strategy with decoupled parameters for Grid-Forming control [97]. 50
Figure 3.8 Block diagram of a GFL controlled converter with droop control. 51
Figure 3.9 Frequency Divider model of a system with a GFM (index 1) and a GFL converter (index 2). 52
Figure 3.10 Block diagram of the SG model with turbine-governor. 53
Figure 3.11 Power set-point step of 0.5 pu on a VSM GFM converter. EMT simulation (“sim”), Frequency Divider model (“FD”), Tie line model (“Tie”) 60

Figure 3.11a Converter power. 56
Figure 3.11b Grid forming converter and synchronous generator frequency. . 56
Figure 3.11c Synchronous generator mechanical and electrical power. 56
Figure 3.12 Power set-point step of 0.5 pu on a decoupled VSM GFM converter. EMT simulation ("sim"), Frequency Divider model ("FD"), Tie line model ("Tie") 60
Figure 3.12a Converter power. 57
Figure 3.12b Grid forming converter and synchronous generator frequency. . 57
Figure 3.12c Synchronous generator mechanical and electrical power. 57
Figure 3.13 Power set-point step of 0.5 pu on a GFL converter. EMT simulation ("sim"), Frequency Divider model ("FD"), Tie line model ("Tie") 60
Figure 3.13a Converter power. 58
Figure 3.13b Grid forming converter and synchronous generator frequency. . 58
Figure 3.13c Synchronous generator mechanical and electrical power. 58
Figure 3.14 Load step of 2 pu. EMT simulation ("sim"), Frequency Divider model ("FD"), Tie line model ("Tie") 60
Figure 3.14a Converter power. 59
Figure 3.14b Grid forming converter and synchronous generator frequency. . 59
Figure 3.14c Synchronous generator mechanical and electrical power. 59
Figure 3.15 Load step of 2 pu with increased SG impedance. EMT simulation ("sim"), Frequency Divider model ("FD"), Tie line model ("Tie") 60
Figure 3.15a Converter power. 60
Figure 3.15b Grid forming converter and synchronous generator frequency. . 60
Figure 3.15c Synchronous generator mechanical and electrical power. 60
Figure 4.1 Hybrid Renewable Power Plant including a photovoltaic, battery energy storage and electrolyzer system. 63
Figure 4.2 Model Predictive Control System for the Grid-connected Hybrid Renewable Power Plant. 63
Figure 4.3 Model to generate the plant reference trajectory. 68
Figure 4.4 Pole-zero plot of the unconstrained MPC for the grid-connected converter system. 69
Figure 4.5 Topology of the CIGRE MV benchmark system in islanded mode with Renewable Energy Sources. 70
Figure 4.6 Model Predictive Control System for the islanded converter-driven power system. 71
Figure 4.7 Pole-zero plot of the unconstrained MPC for the islanded converter-driven system. 74
Figure 4.8 Closed-loop control system with the delay- and loss-aware Model Predictive Control Strategy. 78

Figure 5.1 PI-based plant control system for the grid-connected Hybrid Renewable Power Plant. 82
Figure 5.2 Nominal simulation of the hybrid renewable power plant response to a load step of 1 pu with different plant control strategies. . . 83
Figure 5.2a RES powers. 84
Figure 5.2b Frequencies. 84
Figure 5.2c Plant power. 84
Figure 5.2d Energy storage level. 84
Figure 5.3 Load step response of the hybrid renewable power plant for an MPC with the reference trajectory algorithm (rt) and a non-predictive reference (no-rt). 85
Figure 5.3a Plant power. 85
Figure 5.3b Energy storage level. 85
Figure 5.4 Nominal simulation of the hybrid renewable power plant response to a load step of −1.5 pu with different plant control strategies. 85
Figure 5.4a RES powers. 86
Figure 5.4b Frequencies. 86
Figure 5.4c Plant power. 86
Figure 5.4d Energy storage level. 86
Figure 5.5 Nominal simulation of the hybrid renewable power plant response to a step disturbance of the PV insolation of −0.2 pu and 0.1 pu with different plant control strategies. 86
Figure 5.5a RES powers. 87
Figure 5.5b Plant power. 87
Figure 5.6 Nominal simulation of the hybrid renewable power plant response to a protection trip of the Electrolyzer with different plant control strategies. 87
Figure 5.6a RES powers. 88
Figure 5.6b Plant power. 88
Figure 5.7 Hardware-in-the-Loop experimental setup for the Model Predictive Control Systems of the Hybrid Renewable Power Plant. 89
Figure 5.8 Hardware-in-the-Loop validation of the hybrid renewable power plant response to a load step of 1 pu with MPC using the Frequency Divider model. Zoom in on the transient. 91
Figure 5.8a BESS power. 91
Figure 5.8b Frequencies. 91
Figure 5.8c Plant power. 91
Figure 5.8d Energy storage level. 91

Figure 5.9 Distribution of the performance indicies in the robustness analysis for the Hybrid Renewable Power Plant for each plant control strategy. 92
Figure 5.9a Integral Squared Error. 93
Figure 5.9b Maximum Frequency Deviation. 93
Figure 5.9c Energy Storage Usage. 93
Figure 5.10 Sensitivity analysis results for the ISE in terms of first order Sobol' and total effect SIs. 94
Figure 5.10a MPC with Frequency Divider model. 95
Figure 5.10b MPC with Tie line model. 95
Figure 5.10c PI controller. 95
Figure 5.10d Decentralized control. 95
Figure 5.11 Sensitivity analysis results for the energy storage usage for the MPC with Frequency Divider model. 96
Figure 5.12 PI-based secondary control system for the islanded CIGRE MV distribution network. 98
Figure 5.13 Nominal simulation of a positive and negative load step in the islanded CIGRE MV distribution network with different control strategies. 99
Figure 5.13a RES powers. 100
Figure 5.13b Average Frequency. 100
Figure 5.13c Energy storage level. 100
Figure 5.14 Nominal simulation of a load step in the islanded CIGRE MV distribution network with and without terminal cost ("no-tc") on the storage level. 100
Figure 5.14a RES powers. 101
Figure 5.14b Average Frequency. 101
Figure 5.14c Energy storage level. 101
Figure 5.15 Nominal simulation of a step disturbance of the PV 1 insolation of -0.2 pu and 0.1 pu in the islanded CIGRE MV distribution network with different control strategies. 102
Figure 5.15a RES powers. 102
Figure 5.15b Average Frequency. 102
Figure 5.16 Nominal simulation of a protection trip of the Electrolyzer in the islanded CIGRE MV distribution network with different control strategies. 102
Figure 5.16a RES powers. 103
Figure 5.16b Average Frequency. 103
Figure 5.17 Hardware-in-the-Loop experimental setup for Model Predictive Control of the islanded CIGRE MV distribution system. 104

Figure 5.18 HiL experiment of a negative load step in the islanded CIGRE MV distribution network and comparison with the nominal simulation. 106
Figure 5.18a RES powers with MPC-FD. 106
Figure 5.18b Average Frequency with MPC-FD. 106
Figure 5.18c RES powers with PI. 106
Figure 5.18d Average Frequency with PI. 106
Figure 5.19 Maximum computation time of the MPC in an OP5707XG for different numbers of converters. 107
Figure 5.20 Results of the robustness analysis of the CIGRE MV distribution network in terms of the performance indices for each control strategy. 108
Figure 5.20a Integral Squared Error. 110
Figure 5.20b Maximum Frequency Deviation. 110
Figure 5.20c Energy Storage Usage. 110
Figure 5.21 Sensitivity analysis results for the ISE in terms of first order Sobol' and total effect SIs. 109
Figure 5.21a MPC with Frequency Divider model. 111
Figure 5.21b MPC with Tie line model. 111
Figure 5.21c PI controller. 111
Figure 5.22 Conceptual representation of the communication network topologies. 114
Figure 5.22a Star topology. 114
Figure 5.22b Ion network - 125 nodes. 114
Figure 5.23 Packet delay in the fiber scenario for different levels of network traffic. 115
Figure 5.23a A - No traffic. 116
Figure 5.23b B - Low traffic. 116
Figure 5.23c C - Moderate traffic. 116
Figure 5.23d D - Heavy traffic. 116
Figure 5.24 Average frequency for variants A and D of each scenario in the microgrid case. 116
Figure 5.24a Fiber. 117
Figure 5.24b DSL. 117
Figure 5.24c Wireless. 117
Figure 5.25 Average frequency for variants A and D in the DSL scenario in the transmission system case. 120
Figure 6.1 External system equivalent for the Distributed Frequency Divider represented by an aggregated generator, equivalent system impedance and the total area load. 122
Figure 6.2 Single-line representation of a power system with four generators. © 2024 IEEE. Reprinted, with permission, from [J2]. 125

Figure 6.3 Construction of partitioned models for generators 1 and 3 in the IEEE 39-bus system. 127
Figure 6.4 Scaled RMSE over all buses as threshold and minimum number of neighbors are varied in Frequency Divider Trimming. © 2024 IEEE. Reprinted, with permission, from [J2]. 128
Figure 6.5 Scaled RMSE at all GFM terminal buses in the IEEE-39-bus system. © 2024 IEEE. Reprinted, with permission, from [J2]. 130
Figure 6.6 Comparison of frequency estimations at bus 10 in the IEEE 39-bus system after a load step. 131
Figure 6.7 Wideband-frequency impedance estimation device setup. 135
Figure 6.8 Frequency control configuration of each control unit int the fully distributed MPC scheme. 136
Figure 6.9 Flowchart of the DMPC scheme based on the partition-based relaxed ADMM. 137
Figure 6.10 Power system test case. a) Topology of the IEEE 39-bus power system. b) System representation with the Distributed Frequency Divider for each power system area. 139
Figure 6.10a IEEE 39-bus power system. 140
Figure 6.10b Representation of the 39-bus system in the DMPC with distributed Frequency Divider. 140
Figure 6.11 Communication/coupling graph of the fully distributed MPC scheme based on Frequency Divider Trimming in the IEEE 39-bus system. 141
Figure 6.12 Frequencies and powers of the GFMs for a load step in area 2 controlled by the zone-based DMPC. 142
Figure 6.12a Frequencies. 142
Figure 6.12b Powers. 142
Figure 6.13 Frequencies and powers of the GFMs for a load step in area 2 controlled by the the fully distributed MPC. 143
Figure 6.13a Frequencies. 143
Figure 6.13b Powers. 143
Figure 6.14 Average GFM frequencies for a load step in area 1 and area 2 for the DMPC based on Distributed Frequency Divider (DMPC-DFD), DMPC based on Frequency Divider Trimming (DMPC-FDT), CMPC and PI controller. 143
Figure 6.14a Load step increase. 144
Figure 6.14b Load step decrease. 144
Figure 6.15 Number of iterations per execution of the zone-based DMPC for each scenario. 145

Figure 6.16 Frequencies and powers of the GFMs controlled by the zone-based DMPC for scenario (iii), while each MPC execution call is terminated after one iteration. 145
Figure 6.16a Frequencies. 146
Figure 6.16b Powers. 146
Figure 6.17 Frequencies and powers of the GFMs controlled by the zone-based DMPC for scenario (ii), while each MPC execution call is terminated after 5 iterations. 147
Figure 6.17a Frequencies. 147
Figure 6.17b Powers. 147
Figure 6.18 Frequencies and powers of the GFMs controlled by the fully distributed MPC for scenario (i), while each MPC execution call is terminated after one iteration. 147
Figure 6.18a Frequencies. 148
Figure 6.18b Powers. 148
Figure 6.19 Frequencies and powers of the GFMs controlled by the fully distributed MPC, during a communication loss of DMPC control unit 4 (5.5 sec - 10.5 sec). 148
Figure 6.19a Frequencies. 149
Figure 6.19b Powers. 149
Figure A.1 Hardware-in-the-Loop validation of the hybrid renewable power plant response to a load step of -1.5 pu with MPC using the Frequency Divider model. Zoom in on the transient. 157
Figure A.1a EL power. 156
Figure A.1b Frequencies. 156
Figure A.1c Plant power. 156
Figure A.1d Energy storage level. 156
Figure A.2 Hardware-in-the-Loop validation of the hybrid renewable power plant response to a step change of the PV insolation of $-200\frac{\mathrm{W}}{\mathrm{m}^2}$ with MPC using the Tie line model. Zoom in on the transient. 157
Figure A.2a RES power. 157
Figure A.2b Plant power. 157
Figure A.3 Hardware-in-the-Loop validation of the hybrid renewable power plant response to a protection trip of the Electrolyzer with MPC using the Tie line model. Zoom in on the transient. 159
Figure A.3a RES powers. 158
Figure A.3b Plant power. 158
Figure A.4 Results of the robustness analysis for the Hybrid Renewable Power Plant in terms of the performance indices for each plant control strategy. 159
Figure A.4a ISE. 159

Figure A.4b Maximum Frequency Deviation. 159
Figure A.4c Energy Storage Usage. 159
Figure A.5 Sensitivity analysis results for the maximum frequency deviation (Hz) in terms of first order Sobol' and total effect SIs. 161
Figure A.5a MPC with Frequency Divider model. 160
Figure A.5b MPC with Tie line model. 160
Figure A.5c PI controller. 160
Figure A.5d Decentralized control. 160
Figure A.6 Sensitivity analysis results for the energy storage usage (MWs) in terms of first order Sobol' and total effect SIs. 161
Figure A.6a MPC with Frequency Divider model. 161
Figure A.6b MPC with Tie line model. 161
Figure A.6c PI controller. 161
Figure A.6d Decentralized control. 161
Figure B.1 HiL experiment of a PV insolation disturbance of $-200\frac{\mathrm{W}}{\mathrm{m}^2}$ in the islanded CIGRE MV distribution network and comparison with the nominal simulation. 164
Figure B.1a Average Frequency with MPC-FD. 164
Figure B.1b Average Frequency with PI. 164
Figure B.2 HiL experiment of a protection trip of the Electrolyzer in the islanded CIGRE MV distribution network and comparison with the nominal simulation. 165
Figure B.2a RES powers with MPC-Tie. 165
Figure B.2b Average Frequency with MPC-Tie. 165
Figure B.3 Boxplots of the robustness analysis of the CIGRE MV distribution network in terms of the performance indices for each control strategy. 169
Figure B.3a ISE. 167
Figure B.3b Maximum Frequency Deviation. 167
Figure B.3c Energy Storage Usage. 167
Figure B.4 Sensitivity analysis results for the maximum frequency deviation (Hz) in terms of first order Sobol' and total effect SIs. 169
Figure B.4a MPC with Frequency Divider model. 168
Figure B.4b MPC with Tie line model. 168
Figure B.4c PI controller. 168
Figure B.5 Sensitivity analysis results for the energy storage usage (MWs) in terms of first order Sobol' and total effect SIs. 169
Figure B.5a MPC with Frequency Divider model. 169
Figure B.5b MPC with Tie line model. 169
Figure B.5c PI controller. 169

Figure C.1 Packet delay in the DSL scenario for different levels of network traffic. 171
Figure C.1a A - No traffic. 171
Figure C.1b B - Low traffic. 171
Figure C.1c C - Moderate traffic. 171
Figure C.1d D - Heavy traffic. 171
Figure C.2 Average frequency for variants A and D in the transmission system case for all communication network scenarios. 172
Figure C.2a Fiber. 172
Figure C.2b DSL. 172
Figure C.2c Wireless. 172

List of Tables

Table 2.1 Tuning parameters of the PI controllers in GFL mode. 27
Table 2.2 Tuning parameters of the PI controllers in GFM mode. 29
Table 3.1 Evaluation of prediction model requirements for different modelling approaches of voltage source components. Requirements are: + fulfilled, ○ partly fulfilled, − not fulfilled . . 48
Table 4.1 Parameters of the optimal control problem for the grid-connected Hybrid Renewable Power Plant. 66
Table 4.2 Parameters of the optimal control problem for the islanded converter-driven power system. 73
Table 5.1 Integral Squared Error (x100) of the grid-connected converter system with different control strategies under nominal conditions. 89
Table 5.2 Maximum frequency deviation (Hz) of the grid-connected converter system with different control strategies under nominal conditions. 89
Table 5.3 Energy storage usage (MWs) of the grid-connected converter system with different control strategies under nominal conditions. 89
Table 5.4 Inputs for robustness and global sensitivity analysis of the grid-connected Hybrid Renewable Power Plant. Nominal values and uncertainty characterization. 92
Table 5.5 Performance Index Median, Lower and Upper Quartile of the robustness analysis for the Hybrid Renewable Power Plant. 92
Table 5.6 Integral Squared Error (x100) of the islanded converter-driven power system with different control strategies under nominal conditions. 104
Table 5.7 Maximum frequency deviation (Hz) of the islanded converter-driven power system with different control strategies under nominal conditions. 104
Table 5.8 Energy storage usage (MWs) of the islanded converter-driven power system with different control strategies under nominal conditions. 104
Table 5.9 Inputs for robustness and sensitivity analysis of the islanded CIGRE MV distribution system. Nominal values and uncertainty characterization. 108
Table 5.10 Performance index Median, Lower and Upper Quartile of the robustness analysis of the CIGRE MV distribution network. . . . 108

Table 5.11 Overview of the microgrid and transmission system. 113
Table 5.12 Overview of the co-simulation scenarios and variants. 115
Table 5.13 IAE (x100) of the average frequency in the microgrid case. 118
Table 5.14 Recovery time [s] of the average frequency in the microgrid case. 118
Table 5.15 IAE (x100) of the average frequency in the transmission system case. 120
Table 6.1 Objective function parameters of the zone-based DMPC, using the Distributed Frequency Divider model. 134
Table 6.2 Objective function parameters of the fully distributed MPC based on Frequency Divider Trimming. 139
Table 6.3 Integral Squared Error ($\times$ 1000) of the average frequency. 145
Table 6.4 Recovery time [s] of the average frequency. 145
Table A.1 Integral Squared Error (x100) of the grid-connected converter system with different control strategies in a Hardware-in-the-Loop experiment. 155
Table A.2 Maximum frequency deviation (Hz) of the grid-connected converter system with different control strategies in a Hardware-in-the-Loop experiment. 155
Table A.3 Energy storage usage (MWs) of the grid-connected converter system with different control strategies in a Hardware-in-the-Loop experiment. 155
Table B.1 Integral Squared Error (x100) of the islanded converter-driven power system with different control strategies in a Hardware-in-the-Loop experiment. 163
Table B.2 Maximum frequency deviation (Hz) of the islanded converter-driven power system with different control strategies in a Hardware-in-the-Loop experiment. 163
Table B.3 Energy storage usage (MWs) of the islanded converter-driven power system with different control strategies in a Hardware-in-the-Loop experiment. 163
Table C.1 Recovery time [s] of the average frequency in the transmission system case. 173

Bibliography

[1] R. Rosso, X. Wang, M. Liserre, X. Lu, and S. Engelken, "Grid-Forming Converters: Control Approaches, Grid-Synchronization, and Future Trends —A Review," *IEEE Open Journal of Industry Applications*, vol. 2, pp. 93–109, 2021.

[2] D. Duckwitz and B. Fischer, "Modeling and Design of df/dt -Based Inertia Control for Power Converters", *IEEE Journal of Emerging and Selected Topics in Power Electronics*, vol. 5, no. 4, pp. 1553–1564, 2017.

[3] M. Kaiss, Y. Wan, D. Gebbran, C. U. Vila, and T. Dragičević, "Review on Virtual Power Plants/Virtual Aggregators: Concepts, applications, prospects and operation strategies," *Renewable and Sustainable Energy Reviews*, vol. 211, p. 115242, 2025.

[4] M. Schwenzer, M. Ay, T. Bergs, and D. Abel, "Review on model predictive control: an engineering perspective," *The International Journal of Advanced Manufacturing Technology*, vol. 117, pp. 1327–1349, 2021.

[5] R. Scattolini, "Architectures for distributed and hierarchical Model Predictive Control – A review," *Journal of Process Control*, vol. 19, no. 5, pp. 723–731, 2009.

[6] J. H. Lee, M. Morari, and C. E. Garcia, "State-space interpretation of model predictive control," *Automatica*, vol. 30, no. 4, pp. 707–717, 1994.

[7] J. M. Maciejowski, *Predictive Control with Constraints*. Harlow, England: Prentice Hall, 2000.

[8] J. B. Rawlings, D. Q. Mayne, and M. M. Diehl, *Model Predictive Control: Theory, Computation, and Design*, 2nd ed. Santa Barbara, CA: Nob Hill Publishing, 2017.

[9] R. Bartlett, A. Wachter, and L. T. Biegler, "Active set vs. interior point strategies for model predictive control," in *Proceedings of the 2000 American Control Conference. ACC (IEEE Cat. No. 00CH36334)*, 2000, pp. 4229–4233.

[10] N. Goswami, S. K. Mondal, and S. Paruya, "A Comparative Study of Dual Active-Set and Primal-Dual Interior-Point Method," *IFAC Proceedings Volumes*, vol. 45, no. 15, pp. 620–625, 2012.

[11] A. Abur and A. Gómez Expósito, *Power System State Estimation: Theory and Implementation*, 1st ed. Boca Raton, FL: CRC Press, 2004. doi: 10.1201/9780203913673.

[12] J. Zhao *et al.*, "Power System Dynamic State Estimation: Motivations, Definitions, Methodologies, and Future Work," *IEEE Transactions on Power Systems*, vol. 34, no. 4, pp. 3188–3198, 2019.

[13] G. Pannocchia and J. B. Rawlings, "Disturbance models for offset-free model-predictive control," *AIChE journal*, vol. 49, no. 2, pp. 426–437, 2003.

[14] A. Bemporad and M. Morari, "Robust model predictive control: A survey," in *Robustness in identification and control*, A. Garulli and A. Tesi, Eds., London: Springer London, 1999, pp. 207–226.

[15] E. Arcari, L. Hewing, M. Schlichting, and M. Zeilinger, "Dual Stochastic MPC for Systems with Parametric and Structural Uncertainty," in *Proceedings of the 2nd Conference on Learning for Dynamics and Control*, A. M. Bayen, A. Jadbabaie, G. Pappas, P. A. Parrilo, B. Recht, C. Tomlin, and M. Zeilinger, Eds., in Proceedings of Machine Learning Research, vol. 120. PMLR, Oct. 2020, pp. 894–903.

[16] S. Thangavel, S. Subramanian, S. Lucia, and S. Engell, "Handling Structural Plant-model Mismatch using a Model-error Model in the Multi-stage NMPC framework.," *IFAC-PapersOnLine*, vol. 51, no. 15, pp. 1074–1079, 2018.

[17] M. Ginocchi, F. Ponci, and A. Monti, "Sensitivity Analysis and Power Systems: Can We Bridge the Gap? A Review and a Guide to Getting Started," *Energies*, vol. 14, no. 24, p. 8274, 2021.

[18] F. Milano, F. Dörfler, G. Hug, D. J. Hill, and G. Verbic, "Foundations and Challenges of Low-Inertia Systems (Invited Paper)," *2018 Power Systems Computation Conference (PSCC)*, pp. 1–25, 2018.

[19] Australian Energy Market Operator, "Black System South Australia 28 September 2016 - Final Report," technical report, 2017. [Online]. Available: https://aemo.com.au/-/media/Files/Electricity/NEM/Market_Notices_and_Events/Power_System_Incident_Reports/2017/Integrated-Final-Report-SA-Black-System-28-September-2016.pdf

[20] J. Driesen and K. Visscher, "Virtual synchronous generators," in *2008 IEEE Power and Energy Society General Meeting - Conversion and Delivery of Electrical Energy in the 21st Century*, 2008, pp. 1–3.

[21] Bundesnetzagentur, "Festlegung gem. §§ 12h Abs. 5, 29 Abs. 1 EnWG zu den Spezifikationen und technischen Anforderungen der transparenten, diskriminierungsfreien und marktgestützten Beschaffung der inhärenten und unverzögerten Reaktion auf ein Wirkleistungsungleichgewicht (Momentanreserve) als Bestandteil der nicht frequenzgebundenen Systemdienstleistung „Trägheit der lokalen Netzstabilität" gem. § 12h Abs. 1 Nr. 2 EnWG [Determination pursuant to Sections 12h(5) and 29(1) of the Energy Industry Act (EnWG) regarding the specifications and technical requirements for the transparent, non-discriminatory, and market-based procurement of the inherent and immediate response to an active power

imbalance (instantaneous reserve) as part of the non-frequency-related system service "inertia of local grid stability" pursuant to Section 12h(1) (2) of the Energy Act (EnWG)]," technical report, 2023. [Online]. Available: https://www.bundesnetzagentur.de/DE/Beschlusskammern/1_GZ/BK6-GZ/2023/BK6-23-010/BK6-23-010_beschluss.html

[22] Australian Energy Market Commission, "Fast Frequency Response Market Ancillary Services." [Online]. Available: https://www.aemc.gov.au/rule-changes/fast-frequency-response-market-ancillary-service

[23] National Energy System Operator, "Dynamic Response Services – Provider Guidance v.10." [Online]. Available: https://www.neso.energy/document/276606/download

[24] Fingrid Oyj, "The Technical Requirements and the Prequalification Process of Fast Frequency Reserve (FFR) as of 22 May 2023." [Online]. Available: https://www.fingrid.fi/globalassets/dokumentit/fi/sahkomarkkinat/reservit/the-technical-requirements-and-the-prequalification-process-of-fast-frequency-reserve-ffr-as-of-22-may-2023.pdf

[25] M. Farrokhabadi *et al.*, "Microgrid Stability Definitions, Analysis, and Examples," *IEEE Transactions on Power Systems*, vol. 35, no. 1, pp. 13–29, 2020.

[26] F. Blaabjerg, Y. Yang, K. A. Kim, and J. Rodriguez, "Power Electronics Technology for Large-Scale Renewable Energy Generation," *Proceedings of the IEEE*, vol. 111, no. 4, pp. 335–355, 2023.

[27] G. De Carne *et al.*, "Which Deepness Class Is Suited for Modeling Power Electronics?: A Guide for Choosing the Right Model for Grid-Integration Studies," *IEEE Industrial Electronics Magazine*, vol. 13, no. 2, pp. 41–55, 2019.

[28] S. Eberlein and K. Rudion, "Impact of Inner Control Loops on Small-Signal Stability and Model-Order Reduction of Grid-Forming Converters," *IEEE Transactions on Smart Grid*, vol. 14, no. 4, pp. 2812–2824, 2022.

[29] Y. Gu, N. Bottrell, and T. C. Green, "Reduced-Order Models for Representing Converters in Power System Studies," *IEEE Transactions on Power Electronics*, vol. 33, no. 4, pp. 3644–3654, 2017.

[30] G. De Carne *et al.*, "On Modeling Depths of Power Electronic Circuits for Real-Time Simulation – A Comparative Analysis for Power Systems," *IEEE Open Access Journal of Power and Energy*, vol. 9, pp. 76–87, 2022.

[31] A. Yazdani and R. Iravani, *Voltage-Sourced Converters in Power Systems: Modeling, Control, and Applications*. Hoboken, NJ: John Wiley & Sons Ltd, 2010.

[32] Y. Li, Y. Gu, and T. C. Green, "Revisiting Grid-Forming and Grid-Following Inverters: A Duality Theory," *IEEE Transactions on Power Systems*, vol. 37, no. 6, pp. 4541–4554, 2022.

[33] Y. Cheng *et al.*, "Real-World Subsynchronous Oscillation Events in Power Grids With High Penetrations of Inverter-Based Resources," *IEEE Transactions on Power Systems*, vol. 38, no. 1, pp. 316–330, 2022.

[34] K. De Brabandere, B. Bolsens, J. Van den Keybus, A. Woyte, J. Driesen, and R. Belmans, "A Voltage and Frequency Droop Control Method for Parallel Inverters," *IEEE Transactions on Power Electronics*, vol. 22, no. 4, pp. 1107–1115, 2007.

[35] J. W. Simpson-Porco, F. Dörfler, and F. Bullo, "Droop-Controlled Inverters are Kuramoto Oscillators," *IFAC Proceedings Volumes*, vol. 45, no. 26, pp. 264–269, 2012.

[36] M. Paolone *et al.*, "Fundamentals of power systems modelling in the presence of converter-interfaced generation," *Electric Power Systems Research*, vol. 189, p. 106811, 2020.

[37] Q.-C. Zhong and G. Weiss, "Synchronverters: Inverters That Mimic Synchronous Generators," *IEEE Transactions on Industrial Electronics*, vol. 58, no. 4, pp. 1259–1267, 2010.

[38] M. Lu, "Virtual Oscillator Grid-Forming Inverters: State of the Art, Modeling, and Stability," *IEEE Transactions on Power Electronics*, vol. 37, no. 10, pp. 11579–11591, 2022.

[39] S. D'Arco and J. A. Suul, "Virtual synchronous machines — Classification of implementations and analysis of equivalence to droop controllers for microgrids," in *2013 IEEE Grenoble Conference*, 2013, pp. 1–7.

[40] B. Johnson, M. Rodriguez, M. Sinha, and S. Dhople, "Comparison of virtual oscillator and droop control," in *2017 IEEE 18th Workshop on Control and Modeling for Power Electronics (COMPEL)*, 2017, pp. 1–6.

[41] A. Tayyebi, D. Groß, A. Anta, F. Kupzog, and F. Dörfler, "Frequency Stability of Synchronous Machines and Grid-Forming Power Converters," *IEEE Journal of Emerging and Selected Topics in Power Electronics*, vol. 8, no. 2, pp. 1004–1018, 2020.

[42] C. Cardozo *et al.*, "Promises and challenges of grid forming: Transmission system operator, manufacturer and academic view points," *Electric Power Systems Research*, vol. 235, p. 110855, 2024.

[43] N. Baeckeland, D. Chatterjee, M. Lu, B. Johnson, and G.-S. Seo, "Overcurrent Limiting in Grid-Forming Inverters: A Comprehensive Review and Discussion," *IEEE Transactions on Power Electronics*, vol. 39, no. 11, pp. 14493–14517, 2024.

[44] I. Jahn *et al.*, "An Architecture for a Multi-Vendor VSC-HVDC Station With Partially Open Control and Protection," *IEEE Access*, vol. 10, pp. 13555–13569, 2022.

[45] I. Jahn, G. Chaffey, E. Prieto-Araujo, M. Hoffmann, R. Alvarez, and A. Monti, "On the Partitioning of MMC Control Systems Using Graph

Theory," *IEEE Open Journal of Power Electronics*, vol. 3, pp. 611–620, 2022.

[46] Z. Zhang *et al.*, "Advances and opportunities in the model predictive control of microgrids: Part I–primary layer," *International Journal of Electrical Power & Energy Systems*, vol. 134, p. 107411, 2022.

[47] S. Vazquez, J. Rodriguez, M. Rivera, L. G. Franquelo, and M. Norambuena, "Model Predictive Control for Power Converters and Drives: Advances and Trends," *IEEE Transactions on Industrial Electronics*, vol. 64, no. 2, pp. 935–947, 2016.

[48] S. Kouro, M. A. Perez, J. Rodriguez, A. M. Llor, and H. A. Young, "Model Predictive Control: MPC's Role in the Evolution of Power Electronics," *IEEE Industrial Electronics Magazine*, vol. 9, no. 4, pp. 8–21, 2015.

[49] P. Kundur, *Power system stability and control*, 1st ed. in EPRI Power System Engineering Series. New York: McGraw-Hill, 1994.

[50] R. Heydari, T. Dragicevic, and F. Blaabjerg, "High-Bandwidth Secondary Voltage and Frequency Control of VSC-Based AC Microgrid," *IEEE Transactions on Power Electronics*, vol. 34, no. 11, pp. 11320–11331, 2019.

[51] O. Babayomi *et al.*, "Advances and opportunities in the model predictive control of microgrids: Part II–Secondary and tertiary layers," *International Journal of Electrical Power & Energy Systems*, vol. 134, p. 107339, 2022.

[52] A. Ahmadifar, M. Ginocchi, M. S. Golla, F. Ponci, and A. Monti, "Development of an Energy Management System for a Renewable Energy Community and Performance Analysis via Global Sensitivity Analysis," *IEEE Access*, vol. 11, pp. 4131–4154, 2023.

[53] C. Bordons, F. Garcia-Torres, and M. A. Ridao, *Model predictive control of microgrids*, vol. 358. in Advances in Industrial Control, vol. 358. Springer Cham, 2020.

[54] A. M. Ersdal, L. Imsland, and K. Uhlen, "Model Predictive Load-Frequency Control," *IEEE Transactions on Power Systems*, vol. 31, no. 1, pp. 777–785, 2015.

[55] P. Ojaghi and M. Rahmani, "LMI-Based Robust Predictive Load Frequency Control for Power Systems With Communication Delays," *IEEE Transactions on Power Systems*, vol. 32, no. 5, pp. 4091–4100, 2017.

[56] A. N. Venkat, I. A. Hiskens, J. B. Rawlings, and S. J. Wright, "Distributed MPC Strategies With Application to Power System Automatic Generation Control," *IEEE Transactions on Control Systems Technology*, vol. 16, no. 6, pp. 1192–1206, 2008.

[57] A. Ulbig, T. Rinke, S. Chatzivasileiadis, and G. Andersson, "Predictive control for real-time frequency regulation and rotational inertia provision in power systems," in *52nd IEEE Conference on Decision and Control*, 2013, pp. 2946–2953.

[58] U. Tamrakar, T. M. Hansen, R. Tonkoski, and D. A. Copp, "Model Predictive Frequency Control of Low Inertia Microgrids," in *2019 IEEE 28th International Symposium on Industrial Electronics (ISIE)*, 2019, pp. 2111–2116.

[59] R. K. Subroto, K. L. Lian, C.-C. Chu, and C.-J. Liao, "A Fast Frequency Control Based on Model Predictive Control Taking Into Account of Optimal Allocation of Power From the Energy Storage System," *IEEE Transactions on Power Delivery*, vol. 36, no. 4, pp. 2467–2478, 2021.

[60] A. Ademola-Idowu and B. Zhang, "Frequency Stability Using MPC-Based Inverter Power Control in Low-Inertia Power Systems," *IEEE Transactions on Power Systems*, vol. 36, no. 2, pp. 1628–1637, 2020.

[61] O. Stanojev, U. Markovic, P. Aristidou, G. Hug, D. Callaway, and E. Vrettos, "MPC-Based Fast Frequency Control of Voltage Source Converters in Low-Inertia Power Systems," *IEEE Transactions on Power Systems*, vol. 37, no. 4, pp. 3209–3220, 2020.

[62] T. Kerdphol, F. S. Rahman, Y. Mitani, K. Hongesombut, and S. Küfeoğlu, "Virtual Inertia Control-Based Model Predictive Control for Microgrid Frequency Stabilization Considering High Renewable Energy Integration," *Sustainability*, vol. 9, no. 5, p. 773, 2017.

[63] B. Long, Y. Liao, K. T. Chong, J. Rodríguez, and J. M. Guerrero, "MPC-Controlled Virtual Synchronous Generator to Enhance Frequency and Voltage Dynamic Performance in Islanded Microgrids," *IEEE Transactions on Smart Grid*, vol. 12, no. 2, pp. 953–964, 2021.

[64] N. Sockeel, J. Gafford, B. Papari, and M. Mazzola, "Virtual Inertia Emulator-Based Model Predictive Control for Grid Frequency Regulation Considering High Penetration of Inverter-Based Energy Storage System," *IEEE Transactions on Sustainable Energy*, vol. 11, no. 4, pp. 2932–2939, 2020.

[65] J. Pahasa and I. Ngamroo, "PHEVs Bidirectional Charging/Discharging and SoC Control for Microgrid Frequency Stabilization Using Multiple MPC," *IEEE Transactions on Smart Grid*, vol. 6, no. 2, pp. 526–533, 2014.

[66] A. K. Verma, H. Gooi, A. Ukil, N. R. Tummuru, and S. K. Kollimalla, "Microgrid frequency stabilization using model predictive controller," in *2016 IEEE PES Transmission & Distribution Conference and Exposition-Latin America (PES T&D-LA)*, 2016, pp. 1–6.

[67] P. A. Gbadega and A. K. Saha, "Load Frequency Control of a Two-Area Power System With a Stand-Alone Microgrid Based on Adaptive Model Predictive Control," *IEEE Journal of Emerging and Selected Topics in Power Electronics*, vol. 9, no. 6, pp. 7253–7263, 2020.

[68] L. Papangelis, M.-S. Debry, T. Prevost, P. Panciatici, and T. Van Cutsem, "Decentralized model predictive control of voltage source converters for

AC frequency containment," *International Journal of Electrical Power & Energy Systems*, vol. 98, pp. 342–349, 2018.

[69] L. Yang, T. Liu, and D. J. Hill, "Distributed MPC-based frequency control for multi-area power systems with energy storage," *Electric Power Systems Research*, vol. 190, p. 106642, 2021.

[70] Z. Guo, S. Li, and Y. Zheng, "Feedback Linearization Based Distributed Model Predictive Control for Secondary Control of Islanded Microgrid," *Asian Journal of Control*, vol. 22, no. 1, pp. 460–473, 2020.

[71] J. S. Gomez, D. Saez, J. W. Simpson-Porco, and R. Cardenas, "Distributed Predictive Control for Frequency and Voltage Regulation in Microgrids," *IEEE Transactions on Smart Grid*, vol. 11, no. 2, pp. 1319–1329, 2019.

[72] N. Ma, F. Bai, and T. K. Saha, "Coordinated Frequency Control Based on Hierarchical MPC Considering Tie-Line Power Flow," *IEEE Transactions on Power Systems*, vol. 41, no. 2, pp. 821–835, 2026.

[73] P. McNamara and F. Milano, "Model Predictive Control-Based AGC for Multi-Terminal HVDC-Connected AC grids," *IEEE Transactions on Power Systems*, vol. 33, no. 1, pp. 1036–1048, 2017.

[74] K. Liu, L. Yang, T. Liu, and D. J. Hill, "Distributed Model Predictive Frequency Control of Inverter-Based Networked Microgrids," *IEEE Transactions on Energy Conversion*, vol. 36, no. 4, pp. 2623–2633, 2021.

[75] C. Ahumada, R. Cárdenas, D. Saez, and J. M. Guerrero, "Secondary Control Strategies for Frequency Restoration in Islanded Microgrids With Consideration of Communication Delays," *IEEE Transactions on Smart Grid*, vol. 7, no. 3, pp. 1430–1441, 2015.

[76] M. Ma, C. Zhang, X. Liu, and H. Chen, "Distributed Model Predictive Load Frequency Control of the Multi-Area Power System After Deregulation," *IEEE transactions on Industrial Electronics*, vol. 64, no. 6, pp. 5129–5139, 2016.

[77] A. S. Badwe, R. S. Patwardhan, S. L. Shah, S. C. Patwardhan, and R. D. Gudi, "Quantifying the impact of model-plant mismatch on controller performance," *Journal of Process Control*, vol. 20, no. 4, pp. 408–425, 2010.

[78] "IEEE Recommended Practice for Hardware-in-the-Loop (HIL) Simulation-Based Testing of Electric Power Apparatus and Controls," *IEEE Std 2004-2025*, pp. 1–146, 2025, doi: 10.1109/IEEESTD.2025.11144468.

[79] A. Benigni, T. Strasser, G. De Carne, M. Liserre, M. Cupelli, and A. Monti, "Real-Time Simulation-Based Testing of Modern Energy Systems: A Review and Discussion," *IEEE Industrial Electronics Magazine*, vol. 14, no. 2, pp. 28–39, 2020.

[80] H. Wu, H. Ni, and G. T. Heydt, "The impact of time delay on robust control design in power systems," in *2002 IEEE Power Engineering Society Winter Meeting. Conference Proceedings (Cat. No. 02CH37309)*, 2002, pp. 1511–1516.

[81] F. Milano and M. Anghel, "Impact of Time Delays on Power System Stability," *IEEE Transactions on Circuits and Systems I: Regular Papers*, vol. 59, no. 4, pp. 889–900, 2011.

[82] B. Wittenmark, "Sampling of a system with a time delay," *IEEE Transactions on Automatic Control*, vol. 30, no. 5, pp. 507–510, 1985.

[83] D. Dotta, A. S. e Silva, and I. C. Decker, "Wide-Area Measurements-Based Two-Level Control Design Considering Signal Transmission Delay," *IEEE Transactions on Power Systems*, vol. 24, no. 1, pp. 208–216, 2009.

[84] L. Cheng, G. Chen, W. Gao, F. Zhang, and G. Li, "Adaptive Time Delay Compensator (ATDC) Design for Wide-Area Power System Stabilizer," *IEEE Transactions on Smart Grid*, vol. 5, no. 6, pp. 2957–2966, 2014.

[85] D. Soudbakhsh, A. Chakrabortty, and A. M. Annaswamy, "A delay-aware cyber-physical architecture for wide-area control of power systems," *Control Engineering Practice*, vol. 60, pp. 171–182, 2017.

[86] X. Liu, Y. Zhang, and K. Y. Lee, "Coordinated Distributed MPC for Load Frequency Control of Power System With Wind Farms," *IEEE Transactions on Industrial Electronics*, vol. 64, no. 6, pp. 5140–5150, 2016.

[87] J. W. Simpson-Porco, Q. Shafiee, F. Dörfler, J. C. Vasquez, J. M. Guerrero, and F. Bullo, "Secondary Frequency and Voltage Control of Islanded Microgrids via Distributed Averaging," *IEEE Transactions on Industrial Electronics*, vol. 62, no. 11, pp. 7025–7038, 2015.

[88] J. Machowski, Z. Lubosny, J. Bialek, and J. Bumby, *Power System Dynamics: Stability and Control*, 3rd ed. West Sussex, UK: Wiley, 2020.

[89] U. Markovic, O. Stanojev, P. Aristidou, E. Vrettos, D. Callaway, and G. Hug, "Understanding Small-Signal Stability of Low-Inertia Systems," *IEEE Transactions on Power Systems*, vol. 36, no. 5, pp. 3997–4017, 2021.

[90] F. Milano and A. Ortega, "Frequency Divider," *IEEE Transactions on Power Systems*, vol. 32, no. 2, pp. 1493–1501, 2016.

[91] A. Ortega, A. Musa, A. Monti, and F. Milano, "Hardware-in-the-Loop Validation of the Frequency Divider Formula," in *2018 IEEE Power & Energy Society General Meeting (PESGM)*, 2018, pp. 1–5.

[92] Y.-Y. Liu, J.-J. Slotine, and A.-L. Barabási, "Observability of complex systems," *Proceedings of the National Academy of Sciences*, vol. 110, no. 7, pp. 2460–2465, 2013.

[93] Y.-Y. Liu, J.-J. Slotine, and A.-L. Barabási, "Controllability of complex networks," *Nature*, vol. 473, no. 7346, pp. 167–173, 2011.

[94] A. N. Montanari and L. A. Aguirre, "Observability of Network Systems: A Critical Review of Recent Results," *Journal of Control, Automation and Electrical Systems*, vol. 31, no. 6, pp. 1348–1374, 2020.

[95] S. D'Arco and J. A. Suul, "Phase Angle Feed-Forward Control for Improving the Power Reference Tracking of Virtual Synchronous Machines," *IEEE Transactions on Industry Applications*, vol. 60, no. 1, pp. 851–864, 2023.

[96] O. Mo, S. D'Arco, and J. A. Suul, "Evaluation of Virtual Synchronous Machines With Dynamic or Quasi-Stationary Machine Models," *IEEE Transactions on Industrial Electronics*, vol. 64, no. 7, pp. 5952–5962, 2016.

[97] T. Qoria, E. Rokrok, A. Bruyere, B. François, and X. Guillaud, "A PLL-Free Grid-Forming Control With Decoupled Functionalities for High-Power Transmission System Applications," *IEEE Access*, vol. 8, pp. 197363–197378, 2020.

[98] Q. Ma, L. Chen, L. Li, Y. Min, Y. Gong, and K. Liang, "Effect of Grid-Following VSC on Terminal Frequency," *IEEE Transactions on Power Systems*, vol. 38, no. 2, pp. 1775–1778, 2023.

[99] J. Liu, C. Wang, and T. Bi, "Revisiting the Effect of Grid-Following Converter on Frequency Dynamics - Part II: Spatial Difference," *IEEE Transactions on Power Systems*, vol. 41, no. 2, pp. 1459–1472, 2026.

[100] Y. Li, T. C. Green, and Y. Gu, "The Intrinsic Communication in Power Systems: A New Perspective to Understand Synchronization Stability," *IEEE Transactions on Circuits and Systems I: Regular Papers*, vol. 70, no. 11, pp. 4615–4626, 2023.

[101] M. Aghahassani, E. D. Castronuovo, P. Ledesma, and F. Milano, "Extended Frequency Divider Formula with Inclusion of DER Control Dynamics," in *2023 IEEE Power & Energy Society General Meeting (PESGM)*, 2023, pp. 1–5.

[102] IEEE Power & Energy Society, Task Force on Turbine-Governor Modeling, "Dynamic Models for Turbine-Governors in Power System Studies," Technical Report (PES-TR1), 2013.

[103] U. Datta, A. Kalam, and J. Shi, "Battery Energy Storage System Control for Mitigating PV Penetration Impact on Primary Frequency Control and State-of-Charge Recovery," *IEEE Transactions on Sustainable Energy*, vol. 11, no. 2, pp. 746–757, 2019.

[104] M. I. Alemany, A. Castillejo-Cuberos, Á. Lorca, and M. Negrete-Pincetic, "Assessing the feasibility of battery energy storage coupled to photovoltaic plants, participating on energy and ancillary services markets, through power system optimization and sub-hourly simulations," *Journal of Energy Storage*, vol. 140, p. 118993, 2025.

[105] J. Pahasa and I. Ngamroo, "Coordinated Control of Wind Turbine Blade Pitch Angle and PHEVs Using MPCs for Load Frequency Control of Microgrid," *IEEE Systems Journal*, vol. 10, no. 1, pp. 97–105, 2014.

[106] S. Adhikari and F. Li, "Coordinated V-f and P-Q Control of Solar Photovoltaic Generators With MPPT and Battery Storage in Microgrids," *IEEE Transactions on Smart Grid*, vol. 5, no. 3, pp. 1270–1281, 2014.

[107] K. S. El-Bidairi, H. D. Nguyen, T. S. Mahmoud, S. Jayasinghe, and J. M. Guerrero, "Optimal sizing of Battery Energy Storage Systems for dynamic

frequency control in an islanded microgrid: A case study of Flinders Island, Australia," *Energy*, vol. 195, p. 117059, 2020.

[108] H. Hao, B. M. Sanandaji, K. Poolla, and T. L. Vincent, "Frequency regulation from flexible loads: Potential, economics, and implementation," in *2014 American Control Conference*, 2014, pp. 65–72.

[109] J. T. Hughes, A. D. Domínguez-García, and K. Poolla, "Identification of Virtual Battery Models for Flexible Loads," *IEEE Transactions on Power Systems*, vol. 31, no. 6, pp. 4660–4669, 2016.

[110] M. D. Galus, S. Koch, and G. Andersson, "Provision of Load Frequency Control by PHEVs, Controllable Loads, and a Cogeneration Unit," *IEEE Transactions on Industrial Electronics*, vol. 58, no. 10, pp. 4568–4582, 2011.

[111] M. G. Dozein, A. M. De Corato, and P. Mancarella, "Virtual Inertia Response and Frequency Control Ancillary Services From Hydrogen Electrolyzers," *IEEE Transactions on Power Systems*, vol. 38, no. 3, pp. 2447–2459, 2022.

[112] N. Taranin, M. G. Dozein, O. Saborío-Romano, and N. A. Cutululis, "On the Ramp-Rate Limitation of Electrolysis Plants: Modeling Fundamentals and System-Level Impact Analysis," *IEEE Transactions on Sustainable Energy*, vol. 17, no. 2, pp. 1238–1249, 2026.

[113] O. Chahir *et al.*, "Improved ADRC-based control of industrial alkaline electrolyzers for green hydrogen production in PV-battery microgrids," *International Journal of Hydrogen Energy*, vol. 190, p. 151925, 2025.

[114] M. Agredano-Torres and Q. Xu, "Decentralized Power Management of Hybrid Hydrogen Electrolyzer–Supercapacitor Systems for Frequency Regulation of Low-Inertia Grids," *IEEE Transactions on Industrial Electronics*, vol. 72, no. 8, pp. 8072–8081, 2025.

[115] M. A. Syed and M. Khalid, "An Intelligent Model Predictive Control Strategy for Stable Solar-Wind Renewable Power Dispatch Coupled with Hydrogen Electrolyzer and Battery Energy Storage," *International Journal of Energy Research*, vol. 2023, no. 1, p. 4531054, 2023.

[116] "Silyzer 300 Factsheet." Siemens Energy, 2025.

[117] T. Heynen, T. Heins, M. Kuhn, W. Leterme, and A. Monti, "Systematic review on fast frequency ancillary services provided by large-scale hydrogen electrolyzer plants," *23rd Wind and Solar Integration Workshop*, 2024.

[118] ENTSO-E, "Potential of P2H2 technologies to provide system services," Technical Report, 2022. Accessed: Aug. 16, 2024. [Online]. Available: https://eepublicdownloads.entsoe.eu/clean-documents/Publications/Position%20papers%20and%20reports/ENTSO-E_Study_on_Flexibility_from_Power-to-Hydrogen___P2H2_.pdf

[119] CIGRE Task Force C6.04, *Benchmark Systems for Network Integration of Renewable and Distributed Energy Resources*. CIGRE, 2014.

[120] M. Moayedi, Y. K. Foo, and Y. C. Soh, "Adaptive Kalman Filtering in Networked Systems With Random Sensor Delays, Multiple Packet Dropouts and Missing Measurements," *IEEE Transactions on Signal Processing*, vol. 58, no. 3, pp. 1577–1588, 2010.

[121] L. Schenato, "Optimal Estimation in Networked Control Systems Subject to Random Delay and Packet Drop," *IEEE Transactions on Automatic Control*, vol. 53, no. 5, pp. 1311–1317, 2008.

[122] P. H. Dana and B. M. Penrod, "The Role of GPS in Precise Time and Frequency Dissemination," *GPS World*, 1990.

[123] Q. Hu *et al.*, "Grid-Forming Inverter Enabled Virtual Power Plants With Inertia Support Capability," *IEEE Transactions on Smart Grid*, vol. 13, no. 5, pp. 4134–4143, 2022.

[124] V. Häberle, A. Tayyebi, X. He, E. Prieto-Araujo, and F. Dörfler, "Grid-Forming and Spatially Distributed Control Design of Dynamic Virtual Power Plants," *IEEE Transactions on Smart Grid*, vol. 15, no. 2, pp. 1761–1777, 2023.

[125] W. Zhong, J. Chen, M. Liu, M. A. A. Murad, and F. Milano, "Coordinated Control of Virtual Power Plants to Improve Power System Short-Term Dynamics," *Energies*, vol. 14, no. 4, p. 1182, 2021.

[126] G. Magdy, H. Ali, and D. Xu, "Effective Control of Smart Hybrid Power Systems: Cooperation of Robust LFC and Virtual Inertia Control Systems," *CSEE Journal of Power and Energy Systems*, vol. 8, no. 6, pp. 1583–1593, 2021.

[127] O. Stanojev, J. Rüssli-Kueh, U. Markovic, P. Aristidou, and G. Hug, "Primary Frequency Control Provision by Distributed Energy Resources in Active Distribution Networks," in *2021 IEEE Madrid PowerTech*, 2021, pp. 1–6.

[128] Z. Tang, T. Liu, C. Zhang, Y. Zheng, and D. J. Hill, "Distributed Control of Active Distribution Networks for Frequency Support," in *2018 Power Systems Computation Conference (PSCC)*, 2018, pp. 1–7.

[129] A. Singh, V. Debusschere, N. Hadjsaid, X. Legrand, and B. Bouzigon, "Slow-Interaction Converter-Driven Stability in the Distribution Grid: Small-Signal Stability Analysis With Grid-Following and Grid-Forming Inverters," *IEEE Transactions on Power Systems*, vol. 39, pp. 4521–4536, 2024.

[130] D. Nouti, F. Ponci, and A. Monti, "Heterogeneous Inertia Estimation for Power Systems with High Penetration of Converter-Interfaced Generation," *Energies*, vol. 14, no. 16, 2021.

[131] F. Zeng, J. Zhang, G. Chen, Z. Wu, S. Huang, and Y. Liang, "Online Estimation of Power System Inertia Constant Under Normal Operating Conditions," *IEEE Access*, vol. 8, pp. 101426–101436, 2020.

[132] T. T. Tran *et al.*, "Enhancing Performance of Andronov-Hopf Oscillator-Based Grid-Forming Converters in Microgrids With Non-Invasive Online Impedance Estimation," *IEEE Transactions on Smart Grid*, vol. 14, pp. 4479–4493, 2023.

[133] S. K. Gurumurthy, M. Pitz, Y. Viknesh Kannan, F. Ponci, and A. Monti, "Operation and Uncertainty Characterization of a Standalone Wideband-Frequency Grid Impedance Measurement Device," *IEEE Transactions on Instrumentation and Measurement*, vol. 74, pp. 1–14, 2025.

[134] J. Fang, H. Deng, and S. M. Goetz, "Grid Impedance Estimation Through Grid-Forming Power Converters," *IEEE Transactions on Power Electronics*, vol. 36, no. 2, pp. 2094–2104, 2021.

[135] G. F. Riley and T. R. Henderson, "The ns-3 Network Simulator," in *Modeling and Tools for Network Simulation*, K. Wehrle, M. Güneş, and J. Gross, Eds., Berlin, Heidelberg: Springer Berlin Heidelberg, 2010, pp. 15–34. doi: 10.1007/978-3-642-12331-3_2.

[136] T. Heins *et al.*, "Delay-aware Model Predictive Control for Fast Frequency Control," *2023 IEEE International Conference on Communications, Control, and Computing Technologies for Smart Grids (SmartGridComm)*, 2023.

[137] MathWorks, "Simulink Toolbox: Specialized Power Systems, version 7.8 (R2022b)." The MathWorks Inc., Natick, MA, US, 2022.

[138] S. Knight, H. X. Nguyen, N. Falkner, R. Bowden, and M. Roughan, "The Internet Topology Zoo," *IEEE Journal on Selected Areas in Communications*, vol. 29, no. 9, pp. 1765–1775, 2011.

[139] A. Amirkhani and A. H. Barshooi, "Consensus in multi-agent systems: a review," *Artificial Intelligence Review*, vol. 55, no. 5, pp. 3897–3935, 2022.

[140] B. Tan *et al.*, "Distributed Frequency Divider for Power System Bus Frequency Online Estimation Considering Virtual Inertia From DFIGs," *IEEE Journal on Emerging and Selected Topics in Circuits and Systems*, vol. 12, pp. 161–171, 2022.

[141] S. Boyd, N. Parikh, E. Chu, B. Peleato, and J. Eckstein, "Distributed Optimization and Statistical Learning via the Alternating Direction Method of Multipliers," *Foundations and Trends in Machine Learning*, vol. 3, no. 1, pp. 1–122, 2011.

[142] A. Monti, S. K. Gurumurthy, R. Uhl, and M. Pitz, " Vorrichtung zur Bestimmung der Impedanz in Abhängigkeit der Frequenz eines zu messenden Versorgungsnetzes," 102019214533, Mar. 25, 2021 [Online]. Available: https://worldwide.espacenet.com/patent/search/family/072665242/publication/DE102019214533A1?q=pn%3DDE102019214533A1

[143] S. K. Gurumurthy, R. Uhl, M. Pitz, F. Ponci, and A. Monti, "Non-Invasive Wideband-frequency Grid Impedance Measurement Device," in *2019 IEEE*

10th International Workshop on Applied Measurements for Power Systems (AMPS), 2019, pp. 1–6.

[144] T. Erseghe, "A Distributed and Scalable Processing Method Based Upon ADMM," *IEEE Signal Processing Letters*, vol. 19, pp. 563–566, 2012, doi: 10.1109/LSP.2012.2207719.

[145] G. Notarstefano, I. Notarnicola, and A. Camisa, "Distributed Optimization for Smart Cyber-Physical Networks," *Foundations and Trends in Systems and Control.*, vol. 7, pp. 253–383, 2019, doi: 10.1561/2600000020.

[146] N. Bastianello, R. Carli, L. Schenato, and M. Todescato, "A Partition-Based Implementation of the Relaxed ADMM for Distributed Convex Optimization over Lossy Networks," *2018 IEEE Conference on Decision and Control (CDC)*, pp. 3379–3384, 2018.

[147] I. Notarnicola, R. Carli, and G. Notarstefano, "Distributed Partitioned Big-Data Optimization via Asynchronous Dual Decomposition," *IEEE Transactions on Control of Network Systems*, vol. 5, pp. 1910–1919, 2018, doi: 10.1109/TCNS.2017.2774010.

[148] R. Carli and G. Notarstefano, "Distributed partition-based optimization via dual decomposition," *52nd IEEE Conference on Decision and Control*, pp. 2979–2984, 2013, doi: 10.1109/CDC.2013.6760336.

[149] F. Milano, "Complex Frequency," *IEEE Transactions on Power Systems*, vol. 37, no. 2, pp. 1230–1240, 2021.

E.ON ERC Band 1
Streblow, R.
Thermal Sensation and Comfort Model for Inhomogeneous Indoor Environments
1. Auflage 2011
ISBN 978-3-942789-00-4

E.ON ERC Band 2
Naderi, A.
Multi-phase, multi-species reactive transport modeling as a tool for system analysis in geological carbon dioxide storage
1. Auflage 2011
ISBN 978-3-942789-01-1

E.ON ERC Band 3
Westner, G.
Four Essays related to Energy Economic Aspects of Combined Heat and Power Generation
1. Auflage 2012
ISBN 978-3-942789-02-8

E.ON ERC Band 4
Lohwasser, R.
Impact of Carbon Capture and Storage (CCS) on the European Electricity Market
1. Auflage 2012
ISBN 978-3-942789-03-5

E.ON ERC Band 5
Dick, C.
Multi-Resonant Converters as Photovoltaic Module-Integrated Maximum Power Point Tracker
1. Auflage 2012
ISBN 978-3-942789-04-2

E.ON ERC Band 6
Lenke, R.
A Contribution to the Design of Isolated DC-DC Converters for Utility Applications
1. Auflage 2012
ISBN 978-3-942789-05-9

E.ON ERC Band 7
Brännström, F.
Einsatz hybrider RANS-LES-Turbulenzmodelle in der Fahrzeugklimatisierung
1. Auflage 2012
ISBN 978-3-942789-06-6

E.ON ERC Band 8
Bragard, M.
The Integrated Emitter Turn-Off Thyristor - An Innovative MOS-Gated High-Power Device
1. Auflage 2012
ISBN 978-3-942789-07-3

E.ON ERC Band 9
Hoh, A.
Exergiebasierte Bewertung gebäudetechnischer Anlagen
1. Auflage 2013
ISBN 978-3-942789-08-0

E.ON ERC Band 10
Köllensperger, P.
The Internally Commutated Thyristor - Concept, Design and Application
1. Auflage 2013
ISBN 978-3-942789-09-7

E.ON ERC Band 11
Achtnicht, M.
Essays on Consumer Choices Relevant to Climate Change: Stated Preference Evidence from Germany
1. Auflage 2013
ISBN 978-3-942789-10-3

E.ON ERC Band 12
Panašková, J.
Olfaktorische Bewertung von Emissionen aus Bauprodukten
1. Auflage 2013
ISBN 978-3-942789-11-0

E.ON ERC Band 13
Vogt, C.
Optimization of Geothermal Energy Reservoir Modeling using Advanced Numerical Tools for Stochastic Parameter Estimation and Quantifying Uncertainties
1. Auflage 2013
ISBN 978-3-942789-12-7

E.ON ERC Band 14
Benigni, A.
Latency exploitation for parallelization of power systems simulation
1. Auflage 2013
ISBN 978-3-942789-13-4

E.ON ERC Band 15
Butschen, T.
Dual-ICT – A Clever Way to Unite Conduction and Switching Optimized Properties in a Single Wafer
1. Auflage 2013
ISBN 978-3-942789-14-1

E.ON ERC Band 16
Li, W.
Fault Detection and Protection inMedium Voltage DC Shipboard Power Systems
1. Auflage 2013
ISBN 978-3-942789-15-8

E.ON ERC Band 17
Shen, J.
Modeling Methodologies for Analysis and Synthesis of Controls and Modulation Schemes for High-Power Converters with Low Pulse Ratios
1. Auflage 2014
ISBN 978-3-942789-16-5

E.ON ERC Band 18
Flieger, B.
Innenraummodellierung einer Fahrzeugkabine in der Programmiersprache Modelica
1. Auflage 2014
ISBN 978-3-942789-17-2

E.ON ERC Band 19
Liu, J.
Measurement System and Technique for Future Active Distribution Grids
1. Auflage 2014
ISBN 978-3-942789-18-9

E.ON ERC Band 20
Kandzia, C.
Experimentelle Untersuchung der Strömungsstrukturen in einer Mischlüftung
1. Auflage 2014
ISBN 978-3-942789-19-6

E.ON ERC Band 21
Thomas, S.
A Medium-Voltage Multi-Level DC/DC Converter with High Voltage Transformation Ratio
1. Auflage 2014
ISBN 978-3-942789-20-2

E.ON ERC Band 22
Tang, J.
Probabilistic Analysis and Stability Assessment for Power Systems with Integration of Wind Generation and Synchrophasor Measurement
1. Auflage 2014
ISBN 978-3-942789-21-9

E.ON ERC Band 23
Sorda, G.
The Diffusion of Selected Renewable Energy Technologies: Modeling, Economic Impacts, and Policy Implications
1. Auflage 2014
ISBN 978-3-942789-22-6

E.ON ERC Band 24
Rosen, C.
Design considerations and functional analysis of local reserve energy markets for distributed generation
1. Auflage 2014
ISBN 978-3-942789-23-3

E.ON ERC Band 25
Ni, F.
Applications of Arbitrary Polynomial Chaos in Electrical Systems
1. Auflage 2015
ISBN 978-3-942789-24-0

E.ON ERC Band 26
Michelsen, C. C.
The *Energiewende* in the German Residential Sector: Empirical Essays on Homeowners' Choices of Space Heating Technologies
1. Auflage 2015
ISBN 978-3-942789-25-7

E.ON ERC Band 27
Rohlfs, W.
Decision-Making under Multi-Dimensional Price Uncertainty for Long-Lived Energy Investments
1. Auflage 2015
ISBN 978-3-942789-26-4

E.ON ERC Band 28
Wang, J.
Design of Novel Control algorithms of Power Converters for Distributed Generation
1. Auflage 2015
ISBN 978-3-942789-27-1

E.ON ERC Band 29
Helmedag, A.
System-Level Multi-Physics Power Hardware in the Loop Testing for Wind Energy Converters
1. Auflage 2015
ISBN 978-3-942789-28-8

E.ON ERC Band 30
Togawa, K.
Stochastics-based Methods Enabling Testing of Grid-related Algorithms through Simulation
1. Auflage 2015
ISBN 978-3-942789-29-5

E.ON ERC Band 31
Huchtemann, K.
Supply Temperature Control Concepts in Heat Pump Heating Systems
1. Auflage 2015
ISBN 978-3-942789-30-1

E.ON ERC Band 32
Molitor, C.
Residential City Districts as Flexibility Resource: Analysis, Simulation, and Decentralized Coordination Algorithms
1. Auflage 2015
ISBN 978-3-942789-31-8

E.ON ERC Band 33
Sunak, Y.
Spatial Perspectives on the Economics of Renewable Energy Technologies
1. Auflage 2015
ISBN 978-3-942789-32-5

E.ON ERC Band 34
Cupelli, M.
Advanced Control Methods for Robust Stability of MVDC Systems
1. Auflage 2015
ISBN 978-3-942789-33-2

E.ON ERC Band 35
Chen, K.
Active Thermal Management for Residential Air Source Heat Pump Systems
1. Auflage 2015
ISBN 978-3-942789-34-9

E.ON ERC Band 36
Pâques, G.
Development of SiC GTO Thyristors with Etched Junction Termination
1. Auflage 2016
ISBN 978-3-942789-35-6

E.ON ERC Band 37
Garnier, E.
Distributed Energy Resources and Virtual Power Plants: Economics of Investment and Operation
1. Auflage 2016
ISBN 978-3-942789-37-0

E.ON ERC Band 38
Calì, D.
Occupants' Behavior and its Impact upon the Energy Performance of Buildings
1. Auflage 2016
ISBN 978-3-942789-36-3

E.ON ERC Band 39
Isermann, T.
A Multi-Agent-based Component Control and Energy Management System for Electric Vehicles
1. Auflage 2016
ISBN 978-3-942789-38-7

E.ON ERC Band 40
Wu, X.
New Approaches to Dynamic Equivalent of Active Distribution Network for Transient Analysis
1. Auflage 2016
ISBN 978-3-942789-39-4

E.ON ERC Band 41
Garbuzova-Schiftler, M.
The Growing ESCO Market for Energy Efficiency in Russia: A Business and Risk Analysis
1. Auflage 2016
ISBN 978-3-942789-40-0

E.ON ERC Band 42
Huber, M.
Agentenbasierte Gebäudeautomation für raumlufttechnische Anlagen
1. Auflage 2016
ISBN 978-3-942789-41-7

E.ON ERC Band 43
Soltau, N.
High-Power Medium-Voltage DC-DC Converters: Design, Control and Demonstration
1. Auflage 2017
ISBN 978-3-942789-42-4

E.ON ERC Band 44
Stieneker, M.
Analysis of Medium-Voltage Direct-Current Collector Grids in Offshore Wind Parks
1. Auflage 2017
ISBN 978-3-942789-43-1

E.ON ERC Band 45
Bader, A.
Entwicklung eines Verfahrens zur Strompreisvorhersage im kurzfristigen Intraday-Handelszeitraum
1. Auflage 2017
ISBN 978-3-942789-44-8

E.ON ERC Band 46
Chen, T.
Upscaling Permeability for Fractured Porous Rocks and Modeling Anisotropic Flow and Heat Transport
1. Auflage 2017
ISBN 978-3-942789-45-5

E.ON ERC Band 47
Ferdowsi, M.
Data-Driven Approaches for Monitoring of Distribution Grids
1. Auflage 2017
ISBN 978-3-942789-46-2

E.ON ERC Band 48
Kopmann, N.
Betriebsverhalten freier Heizflächen unter zeitlich variablen Randbedingungen
1. Auflage 2017
ISBN 978-3-942789-47-9

E.ON ERC Band 49
Fütterer, J.
Tuning of PID Controllers within Building Energy Systems
1. Auflage 2017
ISBN 978-3-942789-48-6

E.ON ERC Band 50
Adler, F.
A Digital Hardware Platform for Distributed Real-Time Simulation of Power Electronic Systems
1. Auflage 2017
ISBN 978-3-942789-49-3

E.ON ERC Band 51
Harb, H.
Predictive Demand Side Management Strategies for Residential Building Energy Systems
1. Auflage 2017
ISBN 978-3-942789-50-9

E.ON ERC Band 52
Jahangiri, P.
Applications of Paraffin-Water Dispersions in Energy Distribution Systems
1. Auflage 2017
ISBN 978-3-942789-51-6

E.ON ERC Band 53
Adolph, M.
Identification of Characteristic User Behavior with a Simple User Interface in the Context of Space Heating
1. Auflage 2018
ISBN 978-3-942789-52-3

E.ON ERC Band 54
Galassi, V.
Experimental evidence of private energy consumer and prosumer preferences in the sustainable energy transition
1. Auflage 2017
ISBN 978-3-942789-53-0

E.ON ERC Band 55
Sangi, R.
Development of Exergy-based Control Strategies for Building Energy Systems
1. Auflage 2018
ISBN 978-3-942789-54-7

E.ON ERC Band 56
Stinner, S.
Quantifying and Aggregating the Flexibility of Building Energy Systems
1. Auflage 2018
ISBN 978-3-942789-55-4

E.ON ERC Band 57
Fuchs, M.
Graph Framework for Automated Urban Energy System Modeling
1. Auflage 2018
ISBN 978-3-942789-56-1

E.ON ERC Band 58
Osterhage, T.
Messdatengestützte Analyse und Interpretation sanierungsbedingter Effizienzsteigerungen im Wohnungsbau
1. Auflage 2018
ISBN 978-3-942789-57-8

E.ON ERC Band 59
Frieling, J.
Quantifying the Role of Energy in Aggregate Production Functions for Industrialized Countries
1. Auflage 2018
ISBN 978-3-942789-58-5

E.ON ERC Band 60
Lauster, M.
Parametrierbare Gebäudemodelle für dynamische Energiebedarfsrechnungen von Stadtquartieren
1. Auflage 2018
ISBN 978-3-942789-59-2

E.ON ERC Band 61
Zhu, L.
Modeling, Control and Hardware in the Loop in Medium Voltage DC Shipboard Power Systems
1. Auflage 2018
ISBN 978-3-942789-60-8

E.ON ERC Band 62
Feron, B.
An optimality assessment methodology for Home Energy Management System approaches based on uncertainty analysis
1. Auflage 2018
ISBN 978-3-942789-61-5

E.ON ERC Band 63
Diekerhof, M.
Distributed Optimization for the Exploitation of Multi-Energy Flexibility under Uncertainty in City Districts
1. Auflage 2018
ISBN 978-3-942789-62-2

E.ON ERC Band 64
Wolisz, H.
Transient Thermal Comfort Constraints for Model Predictive Heating Control
1. Auflage 2018
ISBN 978-3-942789-63-9

E.ON ERC Band 65
Pickartz, S.
Virtualization as an Enabler for Dynamic Resource Allocation in HPC
1. Auflage 2019
ISBN 978-3-942789-64-6

E.ON ERC Band 66
Khayyamim, S.
Centralized-decentralized Energy Management in Railway System
1. Auflage 2019
ISBN 978-3-942789-65-3

E.ON ERC Band 67
Schlösser, T.
Methodology for Holistic Evaluation of Building Energy Systems under Dynamic Boundary Conditions
1. Auflage 2019
ISBN 978-3-942789-66-0

E.ON ERC Band 68
Cui, S.
Modular Multilevel DC-DC Converters Interconnecting High-Voltage and Medium-Voltage DC Grids
1. Auflage 2019
ISBN 978-3-942789-67-7

E.ON ERC Band 69
Hu, J.
Modulation and Dynamic Control of Intelligent Dual-Active-Bridge Converter Based Substations for Flexible DC Grids
1. Auflage 2019
ISBN 978-3-942789-68-4

E.ON ERC Band 70
Schiefelbein, J.
Optimized Placement of Thermo-Electric Energy Systems in City Districts under Uncertainty
1. Auflage 2019
ISBN 978-3-942789-69-1

E.ON ERC Band 71
Ferdinand, R.
Grid Operation of HVDC-Connected Offshore Wind Farms: Power Quality and Switching Strategies
1. Auflage 2019
ISBN 978-3-942789-70-7

E.ON ERC Band 72
Musa, A.
Advanced Control Strategies for Stability Enhancement of Future Hybrid AC/DC Networks
1. Auflage 2019
ISBN 978-3-942789-71-4

E.ON ERC Band 73
Angioni, A.
Uncertainty modeling for analysis and design of monitoring systems for dynamic electrical distribution grids
1. Auflage 2019
ISBN 978-3-942789-72-1

E.ON ERC Band 74
Möhlenkamp, M.
Thermischer Komfort bei Quellluftströmungen
1. Auflage 2019
ISBN 978-3-942789-73-8

E.ON ERC Band 75
Voss, J.
Multi-Megawatt Three-Phase Dual-Active Bridge DC-DC Converter
1. Auflage 2019
ISBN 978-3-942789-74-5

E.ON ERC Band 76
Siddique, H.
The Three-Phase Dual-Active Bridge Converter Family: Modeling, Analysis, Optimization and Comparison of Two-Level and Three-Level Converter Variants
1. Auflage 2019
ISBN 978-3-942789-75-2

E.ON ERC Band 77
Heesen, F.
An Interdisciplinary Analysis of Heat Energy Consumption in Energy-Efficient Homes: Essays on Economic, Technical and Behavioral Aspects
1. Auflage 2019
ISBN 978-3-942789-76-9

E.ON ERC Band 78
Möller, R.
Untersuchung der Durchschlagspannung von Mineral-, Silikonölen und synthetischen Estern bei mittelfrequenten Spannungen
1. Auflage 2020
ISBN 978-3-942789-77-6

E.ON ERC Band 79
Höfer, T.
Transition Towards a Renewable Energy Infrastructure: Spatial Interdependencies and Stakeholder Preferences
1. Auflage 2020
ISBN 978-3-942789-78-3

E.ON ERC Band 80
Freitag, H.
Investigation of the Internal Flow Behavior in Active Chilled Beams
1. Auflage 2020
ISBN 978-3-942789-79-0

E.ON ERC Band 81
Razik, L.
High-Performance Computing Methods in Large-Scale Power System Simulation
1. Auflage 2020
ISBN 978-3-942789-80-6

E.ON ERC Band 82
Mirz, M.
A Dynamic Phasor Real-Time Simulation Based Digital Twin for Power Systems
1. Auflage 2020
ISBN 978-3-942789-81-3

E.ON ERC Band 83
Schmitz, H.
Energy Consumption Behavior of Private Households: Heterogeneity, Prosuming, and Rebound
1. Auflage 2020
ISBN 978-3-942789-82-0

E.ON ERC Band 84
Cupelli, L.
Data-driven Methods for Voltage Control in Distribution Networks: A Bottom-Up Approach
1. Auflage 2020
ISBN 978-3-942789-83-7

E.ON ERC Band 85
Happ, S.
A Scalable Simulation Method for Cyber-Physical Power Systems
1. Auflage 2020
ISBN 978-3-942789-84-4

E.ON ERC Band 86
Rewitz, K.
Modellierung des thermischen Komforts in Kabinen-innenräumen
1. Auflage 2021
ISBN 978-3-948234-00-3

E.ON ERC Band 87
Wesseling, M.
Probabilistische Bewertung von Entrauchungsanlagen
1. Auflage 2021
ISBN 978-3-948234-01-0

E.ON ERC Band 88
Stoyanova, I.
Cooperative Energy Management and Cross-Domain Optimization for Electro-Thermal Devices at City-District and City-Level
1. Auflage 2021
ISBN 978-3-948234-02-7

E.ON ERC Band 89
Tran, T.
Advanced hierarchical control structure for Virtual Oscillator-based distributed generation in multi-bus microgrids under different grid dynamics and disturbances
1. Auflage 2021
ISBN 978-3-948234-03-4

E.ON ERC Band 90
Yang, Z.
On the Stability of Three-Phase Grid-Tied Photovoltaic Inverter Systems
1. Auflage 2021
ISBN 978-3-948234-04-1

E.ON ERC Band 91
Wang, T.
Fault Detection and Isolation in DC Distribution Grids
1. Auflage 2021
ISBN 978-3-948234-05-8

E.ON ERC Band 92
Beushausen, S.
A GaN-Based Switched-Mode Gate-Drive Unit for Medium-Voltage IGBTs
1. Auflage 2021
ISBN 978-3-948234-06-5

E.ON ERC Band 93
Schumacher, M.
Design and Assessment of Grid-driven Distributed Cogeneration
1. Auflage 2021
ISBN 978-3-948234-07-2

E.ON ERC Band 94
Joebges, P.
Distributed Real-Time Simulation of Modular Bidirectional DC-DC Converters for Control-Hardware-in-the-Loop
1. Auflage 2021
ISBN 978-3-948234-08-9

E.ON ERC Band 95
Averous, R.
Analysis of the Application of a Grid Emulator to Conduct Grid Compliance Tests for Multi-Megawatt Wind Turbines A Contribution towards Ground Testing of Wind Turbines
1. Auflage 2021
ISBN 978-3-948234-09-6

E.ON ERC Band 96
Virdag, A.
Design, Implementation and Analysis of DC Circuit-breaker for Low-Voltage DC Grids with Counter-current Injection Principle
1. Auflage 2021
ISBN 978-3-948234-10-2

E.ON ERC Band 97
Dähling, S.
Cloud-based Multi-Agent Systems for Flexibility Management in Future Distribution Grids
1. Auflage 2021
ISBN 978-3-948234-11-9

E.ON ERC Band 98
Qawasmi, A.
Fault Current Interruption Analysis and Development of a Power Semiconductor Switch for a Medium-Voltage DC Hybrid Circuit Breaker
1. Auflage 2021
ISBN 978-3-948234-12-6

E.ON ERC Band 99
Nolting, L.
Die Versorgungssicherheit mit Elektrizität im Kontext von Liberalisierung und Energiewende
1. Auflage 2021
ISBN 978-3-948234-13-3

E.ON ERC Band 100
Mathis, P.
Heat Transfer Enhancement in Natural Convective Channel Flows by Vortex Streets
1. Auflage 2022
ISBN 978-3-948234-14-0

E.ON ERC Band 101
Wolff, S.
Stated Preferences Concerning Private Passenger and Light-Duty Electric Vehicles in Germany
1. Auflage 2022
ISBN 978-3-948234-15-7

E.ON ERC Band 102
Hackbarth, A.
Private Households' Preferences for Alternative Fuel Vehicles in Germany – An Empirically Founded Analysis of Adoption Decisions, Willingness-to-Pay, and Policy Scenarios
1. Auflage 2022
ISBN 978-3-948234-16-4

E.ON ERC Band 103
Ge, L.
Performance Enhancement of Switched Reluctance Machines for High-speed Backup Generators: Design, Measurement and Control
1. Auflage 2022
ISBN 978-3-948234-17-1

E.ON ERC Band 104
Atasoy, T.
Strategic and Behavioral Responses of Consumers and Producers to Energy and Environmental Policies
1. Auflage 2022
ISBN 978-3-948234-18-8

E.ON ERC Band 105
Remmen, P.
Automated Calibration of Non-Residential Urban Building Energy Modeling
1. Auflage 2022
ISBN 978-3-948234-19-5

E.ON ERC Band 106
Schild, T.
Systematische Entwicklung strukturierter Steuerungs-algorithmen für die Gebäude- und Anlagentechnik
1. Auflage 2022
ISBN 978-3-948234-20-1

E.ON ERC Band 107
Sidik, Y.
Modeling, Control, and Dynamic Stability Analysis of Two-Stage DC Collector Grids in Offshore Wind Park Clusters
1. Auflage 2022
ISBN 978-3-948234-21-8

E.ON ERC Band 108
Sadu, A.
Towards resilient design of distribution grid automation system: An evaluation of its reliability against random failures and susceptibility to targeted attacks
1. Auflage 2022
ISBN 978-3-948234-22-5

E.ON ERC Band 109
Hinz, A.
Electrical Propulsion Systems for Civil Transportation Aircraft
1. Auflage 2022
ISBN 978-3-948234-23-2

E.ON ERC Band 110
Mehrfeld, P.
Evaluation of Heat Pump Systems Under Dynamic Operating Conditions
1. Auflage 2022
ISBN 978-3-948234-24-9

E.ON ERC Band 111
Teichrib, J.
A Hybrid Semiconductor Device for Medium-Voltage DC-DC Converters - The Combination of Thyris-tor and Transistor Technologies
1. Auflage 2022
ISBN 978-3-948234-25-6

E.ON ERC Band 112
Frehn, A.
Under voltage ride through tests on nacelle test benches equipped with a power hardware in the loop setup
1. Auflage 2023
ISBN 978-3-948234-26-3

E.ON ERC Band 113
Bode, G.
Generation of Training Data for Fault Detection and Diagnosis Algorithms Using Fault Simulation and Parameter Uncertainty
1. Auflage 2023
ISBN 978-3-948234-27-0

E.ON ERC Band 114
Vering, C.
Optimale Auslegung von Wärmepumpensystemen für Bestandsgebäude
1. Auflage 2023
ISBN 978-3-948234-28-7

E.ON ERC Band 115
Bogdanović, M.
Towards model partitioning automation of distributed real-time power systems simulations of distribution networks
1. Auflage 2023
ISBN 978-3-948234-29-4

E.ON ERC Band 116
Hering, D.
Optimization of district heating networks using mixed integer quadratically constrained programs
1. Auflage 2023
ISBN 978-3-948234-30-0

E.ON ERC Band 117
De Din, E.
Multi-Timescale Framework for the Voltage Control of Active Distribution Grids
1. Auflage 2023
ISBN 978-3-948234-31-7

E.ON ERC Band 118
Specht, J.
The Energy Supplier 2.0 – Activating Private Households' Flexibility Potential for Value Creation and Services Supply
1. Auflage 2023
ISBN 978-3-948234-32-4

E.ON ERC Band 119
Teichmann, J.
Auswirkungen der Hydraulik auf das Betriebsverhalten von raumlufttechnischen Anlagen
1. Auflage 2023
ISBN 978-3-948234-33-1

E.ON ERC Band 120
Haghgoo, M.
Semantic Interoperability as a Service for the Smart Energy System
1. Auflage 2023
ISBN 978-3-948234-34-8

E.ON ERC Band 121
Roy, G.
Automation Architectures for hybrid ac-dc grid
1. Auflage 2023
ISBN 978-3-948234-35-5

E.ON ERC Band 122
Mork, M.
Model Predictive Control of Building Energy Systems
1. Auflage 2023
ISBN 978-3-948234-36-2

E.ON ERC Band 123
Zargar, B.
Data-Driven Distribution System State Estimation Using Synchrophasor Measurements
1. Auflage 2023
ISBN 978-3-948234-37-9

E.ON ERC Band 124
Rohn, M.
Einseitiges Induktionsverhalten von multiplen Luftstrahlen unterschiedlicher Düsengeometrien
1. Auflage 2024
ISBN 978-3-948234-38-6

E.ON ERC Band 125
Sheykhha, S.
Four essays on the sustainable energy transition: Model-based analyses of regional energy market structures and regulations
1. Auflage 2024
ISBN 978-3-948234-39-3

E.ON ERC Band 126
Warmuz, J.
Current Interruption Capability and Feasibility Assessment for a Medium-Voltage Direct Current Hybrid Circuit Breaker Application
1. Auflage 2024
ISBN 978-3-948234-40-9

E.ON ERC Band 127
Gürses, G.
Machine learning techniques for time series forecasting in power systems operation
1. Auflage 2024
ISBN 978-3-948234-41-6

E.ON ERC Band 128
Baranski, M.
Design of Distributed Model-based Control Agents for Building Automation Systems
1. Auflage 2024
ISBN 978-3-948234-42-3

E.ON ERC Band 129
Karami, M.
Driving Sustainability Through Business Model Innovation in the Energy Industry and Related Sectors
1. Auflage 2024
ISBN 978-3-948234-43-0

E.ON ERC Band 130
Hoffmann, M.
Entwicklung eines Simulationsmodells zur Vorhersage und Optimierung eines Luftwäschers mittels 3-dimensionaler Mehrphasen-Strömungssimulation
1. Auflage 2024
ISBN 978-3-948234-44-7

E.ON ERC Band 131
Stoffel, P.
Learning Strategies for Data-Driven Model Predictive Control of Building Energy Systems
1. Auflage 2024
ISBN 978-3-948234-45-4

E.ON ERC Band 132
Dognini, A.
Multi-criteria service restoration methods for AC and AC/DC distribution grids
1. Auflage 2024
ISBN 978-3-948234-46-1

E.ON ERC Band 133
Schreiner, L.
International Public-Private Strategies in Sustainable Investment and Finance
1. Auflage 2024
ISBN 978-3-948234-47-8

E.ON ERC Band 134
Priesmann, J.
Verteilungseffekte im Kontext der Energiewende: Herausforderungen und regulatorische Lösungsansätze
1. Auflage 2024
ISBN 978-3-948234-48-5

E.ON ERC Band 135
Mortimer, B.
Horizontal Network Coupling for Charging Infrastructure Based on Three-Phase Solid-State Transformers
1. Auflage 2024
ISBN 978-3-948234-49-2

E.ON ERC Band 136
Gümrükcü, E.
A Versatile Strategy for Optimizing Electric Vehicles' Charging Spot Selections in Distribution Grids
1. Auflage 2024
ISBN 978-3-948234-50-8

E.ON ERC Band 137
Pan, Z.
Large Language Model Based Semantic Interoperability Enhancement for Energy Data Management
1. Auflage 2025
ISBN 978-3-948234-51-5

E.ON ERC Band 138
Korompili, A.
Two-Level Control for Multi-Terminal DC Distribution Grids
1. Auflage 2025
ISBN 978-3-948234-52-2

E.ON ERC Band 139
Dinkelbach, J.
Enabling the Real-Time Simulation of Low-Inertia Power Systems by Dynamic Phasor Modelling and Efficient Computing Methods
1. Auflage 2025
ISBN 978-3-948234-53-9

E.ON ERC Band 140
Kümpel, A.
Adaptive agentenbasierte modellprädiktive Regelung für Gebäudeenergiesysteme
1. Auflage 2025
ISBN 978-3-948234-54-6

E.ON ERC Band 141
Gurumurthy, S.
Advanced Harmonic Stability Monitoring and Control of Power-Electronics Dominated Grids
1. Auflage 2025
ISBN 978-3-948234-55-3

E.ON ERC Band 142
Sowa, I.
Distributed Consensus Control Supported by High Reporting Rate Meters in Cyber-Physical Microgrids
1. Auflage 2025
ISBN 978-3-948234-56-0

E.ON ERC Band 143
Klingebiel, J.
Bedarfsgesteuerte Abtauung von Luft-Wärmepumpen durch Reinforcement Learning
1. Auflage 2025
ISBN 978-3-948234-57-7

E.ON ERC Band 144
Ginocchi, M.
Sensitivity Analysis for Power System Applications
1. Auflage 2025
ISBN 978-3-948234-58-4

E.ON ERC Band 145
Ahmadifar, A.
Resilient Microgrid Management in Active Distribution Systems for Normal and Contingency Operations
1. Auflage 2025
ISBN 978-3-948234-59-1

E.ON ERC Band 146
Höges, C.
Kältemittelkreislaufkonfigurationen von Wärmepumpen für die Gebäudebeheizung
1. Auflage 2025
ISBN 978-3-948234-60-7

E.ON ERC Band 147
Stock, J.
Separation of Existing District Heating Networks for Optimal Utilisation of Sustainable Heat Sources
1. Auflage 2025
ISBN 978-3-948234-61-4

E.ON ERC Band 148
Penthong, T.
Towards Automatization of Distance Protection Coordination and Interoperability Testing for Digital Substations
1. Auflage 2026
ISBN 978-3-948234-62-1

E.ON ERC Band 149
Holtwerth, A.
Model Predictive Control of Hybrid Battery-Hydrogen Energy Storage Systems Using Mixed Integer Linear Programming
1. Auflage 2026
ISBN 978-3-948234-63-8

E.ON ERC Band 150
Ostmann, P.
Aeroakustische Emissionen von Luftdurchlässen
1. Auflage 2026
ISBN 978-3-948234-64-5

E.ON ERC Band 151
Kockel, C.
Globale Wasserstoff-wertschöpfungsketten für die Energiewende in Deutschland: Umweltauswirkungen und Kosten unter Unsicherheiten
1. Auflage 2026
ISBN 978-3-948234-65-2

E.ON ERC Band 152
Herzog, F.
Common-Mode Currents in Low-Voltage DC Underlay Grids with AC-Side Grounding
1. Auflage 2026
ISBN 978-3-948234-66-9

E.ON ERC Band 153
Hetzenecker, K.
Optimizing Three-Phase DC-DC Converters for MVDC Grids
1. Auflage 2026
ISBN 978-3-948234-67-6

The global transition to renewable energy reduces power system inertia, threatening frequency stability. Classical control methods struggle to manage operational constraints and coordinate heterogeneous Grid-Forming and Grid-Following resources. To solve this, the dissertation develops advanced Model Predictive Control (MPC) strategies for dynamic frequency and power control in converter-dominated grids. The research introduces a control-oriented prediction model utilizing the Frequency Divider concept. By treating load disturbances as process noise, it ensures full system observability without needing additional states. Using this, MPC strategies for grid-connected hybrid plants to provide virtual inertia, and for islanded microgrids to act as fast secondary control are designed. These methods seamlessly integrate photo-voltaics, battery energy storage systems, and hydrogen electrolyzers. Through Hardware-in-the-Loop experiments and Global Sensitivity Analysis, the superior robustness of the proposed MPCs over classical controllers is thoroughly validated. The dissertation further investigates partitioning of the global prediction model to create resilient distributed MPC architectures. Finally, the controllers are adapted to handle communication delays and signal losses.

ISBN 978-3-948234-68-3

Thinking the Future
Zukunft denken